A GNSS Velocity Field for Estimating Tectonic Plate Motion and Testing Global Glacial Isostatic Adjustment Models

Katarina Vardić

Thesis submitted for the degree of
Doctor of Philosophy

School of Engineering
Newcastle University
Newcastle upon Tyne
United Kingdom

February 2021

Abstract

The two main causes of the long-term deformation of the Earth on a global scale are tectonic plate motion and Glacial Isostatic Adjustment (GIA). GIA results in vertical as well as lateral movements of the Earth's surface. It is difficult to distinguish from local and regional effects, such as the deformational response to decadal and longer-term changes in continental water storage and the mass balance of glaciers and ice sheets. On a global scale, GIA is also, to some extent, difficult to distinguish from millennial-term lateral motion due to plate tectonics. The effects of GIA must therefore be modelled. GIA models use an ice sheet history combined with an estimate for Earth rheology to produce predictions of present-day GIA velocities. GIA models are typically tuned to fit evidence for past and present vertical motion, as determined from historical relative sea-level data, and they may additionally be tuned to fit GNSS-derived present-day uplift rates. However, GNSS-derived horizontal rates have not traditionally been used to tune GIA models. Lateral Earth structure can significantly influence horizontal GIA rates, and most GIA models do not account for lateral structure, these are so-called 1D GIA models. Recently, GIA models accounting for lateral Earth structure have been developed, known as 3D GIA models.

Vertical GIA velocities are important for studies of surface mass loading, sea-level change, mass balance of glaciers and ice sheets, and vertical reference systems. Horizontal GIA velocities are also important for interpreting surface mass loading, as well as tectonic plate rigidity, with implications for horizontal components of reference systems.

Consequently, this project aims to create a bespoke 3D GNSS surface velocity field to test and compare a set of recent 1D and 3D GIA models and investigate tectonic plate motion. In turn, this velocity field has several applications beyond this project. It may be used to investigate present-day surface loading due to ice melting as well as other aspects of the global hydrological cycle, and loading studies in general. The main motivation for creating a bespoke 3D velocity field (as opposed to using, e.g. the most recent International Terrestrial Reference Frame ITRF2014) is to include a larger number of GNSS sites in the GIA-affected areas of investigation, namely North America, Europe, and Antarctica.

GIA and plate motion velocities are at the mm level so the choice of a stable and accurate reference frame plays a crucial role. Here I create the GNSS surface velocity field using the IGS repro2 data and other similarly processed GNSS datasets. The networks are deconstrained, combined and aligned to ITRF2014 on a daily level. For this, I use the Newcastle University-developed reference frame combination software Tanya. Within this project, the software has been updated to be compatible with ITRF2014, including the

discontinuity information and post-seismic deformation models. This resulted in 57% reduction of the WRMS of the alignment post-fit residuals compared to the alignment to ITRF2008. The time series of daily GNSS solutions were used to create the GNSS velocity field. After additional data screening and quality control, the final GNSS velocity field has horizontal uncertainties mostly within 0.5 mm/yr, and vertical uncertainties mostly within 1 mm/yr, which make it suitable for testing GIA models.

I use a suite of GIA models that have been produced by combining three different ice models (ICE-5G, ICE-6G and W12) with a range of 1D and 3D Earth models. By subtracting this ensemble from the velocity field, I identify and compare a range of plate motion models (PMMs), which are then expected to be unaffected by GIA. The impact of GIA on the PMM estimates is investigated and the resulting PMMs are compared with previously published ones. The results show that there can be significant GIA-related horizontal motion which may be modelled into the plate motion if left uncorrected. Using an extensive set of 1D and 3D GIA models allows to include more GNSS sites in the PMM estimate. These sites are in GIA-affected areas which have typically been excluded from PMM estimates. A joint estimation of PMM with GIA is beneficial when investigating GIA with GNSS observations because it reduces dependency on a pre-existing PMM which can be contaminated by GIA.

Next, the predicted horizontal and vertical velocities of each GIA model are subtracted from the GNSS surface velocity field after removing the respective PMM. Median Absolute Deviations (MADs) are computed for the suite of residual fields including the null-GIA case, where GIA predictions were not taken into account. For the 3D GIA models, applying GIA corrections reduces the MAD in all regions. For 1D GIA models, applying GIA corrections reduces the MAD in the majority of regions. Exceptions are found for the vertical component of the velocity field in Antarctica, and the horizontal component in the global case. The latter result indicates that it is not possible to replicate the global horizontal GIA velocity field by combining a 1D Earth model with the global ice models being tested here. Based on the results of this project, it is not possible to conclude that 3D GIA models consistently outperform 1D GIA models or vice-versa. However, it is possible to identify common GIA model features that correspond to better MADs.

Furthermore, a group of best-performing GIA models is selected for each region of interest based on their MADs, and the range of GIA predictions from this group is assumed to represent the uncertainty of GIA models. For Antarctica, a range of equivalent water height values is computed from the group of best-performing GIA models, which in turn can be used as an uncertainty measure when applying GIA corrections in GRACE studies of ice mass change. The total GIA contribution to annual mass change in Antarctica ranges from 5 Gt/yr to 45 Gt/yr depending on which of the best-performing GIA models is used.

Acknowledgements

Firstly I would like to express gratitude to my supervisor professor Peter Clarke and co-supervisor professor Pippa Whitehouse for their guidance and patience over the last four years. Pete, thank you for giving me the opportunity to undertake this PhD, for teaching me to look at the bigger picture, for all the discussions about Tanya when it gave us both such headaches and for your absolutely impeccable sense of humour. Pippa, your approach to work and passion for research have always motivated me. Thank you for coming up with exciting ideas, for the late night emails and for your positive spirit and kind encouragements.

I would like to thank my colleague Dr Achraf Koulali for providing me with the elastic correction data for Antarctica and for some useful discussions in the lunch breaks. I would like to thank Dr Halfdan Pascal Kierulf for providing me with the GNSS data for Fennoscandia and the Baltic. I would like to acknowledge the efforts of New Mexico Tech and all the contributing members of the IGS community for making their data freely available.

I wish to also thank my viva examiners Dr Wouter van der Wal and Dr Nigel Penna for an interesting viva and their useful comments.

Thanks must go to all my colleagues in the Geomatics section for a great work atmosphere and making it a pleasure to go to work. Special thanks to my friends and colleagues (in order of appearance in G.19): Pippa Cowles, Chris Pearson, Maria Peppa, Elias Berra, Miles Clement, Craig Robson, Lesley Davidson, James Goodyear and Andreja Sušnik. Thanks to Ahmed Elsherif for making the weekends in the office fun.

I would like to thank my colleague, friend and apocalypse partner, Marine Roger for all her kindness and the nice times we have had in our office and out of the office in the last three years. Special thanks for the months of the pandemic when you were the only person I was seeing within two metres, the lockdown was made bearable by your down-to-Earth spirit and home-made biscuits.

And out of the work bubble, into a bubble where romance tried to prevail but ended up often enough getting interrupted by geodesy, comes Vegard whom I don't know where to start thanking. Thank you for making me laugh, calming down my worries, and sometimes worrying instead of me. Thank you for your advice, the ones that I took and the ones I ignored. Thank you for being there for me during this entire PhD even when you were on the other side of the North Sea.

I must thank my little brother Petar Krešimir for being an inspiration with his own hard work and persistence. I also want to acknowledge my late grandmother Nediljka who stopped going to school when she was ten years old but still managed to tell her entire village about my PhD. In the end my biggest gratitude goes to my parents without whose support I wouldn't have even gotten to starting this PhD. Thank you for everything you have done for me, for encouraging me to learn and supporting me throughout my entire education, even when it took me to the other side of the continent from you. Thank you for trying to understand what I do and I promise I will not take any more university degrees.

This PhD project was jointly funded by NERC Iapetus Doctoral Training Partnership and School of Engineering at Newcastle University.

Contents

List of abbreviations

AC .... Analysis Centre

BSF .... Block Scaling Factor

CE .... Centre of the solid Earth

CF .... Centre of surface figure

CFEM .... Reference frame origin of a finite element method GIA model

CG .... Reference frame origin of a GIA model

CL .... Centre of Lateral Figure

CM .... Centre of Mass of Earth System

COD .... AC at Centre for Orbit Determination Europe

DORIS .... Doppler Orbitography and Radiopositioning Integrated by Satellite

EMR .... AC at Natural Resources Canada

ESA .... AC at European Space Agency

EOP .... Earth Orientation Paremeters

EUREF ...... European Permanent GNSS Network

GFZ .... GeoForschungZentrum (Germany)

GIA .... Glacial Isostatic Adjustment

GLONASS ... GLObalnaya Navigatsionnaya Sputnikovaya Sistema

GMT .... Generic Mapping Tools

GNAAC ..... Global Network Associate Analysis Centre

GNSS .... Global Navigation Satellite System

GPS .... Global Positioning System

GRACE ...... Gravity Recovery and Climate Change Experiment

GRACE FO . GRACE Follow On

GRG .... AC at Groupe de Recherche en Géodésie Spatiale

IERS .... International Earth Rotation Service

IGS .... International GNSS Service

ITRF .... International Terrestrial Reference Frame

JPL .... AC at Jet Propulsion Laboratory

LGM .... Last Glacial Maximum

MAD .... Median Absolute Deviation

MIDAS ...... Median Interannual Difference Adjusted for Skewness

MIT .... AC at Massachusetts Institute of Technology

NNR .... No Net Rotation

PMM .... Plate motion model

PREM .... Preliminary Reference Earth Model

PSD .... Post-Seismic Deformation

RMS .... Root Mean Square Error

RSL .... Relative Sea Level

SINEX .... Solution Independent Exchange Format

SIO .... AC at Scripps Institute of Technology

SLE .... Sea Level Equation

SLR .... Satellite Laser Ranging

TRF .... Terrestrial reference frame

TRS .... Terrestrial reference system

VCM .... Variance Covariance Matrix

VLBI .... Very Long Baseline Interferometry

WRMS .... Weighted Root Mean Square Error

η_{LM} .... Lower mantle viscosity

η_{UM} .... Upper mantle viscosity

List of Figures

List of Tables

Chapter 1

Introduction

1.1 Background and motivation

Geodetic observations of the Earth provide invaluable insights into its geometry and physics (gravity field), including a large variety of terrestrial dynamic processes on a wide range of spatial and temporal scales (Plag and Pearlman, 2009). Detailed knowledge of these processes is essential for the realization of accurate, long-term stable reference systems which in turn are decisive for assigning time-dependent coordinates to points and objects. The geodetic monitoring of the time-varying geophysical processes in the solid Earth as well as in the hydrosphere and the atmosphere, contributes to research in geodynamics (Torge and Müller, 2012). Many processes in the Earth's interior are still not fully understood. These include core-mantle dynamics and motions in the fluid outer core, mantle convection and the interaction of mantle and lithosphere (plate tectonics), which give rise to crustal deformations (i.e. horizontal and vertical displacements) as well as gravity changes.

Local-to-regional crustal deformation is typically due to plate boundary deformation, earthquakes, volcanoes, erosion, and land slides (Bock and Melgar, 2016). Other local crustal deformations are anthropogenic, and related to oil, natural gas and geothermal field exploration, depletion of groundwater, mining, and disruption of surface loads in water reservoirs (Torge and Müller, 2012). Anthropogenic crustal deformation is typically in the form of land subsidence. Globally, tectonic plate motion and glacial isostatic adjustment (GIA) are the dominant long-term (secular) crustal/surface deformation processes. GIA is the secular response of the solid Earth to past ice surface load change. Quantifying and modelling crustal deformation at local to global scales improves our understanding of the underlying processes, and this understanding in turn helps mitigate the impact of natural hazards on life and infrastructure (Bock and Melgar, 2016).

The advent of space geodesy has contributed substantially to studies of crustal deformation (Bock and Melgar, 2016). For example, crustal deformation may be directly observed using 3D geometric positioning techniques such as Global Navigation Satellite Systems (GNSS), at certain observation sites on Earth's surface repeatedly or continuously (Torge and Müller, 2012). Global space-geodetic networks can give geocentric site coordinates for specific epochs as well as their velocities. Space geodetic techniques include GNSS, Very Long Baseline Interferometry (VLBI), Satellite Laser Ranging (SLR), and Doppler Orbitography and Radiopositioning Integrated by Satellite (DORIS). Individual network solutions are combined to form the integral part of the International Terrestrial Reference Frame (ITRF). A reference frame is a physical realization of a conventional reference system, i.e. a set of estimated positions and velocities. ITRF2014 (Altamimi et al., 2016) is the most recent ITRF. Besides using a longer time-span of measurements than the previous ITRF, a part of the ITRF2014 data is the International GNSS Service (IGS) second reprocessing campaign (repro2), a full reanalysis of GNSS data since 1994 which provides a more extensive and accurate dataset of surface velocities than previously. Unlike the previous ITRF realizations, ITRF2014 provides post-seismic deformation models for sites affected by earthquakes and it takes into consideration annual and semi-annual signals. It is therefore the most accurate ITRF to date, at the mm/yr level. A measurement can only be as accurate as the realization of the coordinate system it is expressed in. Consequently, a high-quality terrestrial reference frame is a decisive element and a limiting factor when interpreting processes on the millimetre level. GIA and plate tectonics are at the mm/yr level and therefore the accuracy of the measurements used to test and constrain them is crucial.

The horizontal velocities derived from global space-geodetic networks are mainly due to tectonic plate motion (Torge and Müller, 2012). Geodetic plate motion models (PMMs) typically assume rigid plates rotating on the Earth's surface. In other words, it is assumed that the plates are capable of transmitting stresses over long horizontal distances without distorting, meaning that the relative motion between plates is taken up only along plate boundaries (Fowler, 2005). Therefore, observing horizontal motion after removing plate motion should allow testing whether tectonic plate motion is rigid, should there be no other large-scale effects. Other large-scale crustal deformation is typically found in regions subject to GIA. GIA causes vertical and horizontal movements of the Earth's surface, especially at higher and mid latitudes.

Horizontal GIA motion can be partially absorbed into a plate-fixed regional reference frame or into PMMs determined from space-geodetic techniques (Plag et al., 2002; Kierulf et al., 2003). Klemann et al. (2008) find that the motion of tectonic plates induced by GIA is at or above the order of accuracy of the plate motions determined by precise GNSS observations. King et al. (2015) conclude that regardless of the fact that the horizontal GIA signal is usually small compared to plate motion, not treating GIA when estimating plate motion may introduce biases. For example, when estimating a geodetic PMM, sites affected by an insufficiently known GIA signal are typically excluded (Altamimi et al., 2017). There, a bias may be introduced due to a suboptimal selection of GIA-affected sites to exclude. Métivier et al. (2020) compare vertical GNSS velocities from different ITRF realizations with a set of recent 1D GIA models, but refrain from analysing horizontal velocities due to possible pollution by an insufficiently known GIA signal.

GIA causes redistribution of masses in the interior and on the surface of the Earth which in turn causes fluctuations over thousands of years in the Earth's gravity field and its rotation axis (Spada, 2016). The vertical GIA signal is larger than the horizontal. We need to evaluate the effect of GIA to properly interpret sea-level change and ice-sheet mass balance from gravity data and sea-level observations such as altimetry, and the global water cycle in general, and ultimately, assist in improving climate change studies (e.g. Shepherd et al. (2018)).

The GIA process is difficult to distinguish from the deformational response to decadal and longer-term changes in continental water storage and mass of glaciers and ice sheets (Bromwich and Nicolas, 2010). GRACE (Gravity Recovery and Climate Change Experiment, 2002-2017) and GRACE-FO (Follow On, 2018 -) gravity missions are used for estimating mass changes from time series of gravity measurements. These measurements are not sensitive to the vertical distribution of mass. In other words, it is not possible to separate between gravity signals caused by present-day mass changes and signals caused by GIA-induced mass redistribution (Baur et al., 2009). Velicogna and Wahr (2006a,b) calculated mass loss estimates for Greenland and Antarctica and showed that the error estimates are dominated by GIA uncertainties.

The GIA signal can be obtained by modelling. The way the Earth deforms due to GIA is governed by the structure and composition of the Earth and the extent and time of the ice and water load. Thus, the two main inputs of a GIA model are an Earth model and an ice-loading history.

Until recently, GIA models have been made as models where the Earth's viscosity and the thickness of the lithosphere vary only radially, so-called 1D GIA models. The fact that the possible lateral variations in mantle viscosity are neglected means that such GIA models may not reproduce horizontal and vertical velocities well. 3D GIA models are the ones where the properties in the Earth model vary both radially and laterally. Viscosity depends on temperature, and spatial variations in mantle seismic velocities are related to temperature. Therefore, the 3D distribution of mantle viscosity in these Earth models is defined using seismic velocity models. A et al. (2012) compared 3D GIA models with 1D models for Canada and Antarctica. They compared the model for Canada with RSL data and compared the Antarctic mass estimate results with GRACE and satellite altimetry data. They found only minor differences. However, only one 3D model was used, which does not allow to quantify the uncertainty in the 3D GIA model predictions. van der Wal et al. (2015) used a range of 3D models with varying viscosity and mantle grain size, as well as choosing wet or dry rheology. They corrected GRACE data for the GIA effect with 3D and 1D GIA models for Antarctica. Corrections based on 3D GIA models resulted in smaller ice mass loss compared to 1D GIA models that use the same ice loading histories, which leads to the conclusion that 3D models should be further investigated.

One way of testing GIA models is comparing them with present-day velocities. GNSS measurements can give valuable constraints on GIA models (King et al., 2010). GIA model uncertainties are a combination of uncertainties in the Earth model and uncertainties in defining the spatial and temporal evolution of the ice load (Martín-Español et al., 2016a) as well as uncertainties in the numerical calculation and assumptions in the physical modelling. Validating different GIA models with GNSS measurements helps us understand these effects. GNSS measurements contain velocities from other effects such as present-day elastic loading, tectonics, local effects etc., which need to be accounted for before constraining and validating GIA models. Some of these effects are small and can be neglected for many areas of the Earth. For example, the influence of local effects can be avoided by careful selection of GNSS sites. Regional effects such as elastic loading due to present-day ice sheet melting need to be measured and modelled. This is the case in Antarctica, which to a large extent is still covered in ice.

Validation of GIA vertical velocities has been a subject of extensive research, globally (e.g., Schumacher et al., 2018), in North America (e.g., Lambeck et al., 2017; Yousefi et al., 2018; Kuchar et al., 2019), Europe (e.g., Lambeck et al., 1998; Milne et al., 2001; Hill et al., 2010; Steffen and Wu, 2011; Kierulf et al., 2014; Vestøl et al., 2019), Greenland (e.g., Simpson et al., 2009; King et al., 2010; Khan et al., 2016; van Dam et al., 2017) and Antarctica (e.g., Riva et al., 2009; Martín-Español et al., 2016a; Whitehouse, 2018). Horizontal GIA predictions have been subject to analysis (James and Morgan, 1990; Wu, 2006) and comparison with present-day measurements in Europe (Milne et al., 2001; Kierulf et al., 2014), North America (Sella et al., 2007; Kreemer et al., 2018) and Antarctica (Kaufmann et al., 2005) but they have not yet been as thoroughly tested as the vertical GIA velocities. King et al. (2010) state that larger differences between the different GIA models are expected in horizontal motions and that considering they are at the mm/year level and occur over a spatial scale of several thousand kilometres, the choice of a stable and accurate reference frame plays a crucial role.

GIA models are typically tuned to fit evidence for past and present vertical motion, as determined from relative sea level (RSL) data and GNSS-derived present-day uplift rates. In contrast, GNSS-derived horizontal rates have not traditionally been used to tune GIA models, because lateral variations in Earth structure can significantly influence horizontal rates (Kaufmann et al., 2005), and most GIA models do not account for lateral structure.

To summarize, horizontal GIA predictions require further analysis and validation. Recent 3D GIA models may give a valuable contribution to predictions of horizontal and vertical GIA. Furthermore, there is an indication of a bias caused by GIA in PMMs. Thus, this project investigates the effect of GIA on the estimation of global PMMs and tests an extensive set of 1D and 3D GIA models in the horizontal and vertical components on both global and regional scales.

1.2 Thesis objectives

The main goal of this thesis is to test and compare a set of recent 1D and 3D GIA models and investigate tectonic plate motion by creating a bespoke GNSS velocity field. This velocity field can subsequently be used for investigating present-day surface loading due to ice melting as well as other aspects related to the global hydrological cycle. The surface velocity field needs to be established in an accurate reference frame and have sufficiently global coverage. I create a range of plate motion models using the GNSS velocity field and a suite of GIA models and I focus particularly on investigating the differences between 1D and 3D GIA models.

The main objectives of this thesis are:

1. Derive a global surface velocity field from GNSS measurements
2. Investigate the effect of GIA on estimates of plate motion models
3. Investigate the features of a set of GIA models, compare them and validate them against present-day surface velocities in the horizontal and vertical components

These objectives result in the following outcomes:

1. An updated in-house reference frame combination software that can work with the most recent ITRF2014, taking into consideration site discontinuities and post-seismic deformation. The software can be used for future network combinations.
2. A global surface velocity field aligned to the most recent ITRF2014. It can be used for loading studies and tuning and testing future GIA models.
3. A plate motion model estimated from a global set of GNSS sites and corrected with GIA predictions. It improves the estimate of plate motion in regions where GIA is a significant component of the surface velocity field.
4. Validation of GIA models contributes to the quantification of uncertainty in the (global/regional) GIA signal.

5. The surface velocity field corrected for GIA is useful worldwide for looking at residual present-day deformation, including interpretation of GRACE data or similar investigations of elastic loading.

1.3 Thesis outline

Chapter 2 of this thesis introduces the two main causes of secular global deformation of the Earth - GIA and plate tectonics. I summarize the basic mathematical foundation of GIA modelling, the main inputs to a GIA model and methods of constraining and validating GIA models followed by a description of the GIA models used in this thesis. The final section of Chapter 2 focuses on tectonic plate theory and lists commonly used plate motion models. Chapter 3 focuses on the concept of GNSS networks and reference frames, which serves as an introduction to the methods used in Chapter 4. Chapter 4 describes the method used to create the GNSS daily global position networks, the methods used to combine the time series of daily position networks into a velocity field, as well as the refinements of the velocity field. The supporting information for this chapter, including developments made in the reference frame combination software Tanya which is used to obtain the GNSS networks, is described in Appendix B.

Chapter 5 explains the determination of plate motion models in this thesis, as well as the results of comparing plate motion models created using different GIA models. In Chapter 5 I focus on the plate motion models that have been created using “good” GIA models. The group of “good”, or as I choose to call them, “near-best” models is defined in Chapter 6, which deals with testing and comparing GIA models against the GNSS velocity field, including investigating differences between the 1D and 3D GIA models. This is done globally and in more detail for three regions of interest which are chosen because they are primarily affected by GIA and they are sufficiently covered by GNSS sites. The three regions of interests are the areas of Europe, North America and Antarctica delimited in Figures A.1, A.2 and A.3, respectively. The final conclusions drawn from the previous chapters and suggestions for future work are summarised in Chapter 7.

Chapter 2

Earth structure and global deformation

This chapter can be divided into two parts, describing the two main long-term causes of the deformation of the Earth on a global scale. Following the introductory section on the structure of the Earth, is a section which describes the theory beneath GIA modelling and the GIA models used in this study. The final section describes the fundamentals of plate tectonic theory.

2.1 Earth internal structure

The Earth has a radially layered structure with a core in its centre, surrounded by mantle and crust (Fig. 2.1). The crust is on average 35 km thick beneath continents and 7-8 km thick beneath oceans (Fowler, 2005). The transition from crust to mantle takes place through the Mohorovičić (Moho) discontinuity. The mantle may be divided into two layers, upper mantle and lower mantle, based on their chemical compositions and densities. The uppermost mantle is very heterogeneous as its structure is dependent on plate processes and history (Fowler, 2005). Standard models vary in representation of the uppermost mantle depending on the assumptions made and data used. The boundary between upper and lower mantle is commonly taken to be at ∼670 km, which is where a major seismic velocity discontinuity takes place, caused by mineral phase changes. Global maps have shown variations of this discontinuity of up to 30 km. The mantle extends down ∼2900 km to the core-mantle boundary, beneath which is the core, divided into outer liquid core and inner solid core (Fowler, 2005).

The division into crust, mantle and core is based on the differences in chemical composition of the different layers. The Earth's interior can also be classified in terms of mechanical and physical properties. In this classification, crust and upper mantle are parts of the lithosphere and asthenosphere (Fig. 2.1). The lithosphere is the solid outer layer of the Earth, which comprises the crust and uppermost mantle. The bottom border of the lithosphere is not uniquely defined, it may be delimited by a change in seismic, thermal or mechanical properties which results in different estimates for lithospheric thickness (Whitehouse, 2009). Beneath the lithosphere lies the asthenosphere. This layer is thought to be partially molten and plays an important role in plate tectonics, because it allows the relative motion of the overlying lithospheric plates (Lowrie, 2007). The layers of the Earth down to the bottom border of the lower mantle are the ones that are modelled in making GIA models.

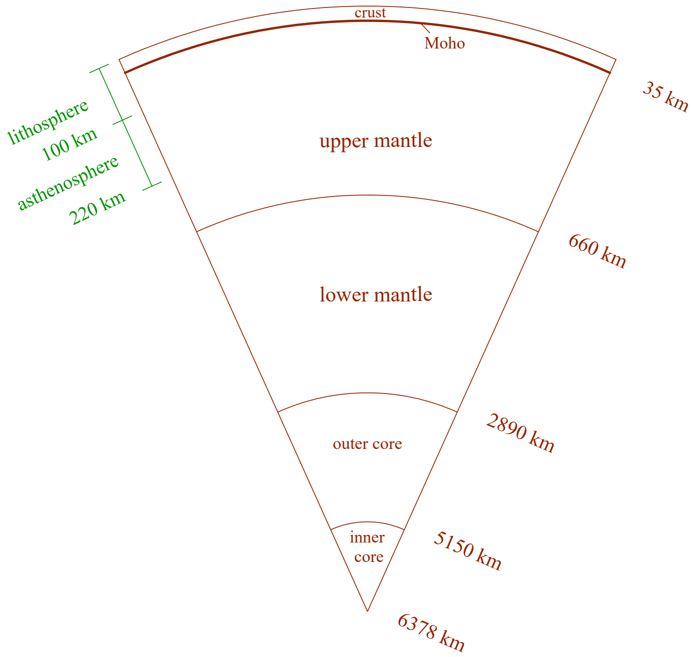

Figure 2.1: Inner structure of the Earth. Based on Fowler (2005) and Montagner (2011).

2.2 GIA modelling

As mentioned, GIA is a result of past surface ice load change. During a glacial period, the ice sheets cover a larger proportion of the Earth's surface. In an interglacial period, some of these ice sheets melt and the water returns to the oceans. The movement of water and ice over the surface of the Earth acts as a change of load on the lithosphere and causes deformation of the Earth. It subsides under the load of an ice sheet and rebounds after it is removed. This deformation is isostatic, i.e. it is an attempt to return the Earth to a state of gravitational equilibrium (Whitehouse, 2009).

The two main inputs of a GIA model are the Earth model and the ice-loading history. The ice loading history determines the ocean loading history through the sea level equation

(Farrell and Clark, 1976) and the combined surface mass distribution of ice and water is then applied as a load to the chosen Earth model (Whitehouse, 2009). The Earth model determines the response of the Earth to the loading.

The Earth's response to loading is typically modelled as rigid, elastic, viscoelastic or anelastic. A material that behaves elastically deforms instantaneously when a force is applied, and returns to its original state immediately after the force has been removed. A viscous material undergoes transient, permanent deformation when a force is applied. The ideal elastic behaviour is defined by three conditions: (1) the strain response to each level of applied stress has a unique equilibrium value, (2) the equilibrium response is achieved instantenously and (3) the response is linear. If the second condition is not met, i.e. if the equilibrium response is not achieved instantaneously, a time delay with the reponse appears which is behaviour known as anelasticity. Therefore, anelasticity represents a response to a load where in addition to an elastic response, there is also a time-delayed non-elastic response. If neither the first nor second conditions are met, a more general behaviour called linear viscoelasticity takes place (Benoit, 2005). For a viscous response, the total response has strain rate proportional to stress, so the relaxation can be complete. In viscoelasticity, a significant part of the response has strain rate proportional to stress, hence the transient but permanent deformation which at least partially relaxes the stress. In anelasticity, the strain rate response and the delay is very small.

The response of the Earth to the loading and unloading in the Last Glacial Maximum is viscoelastic, it entails both instantaneous elastic and longer term viscous deformation, whereas the response of the Earth to present-day mass changes is thought to be mainly elastic (Lange et al., 2014). However, recent research shows the possibility of a viscoelastic response to mass change on decadal time scales (Simpson et al., 2011; Nield et al., 2014). In the following, I will first describe the governing equations and then the Earth and ice models.

2.2.1 Green's functions

A surface load may be defined as a mass resting on the surface of the Earth, causing geometrical surface deformation (displacements) as well as a change in the gravity potential (Torge and Müller, 2012). Green's functions can be used to evaluate the geometrical displacement and the variation of the gravitational potential when a load is applied to the surface of an Earth model. The form of a Green's function depends on the rheological model assumed for the Earth (Peltier, 1974; Farrell and Clark, 1976). Rheology studies the flow of matter and the rheological model refers to the choice of properties for modelling the Earth. Spada and Stocchi (2006) present the Green's functions for the three components of the displacement field and for the incremental gravitational potential in the cases of rigid, elastic and viscoelastic layered Earth models, and the sea level Green's function which is summarized in this section.

A rigid model assumes that the Earth does not change shape when a surface load is applied or removed. If a point mass is applied at the surface of a rigid spherically symmetric Earth, the dynamic mass of the surface load is defined as:

$$\mu(t) = f(t)m_s, \tag{2.1}$$

where $f(t)$ describes the time-evolution of the dynamic mass and m_s is the static mass.

The gravitational potential per unit time exerted by the mass at a point P on the Earth surface, is $\phi^r(\alpha, t)$, where superscript r denotes the rigid Earth and α is the spherical distance between the mass and P. As $\phi^r(\alpha, t)$ adds to the existing background potential of the Earth, Spada and Stocchi (2006) refer to it as the incremental gravitational potential. The Green's function for the incremental gravitational potential for a rigid Earth is defined as:

$$G^r_\phi(\alpha, t) = \frac{\phi^r(\alpha, t)}{m_s} \tag{2.2}$$

In the case of an elastic Earth, the impulsive mass produces two effects in addition to the one caused for a rigid Earth. Firstly, the Earth's shape changes under the pressure of the load, and secondly, it causes a change in the gravitational potential because of the change in the shape of the Earth. The total Green's function for the incremental gravitational potential is a combination of the rigid and elastic components:

$$G_\phi(\alpha, t) = G^r_\phi(\alpha, t) + G^e_\phi(\alpha, t), \tag{2.3}$$

where $G^e_\phi(\alpha, t)$ is the Green's function for the elastic component.

For the case of a viscoelastic Earth, a function for the delayed response of the Earth to the surface load is added to the Green's function for the total incremental gravitational potential which is then:

$$G_\phi(\alpha, t) = G^r_\phi(\alpha, t) + G^e_\phi(\alpha, t) + G^v_\phi(\alpha, t) \tag{2.4}$$

where $G^v_\phi(\alpha, t)$ is the viscous component of the equation which depends on the relaxation times of the employed Earth model.

$G_u(\alpha, t)$ and $G_v(\alpha, t)$ are the Green's functions used to compute the vertical and horizontal components of the (viscoelastic) displacement caused by the applied load. They are sums of the viscous and elastic parts of each component.

The Green's functions for the vertical displacement $G_u(\alpha, t)$, horizontal displacement

$G_v(\alpha, t)$ and the gravitational potential $G_\phi(\alpha, t)$ can be expressed in terms of load-deformation coefficients and Legendre polynomials as (Spada and Stocchi, 2006):

$$\begin{Bmatrix} \frac{1}{\gamma} G_\phi \\ G_u \\ G_v \end{Bmatrix} (\alpha, t) = \frac{a}{m_e} \sum_{l=0}^{\infty} \begin{Bmatrix} k_l \\ h_l \\ l_l \end{Bmatrix} (t) \begin{Bmatrix} 1 \\ 1 \\ \partial_\alpha \end{Bmatrix} P_l(\cos \alpha) \tag{2.5}$$

where γ is the surface gravity acceleration in spherical approximation, m_e is the mass of the Earth, k_l are the viscoelastic loading deformation coefficients for the incremental potential and h_l and l_l are the viscoelastic loading deformation coefficients related to the radial and horizontal components of the displacement, respectively.

The load-deformation coefficients h_l, l_l and k_l used in Eq. (2.5) are called load Love numbers. Love numbers are typically used to model the effects of surface loads connecting the potential of a unit load to vertical and horizontal deformations, and the resulting change in Earth's gravity potential, respectively. The Love numbers are obtained through integration of the equation of motion, stress-strain relations, as well as the Poisson equation for a specific Earth model (Farrell, 1972). Several families of Love numbers exist, and the appropriate numbers must be selected depending on the phenomenon to be modelled. If we want to model surface load, we must use load Love numbers. Due to the computation cost, Love numbers are often tabulated (e.g. Pagiatakis, 1990). The Green's functions (Eq. (2.5)) are infinite sums of Love numbers and Legendre polynomials of spherical harmonic degree l, $P_l(\cos \alpha)$, or derivatives of the latter. The Legendre polynomials act as weights, determining the Earth's response to the surface mass load located at a spherical distance α from a computation point. The spherical harmonic representations are series representations of the vertical, horizontal, and gravity displacement functions on the sphere, and the 2D equivalent to the representation of a 1D function using a Fourier series. In practice, the infinite sums of Love numbers must be truncated at a cutoff value L_{max}.

When using a load Love number formalism, a viscoelastic loading problem can be computed in a reference frame (cf. section 3.2) of choice by transforming the degree 1 Love numbers (Rietbroek, 2016). If the density (volume) change caused by the load is neglected in modelling, the model is said to be incompressible. When dealing with an incompressible Earth model, Love numbers of degree $n = 0$ disappear (Spada et al., 2011). Tanaka et al. (2011) compare results from compressible and incompressible models and find that the present-day vertical velocities due to GIA are only slightly affected by compressibility. However, they find that in the presence of compressibility, the horizontal GIA velocities are larger. Hermans et al. (2018) find for their GIA models that although the magnitudes of the horizontal velocities differ, the directions of the horizontal velocities with incompressible and compressible models agree.

2.2.2 Sea level equation

Sea level is defined as the difference between the geoid and the solid Earth surface at a given point. The sea level Green's function G_s represents the offset between the geoid and the bedrock topography and is defined as:

$$G_s(\alpha, t) \equiv G_\phi - G_u \gamma \tag{2.6}$$

The Green's functions describe the response to a point mass load, which can further be used to evaluate the response of the Earth to time-evolving finite-size surface loads (Spada and Stocchi, 2006).

An ice sheet melting, i.e. a rearrangement of ice and water mass on Earth, causes a change in gravity and relative sea level. GIA models seek to reconstruct the historical ice sheet load and the viscoelastic response of the Earth to ice sheet melting. The sea level equation (SLE), presented by Farrell and Clark (1976), is used to describe the change in relative sea level as a result of GIA. Eustatic sea level change denotes a change in sea level that occurs when a volume of water is taken from the ocean into an ice sheet, or vice versa (Whitehouse, 2009). This sea level change is spatially uniform, it is the change that would occur on a rigid, non-gravitating Earth with fixed ocean shorelines (Spada, 2016). Isostatic sea level change denotes ocean variation in both space and time and is the result of perturbations of the shape of the solid Earth and the geoid due to temporal variations in ice and water loading (Whitehouse, 2009). The SLE describes the changes in sea level which occur due to the adjustment in ice and ocean mass. The explicit form of the SLE is given by (Spada and Stocchi, 2006):

$$S(\alpha, \lambda, t) = \frac{\rho_i}{\gamma} G_s \otimes_i I + \frac{\rho_w}{\gamma} G_s \otimes_o S - \frac{m_i(t)}{\rho_w A_O} - \frac{\rho_i}{\gamma} \overline{G_s \otimes_i I} - \frac{\rho_w}{\gamma} \overline{G_s \otimes S}, \tag{2.7}$$

where $S(\alpha, \lambda, t)$ is the relative sea level change at colatitude α and longitude λ in time t. I and ρ_i are ice load and ice density, respectively, while S on the right hand side is the ocean load and ρ_w the density of water. The terms $\otimes_i$ and $\otimes_o$ represent convolution integrals over the Earth surface covered with ice sheets and over the oceans, respectively. Thus, the first two terms represent the influence of the change of ice sheet load and ocean load to the sea level change. The last two terms represent spatially homogeneous elements where the overbar denotes the mean of the variable over the oceans. The third term represents the eustatic term of the SLE. The final three terms together provide the conservation of mass in the interaction between ice and oceans. The sea level change appears on both sides of the equation making it an integral equation that must be solved iteratively. For a more detailed description of SLE see e.g. Farrell and Clark (1976); Spada and Stocchi (2006).

Solving the SLE gives the relative sea level change with respect to a time in remote history. Indirectly, the SLE can be used to estimate present-day sea level change, displacements (i.e. present-day velocity rates), and the change in geoid. As such, it is used in GIA modelling.

Several processes were neglected in the original definition of the SLE, including shoreline migration, rotational feedback, presence of grounded or floating ice and a 3D Earth structure. When sea level rises, shorelines migrate inland and vice-versa, as sea level falls, shorelines migrate towards the sea. This changes the extent of the area covered with sea which was not taken into consideration in the original form of the SLE. The SLE presented by Farrell and Clark (1976) is valid for a non-rotating Earth. Redistribution of the Earth's surface mass load from ice and oceans perturb the Earth's rotational vector. This in turn deforms the geoid and the solid Earth surface, affecting the relative sea level and further changing the Earth's surface mass load. Rotational feedback only affects the harmonic degree two, order one component in the spherical expansion of sea level variations, therefore a rise and fall in sea-level occur in opposite quadrants of the Earth (Whitehouse, 2009), where the quadrants are defined by axes parallel and perpendicular to the rotation axis (see Fig. 2.2). The presence of a 3D Earth structure (cf. 2.2.3) and floating and marine-grounded ice adds further modifications to the SLE (Whitehouse, 2009).

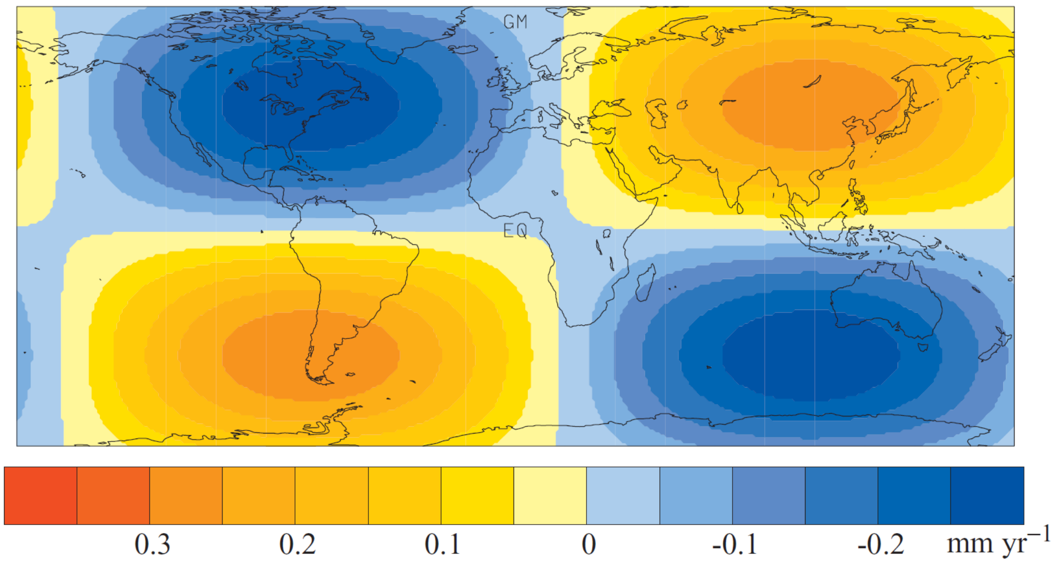

Figure 2.2: The effect of rotational feedback on the present-day rates of vertical solid surface change. Figure taken from Mitrovica et al. (2005).

2.2.3 Earth models

When placed under stress, in the time scale of a glacial cycle of ~100 000 years, the lithosphere shows elastic behaviour, while the mantle shows viscoelastic behaviour. The most common Earth models used in GIA modelling assume a spherically symmetric Earth.

Such models typically consist of an elastic lithosphere of constant thickness. Below the lithosphere lies the mantle, divided into 1 to ∼20 viscoelastic layers. It is most common to divide it into the upper and lower mantle (Whitehouse, 2009). The viscosity in each layer is usually taken to be laterally uniform. The Preliminary Reference Earth Model (PREM, Dziewonski and Anderson (1981)) is the current standard model of the Earth's internal structure and it is used for most spherically symmetric Earth models for determining the Earth's elastic model parameters and density. It is based on the inversion of body-wave, surface-wave and free-oscillation observation data. In Earth models, the viscosity values are obtained by inversion or from independent geophysical studies. Continental lithospheric thicknesses usually range between 70 km and 200 km and the mantle viscosities between 10^{18} Pa s and 10^{24} Pa s. When dividing the mantle into the upper and lower mantle in GIA modelling, the lower mantle typically is found to have a 1-2 orders of magnitude higher viscosity than the upper mantle (Lowrie, 2007; Whitehouse, 2009).

The models described above are typically denoted 1D Earth models since they vary only in the radial direction. The radially layered model of the Earth's interior assumes spherical symmetry which is not valid for the crust, mantle and the core-mantle boundary (Lowrie, 2007). These layers of the Earth show lateral variations. In recent years, models where lithospheric thickness and/or mantle viscosities vary in the lateral direction as well have been developed. These models are termed 3D Earth models. In section 2.2.6 I present the 1D and 3D Earth models used in this study.

2.2.4 Ice sheet modelling

The deformation of the Earth depends on the load set up on it, and ice sheet histories provide the loading or unloading history from the Last Glacial Maximum (LGM) which took place around 20 000 years ago. The accuracy of a GIA model strongly depends on the accuracy of the input ice model. Early ice models use loading "disks" of ice, where the height of a given disk is the change in ice thickness over a specified time period. More recent ice models specify ice thicknesses as a function of both position and time where the ice extent and ice thickness are defined at a series of discrete times. The ice thickness is specified for a given time at a set of discrete points on the surface of the Earth and the distribution of the ice thickness is converted into a spherical harmonic loading function (Whitehouse, 2009).

Ice models may be constrained by geological markers in the areas of the former ice sheet which provide information on past ice extent. The ice models may be further tuned by solving the SLE with a first estimate of the ice-sheet history and comparison to historical sea-level observations. Ice models may then, in creating GIA models, be additionally constrained with observations of relative sea-level history at locations far from the LGM

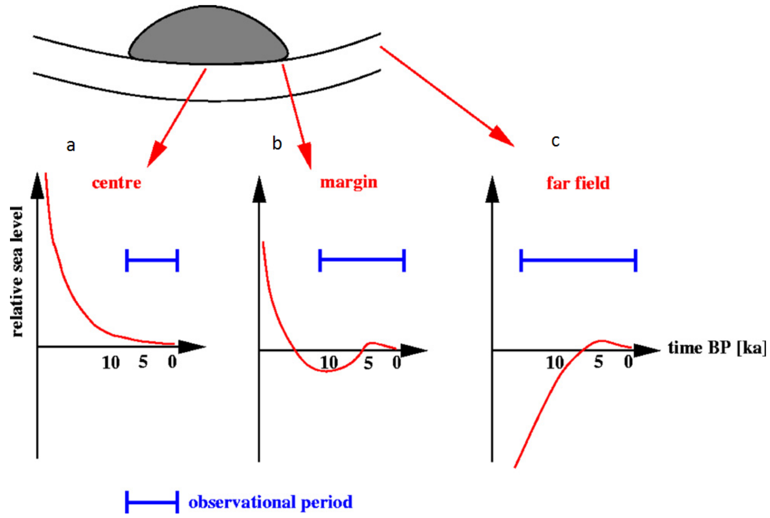

Figure 2.3: Typical variation of sea-level records at different distances from the ice sheet: near field/centre of the ice sheet (a), margin (b), far field (c). Taken from Steffen and Wu (2011)

ice sheets. Past relative sea-level change is preserved in the geological records as a change in the position of the shoreline or a change in water depths (Whitehouse, 2018). The ice models can also be tuned using present-day observations such as GNSS measurements. Besides tuning the ice model, the Earth model may be adjusted in parallel in order to better fit present-day observations. The most widely used global ice models are ICE-5G and ICE-6G described in section 2.2.6.

2.2.5 Datasets used to constrain and validate GIA models

GIA models are constrained using data sets covering different time spans and geographical areas. RSL records cover the longest time span, dating back several thousands of years from deglaciation to present day. They record the height of the land with respect to the sea. Classical RSL data consists of dated paleo-shorelines which may be identified as beach formations or biological sea-level markers (Whitehouse, 2009). Biological sea-level markers are shells, corals, wood, whale bones and pollen with the exact location in relation to the former and present-day sea level (Steffen and Wu, 2011). The sea-level indicators must be only a few kilometres apart to form a sea-level curve, since the shape of the curve varies with location (Fig. 2.3). Historical RSL records come with errors, for instance errors in the local tide range, dating errors or errors due to possibly relocated materials.

Tide gauge measurements observe the height of the sea level with respect to land. They provide an historical record of relative sea-level change with the longest records exceeding 100 years (Douglas, 1991; Woodworth, 2006; Koohzare et al., 2008). GIA, present-day ice mass changes, thermal expansion of ocean water, tectonics or subsidence caused by groundwater extraction are among the geophysical processes that cause relative sea level change.

Present-day deformation rates are constrained by terrestrial and space geodetic techniques. The geodetic data with the longest time span are levelling data, with records of over 100 years in Canada and Fennoscandia. Re-levelling and comparison to older levelling data allows to detect land uplift or subsidence (Ekman and Mäkinen, 1996; Pagiatakis and Salib, 2003). Terrestrial gravity measurements have been performed in Fennoscandia and North America since the 1960s (Pagiatakis and Salib, 2003; Lambert et al., 2006; Olsson et al., 2019), but their spatial extent is limited. Space geodetic techniques including GNSS, VLBI, SLR, satellite gravity missions such as Gravity Field and Steady-State Ocean Circulation Explorer (GOCE) and GRACE, provide a good spatial coverage, but a relatively short time span (Whitehouse, 2009, 2018). Unlike other space geodetic techniques, GNSS observes both horizontal and vertical velocities (Bock and Melgar, 2016). However, GIA models are traditionally not constrained using horizontal GNSS velocities. Recent 3D Earth models (e.g. van der Wal et al. (2015); Goldberg et al. (2016); Gomez et al. (2018)) have been constrained using seismic velocity measurements.

The solutions of GIA modelling obtained from the SLE may be used to improve the input ice and Earth models. Outputs such as historical relative sea level or present-day horizontal and vertical surface deformation are compared with observations, and the input models are then tuned to improve agreement between predictions and observations.

When constraining and validating GIA models, caution must be taken when interpreting the fit of the observations and the models considering the trade-offs between the magnitude and timing of the ice loading history and Earth rheology (Whitehouse, 2018). Fig. 2.4 (a) shows a synthetic example of the trade-off between the timing and magnitude of past surface load. A large ice loss at an earlier time in history can result in the same observed present-day uplift rate as a small ice loss at a later time in history. Fig. 2.4 (b) illustrates a trade-off between an ice model and an Earth model. Large ice loss combined with a weak rheology (lower viscosity) would cause a faster relaxation rate directly after the deglaciation, and produce the same present-day uplift rate as small ice loss combined with a strong rheology (higher viscosity).

An alternative to GIA forward modelling is an empirical inverse approach of estimating the present-day uplift and simultaneously estimating the ice mass change signal from a combination of instrument observations (Wahr et al., 2000; Riva et al., 2009; Gunter et al., 2014; Martín-Español et al., 2016b). Gunter et al. (2014) used GRACE gravity data in combination with ICESat (Ice, Cloud and land Elevation Satellite) satellite altimetry data to estimate present-day effects of GIA and ice mass changes in Antarctica. Satellite altimetry tracks elevation, i.e. volume changes, and GRACE observes variation in gravity, i.e. mass changes. This makes it possible to separate the GIA and ice mass change due to

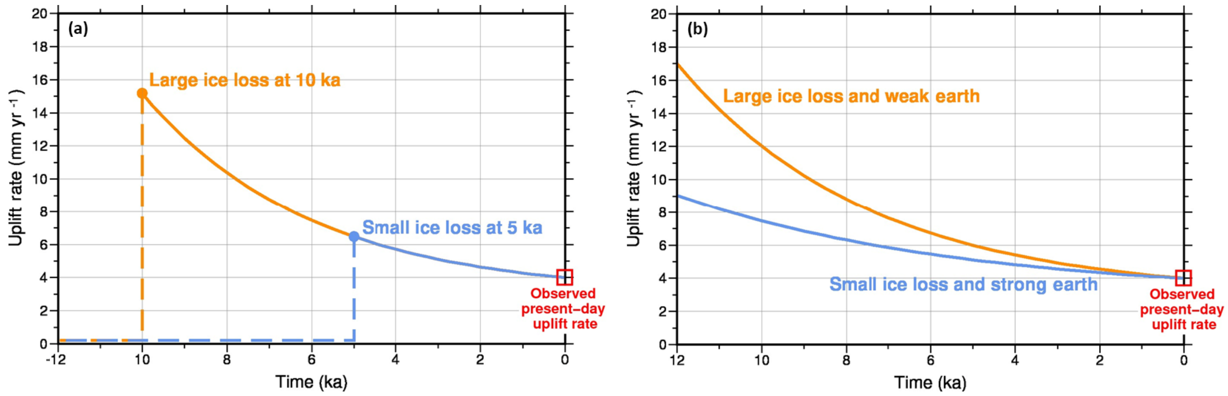

Figure 2.4: Trade-offs between the magnitude and timing of the ice loading history (a) and between magnitude of ice loading history and Earth rheology in GIA modelling (b), that can explain present-day observations. Taken from Whitehouse (2018).

the large difference in density between ice/snow and solid Earth. Martín-Español et al. (2016b) used satellite altimetry, gravity and GNSS data to derive, among other, GIA predictions.

2.2.6 GIA models used in this project

In this project, a suite of GIA models is obtained by combining three different ice models, ICE-5G (Peltier, 2004), ICE-6G (Peltier et al., 2015) and W12 (Whitehouse et al., 2012) with a range of 1D and 3D Earth models. The GIA models have been created by Pippa Whitehouse (personal communication, 2016, 2019). They are named 1D GIA models and 3D GIA models, depending on the Earth model structure.

The 1D GIA models (cf. Table 2.2) have been created with an adaptation of a code developed by Glenn Milne (Mitrovica et al., 2001; Mitrovica and Milne, 2003; Kendall et al., 2005). The 1D Earth models assume a spherically symmetric, self-gravitating Earth with elastic lithosphere and viscoelastic mantle with linear viscosity. The elastic structure of the Earth model is given by PREM. The SLE in the 1D GIA models is solved for including the rotational feedback and shoreline migrations. The parameters varying in the different 1D Earth models are lithosphere thickness and viscosity of the upper and lower mantle. The models have a globally uniform lithosphere thickness of 71 km, 96 km or 120 km. The mantle is divided into upper and lower mantle with laterally uniform viscosity for the upper mantle η_{UM} of $0.3 \cdot 10^{21}$ Pa s, $0.5 \cdot 10^{21}$ Pa s or $0.8 \cdot 10^{21}$ Pa s and lower mantle viscosity η_{LM} $5 \cdot 10^{21}$ Pa s, $10 \cdot 10^{21}$ Pa s or $20 \cdot 10^{21}$ Pa s). Combining these parameters with the three ice models, the number of 1D GIA models amounts to $3{\times}3{\times}3{\times}3 = 81$.

The 3D Earth models used in this thesis do not have a division into lithosphere and upper and lower mantle, but instead five layers defined by the following depths: 35-70 km, 70-120 km, 120-170 km, 170-230 km and 230-400 km. The viscosity varies laterally in each layer and it is derived from mantle temperatures of two seismic velocity models: a velocity model by Schaeffer and Lebedev (2013), termed SL, and a model by Ritsema et al. (2011), termed S40RTS. The 3D models used in this thesis were based on a code developed by Wouter van der Wal (e.g. van der Wal et al., 2013). In the 3D Earth models, the mineral olivine is assumed to be the main mantle material, and the varying input parameters for the 3D Earth models are the grain size and water content. Varying these parameters creates variations in the viscosities derived from the seismic velocity models. These models do not account for rotational feedback. The maximum effect of neglecting the rotational feedback is in the middle of the quadrants as per Fig. 2.2 and it can be up to -0.5 mm/yr subsidence and up to 0.3 mm/yr uplift in predicted present-day GIA velocities (Mitrovica et al., 2005). The dependence of strain on stress can be described with a linear relation or a non-linear one. Most of the GIA models (including the 1D GIA models described above) assume linear (Newtonian) rheology, but in most of the laboratory deformation experiments, stress-strain-rate relations are non-linear (Karato, 2008). With a linear rheology, the effective viscosity is not dependent on stress. When creating GIA models using a non-linear, power law rheology, the effective viscosity depends on stress, i.e. ice model. A flow law for olivine aggregates which describes the dependence of strain rate $\dot{\varepsilon}$ on differential stress σ is (Hirth and Kohlstedt, 2003):

$$\dot{\varepsilon} = A\sigma^n d^{-p} fH_2O^r \ \exp(\alpha\phi) \ \exp(-\frac{E+PV}{RT}) \tag{2.8}$$

where A and α are constants, σ is differential stress and n is the stress exponent, d is grain size and p is the grain size exponent, fH_2O is water fugacity, i.e. water content, and r is the water fugacity exponent, ϕ is the melt fraction, E is the activation energy, V is the activation volume, R is the gas constant and T is the absolute temperature. The two main deformation mechanisms are diffusion and dislocation creep (van der Wal et al., 2013; Turcotte and Schubert, 2002). The creep parameters for diffusion and dislocation creep B_{diff} and B_{disl} are computed from the flow law in Eq. (2.8). Individual strain components are calculated as (van der Wal et al., 2013):

$$\varepsilon = B_{diff} q\Delta t + B_{disl} q^n \Delta t \tag{2.9}$$

where t is time, n is the stress exponent and q is the von Mises stress $q = \sqrt{\frac{3}{2}\sigma'_{ij}\sigma'_{ij}}$ where σ'_{ij} is an element of the deviatoric stress tensor. Effective viscosity can finally be calculated by (van der Wal et al., 2013):

$$\eta_{eff} = \frac{1}{3B_{diff} + 3B_{disl} q^{n-1}} \tag{2.10}$$

For the Earth layers below 400 km, values for B_{diff} and B_{disl} are assumed to vary only radially, since the olivine flow law from Eq. (2.8) is not valid for these depths. When applying Eq. (2.8), E, V, p, r and A are taken from Hirth and Kohlstedt (2003). The pressure as a function of depth is calculated by assuming that the pressure gradient is equal to 0.033 GPa/km and the melt content is set to zero (van der Wal et al., 2015). Grain size, water content and temperature are unknown and are varied depending on the chosen input parameters. The temperature is derived through the density from the above mentioned seismic velocity models SL and S40RTS. The grain size is varied between 1, 4 and 10 mm. The mantle water content is varied between a fully wet (1000 ppm H_2O) and a fully dry state. In combinations with three ice models, this amounts to $2{\times}3{\times}2{\times}3 = 36$ different GIA models with a 3D Earth structure. To facilitate a rough comparison of the viscosities of the 3D GIA models investigated here, Table 2.1 illustrates the dependence of viscosity on the input parameters. Typically a smaller grain size contributes towards lower viscosity while a lower temperature contributes towards higher viscosity. A wet mantle rheology contributes towards lower viscosity, while a dry mantle rheology contributes towards higher viscosity. Note that these are only simplified indications, see Figure 6.1 in Chapter 6 for an example of mantle viscosities of several 3D GIA models.

	low viscosity	**high viscosity**
grain size	small(er)	big(ger)
temperature	high	low
water content	wet	dry

Table 2.1: A rough guide for the relationship between the varying features in 3D Earth models and viscosity, which is used traditionally as a varying parameter in 1D Earth models.

The 1D and 3D GIA models described above are not expressed in the same reference frame. The 1D models are expressed in the centre of mass of the solid Earth (CE, see section 3.2) and the 3D models are expressed in a reference frame that assumes no centre of mass motion (which I denote in this thesis as CFEM since the models are created using a finite element method). The 3D GIA models do not assume compressibility, whereas the 1D GIA models do.

ICE-5G and ICE-6G are global ice models from the ICE-x series and have been developed as parts of GIA modelling efforts. The ICE-x models are based on dated observations of ice-sheet margins, RSL curves and the global mean sea level data curve. ICE-5G was developed together with a VM2 (viscosity model 2) Earth model, resulting in a GIA model ICE-5G VM2 (Peltier, 2004). ICE-6G was developed together with the VM5a Earth model, resulting in the ICE-6G_C (VM5a) GIA model. ICE-6G_C is a refinement of the ICE-5G (VM2) GIA model. The VM5a viscosity depth profile is similar to the VM2 viscosity depth profile. VM2 has a larger number of layers but VM5a is a multilayer fit of VM2. The ICE-6G ice model has been tuned to vertical GPS measurements with the assumption of the VM5a mantle viscosity model. Tuning the ice model with a fixed assumption of the Earth model has directed the focus of improving misfits onto modifications of glaciation history (Peltier et al., 2015). Otherwise, if the Earth model is adjusted, the GIA model fit changes and the ice model would have to be readjusted. W12 is a model of ice sheet history for Antarctica which is combined with the ICE-5G ice model for the northern hemisphere for solving the SLE and creating a GIA model. The W12 ice sheet history for Antarctica is, unlike the ICE-x series, not created by coupling with a viscosity model but instead from an extensive data base of geological and glaciological data.

The naming conventions for the 81 1D GIA models and the 36 3D GIA models are listed in Tables 2.2 and 2.3. The global mean vertical and mean horizontal GIA predictions are shown in Figure 2.5. It can be noticed that the interest regions Europe, Antarctica and North America are markedly affected by GIA.

Figures 2.6 - 2.11 show examples of a 1D and 3D GIA model for the three regions of interest in this study. The example models are the ones that give the smallest residual vertical/horizontal velocity field after correcting for plate motion (Chapter 5) and GIA. The figures are commented on in Chapter 6. The tectonic plate theory is introduced in the next subchapter.

GIA model name	Lithosphere [km] thickness	Upper mantle viscosity [$\cdot 10^{21}$ Pa s]	Lower mantle viscosity [$\cdot 10^{21}$ Pa s]
ilh_96p55	96	0.5	5
ilh_96p510	96	0.5	10
ilh_96p520	96	0.5	20
ilh_96p35	96	0.3	5
ilh_96p310	96	0.3	10
ilh_96p320	96	0.3	20
ilh_96p85	96	0.8	5
ilh_96p810	96	0.8	10
ilh_96p820	96	0.8	20
ilh_120p55	120	0.5	5
ilh_120p510	120	0.5	10
ilh_120p520	120	0.5	20
ilh_120p35	120	0.3	5
ilh_120p310	120	0.3	10
ilh_120p320	120	0.3	20
ilh_120p85	120	0.8	5
ilh_120p810	120	0.8	10
ilh_120p820	120	0.8	20
ilh_71p55	71	0.5	5
ilh_71p510	71	0.5	10
ilh_71p520	71	0.5	20
ilh_71p35	71	0.3	5
ilh_71p310	71	0.3	10
ilh_71p320	71	0.3	20
ilh_71p85	71	0.8	5
ilh_71p810	71	0.8	10
ilh_71p820	71	0.8	20

Table 2.2: The table shows the naming convention used for 1D Earth models throughout this thesis. The first part of the GIA model name "*ilh*" stands for ice loading history and it is in the GIA model names replaced with one of the three ice models - 5G for ICE-5G, 6G for ICE-6G and W12 for W12. The first number after the ice model represents lithosphere thickness in kilometres, the second number upper mantle viscosity η_{UM}in powers of 10^{21}, third number the lower mantle viscosity η_{LM}in powers of 10^{21} Pa s. For example, 6G_120p35 stands for a combination of ICE-6G ice model with an Earth model with lithopshere thickness of 120 km, upper mantle viscosity of $3 \cdot 10^{20}$ and lower mantle viscosity of $5 \cdot 10^{21}$

GIA model name	Mantle velocities model	Water content	Grain size [mm]
ilh_S_dry_10mm	S40RTS	dry	10
ilh_S_dry_1mm	S40RTS	dry	1
ilh_S_dry_4mm	S40RTS	dry	4
ilh_SL_dry_10mm	SL	dry	10
ilh_SL_dry_1mm	SL	dry	1
ilh_SL_dry_4mm	SL	dry	4
ilh_S_wet_10mm	S40RTS	wet	10
ilh_S_wet_1mm	S40RTS	wet	1
ilh_S_wet_4mm	S40RTS	wet	4
ilh_SL_wet_10mm	SL	wet	10
ilh_SL_wet_1mm	SL	wet	1
ilh_SL_wet_4mm	SL	wet	4

Table 2.3: The table shows the naming convention used for 3D Earth models throughout this thesis. The first part of the GIA model name "*ilh*" stands for ice loading history and it is in the GIA model names replaced with one of the three ice models - 5G for ICE-5G, 6G for ICE-6G and W12 for W12. The first number after the ice model represents the seismic velocity model from which the mantle viscosities were derived - SL for (Schaeffer and Lebedev, 2013) and S for S40RTS (Ritsema et al., 2011). The third part of the name is the water content of the rheology and last part of the name is grain size. For example, 5G_S_wet_4mm stands for a combination of ICE-5G ice model with S40RTS mantle viscosities, wet rheology and 4 mm grain size.

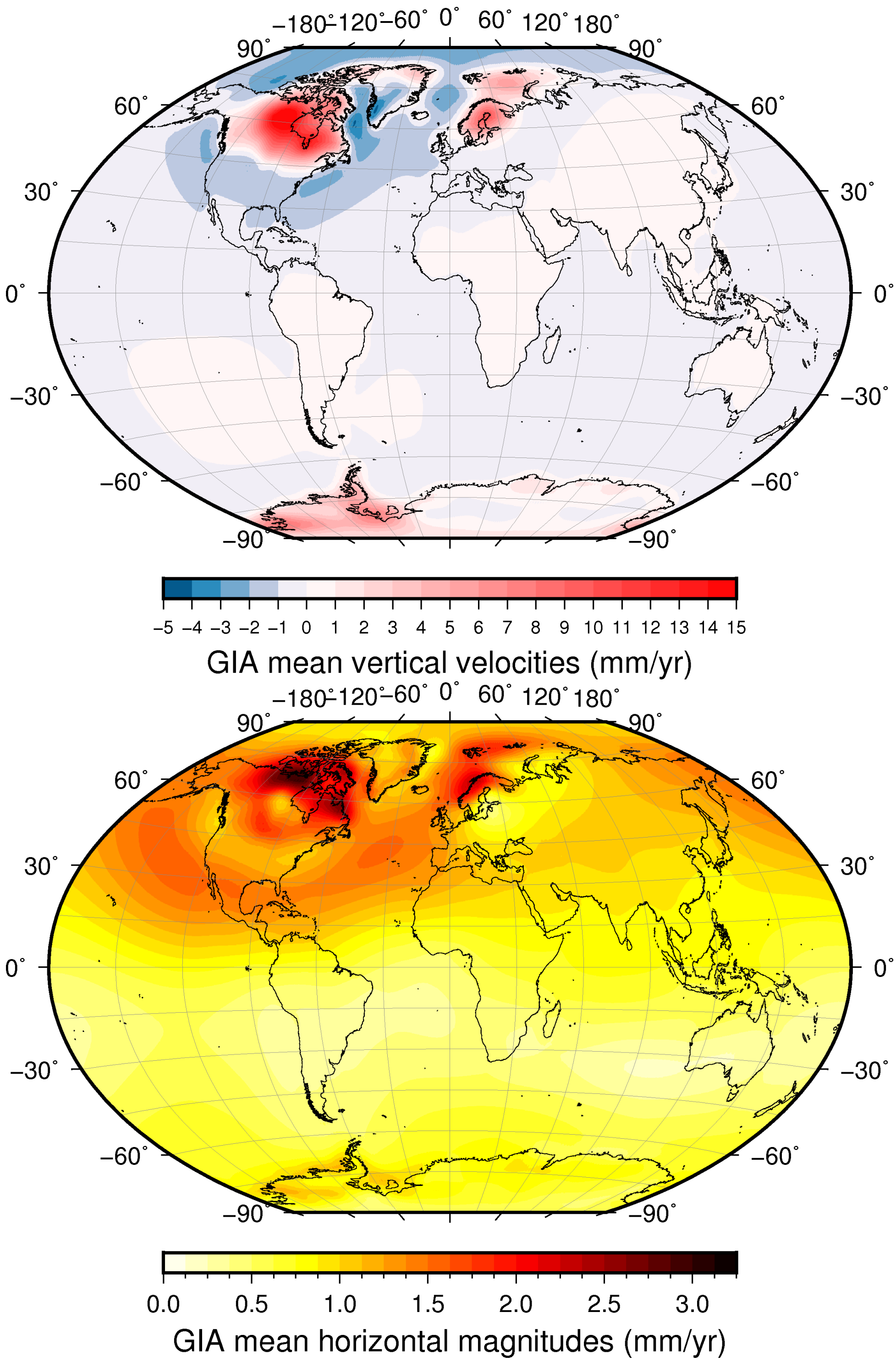

Figure 2.5: Mean GIA vertical velocities (top) and horizontal magnitudes (bottom). The vertical colourbar saturates at 15 mm/yr, with values up to 17 mm/yr in North America

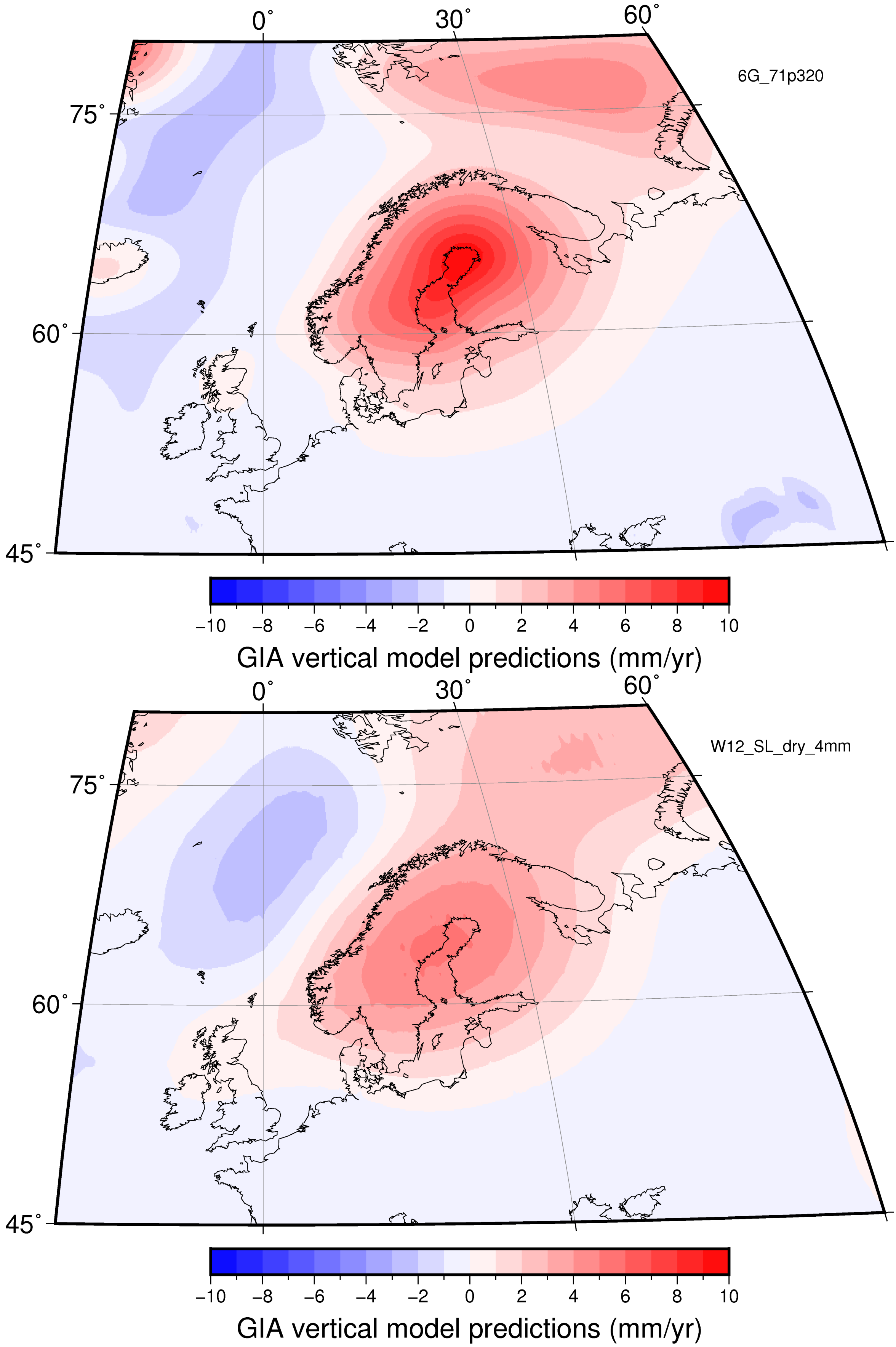

Figure 2.6: GIA vertical predictions in Europe with a 1D GIA model (top, 6G_71p320 which is selected as the best 1D GIA model in the vertical component according to the method from section 6.2.1) and a 3D GIA model (bottom, W12_SL_dry_4mm which is selected as the best 3D GIA model in the vertical component according to the method from section 6.2.1)

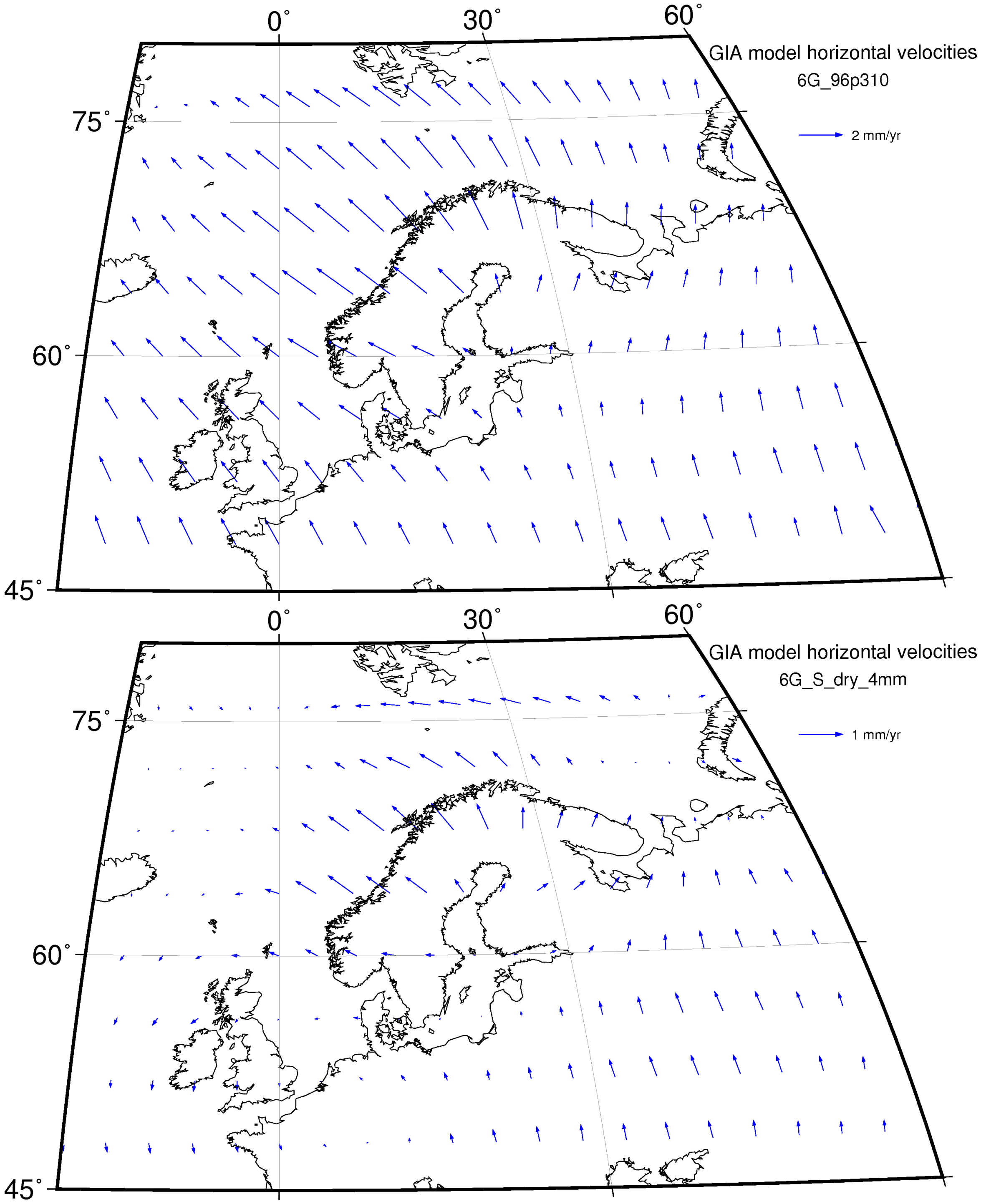

Figure 2.7: GIA horizontal predictions in Europe with a 1D GIA model (top, 6G_96p310) and a 3D GIA model (bottom, 6G_S_dry_4mm). Models selected as per Fig. 2.6.

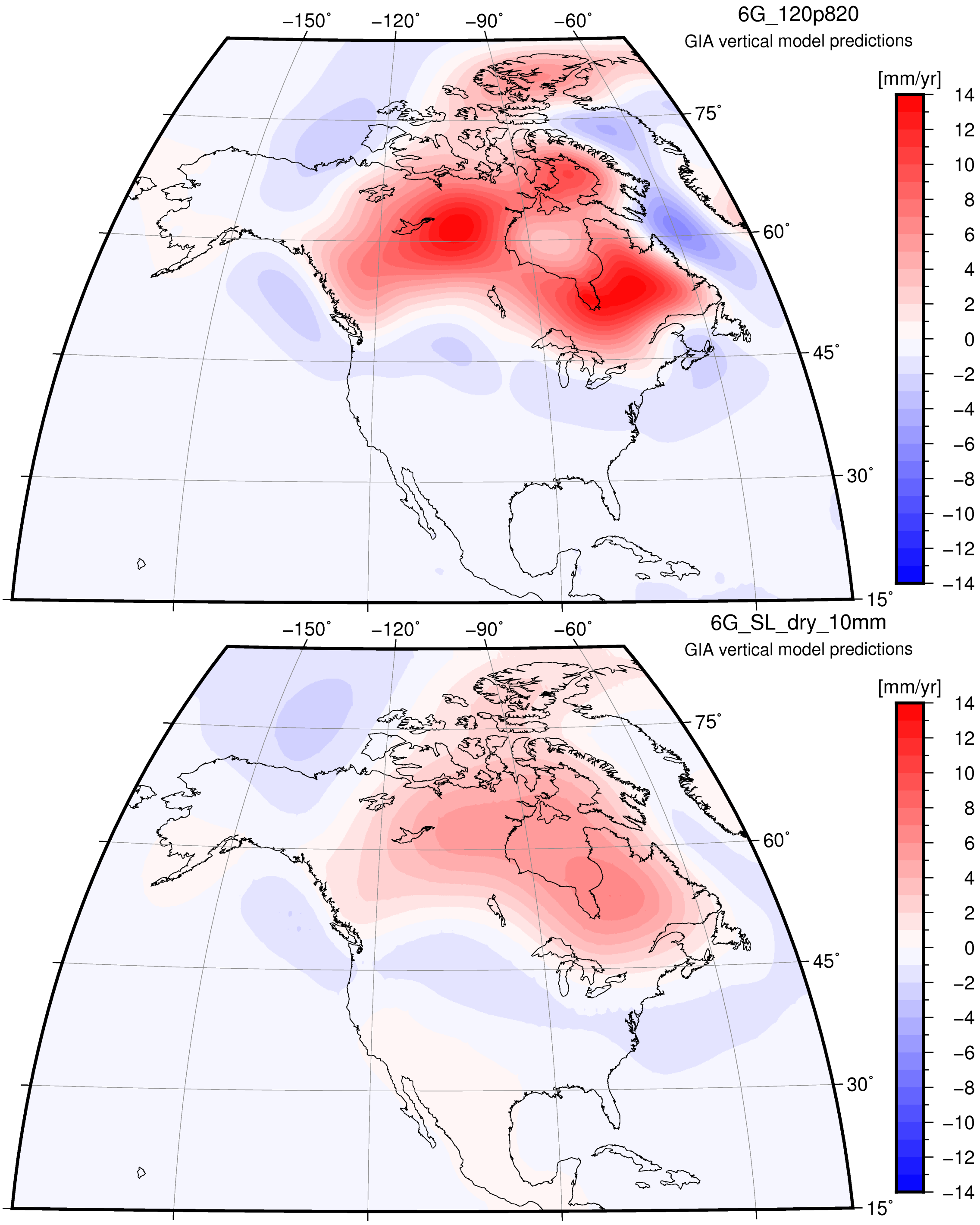

Figure 2.8: GIA vertical model predictions in North America with a 1D GIA model (top, 6G_120p820) and a 3D GIA model (bottom, 6G_SL_dry_10mm). Models selected as per Fig. 2.6.

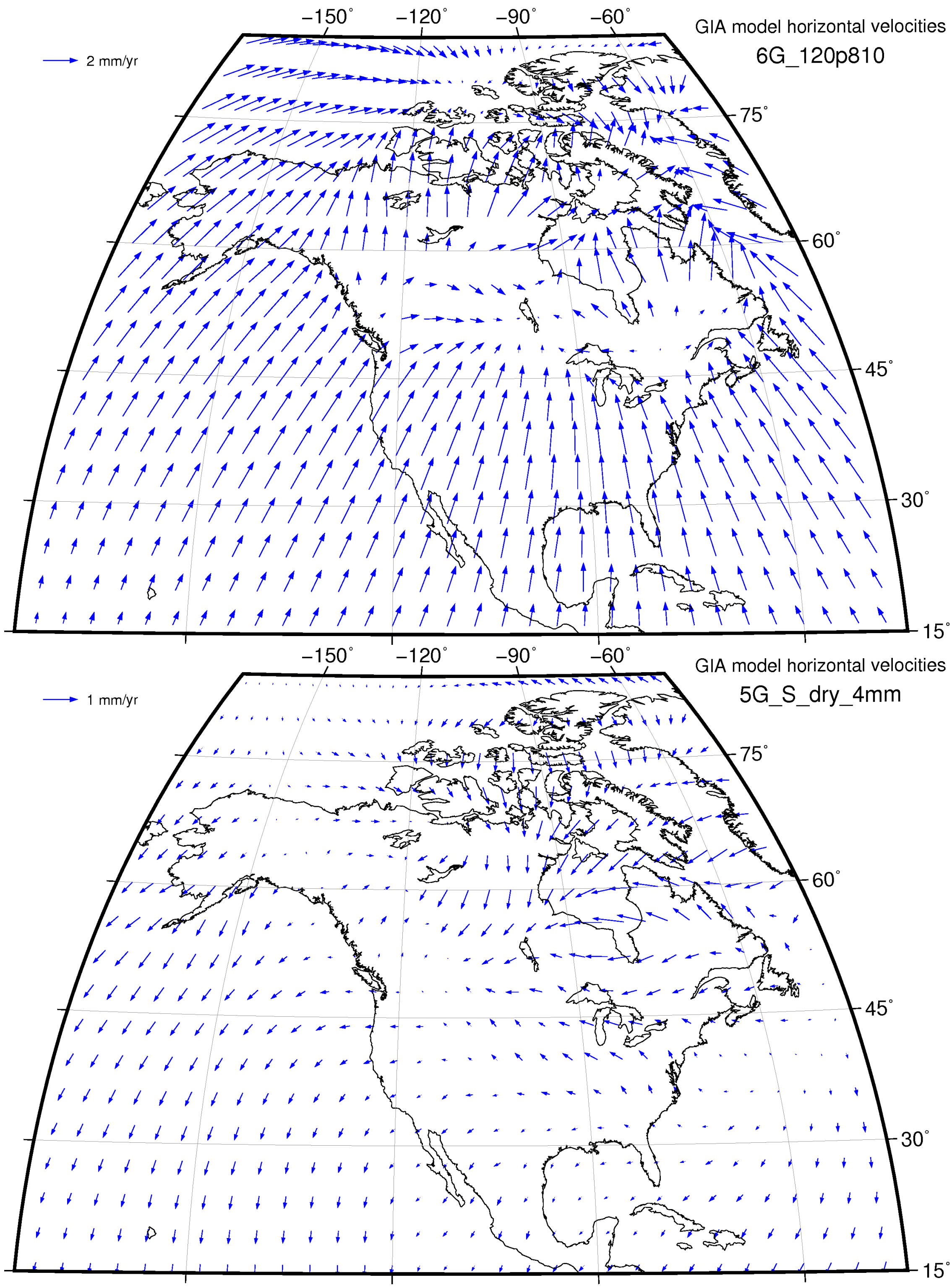

Figure 2.9: GIA horizontal predictions in North America with a 1D GIA model (top, 6G_120p810) and a 3D GIA model (bottom, 5G_S_dry_4mm). Models selected as per Fig. 2.6.

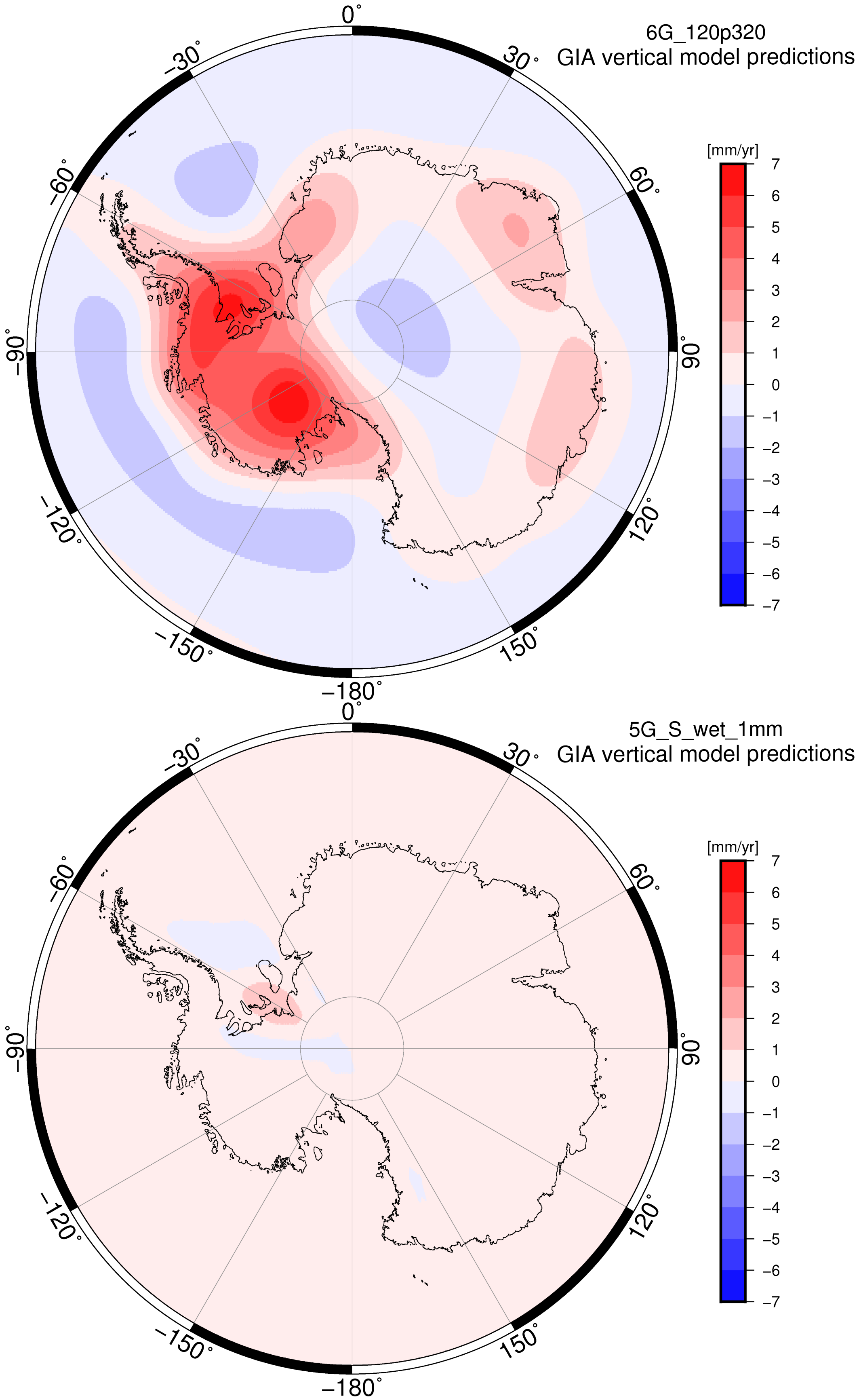

Figure 2.10: GIA vertical model predictions in Antarctica with a 1D GIA model (top, 6G_120p320) and a 3D model (bottom, 5G_S_wet_1mm). Models selected as per Fig. 2.6.

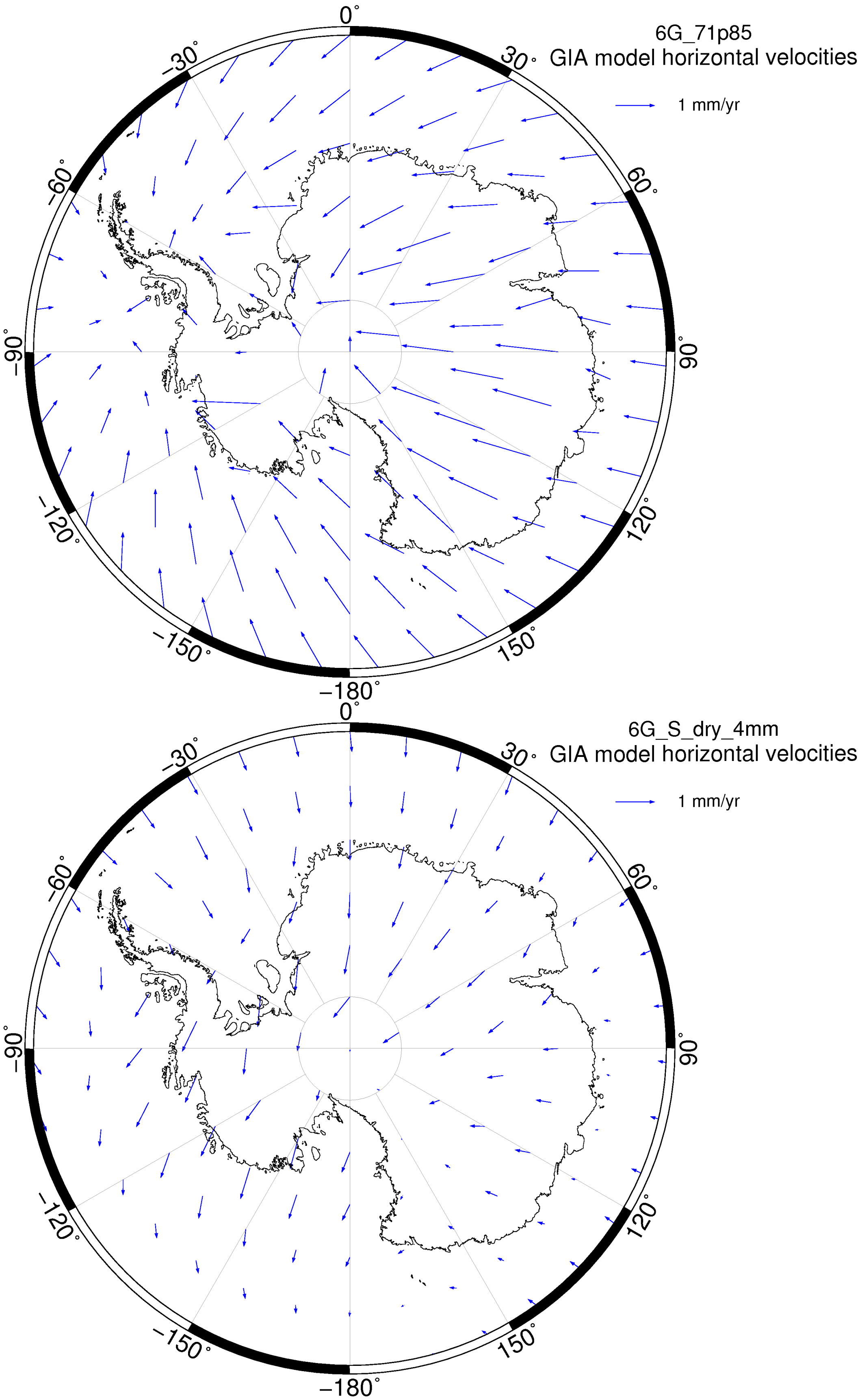

Figure 2.11: GIA horizontal predictions in Antarctica with a 1D GIA model (top, 6G_71p85) and a 3D GIA model (bottom, 6G_S_dry_4mm). Models selected as per Fig. 2.6.

2.3 Plate tectonics

Tectonic plate theory is based on the fact that the lithosphere is divided into a number of rigid plates which are moving over the asthenosphere. The tectonic plate theory is relatively recent. Alfred Wegener (1915) suggested his theory of continental drift in the beginning of the 20th century, stating that the continents used to be one large mass that has undergone processes causing them to drift to their current locations. This theory was developed during the mid-century and confirmed when new geophysical data had been collected (Lambeck, 1988). Tectonic plates are encircled by plate boundaries. It is commonly considered that there are about 14 major plates and a larger number of smaller plates (Bird, 2003). At the plate boundaries, which can be divergent, convergent or conservative, the tectonic plates are subject to plate boundary processes. Along divergent (constructive) plate boundaries, the plates are moving away from each other. At such boundaries new lithospheric material is derived from the mantle (Fowler, 2005). Along convergent (destructive) plate boundaries, plates move towards each other. When plates collide, one of them subsides under another in a so-called subduction zone. Since the plates are thin in relation to their breadth, the lower plate bends sharply before sinking into the upper mantle where it is consumed (Lowrie, 2007). Along conservative boundaries, the lithosphere is neither created nor destroyed. These plate boundaries are represented by transform faults which can be of different types but by far the most common type of transform fault is the one where the relative motion of adjacent plates is parallel to the strike of the shared fault (Fowler, 2005; Lowrie, 2007). Fig. 2.12 shows the major lithospheric plates and direction of plate movements, according to the plate motion model NUVEL-1 (DeMets et al., 1990). At the edge of each plate there is elastic deformation of the plate due to the fact that the faults that form the plate boundaries are locked. Earthquakes relieve this elastic deformation which is then building up again in the next earthquake cycle (Harrison, 2016). Most earthquakes take place along plate boundaries as a direct result of plate motions, these are interplate (between-plates) earthquakes. Intraplate (within-plate) earthquakes can be large and can cause considerable damage but they amount to only a small proportion of the total number of earthquakes occurring (Fowler, 2005). Apart from the rare intraplate earthquakes, the plate interiors are aseismic. This suggests that, in the global motion of the lithospheric plates over the asthenosphere, the plates can be assumed to be rigid (Lowrie, 2007).

2.3.1 Euler poles

The motion of the (rigid) plates on the Earth can be described by Euler's rotation theorem, which states that the displacement of a rigid body on the surface of a sphere is equivalent to a rotation about an axis that passes through the centre of the sphere. In other words,

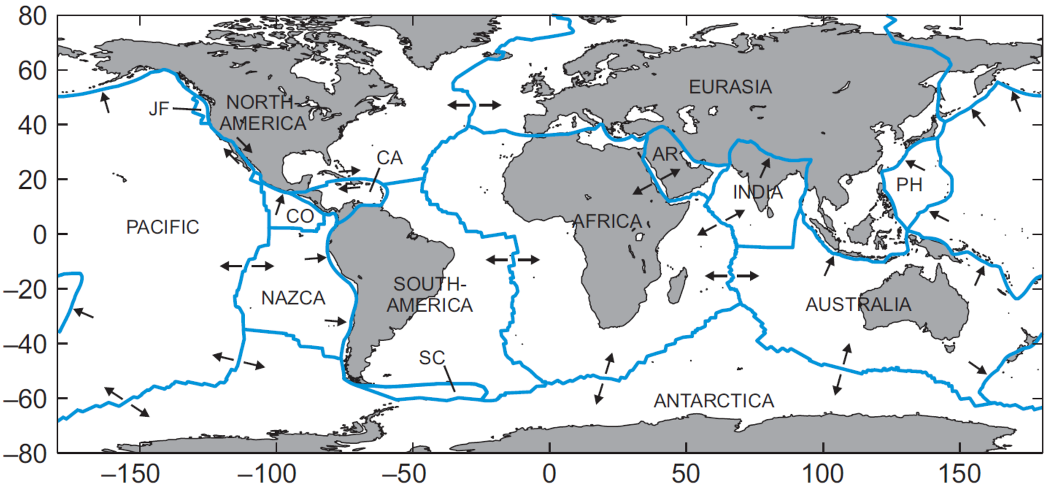

Figure 2.12: Major lithospheric plates and direction of plate movements, according to the plate motion model NUVEL-1. AR = Arabian, CA = Caribbean, CO = Cocos, JF = Juan de Fuca, PH = Philippines, SC = Scotia, after DeMets et al. (1990). Figure taken from Torge and Müller (2012).

this theory allows to model the motion of tectonic plates around a series of fixed points on the surface of the Earth. The rotation axis of a tectonic plate cuts the Earth surface at two points called the poles of rotation. These are purely mathematical points that have no physical reality. By sign convention, the rotation that is clockwise when viewed from the centre of the Earth is positive. That same rotation viewed from outside the Earth is anticlockwise. Therefore, one rotation pole is positive and the other is negative (Fowler, 2005). The positive pole of rotation is considered the Euler pole of the plate. The location of the Euler pole is at the intersection of the great circles perpendicular to the velocity of points on the plate (Lowrie, 2007).

In Cartesian coordinates, the Euler pole and the rotation rate are expressed by a 3×1 vector known as the Euler vector. The Euler vector $\Omega_p = [\omega_x\ \omega_y\ \omega_z]^T$ of a plate p is:

$$\Omega_p = \omega e \tag{2.11}$$

where $\omega = \sqrt{\omega_x^2 + \omega_y^2 + \omega_z^2}$ and e is the unit vector along the Euler pole's rotation axis. The absolute Euler vector of a plate can be used to determine the plate velocity of any station on the plate. The velocity $\dot{X}$ of a station at position X on plate p with rotation described by the absolute Euler vector Ω_p is given by the vector cross product:

$$\dot{X} = \Omega_p \times X \tag{2.12}$$

The equation above approximates the rigid motion of the plates on the Earth as motion tangential to a sphere. However, the Earth is not spherical and a rotational ellipsoid is a better approximation. The largest errors in computing the plate motion with this theory occur when the angle between the tangent to the sphere and the tangent to the ellipsoid is the greatest. Lavallée (2000) found that the difference in plate velocities between using spherical or ellipsoidal approximation is ∼0.02 mm/yr in the worst case scenario. This error is significantly smaller than the level of noise of GNSS observations and can be disregarded.

2.3.2 Development of plate motion models

The earliest plate motion models, such as Chase (1978) and Minster and Jordan (1978), were based on geophysical and geological data. More recent geological/geophysical models include NUVEL-1 (DeMets et al., 1990) and its updated version NUVEL-1A (DeMets et al., 1994), PB2002 (Bird, 2003) and MORVEL (DeMets et al., 2010). Models based on geological and geophysical data use records such as ocean floor magnetic anomalies, transform faults, earthquake slips etc. to produce an estimation of the motion of the plates (Bastos et al., 2010). The development of space-geodetic techniques and systems over the last three decades made it possible to create plate motion models from geodetic observations (Larson et al. (1997), Lavallée (2000), GEODVEL - Argus et al. (2010), ITRF2008 PMM - Altamimi et al. (2012), Booker et al. (2014), ITRF2014 PMM - Altamimi et al. (2017)). With increased coverage and accuracy of space-geodetic techniques, the accuracy of the plate motion models from geodesy increases.

The movements of tectonic plates can be described as relative motion of one plate with respect to another, or as absolute motion in a chosen reference frame. It is not possible to directly estimate the absolute movements of individual plates as there is no method to determine the absolute orientation of the Earth's lithosphere in inertial space. It is, nonetheless, possible to define an arbitrary orientation in which absolute plate motion models can be expressed. One of the methods used to derive absolute plate motion assumes that there is no net rotation (NNR) of the plates, and implicitly the lithosphere, over the mesosphere. In other words, the no net rotation, or mean lithosphere, specifies the velocity of the plates relative to the mesosphere (Argus and Gordon, 1991; Altamimi et al., 2002). In NNR, the surface integral of all plate velocities over the Earth's surface yields to zero. NNR-NUVEL-1A (Argus and Gordon, 1991) is a NNR geological model to which the orientation rate of ITRF2000 and, implicitly, consecutive ITRF solutions are aligned. MORVEL56 NNR (Argus et al., 2011) is a more recent geological NNR plate motion model and a successor of NNR-NUVEL-1A.

There is a relatively good agreement between geological/geophysical and geodetic plate motion models, e.g. the agreement between ITRF2008 PMM and NNR-MORVEL56 (Argus et al., 2011) at 206 sites from ITRF2008 PMM gives an RMS of the differences of 1.8 mm/yr and 1.9 mm/yr for the east and north components, respectively. The consistency between two geodetic PMMs, ITRF2008 PMM and ITRF2014 PMM is, however, much higher than the consistency between available NNR geological models NNR-NUVEL-1A and NNR-MORVEL56 (Altamimi et al., 2017). Space geodetic observations give motions over a short time interval, for some plates just a decade, which shows the recent plate motion in comparison to the geological/geophysical motion which provides the average motion over a few million years. Sella et al. (2002) estimate that the time span of space geodetic observations is representative of plate motions of the previous 10 000 years. If the secular motion of tectonic plates can change over time, the geological/geophysical models will not portray exactly the present plate velocities. Nevertheless, geological/geophysical models still provide useful information for studying present-day motion in areas such as oceans, where geodetic measurements are not available. Geodetic observations such as GNSS also observe any local effects or intra plate movements and give inconsistencies in plate boundary zones, which may bias the PMM estimate (Bastos et al., 2010). In this thesis, I create a GNSS surface velocity field and remove GIA from it to mitigate one of the possible biases to the plate motion model (Chapter 5).

Chapter 3

Reference frames and GNSS networks

3.1 Reference systems

Reference systems describe the position and motion of the Earth or other celestial bodies including positions and movements on the surface of the Earth (Torge and Müller, 2012). Reference systems describe this motion in a theoretical space represented by coordinate systems. Reference systems in geodesy are usually three-dimensional, consisting of a set of three-dimensional geometric coordinates, or four-dimensional with the addition of a time coordinate. The systems are defined by scale, origin and orientation of the axes of a Cartesian coordinate system or of the fundamental planes (Torge and Müller, 2012).

A Terrestrial Reference System (TRS) is a reference system co-rotating with the Earth in its daily motion in space (Petit and Luzum, 2010). While a TRS is Earth-fixed, a celestial reference system (CRS), is a space-fixed reference system whose origin and orientation is defined with respect to the motion of stars and quasars. TRSs are created to be used for describing positions and movements of objects on the Earth's surface and objects close to it. They are used in, e.g. navigation, national surveys and for monitoring instantaneous, decadal and long-term deformation of the Earth's surface. In the global geodetic community, the International Terrestrial Reference System (ITRS), defined by the International Earth Rotation Service (IERS), is conventional. The ITRS is a Cartesian coordinate system defined by the following criteria (Altamimi et al., 2002; Petit and Luzum, 2010):

- It is geocentric, the origin of the system is in the Earth's centre of mass (CM), which is the centre of mass of the entire Earth system, including oceans and atmosphere.

- Its orientation is equatorial meaning that the Z axis is in the direction of the pole, and X axis is the prime meridian, given by the Bureau International de l'Heure orientation at epoch 1984.0

- Its scale is defined to be the SI unit of the metre

- Its time evolution in orientation will create no residual global rotation with regards to the crust, which is ensured by a NNR condition

Earth Orientation Parameters (EOPs) are parameters which provide the rotation of the ITRS with respect to the International Celestial Reference System (ICRS) as a function of time. They include pole coordinates in the terrestrial system, celestial pole offsets and the Earth rotation angle provided by UT1-UTC. In addition, the IERS also publishes the observed time rates of polar motion and UT1. The latter is also known as length of day excess (Torge and Müller, 2012). There are other TRSs in use, such as regional ones which are fixed to the stable part of the relevant tectonic plate, which circumvents the need to consider plate motion and simplifies local surveying tasks. For example, the European Terrestrial Reference System (ETRS) is fixed to the stable part of the Eurasian tectonic plate.

3.2 Reference Frames

While a reference system is a theoretical definition, a reference frame is its practical realization using particular reference objects. A terrestrial reference frame (TRF) describes the physical points of attachment of the Earth to the geometric model defined by a TRS. The reference objects in a TRF are geodetic monuments fixed to the crust of the Earth, which are given particular coordinates, most commonly position and velocity. This is done in order to define the parameters of the frame in a suitable way with respect to the theoretical criteria set up by the TRS. The observations of reference objects are used to establish the reference frame by solving for reference system parameters, through e.g. least-squares adjustment, defining the extrinsic geometry of the model. Once a reference frame is established, the positions and velocities of objects are expressed in the reference system through the inclusion of the reference object positions as a priori information (Davies, 1997). A user can then include the reference objects in their measurements and thus obtain their measurements in the same reference frame.

To establish a TRF at a given epoch in time, seven parameters are needed (three rotations, three translations and origin). To define the time evolution of the TRF, an additional seven parameters are needed, which are time derivatives of the previous seven parameters. Thus, 14 parameters establish the TRF origin, scale, orientation and their time evolution

(Petit and Luzum, 2010). A solution of a TRF is defined as a set of coordinates with their uncertainties in the form of covariance information (variance-covariance matrix - VCM) or an equivalent form (e.g. normal equations).

TRFs are important for studies of geophysical processes and the convention for the origin varies depending on the application. Blewitt (2003) discusses several main origins used in geophysical studies including:

- Centre of mass of the solid Earth (CE)
- Centre of mass of the entire Earth system (CM) - including the atmosphere, the oceans, continental water and ice
- Centre of surface figure (CF)
- Centre of surface lateral figure (CL)

A reference frame with its origin in CE is fixed to the centre of mass of the solid Earth only. For a reference frame tied to the CE, degree 1 mass loading produces a rigid-body translation of the centre of mass (Martens et al., 2019). CE changes its trajectory in inertial space when surface mass is redistributed, but once the mass has been redistributed to its final configuration, any further resulting deformation of the solid Earth cannot change the solid Earth's centre of mass. The CE frame is thus a natural frame for computing the dynamics of solid Earth deformation and modelling load Love numbers (Blewitt, 2003). Some GIA models (such as the 1D GIA models used in this thesis) are therefore expressed in the CE frame. Nonetheless, there will never truly be a final configuration of the mass because the further resulting deformation of the solid Earth will alter the shape of the geoid and hence the distribution of surface mass, which in turn alters the surface load causing more deformation with implications for CE. However, for present-day changes of GIA, the CE is close to the centre of mass of the entire Earth system (CM) and the motion between CE and CM is small, max ± 0.03 mm/yr (Klemann and Martinec, 2011). If the degree 1 coefficients are set to zero (such as in the 3D GIA models used in this thesis), the model assumes no centre of mass motion.

Spada et al. (2011) compare the present-day GIA velocities obtained from a model which includes degree 1 coefficients with a model where degree 1 coefficients are not included. They find that the overall effect of degree 1 is to increase the up component by up to 10% beneath the load and to alter the horizontal velocities up to $\sim$10% at the load margins.

A disadvantage of the CE frame is that it is not directly accessible from geodetic observations. CM, being the centre of mass of the entire Earth system - the solid Earth and the surface load including all the masses in the atmosphere and hydrosphere - is the centre around which the Earth's satellites orbit. It is therefore observable with space-geodetic techniques, and the positions of stations in GNSS, SLR, LLR or DORIS networks are naturally expressed with CM origin. However, the accuracy of estimating CM through global networks depends on which space-geodetic technique was used. The definition is highly dependent on the accuracy of the satellite force models. A CM origin solution also depends on the accuracy and temporal resolution of the reference frame it is tied to (Blewitt, 2003). CF is the centre of figure of the outer surface of the solid Earth (Dong et al., 1997). It is defined geometrically "as though the Earth's surface were covered by a uniform, infinitely dense array of points and the motions of these points are taken into account" (Blewitt, 2003). In practice, this may be realised by averaging over a sufficiently dense global distribution of geodetic stations, such as GNSS. Theoretically, the surface integral of the vector displacements in a frame with CF centre is zero. The tectonics of rigid plates produces a net translation of CF in the CM frame. When estimating a plate motion model from surface velocity measurements, as is done in this thesis, the plate motion is expressed in a frame with an origin in the centre around which tectonic plates rotate. Blewitt (2003) defines the center of lateral figure (CL) as a frame where the surface integral of the horizontal vector displacement is zero. This has been applied to residuals of observed tectonic motions minus modelled plate tectonic motions. Lavallée (2000) defines a reference frame that minimizes the rate of spherical distance between sites on rigid plate interiors without using an a priori plate motion model, which Blewitt (2003) characterises as a type of residual CL frame.

It is important that models of the Earth's response to surface mass loading are computed in the same reference frame as any observations considered in a comparative analysis (Blewitt, 2003). Argus et al. (1999) define the geocentre as the translation of the origin of any geometrical centre of figure with respect to CM. Altamimi et al. (2016) define the geocentre motion as the motion of CM with respect to CF. As a consequence of the above, the velocities in this thesis are given with respect to different origins. This is accounted for (in Chapters 5 and 6) by including the motion of different frame origins with respect to each other in the plate motion model estimate and residual (models versus observations) estimate.

As mentioned, TRFs are realised mainly through observations by space-geodetic techniques. A reference frame is established through a network of highly accurate geodetic stations which can then be used as reference objects for any other measurements. To establish a fully consistent reference frame, several geodetic techniques are needed since no single technique is sensitive to all the parameters of the TRF definition with high accuracy. The origin, being the CM, is theoretically estimable through any technique relying on satellites, since they orbit around the centre of mass. These include GNSS, DORIS, LLR and SLR but mostly SLR and DORIS are used (Torge and Müller, 2012). The scale is defined through universal constants such as the speed of light (indirectly the SI metre unit) and the gravitational constants in the satellite force model (Lavallée, 2000). The scale depends on physical parameters and relativistic modelling and is subject to technique systematic errors, such as VLBI, GNSS and DORIS antenna-related effects, and SLR station-dependent ranging biases (Petit and Luzum, 2010; Altamimi et al., 2002). The scale rate is also influenced by station vertical motions. The definition of the scale is important for the definition of the origin of a TRF. If there is an error in the scale, this influences the true distance to the orbiting satellites which subsequently affects the CM estimate (Booker, 2012). The orientation of the TRF is conventional and unobservable by any technique, but it should have a geophysical meaning due to tectonic plate motions (Altamimi et al., 2002).

3.2.1 International Terrestrial Reference Frame

Primary realizations of the ITRS, governed by the IERS, are called the International Terrestrial Reference Frame (ITRF). Since the IERS was established in 1988, and the first ITRS realization named ITRF88, multiple versions of ITRF have been established, each superseding the previous one. ITRF reference frame solutions are kinematic solutions, meaning that they express coordinates in a reference epoch with their time derivatives. ITRF2000 (Altamimi et al., 2002) was the first ITRF that combined unconstrained space-geodetic solutions which were free from direct influence of any tectonic plate motion model. Up to and including ITRF2000 (Altamimi et al., 2002), ITRF versions were combined from global long-term solutions comprising station positions and velocities. ITRF2005 (Altamimi et al., 2007) was the first to use time series as input (weekly for GPS, DORIS, SLR and daily for VLBI) of station positions and daily EOPs. ITRF2005 was followed by ITRF2008 (Altamimi et al., 2011), in turn followed by the most recent ITRF solution, ITRF2014 (Altamimi et al., 2016). The reference epoch of ITRF2014 is 2010.0. It is the first ITRF solution with enhanced modelling of nonlinear site motions, which includes modelling the site periodic seasonal signals and modelling post-seismic deformation for sites that were affected by major earthquakes (Altamimi et al., 2016).

ITRF2014 is created using the full observation history of VLBI, SLR, GNSS and DORIS with reprocessed time series: daily solutions from VLBI and GNSS, and weekly solutions from DORIS and SLR (SLR fortnightly until 1993). In ITRF2014, as in previous ITRF solutions, the origin of the reference frame is defined by SLR data from the International Laser Ranging Service (ILRS). This means that there is zero translation between ITRF2014 and the mean origin of the ILRS SLR time series at epoch 2010.0, and zero translation rates between them. The scale of ITRF2014 is determined similarly to the scale of ITRF2008, using the arithmetic average of the scales derived from SLR and VLBI solutions. There is no basis to discriminate between the two techniques which is why their simple average is used. The scale from the SLR and VLBI networks is determined by physical parameters (such as the gravitational constant and the speed of light) and modelling of relativity (Petit and Luzum, 2010). DORIS solutions also give a good estimate of the reference frame scale, but are not used. The orientation of ITRF2014 is defined in such a way that there are zero rotation parameters at epoch 2010.0 and zero rotation rates between ITRF2014 and ITRF2008 (Altamimi et al., 2016).

The combination of the different techniques used in the ITRF solutions is done with the aid of colocation sites, which are sites where two or more geodetic instruments of different techniques are operated, or where local surveys between instrument measuring points are available (Altamimi et al., 2016). The majority of colocation sites are the ones with GNSS observations in addition to another space-geodetic technique. The procedure of forming recent ITRF solutions includes two steps (Altamimi et al., 2002, 2007, 2011, 2016):

1. using the individual time series to estimate a long term solution per technique comprising station positions at a reference epoch, station velocities and daily EOPs
2. combining the resulting long-term solutions of the different techniques at colocation sites

The analysis of time series of site positions allows for determining site positions and linear velocities. To achieve this with high accuracy, it is important to accurately model any non-linear site motion. Discontinuities in the time series, caused by e.g. equipment change or instantaneous movement due to an earthquake, are accounted for by making the coordinates and velocities valid only for a specific time interval, while another interval, for example after an equipment change, has new coordinate and velocity values. The discontinuities in the time series of ITRF solutions are detected through visual inspection. Discontinuities (offsets) in the time series are usually detected manually due to difficulties in algorithmic detection of outliers. Gazeaux et al. (2013) designed the Detection of Offsets in GPS Experiment (DOGEx) to objectively test and evaluate different offset detection approaches. They showed that undetected offsets are among the largest contributors to the error of the estimated trend and found that the manual detection of offsets is superior to the available automated ones. Recent publications (Amiri-Simkooei et al., 2019; Wu et al., 2018) propose new methods for automatic offset detection in GNSS time series but the field is in the early stages of development.

The periodic signals in the site position time series do not affect the parameters defining ITRF, especially the origin and the scale (Collilieux et al., 2010), although Blewitt and Lavallée (2002) show that this might be the case for velocities of stations with less than 2.5 years of observations. Nonetheless, estimating periodic signals can improve the determination of the linear velocity of the site, especially at those with large seasonal signals, and helps the detection of discontinuities in the time series (Altamimi et al., 2016). As mentioned above, ITRF2014 is the first ITRF solution which includes modelling of periodic seasonal signals for sites with sufficient time span, longer than two years, for all four techniques (Altamimi et al., 2016). Apart from ITRF solutions, Bevis and Brown (2014) present an extended site trajectory model for reference frame realization, which in addition to the standard linear trajectory that considers discontinuities, includes logarithmic models for post-seismic deformation (PSD). In ITRF2014, the modelling of PSD is done using logarithmic and exponential models. After an earthquake, a site affected by it experiences post-seismic relaxation and its velocity is not linear. The PSD models describe the motion of the site after the earthquake. Unlike the modelling of seasonal signals, which is only used by ITRF working groups to construct the ITRF solution, the PSD models are available to users as a product of ITRF2014, in addition to the site positions, linear velocities and EOPs (as in ITRF2008). For each site affected by a major earthquake, ITRF2014 published logarithmic and exponential PSD parameters of the equations of the PSD models together with their VCMs. A user can then use the PSD models to propagate the ITRF solution to a desired epoch in time. For sites affected by major earthquakes, modelling the PSD has in previous ITRF solutions been done by piecewise linear functions. However, the estimated linear velocities of the segmented station time series are not precise enough and do not adequately describe the actual station trajectories after an earthquake (Altamimi et al., 2016). More details on the ITRF2014 PSD models are given in section B.2, being a novel ITRF feature that was implemented into the Tanya software and used for creating the GNSS networks within this project.

3.3 Reprocessed GNSS data

The International GNSS Service (IGS) is the global governing body of scientific GNSS operations. It is a non-commercial federation of more than 200 worldwide agencies and institutions which together provide, on an open-service basis, the highest quality GNSS data and services in support of the TRF, Earth observation, positioning, navigation, timing etc. The IGS operates a global network of GNSS ground stations, data centres and analysis centres (Dow et al., 2009). Analysis Centres (ACs) process the GNSS measurements and the IGS products are generated by combining the results from different ACs. Global Network Associate Analysis Centres (GNAACs) combine the station coordinate and velocity covariance information contributed by other centres to form global combinations (Dow et al., 2009).

In 2008, the IGS ACs completed the first reanalysis of GNSS data collected since 1994 for a global network of tracking stations (Steigenberger et al., 2006, 2009; Collilieux et al., 2011). In the timeline of operational GNSS processing, new models and processing techniques were introduced which improved the precision and accuracy, but made the long term time series heterogeneous. The 2008 reprocessing campaign, named repro1, recomputed the set of IGS combination data products - site coordinates, satellite orbits and clocks and EOPs

- using consistent analysis models and methodologies. This included: a switch to absolute calibrations for receiver and satellite antennas; adoption of the IGS05/igs05.atx antenna calibrations and reference frame aligned to ITRF2005; the implementation of IERS 2003 Conventions (McCarthy et al 2003). The Weighted Root Mean Square Error (WRMS) of the post-fit residuals of the IGS operational orbit combination with respect to the repro1 orbit combination decreased from ∼100 mm in 1994 to ∼10 mm in 2008 (Griffiths, 2019). The WRMS of the post-fit residuals of the repro1 solutions to their reference frame is up to seven times smaller than the WRMS of the post-fit residuals of the operational IGS solutions to their respective reference frames (Booker et al., 2014). While the accuracy and precision of the products achieved a remarkable improvement from the operational solutions (prior to repro1) to repro1, significant deficiencies continue to affect the products at the centimetre level and below. These errors include a combination of unattributed seasonal errors, effects of background power-law noise in site coordinates on site velocities, effects of discontinuities on site velocities and frame stability, effects of terrestrial frame misalignments on EOPs and site time series residuals, subdaily EOP alias and draconitic errors in the satellite orbits, and other harmonics in time series of ground site positions. Additionally, errors arise from e.g. local near-field multipath or excessive positional offsets caused by equipment changes (Griffiths, 2019).

Following repro1, in 2015, the IGS ACs completed a second reanalysis of GNSS data, named repro2, using the latest analysis models and methodologies (Rebischung et al., 2016). As such, it further reduces the remaining error contributors, and resulting spurious signals in the coordinate time series (Griffiths, 2019). For example, unlike repro1 which produced weekly station positions, repro2 produced daily products, enabling the identification of signals with sub-weekly frequencies (Rebischung et al., 2012a). Furthermore, the data span used for repro2 is longer, ∼21 years, starting with GPS week 730 through to 1831, with the exact weeks and days differing slightly for different ACs. The standards for repro2 are listed on the IGS repro2 website (`http://acc.igs.org/reprocess2.html`, last accessed 19.07.2020). Among these standards, the main model and method changes since the repro1 campaign are (Rebischung et al., 2016; Griffiths, 2019):

- a switch from weekly to daily terrestrial frame integrations made to facilitate the study of station displacements at higher temporal resolutions
- in addition to GPS, inclusion of GLONASS by three ACs (COD, ESA, GRG)
- the implementation of the IGb08/IGS08.ATX reference frame and calibration framework (Rebischung et al., 2012b), including antenna calibrations
- the implementation of the IERS 2010 conventions (Petit and Luzum, 2010)
- the implementation of new attitude models for eclipsing satellites by some ACs

- the modelling of Earth radiation pressure and antenna thrust acting on satellites
- higher order ionospheric and updated trosposperic models for propagation delays

An indication of the improvement of repro2 over repro1 is given in section 4.4 where the network coordinate solutions from this thesis (repro2) are compared with those from a previous study (repro1).

As with repro1, in repro2 the ACs were requested not to apply model corrections for the load displacements caused by large-scale non-tidal atmospheric, ocean and hydrological surface motions, in order to allow them to be removed in the long-term stacking process in forming ITRF2014. Repro1 provided the IGS input to ITRF2008 and repro2 provided the IGS input to ITRF2014 (Rebischung et al., 2016).

The ACs which participated in the second reprocessing campaign are listed in Table 3.1. Even though the ACs are adhering to the repro2 standards, there are still some differences in the processing. The column with remarks indicates the AC specifics and the main departures from the repro2 standards. The ACs process GNSS observations from sites which are a part of the so-called tracking network. The last two rows in the table denote centres which did not contribute to the tracking network but to the IGS tide gauge benchmark monitoring working group (TIGA, Schöne et al. (2009)), which serves to densify the tracking network with GNSS stations which are co-located with tide gauges. In this way, the tide gauges are directly tied to ITRF2014 (Griffiths, 2019).

AC	Institution	Remarks
COD	Center for Orbit Determination in Europe	GLONASS data included starting from 2002
EMR	Natural Resources Canada	
ESA	European Space Operations Center	GLONASS data included starting from 2009
GFZ	GeoForschungsZentrum	
GRG	Groupe de Recherche en Géodésie Spatiale	GLONASS data included starting from 2009
JPL	Jet Propulsion Laboratory	30h data integrations
MIT	Massachusetts Institute of Technology	
GTZ	GeoForschungsZentrum	GFZ contribution to the IGS TIGA project
ULR	Université de la Rochelle	Contribution to the IGS TIGA project

Table 3.1: AC contibutions to the repro2 campaign. Adopted from Rebischung et al. (2016).

The repro2 solutions and the following operational solutions are expressed in IGb08. IGb08 is the IGS realization of ITRF2008. When IGb08 was adopted, simultaneously a set of respective antenna phase centre calibrations were adopted, igb08.atx. The repro2 and operational solutions in the IGb08 reference frame and calibration framework contributed to creating ITRF2014 (Rebischung et al., 2016). Similarly, in GPS week 1934, IGS ACs' operational solutions switched their reference frame to IGS14 and calibration framework to igs14.atx. IGS14 is the IGS realization of ITRF2014. In other words, the GNSS networks expressed in IGb08 were used to create ITRF2014, which was in turn used to create IGS14.

The repro2 and operational products following repro2 from IGS ACs, together with other similarly processed solutions (cf. section 4.1.1), are a part of the network combination of this project. This network is aligned to GNSS sites which were a part of the GNSS contribution to ITRF2014 (ITRF2014-IGS).

3.4 Network solution files

SINEX (Solution/Software INdependent EXchange format) is a file format for exchanging space-geodetic coordinate solutions. It was suggested by Blewitt et al. (1994). It started with the idea of creating a universally acceptable format for exchanging solutions. A SINEX file can contain detailed site information, all estimated parameters, their VCM, any a priori VCMs and normal equations. A SINEX file is subdivided into groups of data called blocks and each block has a fixed format. There are about 25 block types in the current version 2.02, each containing information specific to that type of block (IERS, 2006). Table 3.2 summarizes the information given by each block. Some blocks are mandatory for all types of solutions, some are mandatory for certain types of solutions and some are optional. A detailed description of the SINEX format can be found in IERS (2006).

In this project I distinguish between epoch solutions and kinematic solutions. Accordingly, I distinguish between epoch SINEX files and kinematic SINEX files. Epoch solutions contain only one set of parameters for each site and they are valid for just one epoch which is usually a day or historically a GPS week. They usually contain only position parameters. Less often we find SINEX files containing only velocity parameters. Kinematic solutions, or free epoch solutions, contain parameters valid for a reference epoch together with velocities, which allow the positions to be propagated to any point in time.

In the most simple case of a kinematic solution with linear velocity, the position in the propagation epoch is computed using the velocity and the time difference between the reference and propagation epoch:

$$X_t = X_0 + \dot{X} \cdot \Delta t, \tag{3.1}$$

X_0 is the position of a site at reference epoch t_0, X_t is the position of a site at time t, Δt is the time that passed since the reference epoch t_0 until t and $\dot{X}$ is the linear velocity of the site.

When referring to a site, we refer to one or more physical monuments at a geodetic

Block group	Block name	Information content
FILE	REFERENCE	general details about the file such as the organization, contact software, hardware etc.
	COMMENTS	additional comments - no fixed format
INPUT	HISTORY	information used to create the current file
	FILES	files used to create the solution of the current solution
	ACKNOWLEDGEMENTS	analysis groups contributing to this solution
	NUTATION/DATA	nutation model used in the analysis - mandatory block for VLBI solutions
	PRECESSION/DATA	precession model used in the analysis - mandatory for VLBI
SOURCE	ID	radio sources - mandatory for VLBI
SITE	ID	site code, point code and/or DOMES and descriptions of sites
	DATA	additional information about the estimated station parameters
	RECEIVER	receiver type at each site
	ANTENNA	antenna type at each site
	GPS_PHASE_CENTER	phase centre offsets for antennas in SITE/ANTENNA (GPS)
	GAL_PHASE_CENTER	phase centre offsets for antenans in SITE/ANTENNA (GLONASS)
	ECCENTRICITY	monument-to-antenna vectors at each site
SATELLITE	ID	GNSS satellites used in the SINEX file if available
	PHASE_CENTER	GNSS satellite antenna phase centre corrections
SOLUTION	EPOCHS	list of epochs for which each estimate is valid numbered by solution numbers (SOLNs)
	ESTIMATE	estimated coordinates or ERPs and the epochs for which they are valid
	APRIORI	same as previous but for a priori information for estimated parameters
	MATRIX_ESTIMATE	depending on the type: variance-covariance matrix of estimated coordinates or correlation matrix of estimated coordinates or normal equations matrix of the constraints applied to the solution
	MATRIX_APRIORI	same as previous but for a priori
	NORMAL_EQUATION_VECTOR	the vector of the right hand side of the normal equation
	NORMAL_EQUATION_BLOCK	normal equation matrix (without constraints)
	STATISTICS	statistical information
BIAS	EPOCHS	epochs of bias parameters if included

Table 3.2: SINEX blocks in the most recent SINEX version (IERS, 2006). Inspired by Davies (1997).

site, each identified by a four-character site code (SITE) and a point code (PT). The SITE code is the unique four-character location identifier and a PT code (usually one letter) can be used to distinguish multiple monuments at the site, or be omitted. Site position and/or velocity can be affected by earthquakes, equipment change or any other known or unknown force which causes a discontinuity in the measurement. In that case, the parameters of the affected site are given in two or more station solutions containing different estimates for the periods before or after the discontinuity had occurred. A record in the SOLUTION/EPOCHS block represents one station in the network solution (Davies, 1997). A station solution is identified in SINEX records by SITE, PT and SOLN (solution number) codes. The SOLN code can be used to distinguish multiple estimates of the site within a network solution, or omitted if not necessary.

Figure 3.1 shows an illustration of the information given in a SINEX file for a kinematic solution with discontinuities. T_0 is the reference epoch of the kinematic solution, P_1 and v_1 are the respective position and velocity parameters for a site at time T_0, and they are used to propagate the position of the site within the time period between the reference epoch until T_1 when a position discontinuity occurred. At T_1, a position discontinuity occurs and causes a shift in position. Subsequently, the propagation trajectory of the site is on a new line of Figure 3.1. To propagate the position of the site within the time period T_1 to T_2 (solution 2), a different pair of parameters will be used. So, the new pair of parameters in SINEX format are then a pair of position and velocity coordinates at the reference epoch T_0 which represent the position and velocity the site would have had, if it had had the same position and velocity from the start as it has in solution 2. In other words, it gives an artificial pair of position and velocity at time T_0, which then gets propagated to the correct position when the propagation epoch is within the time span T_1-T_2 (solution 2 time period). Similarly, at time T_2 both a position and a velocity discontinuity occur, and to propagate the position of the site within the time span between T_2 and T_3, parameter pairs P_3 and v_3 are used.

The process described above is illustrated for a site with the most simple case of displacement, namely linear velocity. The same is also valid for non-linear displacement. In other words, each of the solutions (the segments of the time series) may also have non-linear velocities (cf. section B.2) and the procedure with regard to choosing the correct propagation parameters still applies.

Recent ITRF solutions publish a discontinuity file which is used to identify the time when the discontinuity occured in order to know which pair of parameters to use. The SOLUTION/DISCONTINUITY block is a SINEX-formatted block but it is not at present an officially recognised SINEX block.

In this project, I combine daily epoch solutions from various GNSS networks. Each of these combined daily solutions is aligned to the ITRF2014 reference frame in its respective epoch. Aligning means estimating transformation parameters between a network and a reference network through a chosen set of mutual sites and applying the estimated transformation parameters to the former network, in order to express it in the reference frame of the latter one. Therefore, to express each combined daily solution in the ITRF2014 reference frame (i.e. align each combined daily solution to ITRF2014), a reference network in the respective epoch and reference frame is needed. The reference networks for alignment are obtained by propagating the ITRF2014-IGS solution to the epochs of the daily solutions in the time series. The processes of working with network solution files and combining the GNSS networks are described in the next chapter.

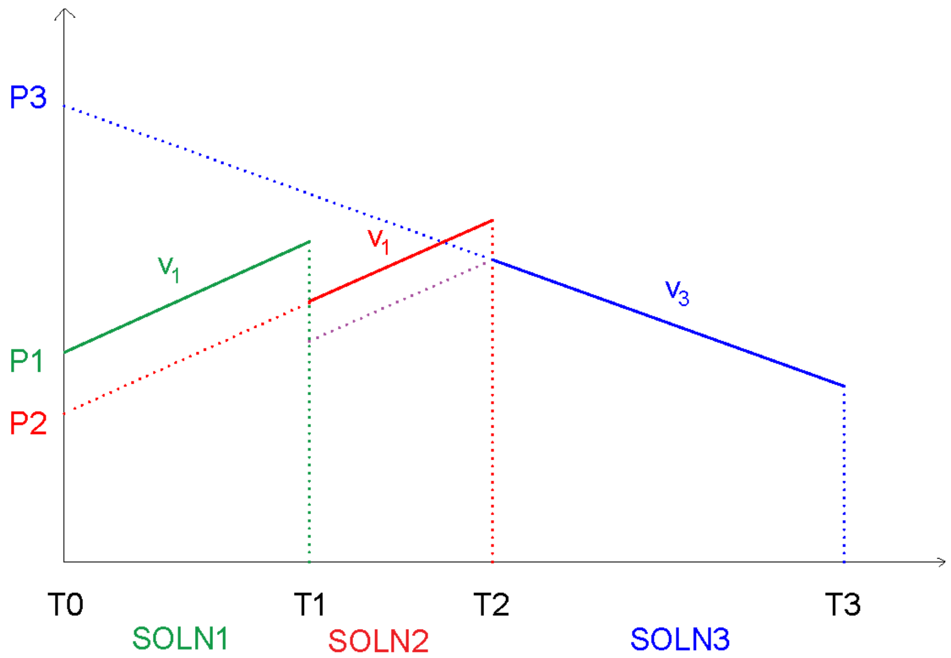

Figure 3.1: The principle of coordinate parameter pairs for different station solutions in SINEX: T_0 is the reference epoch of the kinematic solution, T_0-T_1, T_1-T_2 and T_2-T_3 are the time periods of station solutions SOLN1, SOLN2 and SOLN3, respectively. (P_1,v_1), (P_2,v_1) and (P_3,v_3) are the position and velocity parameters for the site, valid in time periods of station solutions SOLN1, SOLN2 and SOLN3, respectively. The position and velocity parameters are used to propagate the position of the site during their corresponding time periods.

Chapter 4

Network combination and time series analysis

This chapter describes the process of creating a GNSS surface velocity field. I combine GNSS daily solutions from multiple global and regional daily networks with different quality control measures throughout the process. The individual global solutions are combined into a unique global solution where each of the individual ACs contributes to the final coordinates and VCMs of the sites. The regional networks are subsequently aligned to the combined global solution. All of these daily networks are aligned to ITRF2014 on a daily level. The time series of daily networks is used to compute velocities on a site by site basis resulting in a global internally consistent set of GNSS velocities.

In the first section of this chapter I introduce the networks which contributed to the combined network and the method of obtaining solutions independent of the original solution reference frame. The second section describes the network combination principle. The third section shows the time series analysis and creating the final GNSS surface velocity field. The fourth and final section summarizes and discusses the chapter.

The network combination is performed using Tanya software. Tanya is a reference frame combination software established by Phil Davies and further developed by David Lavallée and David Booker (Davies, 1997; Lavallée, 2006; Booker, 2012) at Newcastle University. The software has been used for Newcastle University GNAAC combinations. It is written in C and governed by a set of scripts written in C-Shell. The Tanya software design allows experienced users a great deal of autonomy and the inclusion of their own scripts. A major part of my work was updating the Tanya software to accommodate the latest ITRF standards. The Tanya software modifications and supporting information for the present chapter are described in Appendix B.

4.1 Analysis Centre epoch solutions

4.1.1 Input GNSS networks

The global GNSS network solution is created by combining solutions from the global and regional ACs listed in Fig. 4.1 and Fig. 4.2. They are published as daily site coordinate network solutions which include site position coordinates with their standard deviations and the correlations between sites and coordinate components. The solutions COD, EMR, ESA, GFZ, GRG, JPL, MIT and SIO are global solutions provided by the IGS ACs, see Table 4.1. The regional solutions are included to densify the network in GIA affected regions in North America, Europe and Antarctica. NMT (North America) and ANT (Antarctica) are regional solutions provided by New Mexico Tech within the Plate Boundary Observation project (ftp://data-out.unavco.org/pub/products/sinex/). The Fennoscandian and Baltic regional solutions, denoted as BAL (Baltic), FIN (Finland), NOR (Norway) and SWE (Sweden), were provided by Halfdan P. Kierulf (personal communication (2019) and Kierulf et al. (2021, submitted)). The EUREF (European Permanent GNSS Network, `http://www.epncb.oma.be/`) provides regional solutions for Europe (EUR).

The solutions used are the operational solutions from the stated ACs and the solutions from the repro2 campaign. The end dates of repro2 generally correspond to the time when an AC updated their processing to repro2 standards and started using them in their operational products (Griffiths, 2019). From GPS week 1832 (February 2015), the IGS officially switched their operational solutions to using the same antenna calibrations and analysis methods as in repro2, the exact GPS weeks for individual ACs are shown in Figs. 4.1 and 4.2. From GPS week 1934 (29$^{\text{th}}$ January 2017), the IGS has switched to using different antenna calibrations (igs14.atx, see section 3.3), hence for consistency, the time series in my network ends there.

Full name of AC	Operational solution ID / abbreviation of AC	Repro2 solution ID
Centre for Orbit Determination Europe	COD	CO2
Natural Resources Canada	EMR	EM2
European Space Agency	ESA	ES2
GeoForschungsZentrum	GFZ	GF2
Groupe de Recherche en Géodésie Spatiale	GRG	GR2
Jet Propulsion Laboratory	JPL	JP2
Massachusetts Institute of Technology	MIT	MI2
Scripps Institute of Technology	SIO	SI2

Table 4.1: IGS ACs whose products were used in the network combination.

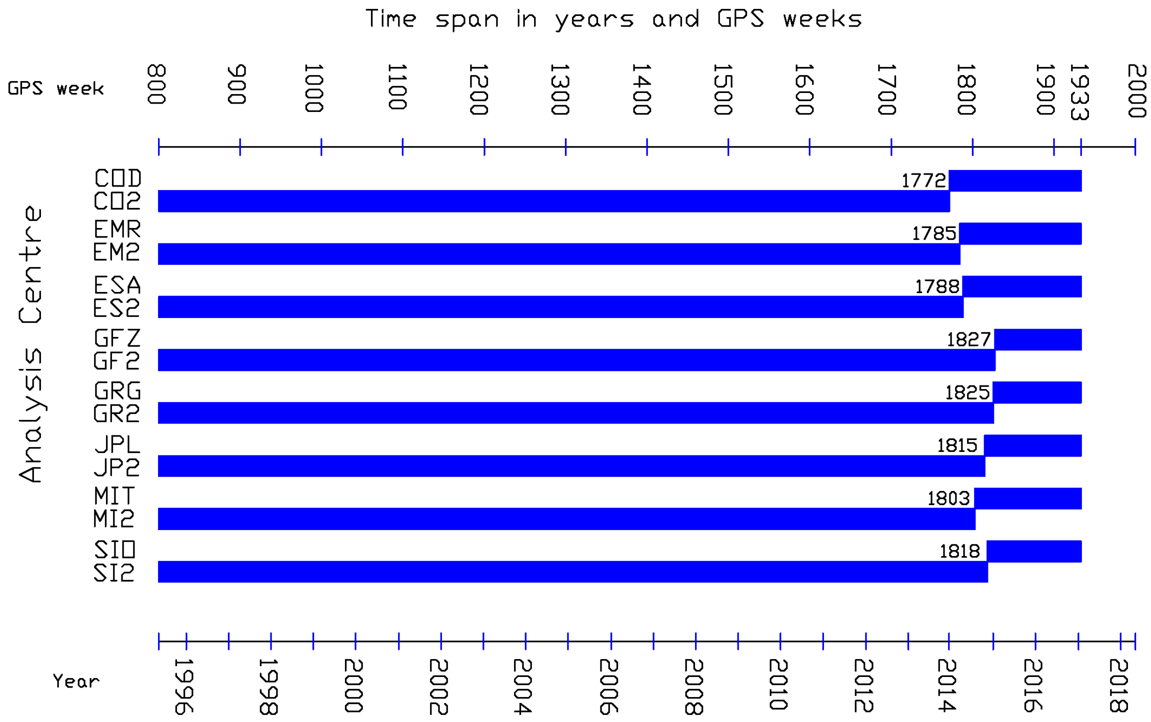

Figure 4.1: Global IGS ACs used in the network combination and their respective time spans. Numbers associated with a shift in the timeline denote the week for which the AC finished their repro2 analysis and started processing operational solutions in the same way.

4.1.2 Deconstraining

When solving for coordinate parameters in a geodetic network, additional constraint information is added to the observations to define the network's reference system parameters (Davies, 1997). This is done with constraint equations, which are not observed, but selected a priori. The daily epoch solutions from the ACs introduced in section 4.1.1 are provided as constrained solutions, and in this project they are deconstrained to get free-network solutions. Free-network solutions are independent of an external reference frame and AC-specific constraining techniques, which makes them more suitable for creating a combined network.

In other reference frame combination software, e.g. the Combination and Analysis of Terrestrial Reference Frames software package (CATREF, Altamimi et al. (2002)), deconstraining is done directly in the parameter domain. In Tanya, deconstraining is performed in the stochastic domain, in two steps: (1) removing constraints stated in the given a priori solution and (2) removing unstated minimum constraints.

Removing stated constraints The parameter vector x and its VCM Q_x, given in the ACs' SINEX blocks SOLUTION/ESTIMATE and SOLUTION/MATRIX_ESTIMATE are solutions subjected to constraints in the ACs processing - x and Q are the solution of a system of

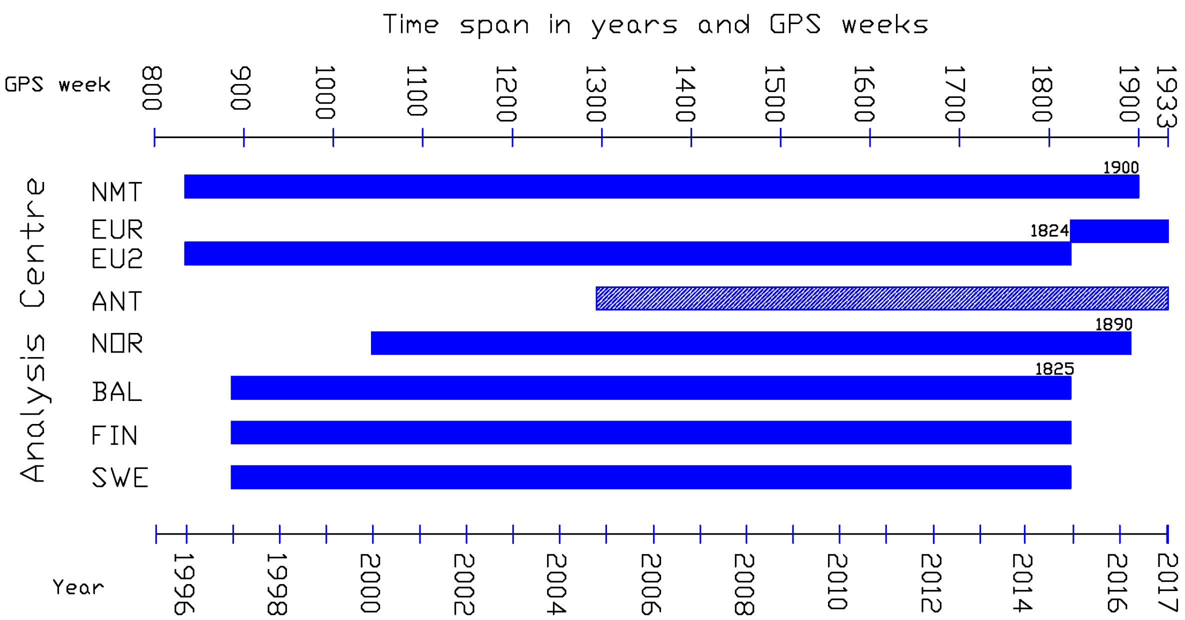

Figure 4.2: As Fig. 4.1 but for the regional ACs. ANT data span exhibits a large data gap of ∼2 years from 2010 to 2012.

constrained normal equations. z and Q_z are the a priori parameter and a priori VCM given in SINEX blocks SOLUTION/APRIORI and SOLUTION/MATRIX_APRIORI. I obtain the deconstrained parameter $\bar{x}$ and the deconstrained VCM $Q_{\bar{x}}$ by subtracting the normal equation components of the a priori solution from the constrained normal equations (Davies and Blewitt, 2000):

$$Q_{\bar{x}} = (\ Q_x^{-1} - A^T Q_z^{-1} A + (C^T C)^{-1} C^T Q_w^{-1} C (C^T C)^{-1}\ )^{-1} \tag{4.1}$$

$$\bar{x} = Q_{\bar{x}} (Q_x^{-1} x - A^T Q_z^{-1} z) \tag{4.2}$$

where A is the design matrix. The third term in Eq. (4.1) represents adding a small minimum constraint of orientation which is done in order to give good matrix conditioning since a solution that is too loose can cause numerical instabilities. The term $(C^T C)^{-1} C^T$ is a generalized inverse of the linearised mapping matrix C of three loose constraints w of 3D-network orientation, i.e. the last three rows of the Jacobian matrix for Helmert transformation. Appropriate rotation factors, diagonal elements of matrix Q_w, are chosen such that it makes the solution just tight enough to not cause numerical instabilities, but not too tight so as to not affect the solution. Two ACs, ESA and COD, instead of providing a priori blocks, provide normal equations of the unconstrained solution, $n = A^T Q_z^{-1} z$ in the SOLUTION/NORMAL_EQUATION_VECTOR block and $N = A^T Q_z^{-1} A$ in the SOLUTION/NORMAL_EQUATION_MATRIX block. Eqs (4.1) and (4.2) are in that case skipped, with the third term in (4.1) being applied to the normal equations which are then simply inverted to obtain the solution without stated constraints.

Removing unstated minimum constraints - augmentation step In this second step the assumption is that the remaining unstated constraints are minimal, which they should be for the epoch solutions used here, as this is the requirement for repro2 and equivalent solutions. The deconstrained solution from the previous step is further loosened by augmenting the deconstrained estimate VCM such that the standard errors of the unobserved Helmert parameters become large. This can be done by either (Davies and Blewitt, 2000):

$$Q_{\tilde{x}} = Q_{\overline{x}} + C^T Q_w C \tag{4.3a}$$

or

$$Q_{\tilde{x}} = (\ Q_{\overline{x}}^{-1} - Q_{\overline{x}}^{-1} C^T (C Q_{\overline{x}}^{-1} C^T + Q_w)^{-1} C Q_{\overline{x}}^{-1}\ )^{-1} \tag{4.3b}$$

where the $\sim$ denotes the augmented deconstrained matrix. Q_w is a diagonal VCM of the augmented parameters. It is constructed by multiplying a 3×3 identity matrix by the square of the chosen standard deviation for a loose orientation constraint. The latter is originally in Tanya chosen to be 10^{-7}, since tests have shown that it gives almost the same results as aligning the networks before combination, or explicitly estimating the rotation parameters alongside the global network combination (Davies, 1997). For this project it has been reduced to 10^{-8} given that the ACs' solutions are more consistent with each other now and the advancement in computation numerical stability in the past 20 years gives smaller matrix condition numbers. In the terminology used by Davies (1997) and Blewitt (1998), Eq. (4.3) is called a loosening transformation. C is made up of the appropriate rows of the Jacobian matrix of Helmert transformation, referring to the reference system parameters which are to be augmented. In case of a global network, the parameters are three orientations, thus the step is done as orientation loosening. The information about geocentre and scale are kept. In case of a regional network, C contains rows referring to all seven parameters of the Helmert transformation, thus the step includes loosening the geocentre and scale information as well as orientation loosening. Therefore, unlike the first step, this step does not involve removing any constraints specific to AC processing. Instead, the augmentation is selected based on the type of network, i.e. it is based on which Helmert parameters are unobserved. Note that this step is not applied to JPL solutions since they are provided as already loose solutions.

4.2 Network combination method

The principle of combining SINEX solutions in Tanya is shown in Fig. 4.3. Firstly, the core network (kinematic solution) ITRF2014-IGS network is loaded into Tanya. To align the combined daily epoch solutions to the ITRF2014 reference frame, i.e. to the kinematic solution ITRF2014-IGS, the latter has to be propagated to each of these epochs.

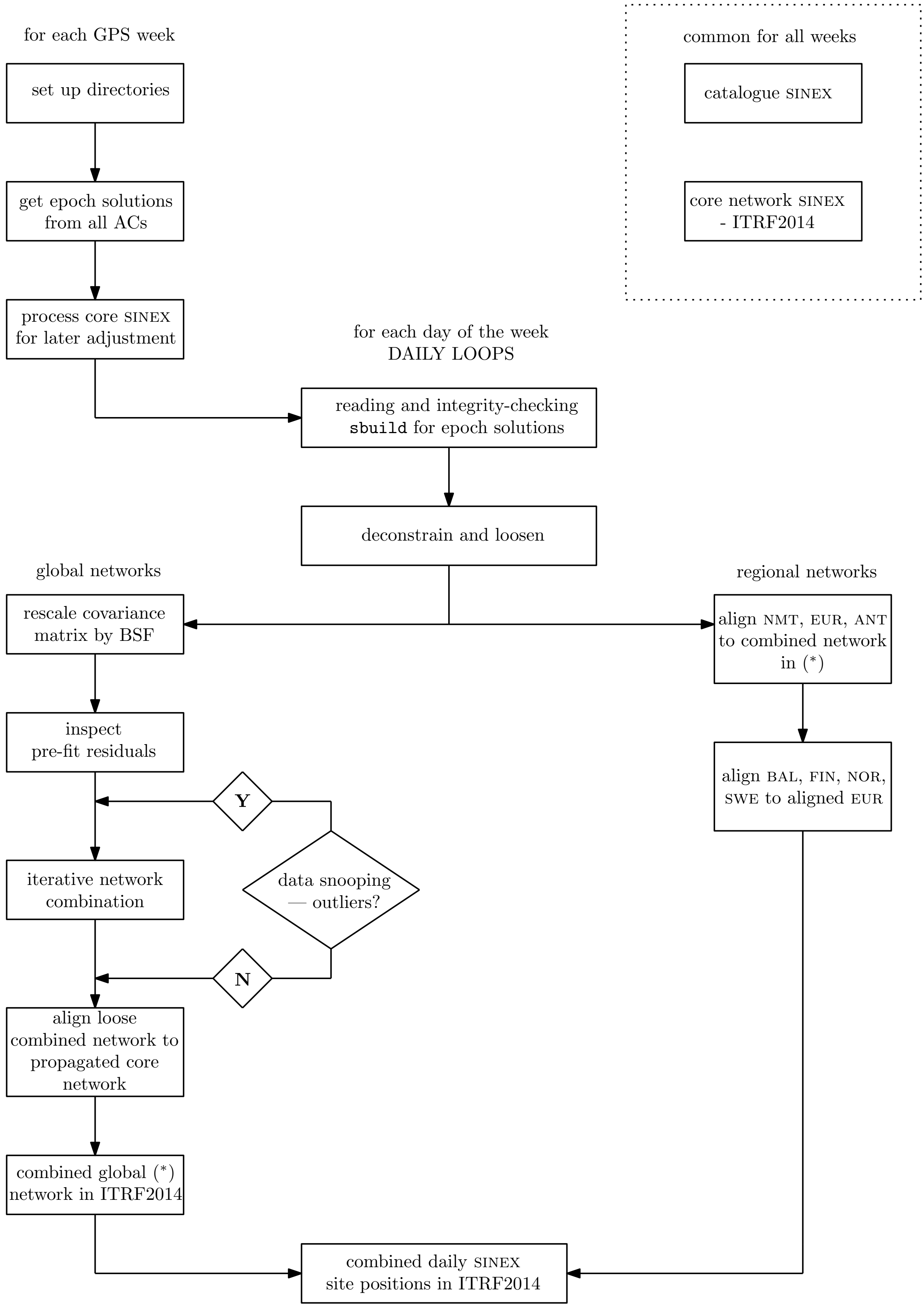

Figure 4.3: The process of creating the combined network

4.2.1 Propagating the core network

To propagate ITRF2014-IGS to the desired epoch, appropriate sets of positions, velocities and VCMs valid for the respective epoch need to be chosen. The previous version of Tanya could not choose the sets of parameters for kinematic solutions according to the propagation epoch. Therefore, a part of the software development in this thesis was modifying this process, which is described in detail in Appendix B and illustrated in Fig. B.1.

Once the appropriate parameters are chosen, the position of the site in ITRF2014-IGS at the relevant epoch is computed using Eq. (3.1). For sites for which PSD models are available, site displacement caused by post-seismic relaxation is also computed and the position is corrected for it.

The propagation of the position of a site X_t^{PSD} through a post-seismic trajectory at time t can be computed as (Altamimi et al., 2016):

$$X_t^{PSD} = X_0 + \dot{X} \cdot \Delta t + \delta X_t^{PSD} \tag{4.4}$$

where X_0 is the position of a site at reference epoch t_0, Δt is $t - t_0$, the time that passed since the reference epoch until time t, $\dot{X}$ is the site linear velocity vector and δX_t^{PSD} is the total sum of the PSD corrections. The first two terms on the right hand side are equivalent to the right hand side of Eq. (3.1) for computing the position for a site with only linear velocity. The last term on the right hand side can be computed for each component $L \in E, N, U$ of δX_t^{PSD} in the local topocentric system (Altamimi et al., 2016):

$$\delta L_t^{PSD} = \sum_{i=1}^{n^l} A_i^l \log(1 + \frac{t - t_i^l}{\tau_i^l}) + \sum_{i=1}^{n^e} A_i^e (1 - e^{-\frac{t - t_i^e}{\tau_i^e}}) \tag{4.5}$$

where:
n^l ... number of logarithmic terms of the parametric model
n^e ... number of exponential terms of the parametric model
A_i^l ... amplitude of the i^{th} logarithmic term
A_i^e ... amplitude of the i^{th} exponential term
τ_i^l ... relaxation time of the i^{th} logarithmic term
τ_i^e ... relaxation time of the i^{th} exponential term
t_i^l ... earthquake time (date) corresponding to the i^{th} logarithmic term
t_i^e ... earthquake time (date) corresponding to the i^{th} exponential term

Eq. (4.5) is only applied if an earthquake is recorded before t. Details of the mathematical setup of PSD models, their uncertainties and implementation in Tanya are described in section B.2 of Appendix B.

It should be noted that for any kind of velocity propagation (either purely linear or with PSD) in Tanya, the VCM information is also retained in the propagation process.

4.2.2 Combining epoch solutions

The epoch network solutions are deconstrained before starting the combination process. Most of the epoch solutions were expressed in the ITRF2008 reference frame, however, deconstraining them removes the information about the reference frame and it is therefore not important which reference frame the epoch solutions were originally expressed in. The global epoch network solutions are called A-networks, and the regional epoch network solutions are called R-networks. Only A-networks are combined in an iterative process creating a so-called G-network, due to computational costs of the iterative process. R-networks are later attached to the G-network (Fig. 4.3).

Combining global solutions

Once the A-networks solutions are loosened, a Block Scaling Factor (BSF) is applied to the VCMs. This determines the influence that each network has on the final combined solution. It is applied because the relative scaling of the input AC network VCMs is not always correct (Davies and Blewitt, 2000). The BSF is determined empirically through consecutive daily network combinations with the idea of following long-term trends in AC networks matrix scaling and solution performance (Davies, 1997). For the repro2 solutions and operational solutions that followed them, each AC uses the same software and models throughout the entire data set, such that the VCMs should be homogenous and a constant BSF can be used for each AC in the entire time series (Booker, 2012; Booker et al., 2014). Note that in the COD AC processing, around GPS week 1910, there was a change (cause unknown) which did not allow COD solutions to be successfully combined with the other ACs. A new BSF was therefore computed for COD from consecutive daily network combinations from weeks 1900-1932, allowing the BSF to fluctuate every day. After a few GPS weeks, the BSF converged around a new value and the average of BSFs for GPS weeks 1906-1929 was taken as a new BSF value, $1.33{\cdot}10^{-4}$. The new value was then applied for COD for the GPS weeks 1901-1933. The values of BSFs for all ACs are listed in Table 4.2.

Analysis Centre	Block scaling factor
EMR	1.16
ESA	2.16
GFZ	6.15
GRG	7.69
JPL	6.62
MIT	$3.10{\cdot}10^{-1}$
SIO	$4.01{\cdot}10^{-1}$
COD (repro2 and operational until GPS week 1900)	$1.61{\cdot}10^{-4}$
COD (GPS weeks 1901-1933)	$1.33{\cdot}10^{-4}$

Table 4.2: BSFs for ACs contributing to the global combined solution. The same BSF is used for repro2 and the following operational solutions.

Next, it is checked whether each of the individual AC networks fits with the core network within a threshold of 3σ, in order to flag potential gross errors before the iterative network combination starts. In the usual Tanya network combination, which is used in Newcastle University GNAAC combination, sites are included in the combined network only if they appear in three or more AC solutions. This was changed in the present project in order to have a dense network suitable for testing GIA models, by including any site which is processed by at least *one* of the ACs into the combined network. The A-networks are combined within the least-squares framework using the step-by-step least-squares method (e.g. Cross, 1992). Reduced normal equations are formed and outliers are removed using data snooping (Baarda, 1968). The data snooping ensures the internal stability of the network. The normal equations are stacked (summed) and solved, giving a loose combined global daily network.

Finally, the loose combined network is then aligned to ITRF2014 using a 7-parameter Helmert transformation between the loose daily combined network and the ITRF2014 network propagated to the corresponding day. The Helmert parameters are estimated in an iterative process where a site is excluded from the Helmert parameter estimation whenever a coordinate difference between the site in the aligned combined network and the same site in ITRF2014 is over 15 cm or 50σ of that site. These values have been empirically chosen as a compromise between having a sufficiently large number of sites for Helmert parameter estimation and not distorting the network. Only one site is excluded in every iteration and the process is iterated until all sites satisfy the coordinate difference condition. This way, an automatic procedure is introduced to exclude sites that show inconsistencies between the epoch solutions and propagated ITRF2014, which would distort the network through suboptimal Helmert transformation parameters. It is also possible to add sites to an exclude list in advance, in case it is known that the site position or velocity has changed since the publication of the kinematic network that the daily solution is being aligned to (e.g. if an earthquake or equipment change has taken place after the publication of ITRF2014).

The estimated Helmert parameters are then applied to all the sites in the network. This transforms the combined daily network solution reference frame into ITRF2014. When the alignment process is over, Tanya produces a report on the network internal geometry and alignment to the kinematic network. The Weighted Root Mean Square Error (WRMS) of the alignment of the combined network with ITRF2014-IGS is ~2.5 mm on average. The time series of WRMS of the combined network with ITRF2014-IGS is shown in Fig. 4.4.

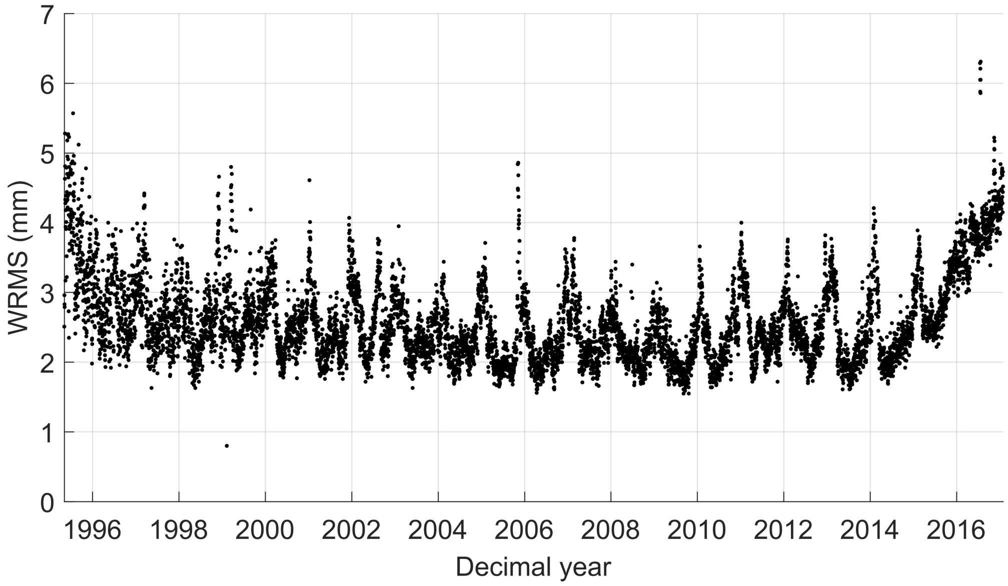

Figure 4.4: WRMS of the post fit residuals of the alignment of the combined global network and ITRF2014

An example of the time series of a site in the aligned combined network compared to the propagated ITRF2014 solution is shown in Fig. 4.5. The Arequipa site experienced a large Earthquake after which the time series of positions was propagated using the PSD models. The figure shows that the propagated ITRF2014 trajectory during post-seismic relaxation closely follows the observed trajectory from the combined epoch solutions.

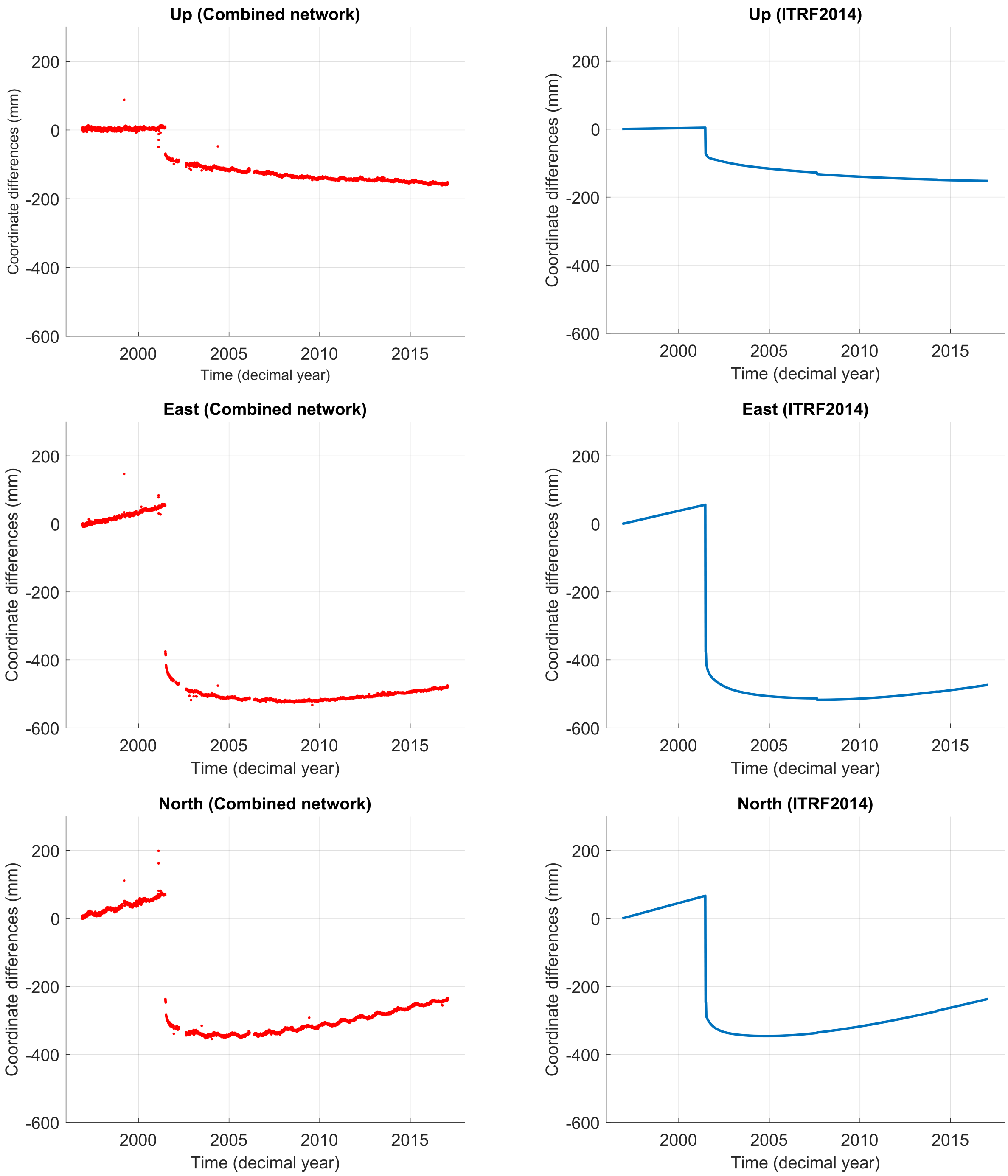

Figure 4.5: Time series for East, North and Up components for the Arequipa site in Peru in the herein combined global network (left column) and ITRF2014 solution propagated to the same epochs (right column).

Combining regional solutions

I attach each daily regional solution to the global solution by aligning it to the final combined network in the ITRF2014 reference frame. Each of the regional solutions is deconstrained as described above and the loose solution is aligned to the global combined solution at each day. As mentioned in section 3.4, aligning is done between a network and a reference network through a set of common sites between the two. The reference network is here the combined global solution obtained in the previous section. EUR, NMT and ANT are aligned to the combined global solution directly. To increase the number of common sites for network alignment, the Fennoscandian and Baltic (BAL, FIN, SWE, NOR) networks are aligned to EUR, which had been aligned to the combined solution. The Helmert parameters are estimated in an iterative process as for the global solutions.

Finally I obtain a global set of daily positions in ITRF2014 named NCL2019. The sites have time spans of up to 20 years depending on the site; see the network time spans in Fig. 4.1 and Fig. 4.2.

4.3 Velocity estimation

The time series of positions in the NCL2019 network is used to estimate a global GNSS surface velocity field. This section describes the process of obtaining the final GNSS surface velocity field from the combined network of site coordinates and it is illustrated in Fig. 4.6. For the velocity estimation, I use the Median Interannual Difference Adjusted for Skewness (MIDAS), a trend estimator introduced by Blewitt et al. (2016). The following section presents a brief summary of their work.

4.3.1 MIDAS trend estimator

MIDAS is based on the Theil-Sen (Theil, 1950; Sen, 1968) estimator. The ordinary Theil-Sen estimator is for the case of coordinate time series defined as the median of slopes between pairs of data:

$$\hat{v} = \mathrm{median}_{j>i}\left(\frac{x_j - x_i}{t_j - t_i}\right), \tag{4.6}$$

where coordinates x_i and x_j are sampled at time t_i and t_j, respectively. The ordinary version of Theil-Sen computes the median slope between all possible pairs in a coordinate time series. To mitigate seasonality in water resources research it has been suggested to select only data that are separated by an integer number of years (Hirsch et al., 1982). Blewitt et al. (2016) further restrict this by choosing data that is separated by just one year, to make the trend estimator less sensitive to offsets or step discontinuities. Should an offset appear in the coordinate time series, the pairs spanning the discontinuity will be on one of the tails of the distribution. By restricting the time separation between pairs to be just one year, instead of any integer number of years, the fraction of pairs that span discontinuities is minimized while still retaining insensitivity to seasonality. While MIDAS mitigates the effects of periodic signals which are harmonics of one year, it is sensitive to large periodic signals that do not repeat from one year to the next or signals of other frequency. Blewitt et al. (2016) tested if relaxing the specific choice of one year to some degree in the interannual Theil-Sen estimator would generate superior results. They investigated if allowing all possible pairs within a wider time window around 1 year might generate superior results. They gradually widened the window up to 100 days to allow up to 10^4 more pairs and found that the velocity estimates change at the $\sim$0.1 mm/yr level, suggesting that the minimal selection of pairs contains all of the independent information available.

If offsets exist in the time series, the interannual Theil-Sen estimator can be biased. Offsets smaller than two standard deviations of the data noise generally produce a skewed unimodal distribution where one tail is more populated than the other. To deal with this, an initial value of the median trend is computed using slopes from all selected data

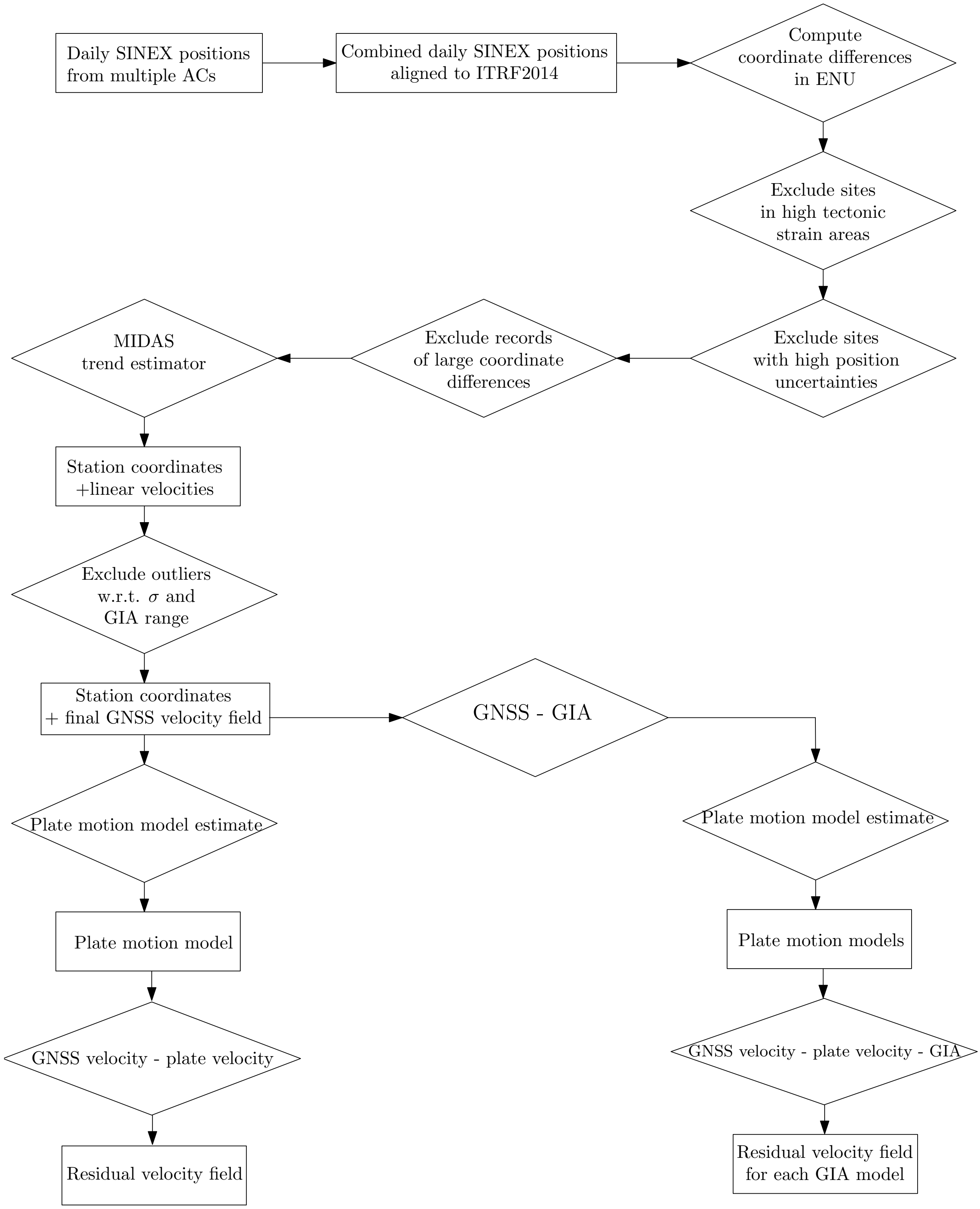

Figure 4.6: From GNSS network positions to the residual velocity fields

pairs and the slopes are defined as outliers (possibly associated with offsets) if they are greater than two standard deviations on either side of the median. Since this requires an estimate of the standard deviation of the distribution which is not sensitive to outliers, the estimate of standard deviation is based on Median of Absolute Deviations (MAD), which is a robust estimator of dispersion. The choice of excluding data at two standard deviations creates a balance between having a small impact on a majority of data that has a Gaussian distribution while effectively removing outliers due to discontinuities (Blewitt et al., 2016).

The selection of pairs of data one year apart works well for sites with continuous time series without any gaps. Sites which have campaign sessions with large gaps between them still contain valuable information, which is why Blewitt et al. (2016) relax the selection criteria of exactly one year. Finally, the MIDAS algorithm is based on the following principles:

1. There should be a negligible difference in the estimates if small gaps in a time series are introduced. There is no threshold which defines whether a time series is treated as continuous or otherwise, the same code applies to all time series.
2. The principle of time symmetry demands that if all the data were reversed in time, the magnitude of the velocity estimate should not change. The code runs the pair selection twice, firstly in time order and secondly in reverse time order.
3. The selection should give priority to pairs separated by one year. When moving forward or backward through the data to select pairs, the first priority is given to pairs exactly one year apart, if they exist.
4. A pair separated by more than one year is selected if a one-year pair cannot be formed. If there is no matching pair one year apart, the next available data point that has not yet been matched is selected.

In the original MIDAS script, if for a certain record, a suitable pair is not found which is exactly one year apart, the next available record is taken regardless of how far apart in time they are. In this project I use a modified algorithm based on a script written by Peter Clarke (personal communication, 2019). The script is based on the MIDAS algorithm but additionally includes a tolerance value away from one year. In this version, if a pair separated by exactly one year cannot be found, it searches for a pair that is within a “tolerance value” before or after the one year difference. For example, a tolerance value of 7 days means that only coordinate pairs that are between 358 (one year minus 7 days) and 372 days (one year plus 7 days) apart can be accepted. I tested which tolerance value to choose by starting with 7 days as being almost the same as one year and 1 month as a safe choice of avoiding seasonal signals. I found that the difference in velocity estimates with 1 week, 2 weeks, 3 weeks and 4 weeks tolerance value is lower than the uncertainty estimate and finally chose 4 weeks to maximise the amount of data. The script cannot estimate long time series due to computational limits, so I used the original MIDAS script for sites with very long time series. Such sites in the NCL2019 generally do not have data gaps which justifies not using a tolerance value.

Blewitt et al. (2016) tested the robustness of the MIDAS estimator for a continuous time series. It can be quantified by its breakdown point, which is defined as the number of arbitrarily large outliers in a data set that can be tolerated before the estimate becomes arbitrarily large. They find that the asymptotic breakdown point of MIDAS is $0.25(1 - 1/T)$ where T is the time spanned by all the data divided by the time separation between data pairs. This means that with MIDAS, up to 25% of the data can be outliers for very long time series (10 years or more), which is lower than the ordinary Theil-Sen estimator and higher than least-squares estimators and the sample mean. To quantify the resistance to discontinuities, Blewitt et al. (2016) introduce an additional "step breakdown point", defined as the minimum number of arbitrarily large steps (offsets) in the time series that cause the estimator to give arbitrarily large values, as a function of the time span T in years. They find that the asymptotic step breakdown point for a continuous time series is $(T - 1)/2$. Assuming the worst case scenario, where steps do not overlap and they are all in the same direction, no arbitrarily large steps can be tolerated for a time series shorter than three years, after which one step can be tolerated. One more step can be tolerated for every two additional years. The breakdown points above refer to the velocity estimate, Blewitt et al. (2016) also find that in terms of breakdown point, the MAD and the MIDAS velocity uncertainty are just as robust as the velocity estimate.

4.3.2 Time series analysis

The MIDAS trend estimator works on one velocity component at a time and therefore cannot take into consideration the correlation between the coordinate components. To mitigate the correlation between components when estimating the trend, I convert the time series from the Cartesian XYZ reference system, to the topocentric East-North-Up (ENU) system. To convert the coordinates, I compute coordinate differences of positions with respect to a reference position (chosen to be the median of all positions in the time series) and convert these coordinate differences and their uncertainties to the ENU system. Before estimating the trend, I perform a three-step refining and filtering of the sites and individual positions' records:

1. Exclude sites in high tectonic strain areas
2. Exclude sites with high position uncertainties

3. Examine sites which show anomalies

(1) The sites in high tectonic strain areas are excluded because they would contaminate the GIA and rigid plate motion study. The sites in high and low tectonic strain areas were selected using the Global Strain Rate Model (Kreemer et al., 2014) by interpolating the strain values to the NCL2019 network sites and choosing only sites where the second invariant of the strain tensor was smaller than 0.1 microstrains. The sites where the second invariant of the strain tensor was larger than 0.1 microstrains are considered sites in high tectonic strain areas and they are excluded. Additionally, the sites which are within 100 km of high tectonic strain areas are excluded. Fig. 4.7 shows the sites in low tectonic strain areas.
(2) MIDAS uses the median to estimate the trend which means that it does not take into consideration the formal errors of the positions. After a visual inspection of the spread of position uncertainties, I consider position records reliable for velocity estimation when σ_E and σ_N is within 10 mm and σ_U within 15 mm as the large majority of records lie well within these values.
(3) Within the remaining records, I exclude coordinate differences larger than 100 m, as these only appear as a small number of individual records (maximum 20 daily records per site in entire time series) that cannot represent a step discontinuity but only outliers. I then investigate the coordinate differences between 1 m and 100 m which could not be due to any long term displacement. Nearly all sites have less than 0.01% of such records per site, which are easily detected as outliers by the MIDAS median estimator in the trend estimate. The rest of the sites (namely AUS1, SMM1, SMM2) which have a large proportion of records with coordinate differences between 1 m and 100 m were analysed manually and remained in the time series at this step.

I estimated velocities for each of the networks - the global combined network and the regional networks. I have combined the velocities giving priority to higher-order networks when a site was estimated in multiple networks. E.g. a global site estimate is prioritised over a regional site estimate, and EUREF sites over Fennoscandian sites. The velocity field consists of 1218 sites which are then further subjected to filtering.

4.3.3 Excluding sites from the velocity field

To make sure that the velocity field is not biased by multiple estimates in the same close area, I remove such duplicate sites from the velocity field. Sites which are within 100 m are likely to be the same site, but situated on different monuments. I select groups of sites that are within 100 m radius from each other and merge them if their velocities are similar. When a group of sites is within 100 m, pairs of sites are formed and for each pair

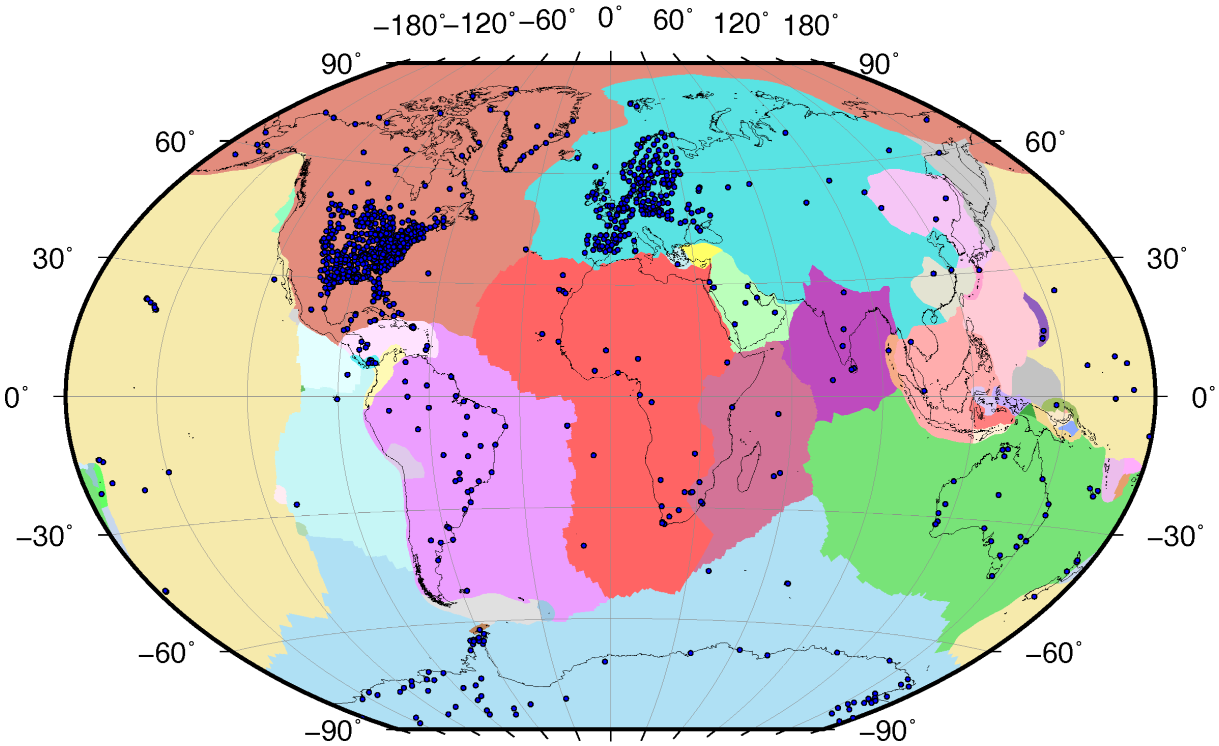

Figure 4.7: Plate boundaries from Bird (2003) and sites in low tectonic strain areas

of sites with velocities v_i and v_j, the z-score is computed:

$$z_{ij} = \frac{|v_i - v_j|}{\sigma_{i-j}} \tag{4.7}$$

where σ_{i-j} is the uncertainty of the difference of the velocities. The pair with the smallest z-score is selected, and if that z-score is ≤ 1, the velocities are considered similar enough and they are merged into one velocity v_{ij} as:

$$v_{ij} = \frac{\frac{v_i}{\sigma_i^2} + \frac{v_j}{\sigma_j^2}}{\frac{1}{\sigma_i^2} + \frac{1}{\sigma_j^2}} \tag{4.8}$$

The uncertainty of the merged velocity σ_{ij} is computed as:

$$\sigma_{ij} = \sqrt{\frac{1}{\frac{1}{\sigma_i^2} + \frac{1}{\sigma_j^2}}} \tag{4.9}$$

New pairs are then formed and the process is iterated until there is only one velocity left within 100 m radius, or until the smallest z-score is greater than 1. When the smallest z-score is greater than 1, the velocities are not considered similar enough to be merged, and instead the velocity with the smallest velocity uncertainty is chosen.

The merged sites which have different SITE ID code, usually have the same first three characters of the four-character SITE ID code. The merged site then gets a new name, i.e. a new four-character SITE ID code, starting with "M" followed by the first three characters of the names of the merging sites.

Monuments are usually within tens of metres from each other. Following this, if sites are more than 100 m and less than 5 km from each other, this is likely not the same site and in that case, the site with the smallest velocity uncertainty is chosen.

To remove outliers, i.e. sites which seem to show velocities that are beyond what could be explained by any natural or long term displacement, I choose a threshold based on the overall range of GIA models at that site. The threshold for the vertical component is the sum of (1) the range of GIA models vertical predictions with (2) an additional 50% of the range as a safety measure, and (3) three standard deviations of the GNSS velocity component. The threshold for the horizontal component is (1) maximum horizontal velocity magnitude from a range of GIA models with (2) additional 50% of that value and (3) three standard deviations of the horizontal speed of the GNSS velocity component. Any site with a velocity larger than the threshold is considered to entail velocities that cannot contribute to the comparison of GIA models.

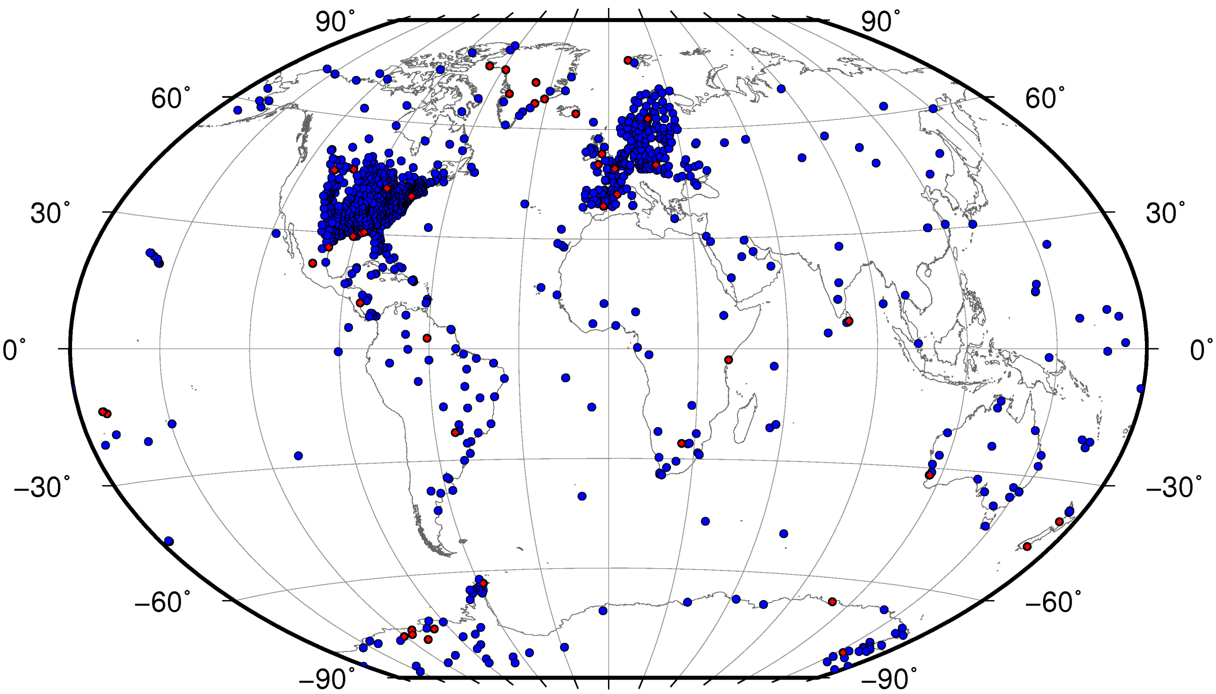

Figure 4.8: Remaining (blue) and excluded (red) sites depending on whether the site velocities are larger than the threshold based on the GIA range

If the vertical velocity component of the site is larger than the vertical threshold, the site is excluded. In the horizontal component, before comparing the horizontal velocity magnitude with the threshold, it is necessary to remove plate motion from the observed site motion. The plate motion model used in this step is a preliminary plate motion model model estimated from the GNSS velocities using the method outlined in Chapter 5. Finally, any site where the horizontal velocity magnitude, without plate motion, is larger than the horizontal threshold, is also excluded. In this step, 47 sites are excluded (Fig. 4.8). This results in the final global GNSS velocity field containing 965 sites,

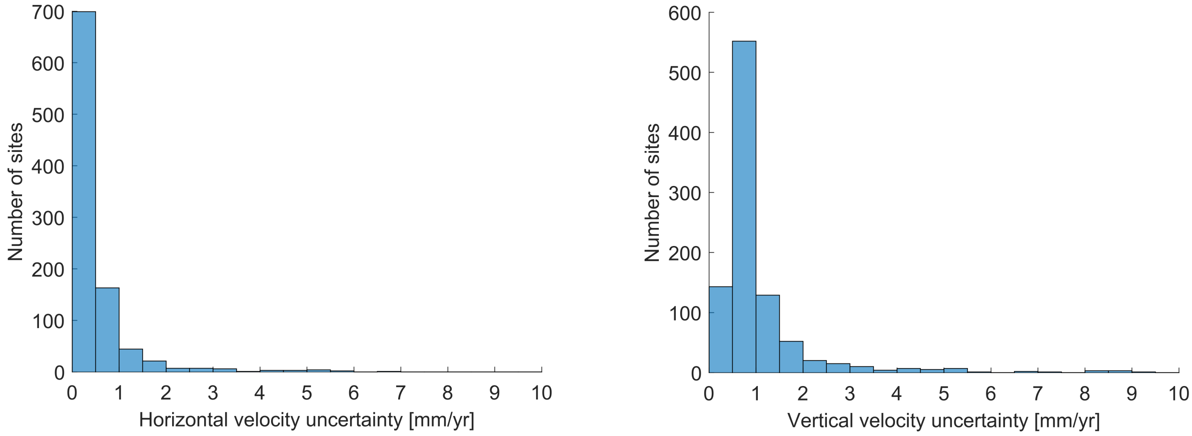

Figure 4.9: Histograms of the site velocity uncertainties in the horizontal (combined Easting and Northing velocity standard deviation into horizontal magnitude uncertainty) and vertical (Up velocity standard deviation) components for the final GNSS velocity field.

where the horizontal velocity uncertainties are mostly within 0.5 mm/yr, and vertical velocity uncertainties mostly within 1 mm/yr (Fig. 4.9). The GNSS site names, locations, velocities and velocity uncertainties are listed in Table C.1.

4.4 Summary and discussion

Within this chapter, multiple global epoch solutions were combined into unique global epoch solutions of high stability. The unique global solutions are aligned to the most recent ITRF2014 reference frame. Additionally, several regional network solutions were aligned to the unique global solutions. The GNSS solutions used are processed with the latest available methods and models: all the global and regional solutions adhere to IGS repro2 standards. Every network solution gives standard deviations of site position coordinates and the correlations between the network sites. Throughout the network combination and alignment, outliers are detected and handled. This process was done using Tanya reference frame combination software which was further developed to facilitate the changes in network combination method and ITRF.

Fig. 4.10 is taken from Booker et al. (2014) and shows the WRMS of the post fit residuals of their combined weekly solutions (using repro1) with respect to the IGS05 reference frame. The WRMS in the present project of the combined daily solutions (using repro2 and equivalent operational solutions) with respect to ITRF2014 is shown in Fig. 4.4. The two figures show that there is an improvement in WRMS which indicates that repro2 is superior to repro1.

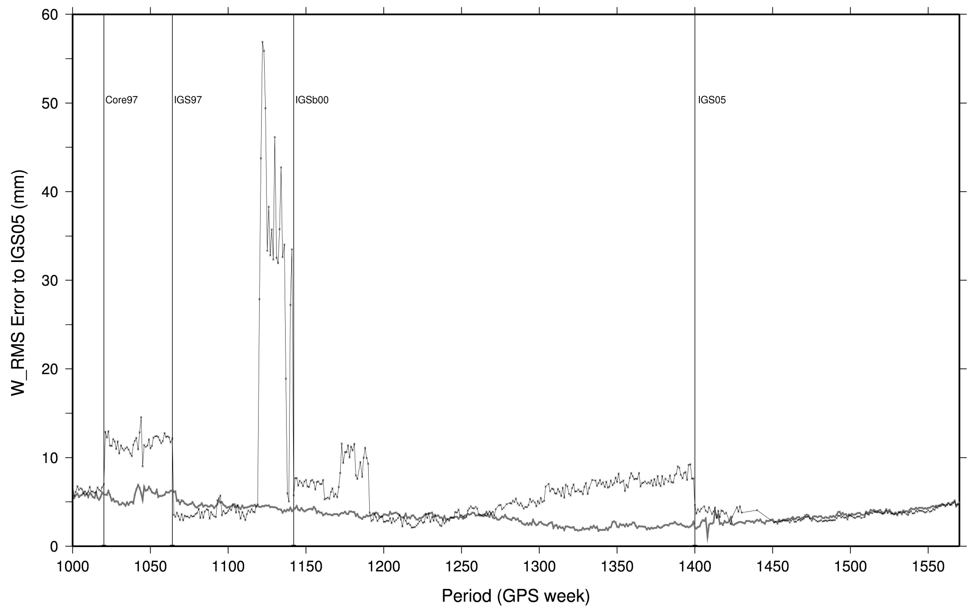

Figure 4.10: WRMS of the post fit residuals of the alignment of the combined weekly solutions (operational - thin, black and repro1 - thick, grey) to IGS05. Black vertical lines represent the adoption of a new reference frame in the operational processing. Taken from Booker et al. (2014).

The operational solutions for GPS weeks 1832-1933 (15th February 2015 – 28th January 2017) use equivalent GNSS processing standards as repro2 and they are therefore comparable with repro2. Fig. 4.11 shows the weighted post fit residuals for GPS weeks 1832-1933. The red dots show the WRMS of the combined Newcastle University GNAAC solutions using the previous version of Tanya with alignment to ITRF2008 (obtained from the IGS report archive at `https://lists.igs.org/pipermail/igsreport/`) and the black dots the WRMS of the present version with alignment to ITRF2014 for comparison (part of the times series from Fig. 4.4). This combination differs from the one in the present project in the reference frame and in the version of Tanya that was used to combine the network. They refer to network combinations using the same input AC solutions. The WRMS from the previous version of Tanya is reduced from 8.0 mm to 3.5 mm (corresponding to 57% reduction) on average when compared with the WRMS of the network alignment in the present project.

The time series of GNSS coordinates from GPS week 900 to 1933 were then used to estimate linear velocities of selected sites. The velocities were estimated using the MIDAS trend estimator. Unlike most trend estimators in geodesy which use least-squares estimation (Montillet and Bos, 2020), MIDAS is based on the median, making it robust to outliers. The MIDAS algorithm allows it to estimate linear velocities without detection of the discontinuities in the time series. MIDAS estimates velocities one component at a time neglecting the correlation between the velocity components. This was alleviated by converting the time series from XYZ to ENU. East, North and Up components are by the nature of GNSS far less correlated than the X, Y and Z components. Notable

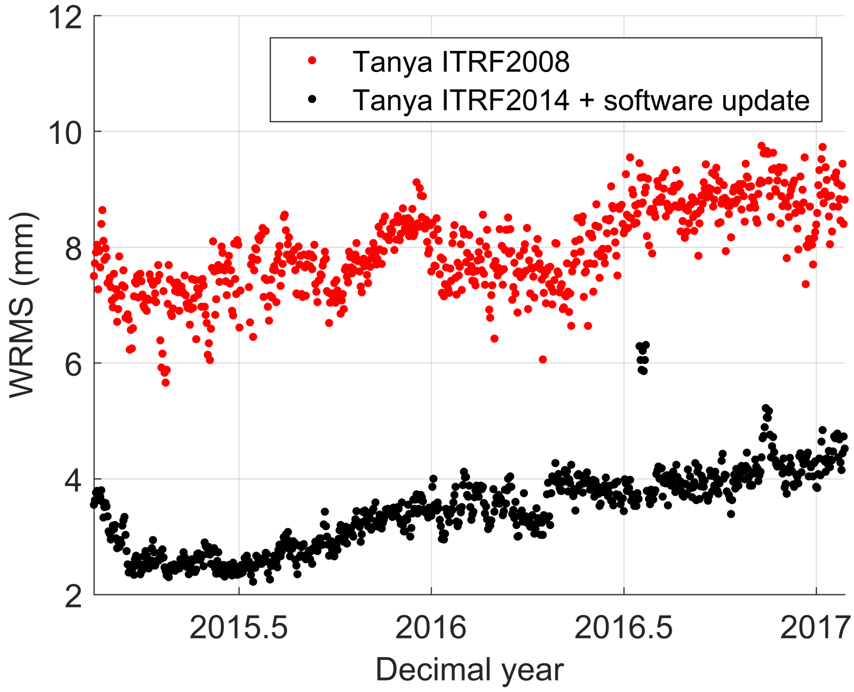

Figure 4.11: WRMS of the post fit residuals of the alignment of the here combined global network and ITRF2014, and the previous Tanya GNAAC combination aligned to ITRF2008

exceptions occur in the polar areas and the crossings of the equator with the prime and 180° meridian where the XYZ and ENU axes align, and thus the X, Y and Z components are also virtually uncorrelated.

The Tanya software is in principle capable of estimating velocities from a time series of networks, taking into consideration correlations between site velocity components and the correlation between sites in the network. In this project, however, I was not able to implement selecting the times when discontinuities occur within the velocity estimate. A similar attempt of using Tanya for velocity estimation was considered within the Resolving Antarctic ice mass TrEndS (RATES) project, but due to similar experience, the velocities were instead estimated with a different software (Elizabeth J. Petrie, personal communication, 2019). A recommendation for future work should therefore be to further adapt and update the Tanya software for velocity estimation.

The sites selected through multiple steps of quality control constitute the final GNSS surface velocity field, consisting of 965 sites which sufficiently cover the GIA-affected regions of interest. Next, plate motion is estimated using this GNSS velocity field, by removing predictions from different GIA models (see Fig. 4.6), which is the topic of the next chapter.

Chapter 5

Plate motion models

When estimating a plate motion model (PMM) from space geodetic techniques, we seek a model of tectonic plate motion that best fits the observed surface velocity field.

In this project it is assumed that the observed site motion consists of rigid plate motion, GIA-induced motion and other present-day motion (e.g. due to local tectonics, ice melting, hydrology, unmodelled GIA etc.) which I denote residual motion, i.e.

$$\dot{X} = \dot{X}_{GIA} + \dot{X}_{plate\_motion} + \dot{X}_{residual} \tag{5.1}$$

As such, PMMs are estimated by taking GIA models into account. The GIA motion is removed from the global GNSS surface velocity field, and the net velocity is used to determine a model for tectonic plate motion. Some PMMs, such as Altamimi et al. (2017), seek to avoid the effect of GIA on the PMM estimate by excluding sites in GIA regions. However, such an approach may bias the PMM since the choice of GIA regions is not straightforward. A bias may be introduced due to retaining sites in peripheral bulge regions which have relatively large horizontal GIA velocities. In this thesis, the plate motion is estimated from 117 GIA-corrected surface velocity fields (one for each of the 117 GIA models) as well as for the null-GIA case which denotes the GNSS velocity field without removing any GIA effect.

In the first and second sections I describe the mathematical model for obtaining PMMs and the method of detecting outliers in the PMM estimate. The third section briefly describes the published ITRF2014 plate motion model. In the fourth section I present the PMMs for three plates on which the three regions of interest lie (Europe, North America and Antarctica) as well as other plates. The fifth section includes the summary and the discussion of the chapter.

5.1 Mathematical model

As mentioned in Chapter 2, the plate velocity of a site i on a plate p due to the rotation of the plate on a sphere can be expressed by the vector cross product of the absolute Euler vector Ω_p and the position vector X_i of the point i.

$$\dot{X}_i = \Omega_p \times X_i, \tag{5.2}$$

where $\Omega_p = [\omega_x \; \omega_y \; \omega_z]^T$ is the Euler vector of the plate p, and $\dot{X}_i$ is the plate velocity of the point. In the inverse form, to estimate the Euler vector of a plate p, observed velocities $\dot{X}_i^{obs}$ of the sites on that plate and their position vectors X_i are used. The PMM can then be estimated using least-squares adjustment:

$$\dot{X}_i^{obs} = \Omega_p \times X_i + \nu \tag{5.3}$$

where ν are the residuals of the PMM. The GNSS velocity field obtained in the previous chapter is aligned to the ITRF2014 reference frame, thus satisfying the NNR condition and allowing to estimate an absolute PMM. The PMM estimation and outlier detection is done on the XYZ components, expressing velocities and PMM in the ITRF2014 reference frame. Hence, when estimating a global PMM from velocities on multiple plates, it is possible to estimate β, the translational vector of the velocity of the centre around which the plates rotate with respect to the geocentre of the ITRF2014-aligned GNSS velocity field. I name β the geocentre origin rate bias, after Altamimi et al. (2017).

$$\dot{X}_i^{obs} = \Omega \times X_i + \beta + \nu \tag{5.4}$$

Seeking to estimate a PMM which is not affected by GIA motion, I follow an approach similar to Booker et al. (2014), where GIA velocity predictions for each GIA model j are subtracted from the GNSS velocities prior to the PMM estimation:

$$\dot{X}_i^{obs} - \dot{X}_i^{GIA_j} = \dot{X}_i^{corr_j} = \Omega^j \times X_i + \beta^j + \nu' \tag{5.5}$$

When estimating a PMM corrected by GIA, the 1D GIA model predictions are expressed in the centre of mass of the solid Earth (CE), $\dot{X}_i^{GIA} \equiv \dot{X}_i^{GIA[CE]}$ (dropping the index of the GIA model j for clarity), the 3D GIA model predictions are expressed in a reference frame that assumes no centre of mass motion (CFEM), $\dot{X}_i^{GIA} \equiv \dot{X}_i^{GIA[CFEM]}$, and GNSS velocities are expressed in the centre of mass of the Earth system (CM), $\dot{X}_i^{obs} \equiv \dot{X}_i^{obs[CM]}$. In the following I let CG represent the GIA model frame which is either CE (for 1D GIA models) or CFEM (for 3D GIA models), and write $\dot{X}_i^{GIA} \equiv \dot{X}_i^{GIA[CG]}$. Thus, the site velocity corrected for GIA can be written as:

$$\dot{X}_i^{corr[CM]} = \dot{X}_i^{obs[CM]} - \dot{X}_i^{GIA[CG]} - v_{CG-CM} \tag{5.6}$$

where v_{CG-CM} is the velocity of a CG with respect to the CM. Considering equations (5.5) and (5.6), it can be written:

$$\dot{X}_i^{obs[CM]} - \dot{X}_i^{GIA[CG]} = \Omega_p \times X_i + \beta + v_{CG-CM} + \nu' \tag{5.7}$$

As v_{CG-CM} is inseparable from β, we form $\beta' = \beta + v_{CG-CM}$ and finally get:

$$\dot{X}_i^{corr[CM]} = \Omega_p \times X_i + \beta' + \nu' \tag{5.8}$$

The resulting vector in the least-squares estimate consists of Euler vectors Ω_p for each plate and β'. The variation of CG with respect to CM and the geocentre origin rate bias are estimated together as the last three components of the resulting vector in least-squares estimate.

The uncertainties of the PMM are propagated from the uncertainties of the input GNSS velocities (variances for each Cartesian component and covariances between the components) through the least-squares adjustment. The Euler pole of each plate (Λ_p, Φ_p) and its rotation rate ω_p are computed from the Euler vector Ω_p using the inverse form of Eq. (2.11). The uncertainties of Λ_p, Φ_p and ω_p are obtained through error propagation from the uncertainties of the Euler vector.

5.2 Outliers

The plate motion models are estimated from all three spatial components and they are first estimated for each plate separately, iteratively excluding outliers with a multiple t-test outlier search (Koch, 1999). An outlier ∇_i is estimated sequentially for each observation i, i.e. each velocity component of all sites, with the advantage that the introduction of the outlier will not affect the estimated parameters. A statistical outlier test is obtained when the null hypothesis $H_0 : \nabla_i = 0$ is tested against the alternative hypothesis $H_1 : \nabla_i \neq 0$. Using the estimated standard deviation of the outlier $\sigma_{\hat{\nabla}_i}$, the t statistic is given by

$$t = \frac{\hat{\nabla}_i}{\sigma_{\hat{\nabla}_i}} \sim t_{n-e-1}, \tag{5.9}$$

with n being the number of observations and e the number of unknown parameters. H_0 is rejected if $|t| > t_{n-e-1,1-\alpha/2}$, where α is the significance level for each individual test. In multiple testing, the chance of making a Type I error increases (i.e., the false rejection of

H_0), which is here compensated by setting $\alpha = 1-(1-\alpha_{tot})^{1/(n-e)}$, where $\alpha_{tot} = 0.05$ is the desired overall significance level (Šidák, 1967; Teunissen, 2017). If a certain measurement record, i.e. velocity component, is rejected, all three velocity components of the site are rejected before the next iteration. Fig. 5.1 shows the sites that were rejected when seeking to determine the PMM for the GNSS-only velocity field. After the removal of outliers for each plate, a PMM is estimated for all plates together neglecting all the rejected sites. Note that these sites will not be excluded from the surface velocity field, they are only excluded in the PMM estimate.

When estimating a PMM including GIA corrections, the process is equivalent to the one with GNSS-only velocities, the only difference is that the GIA velocities are subtracted from the GNSS velocities before estimating the PMM.

I use the tectonic plate boundaries from Bird (2003) to assign a plate to each site (cf. Fig. 4.7 in Chapter 4). The PMMs are only estimated for plates that have three or more GNSS sites on them. The plates which include more than three of the network sites are: Africa, Antarctica, Somalia, India, Australia, Eurasia, North America, South America, Nazca, Pacific, Arabia, Sunda, Caribbean, Amur, Mariana, Yangtze and Panama (nomenclature from Bird (2003)). Given that some sites are excluded in the PMM estimate outlier search process, it is possible that some plates will not have the required minimum three sites after the outlier rejection and will not be estimable any more. The outlier search depends on the input velocities, thus the rejected sites will be different for different GIA models. Plates that are estimated using the GNSS-only velocity field and all GIA corrected velocity fields are: Africa, Antarctica, Somalia, India, Australia, Eurasia, North America, South America, Pacific, Arabia, Sunda, Caribbean, Yangtze and Panama. Plates Amur and Mariana were only estimated with some of the GIA corrected velocity fields.

Fig. 5.2 shows the frequency at which each site is rejected when estimating PMMs using the full suite of 1D (top) and 3D (bottom) GIA models. Compare with Fig. 4.8 for the full GNSS site network. It can be seen that some sites are excluded with almost all GIA models, whereas some are excluded with a small number of GIA models. There are more excluded sites with 1D GIA models, but there is also a larger number of 1D GIA models. The majority of rejected sites in Figures 5.1 and 5.2 are situated in North America and Greenland. However, in North America there is a very high density of sites so neglecting a portion of sites there for the PMM estimate is not critical. The sites on the west coast of Hudson Bay are excluded in the majority of cases and this is where large GIA uplift is expected. The model fit for estimating PMMs is in three Cartesian dimensions (Eq. 5.8) because it seeks to determine global plate motion. Therefore the PMM estimate can be affected by vertical outliers as well as horizontal.

The GNSS-only PMM excludes from the estimate all the sites in the northernmost part of North America and Greenland where the density of sites is sparse, as well as several sites in

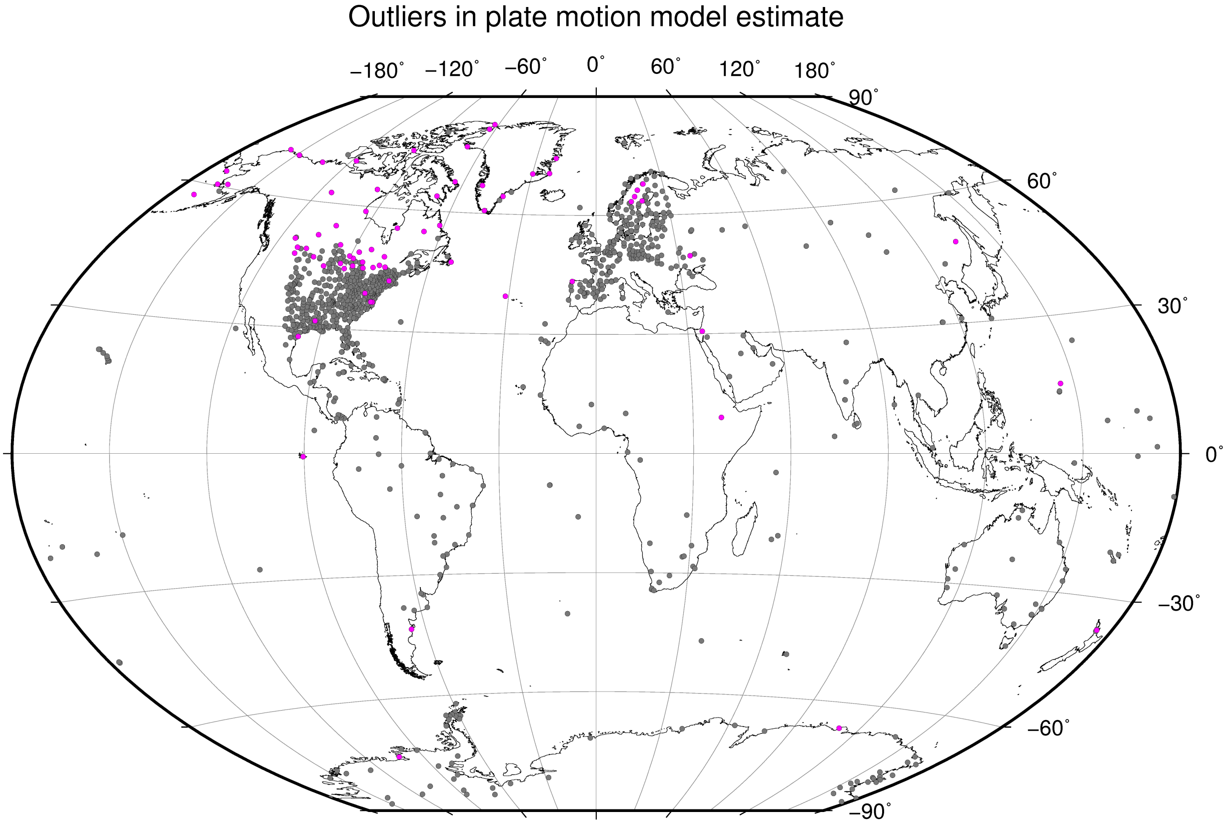

Figure 5.1: Suspected outliers (marked in magenta) of the PMM based on the GNSS-only velocity field. Gray denotes sites that were included in the final PMM estimate.

the middle of the Scandinavian peninsula. For GIA PMMs, the sites in the northernmost parts of North America are excluded in the majority of cases. In Fennoscandia, a few sites are excluded in a smaller number of cases. For 1D GIA PMMs (Fig. 5.2 top), a cluster of sites in the United States and south Canada are excluded, mostly in a small number of cases, with a few sites in the west excluded in the majority of cases.

5.3 ITRF2014 plate motion model

ITRF2014 plate motion model (ITRF2014 PMM) is a PMM consistent with the ITRF2014 reference frame created by Altamimi et al. (2017). This section is a brief summary of ITRF2014 PMM, an extensive description can be found in Altamimi et al. (2017). Since the ITRF2014 reference frame satisfies the NNR condition applied to the Earth's surface, ITRF2014 PMM is in NNR. The plate angular velocities and origin rate bias are estimated following a similar approach to the one outlined in section 5.1 using a global network of surface velocities. Their velocity field consists of GNSS, VLBI, SLR and DORIS ITRF2014 sites. The sites are chosen to satisfy several criteria, one of which is that the sites must be located far from GIA regions. Altamimi et al. (2017) satisfy this condition by excluding sites that show vertical GIA velocities of ≥0.75 mm/yr based on the Australian National

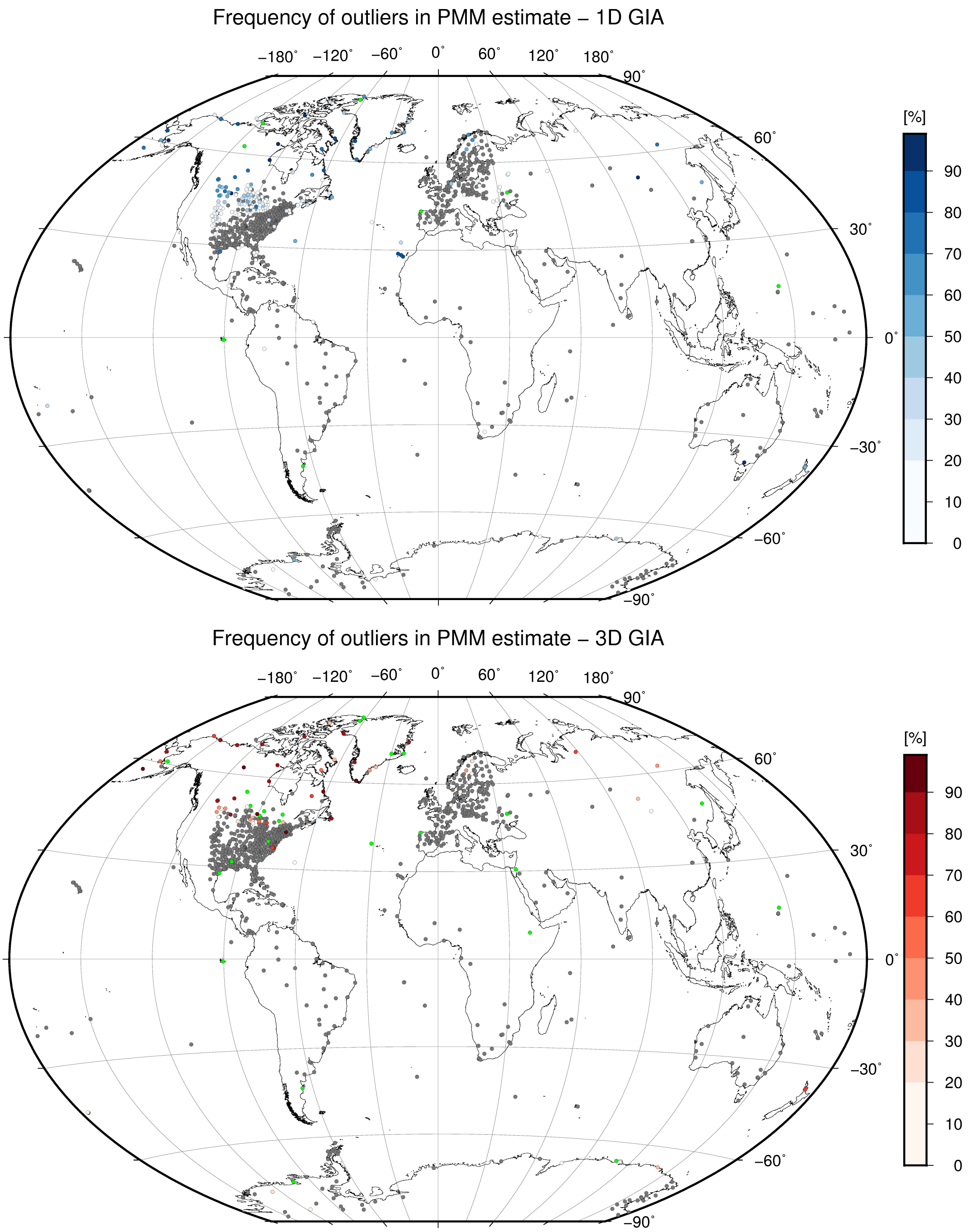

Figure 5.2: The frequency of outliers to the PMM estimate for the velocity fields corrected with 1D (top) and 3D (bottom) GIA models. Green denotes the sites that are excluded for all the PMMs. Gray denotes sites that were always included in the final PMM estimate.

University GIA model of Lambeck et al. (2014, 2017). They keep the sites in Antarctica regardless of this condition, in order to be able to estimate the Antarctic plate and because their tests indicated that the Euler pole of the Antarctic plate could only marginally be biased by GIA effects. They do not take horizontal velocities due to GIA into account, and state that far from GIA regions, horizontal velocities due to GIA of up to 3-4 mm/yr may be found. Thus, the ITRF2014 PMM is not ideal for GIA studies since it excludes sites in most GIA regions. Also, it may be biased due to the presence of residual GIA-associated horizontal velocities outside of the above mentioned GIA regions.

ITRF2008 PMM (Altamimi et al., 2012) is the predecessor of the ITRF2014 PMM, aligned to the ITRF2008 reference frame (Altamimi et al., 2011). In creating the ITRF2008 PMM, Altamimi et al. (2012) attempted to correct the network velocities for GIA before estimating plate models, using ICE-5G/VM2 and VM4 (Peltier, 2004) and a GIA model by Schotman and Vermeersen (2005) for the three plates affected the most by GIA: Antarctica, Eurasia and North America. They found for Eurasia that ICE-5G/VM2 and VM4 (hereafter VM2 and VM4) only improve the plate model fit in the north component while the model from Schotman and Vermeersen (2005) (hereafter SV) decreases the WRMS in both east and north components. When they exclude sites in GIA regions, applying the VM2 and VM4 GIA models degrades the fit, while the SV model only marginally improves it. They perform the same comparison for the North American and Antarctic plate and find that in North America, the VM2 and VM4 models degrade the results significantly and the SV model slightly improves the fit in the north component. For the Antarctic plate, they find that the VM2 and VM4 models improve the fit in the north component only, and the SV model degrades the fit in both horizontal components. Consequently, ITRF2008 PMM also does not correct the velocity field for GIA as per ITRF2014 PMM. It is also created using only sites where the GIA vertical velocity is up to 0.75 mm/yr.

I extend the ITRF PMM approach by introducing an updated suite of GIA models, including 3D GIA models. GIA vertical motion is expected to be the largest in the centre of the former ice sheet, whereas the largest horizontal velocities are expected in the fore-bulge. The approach that excludes sites in the area of large vertical velocities might introduce a bias by retaining sites in peripheral bulge regions which may have small GIA-related vertical velocities, but relatively large GIA-related horizontal velocities. This is an additional reason as to why it is difficult to select areas that are not affected by GIA, besides not being able to know the uncertainty of the vertical predictions of GIA models. Thus, it is expected in this project that the additional consideration of horizontal velocities due to GIA should improve the estimation of PMMs.

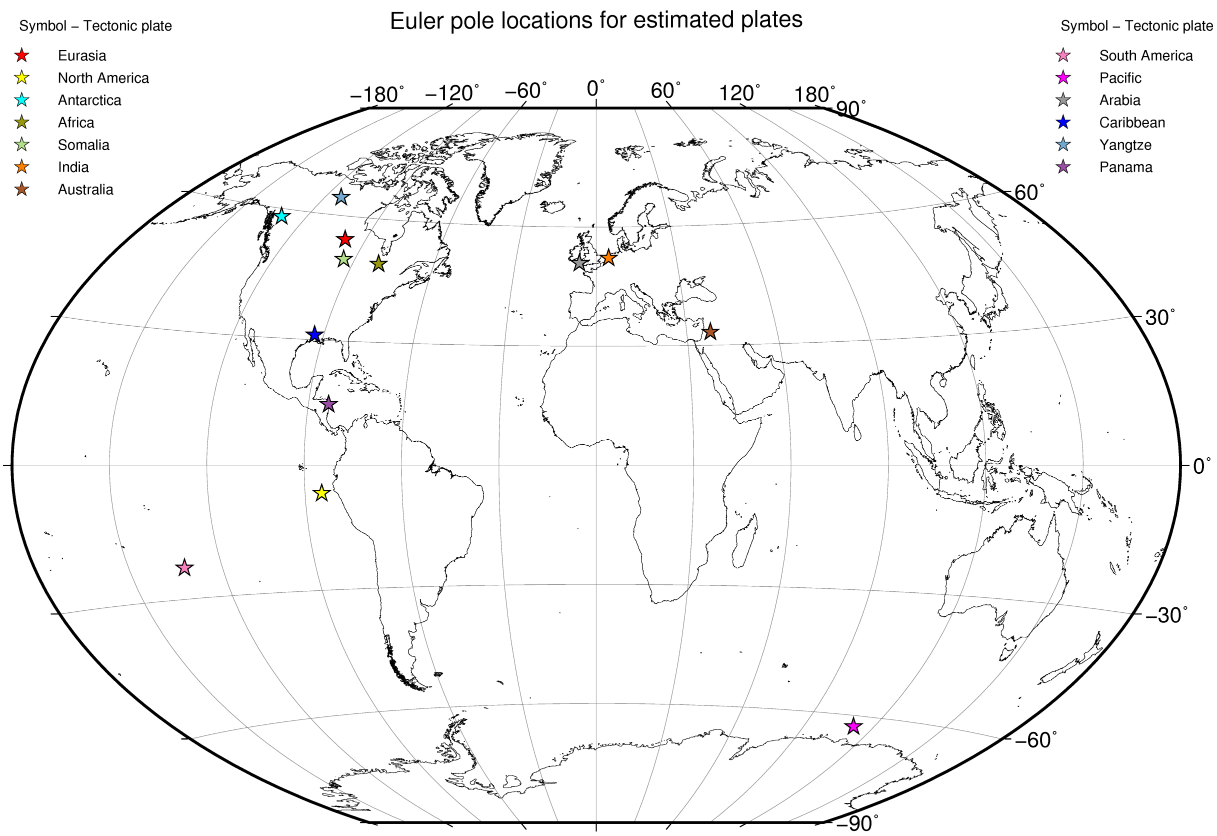

Figure 5.3: Euler pole locations for all tectonic plates estimated with the GNSS velocity field.

5.4 Results

The plate motion models were estimated as in equations (5.3) and (5.8) which resulted in 117 global PMMs estimated with velocity fields corrected with each of the GIA models (81 1D GIA models and 36 3D GIA models) and a global PMM estimated using the GNSS velocity field without any GIA corrections.

The locations of Euler poles estimated using the uncorrected GNSS velocity field (null-GIA) are shown on a global map in Fig. 5.3.

MADs are used as a measure of GIA model goodness of fit. An MAD describes the residual velocity field which remains after removing a GIA model and the corresponding plate motion model from the GNSS velocities (see Eq. (6.5)). The "best" GIA model and "near-best" GIA models are chosen according to the MADs. This is defined and explained in Chapter 6, particularly in section 6.2. The GIA models are ranked separately for the global case and for each region of interest (Europe, North America and Antarctica). The best and near-best PMMs are also chosen according to these MADs, i.e. the ranking of the PMM is based on the ranking of the GIA model that was used to create that PMM. The best GIA models in the horizontal component are not necessarily the best GIA models in the vertical component, and vice-versa. Since the horizontal component is the one that is more likely to contaminate the PMM estimate, given that the rigid plate motion is horizontal only, I choose the best PMMs as the ones that are estimated with the best GIA models in the horizontal component.

For each region of interest the following plate models are analysed:

- PMM estimated using uncorrected GNSS velocities from the network established within this project (named GNSS-only PMM)
- PMM estimated correcting GNSS velocities with the best 1D GIA model for that region (named best 1D GIA PMM)
- PMM estimated correcting with the best 3D GIA model for that region (named best 3D GIA PMM)
- PMMs estimated correcting with each of the 1D GIA models (named 1D GIA PMMs)
- PMMs estimated correcting with each of the 3D GIA models (named 3D GIA PMMs)
- PMMs estimated correcting with each of the 1D GIA models from the near-best group for that region (named near-best 1D GIA PMMs)
- PMMs estimated correcting with each of the 3D GIA models from the near-best group for that region (named near-best 3D GIA PMMs)
- ITRF2014 PMM estimated by Altamimi et al. (2017).

Figs. C.1, C.2 and C.3 in Appendix C are examples of the observed GNSS velocity field where the rigid plate motion and geocentre origin rate bias have been removed. Figs. C.1 and C.2 show the velocities for Europe and North America where the GNSS-only PMM was used. For Antarctica (Fig. C.3), the best GIA PMM (6G_71p85) was used, since the majority of the Antarctic tectonic plate is affected by GIA.

5.4.1 Eurasia

Fig. 5.4 shows Euler pole locations and rotation rates for all plate models estimated for the Eurasia tectonic plate with either the GNSS-only velocity field or the velocity field corrected for GIA with 1D and 3D GIA models, as well as the pole location and rotation rate from ITRF2014 PMM. The radius of the GIA PMMs symbol depends on the goodness of fit of the GIA model. A smaller MAD indicates a better GIA model, shown as a larger symbol in the figure.

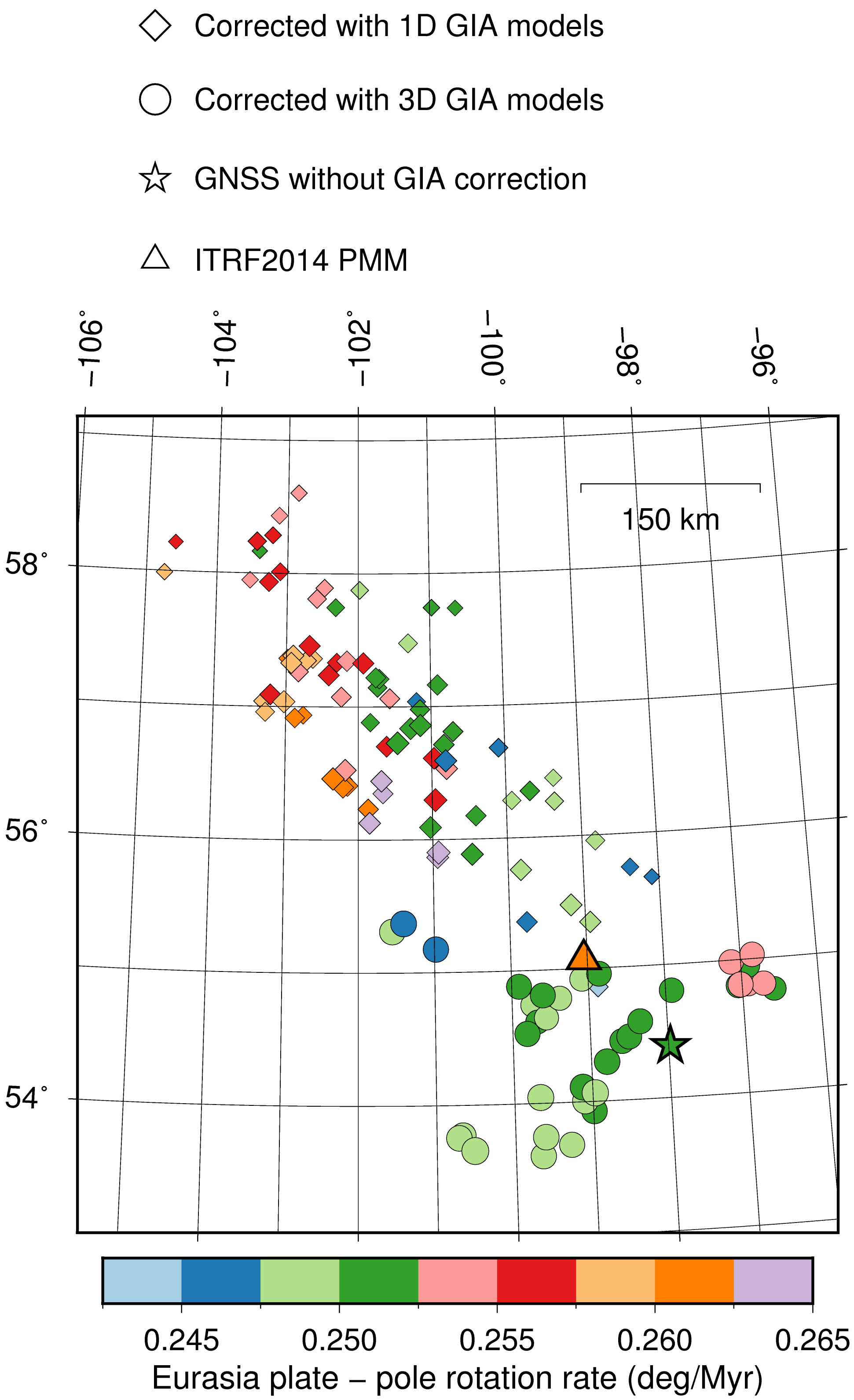

Figure 5.4: Euler pole locations for Eurasia tectonic plate. See Fig. 5.3 for location in world map.

The Euler poles estimated after correcting for GIA with 1D GIA models are grouped in an area spanning ∼400 km East-West and ∼330 km North-South. The 3D GIA PMM poles spread over ∼330 km East-West and ∼220 km North-South, and they are grouped in a different area, southeast of the 1D GIA PMM poles.

Fig. 5.5 shows the same as Fig. 5.4 but for only the groups of near-best GIA models, where the bold symbol represents the best model. The tectonic plate to which the site velocities are fitted is Eurasia, whereas GIA models are chosen to be the best for only the GIA relevant area in northern Europe as this is the only area on the Eurasian plate where the change of a GIA model can significantly affect the plate model (cf. Chapter 2 Fig. 2.5 with global GIA predictions). The ellipses show the Euler pole position with 99% confidence.

The Euler poles for near-best 1D GIA PMMs are grouped closely together over ∼50 km East-West and ∼130 km North-South and the near-best 3D GIA PMM poles are grouped in two areas and span over ∼250 km East-West and ∼140 km North-South. The Euler pole locations in Fig. 5.5 show that the 1D GIA PMMs are closer together in pole location (and some within their 99% position probability) than the 3D GIA PMM Euler poles. The best 3D GIA PMM Euler pole is significantly closer to the ITRF2014 PMM and GNSS-only PMM than the best 1D GIA PMM. As ITRF2014 PMM has been created empirically excluding sites in GIA affected areas, this indicates that the 3D GIA models could be better at correcting for plate-like GIA motion since their pole location estimates are closer to ITRF2014 PMM. The rotation rates of the near-best 3D GIA PMM poles however differ more from the ITRF2014 PMM estimate than the near-best 1D GIA PMM Euler poles (Fig. 5.5). The rotation rates are mostly larger with the 1D GIA PMMs. The two near-best groups show a similar spread of rotation rates within the respective group. The uncertainty of the rotation rates for the PMMs estimated with GNSS-only velocity field and near-best GIA models is 0.0005°/Myr. The difference in rotation rates between the herein estimated PMMs and ITRF2014 PMM for Eurasia is therefore significant.

To investigate whether the differences in Euler poles and rotation rates have a significant effect on the plate velocities of the sites on the plate and to further the analysis of GIA models' effect on PMMs, plate velocities are estimated using different PMMs. For Europe they are estimated on a $5° \times 5°$ grid. Fig. 5.6 shows the plate velocities for the Eurasian plate in the selected area in Europe using the best 1D GIA PMM and the best 3D GIA PMM. It also shows the differences between the plate velocities evaluated with the best 1D/3D GIA PMM and the plate velocities evaluated with the near-best 1D/3D GIA PMMs. Plate velocities in Europe are all pointing in a NE direction and are ∼15 mm/yr.

The differences between plate velocities estimated with the best 1D GIA PMM and near-best 1D GIA PMMs are below 0.5 mm/yr and point in different directions northward (NW-NE). The same differences for the 3D models are up to 1 mm/yr, where there is a

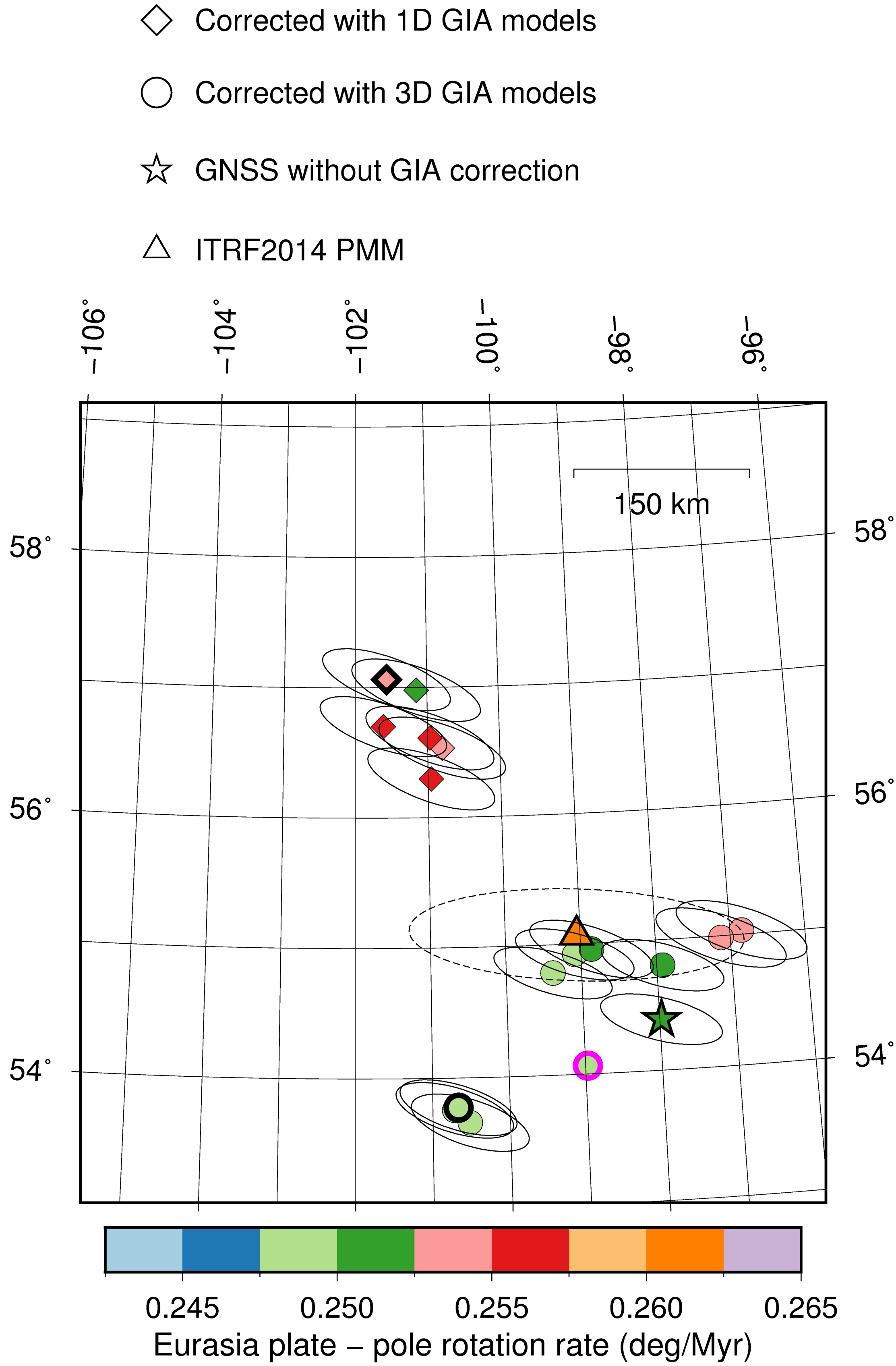

Figure 5.5: Euler pole locations for the Eurasia tectonic plate for near-best GIA PMMs. The error ellipse represents 99% probability of the pole location (dashed error ellipse is for ITRF2014 PMM). The uncertainty of the rotation rate is 0.00047 °/Myr. The bold black outlined symbol represents the best models for Eurasia among 1D GIA PMMs and 3D GIA PMMs. The magenta outlined symbol represents the globally best model.

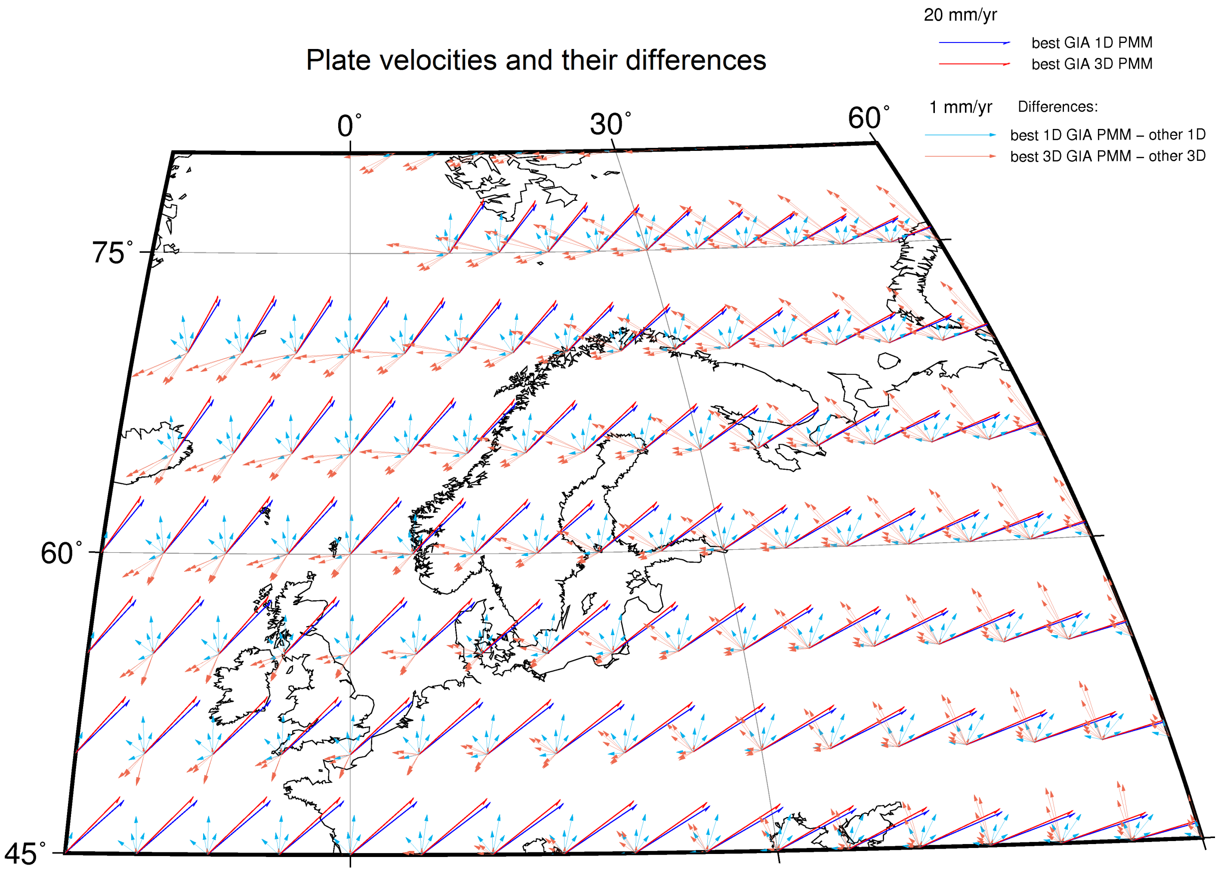

Figure 5.6: Plate velocities on Eurasia plate estimated with best 1D GIA PMM and best 3D GIA PMM and the differences between those and the ones estimated with near-best 1D GIA PMM and near-best 3D GIA PMM, respectively. Note the difference in scale.

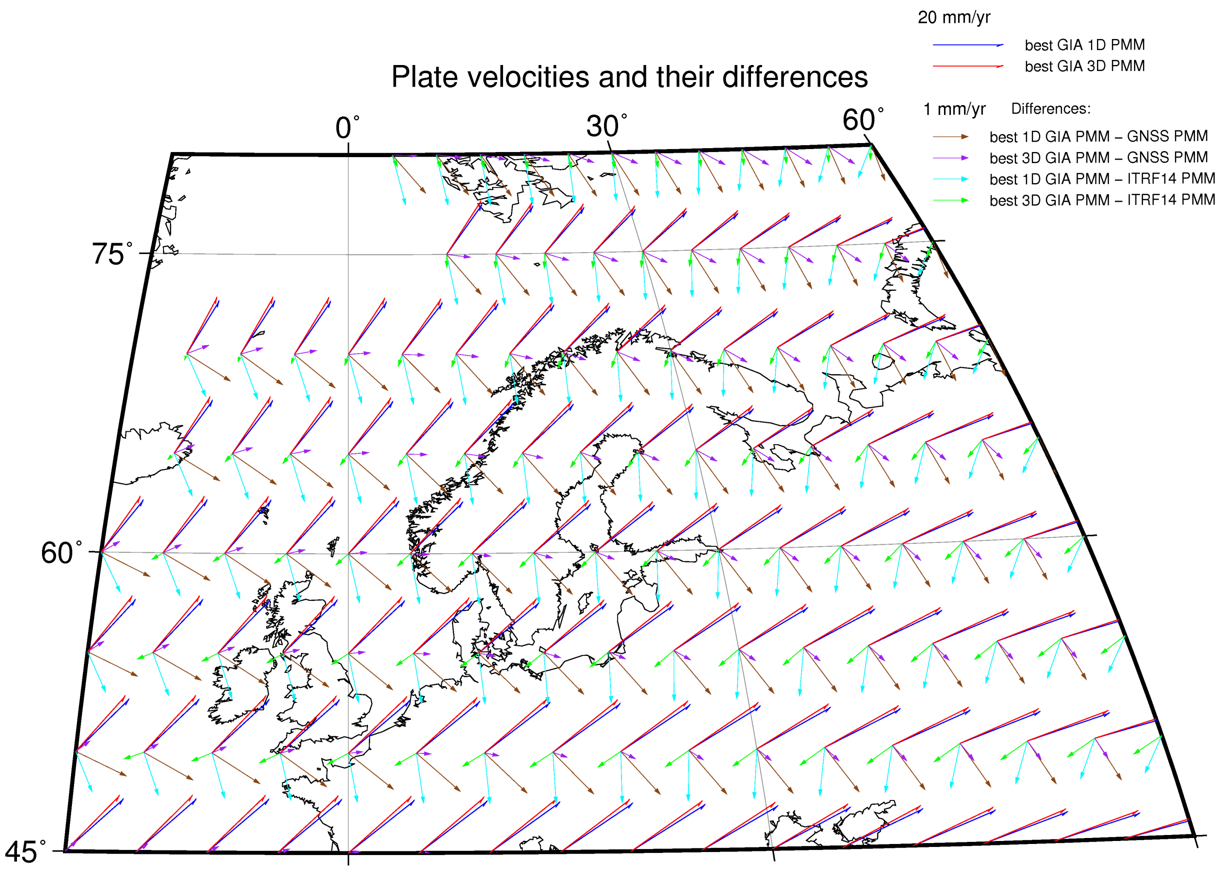

Figure 5.7: Plate velocities on Eurasia plate estimated with best 1D and 3D GIA PMMs and the differences between those and the ones estimated with GNSS-only PMM and ITRF2014 PMM. Note the difference in scale.

group of negligibly small differences, a group of ∼0.5 mm/yr and a group of ∼1 mm/yr. The differences within the 3D models are pointing mostly westwards (SW-NW). The differences in plate velocities with 3D models are slightly smaller in western continental Europe than in the rest of the interest area.

Similar to Fig. 5.6, Fig. 5.7 shows the plate velocities estimated with the best 1D/3D GIA PMM, but with differences from the plate velocities evaluated with GNSS-only PMM and ITRF2014 PMM. The difference between the best 1D GIA PMM plate velocities and the ITRF2014 PMM and GNSS-only PMM plate velocities are up to 2 mm/yr in Europe. The equivalent differences for the best 3D GIA PMM are mostly up to 1 mm/yr.

The above shows that the Euler pole location (Fig. 5.5) and the plate velocities (Fig. 5.7) of the ITRF2014 and GNSS-only PMMs are more similar to the ones of the best 3D GIA PMM than the ones of the best 1D GIA PMM. The pole rotation rates (Fig. 5.5), on the other hand, are more similar to the best 1D GIA PMM. This indicates that for the PMMs obtained with different velocity fields, in Europe the difference in Euler pole location has a greater impact on the plate velocity than the difference in rotation rate.

5.4.2 North America

Fig. 5.8 shows Euler poles for the North American tectonic plate estimated with the GNSS-only PMM, 1D GIA PMMs, 3D GIA PMMs and ITRF2014 PMM. The Euler poles estimated correcting with the 1D GIA models are spread out more in the East-West direction (∼1400 km compared to ∼470 km with the 3D GIA PMMs). The 1D GIA PMMs have generally larger rotation rates than the 3D GIA PMMs.

Fig. 5.9 shows the Euler poles for only the PMMs estimated with the groups of near-best GIA models for North America. As for Eurasia, the uncertainty of the rotation rates of the PMMs is 0.0005°/Myr.

The near-best 1D GIA PMMs have a more similar rotation rate to ITRF2014 PMM than the 3D GIA PMMs. However, the Euler poles of the 1D GIA PMMs are located further from the ITRF2014 PMM Euler poles than the 3D GIA PMMs. This is similar to what was observed for Eurasia.

Within the near-best 1D GIA PMMs, the magnitudes are similar, varying mostly up to 0.001°/Myr. Within the near-best 3D GIA PMMs, they are varying more, up to 0.02°/Myr but the majority of the models are closer in location. A small group of 3D GIA PMMs is ∼400-500 km NE of the best model. Considering that the North American plate Euler pole is located close to the plate itself (cf. Fig. 5.3), a change in pole location has a great impact on the plate velocity of the points on the plate.

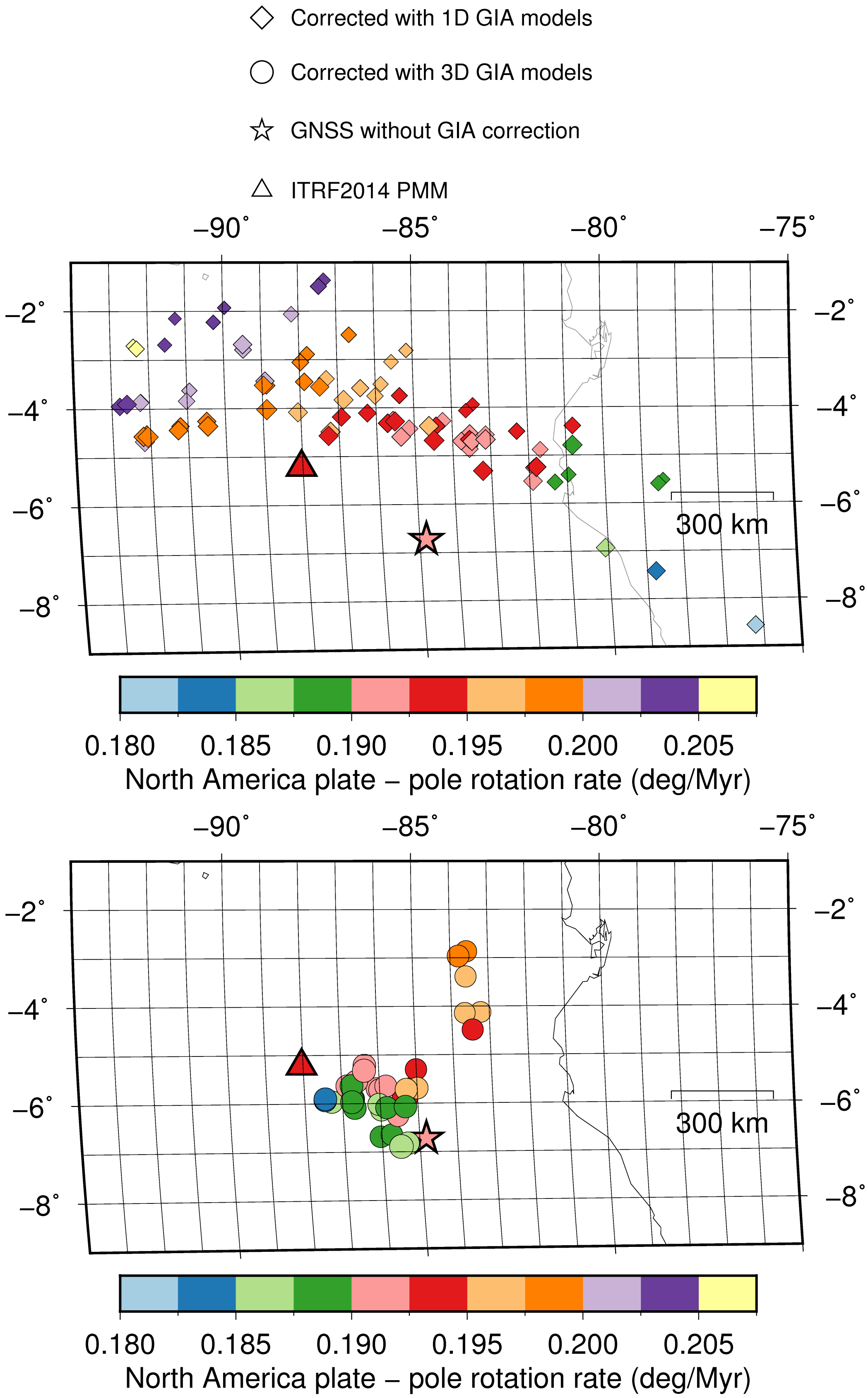

Figure 5.8: Euler pole locations for the North America tectonic plate. See Fig. 5.3 for location in world map.

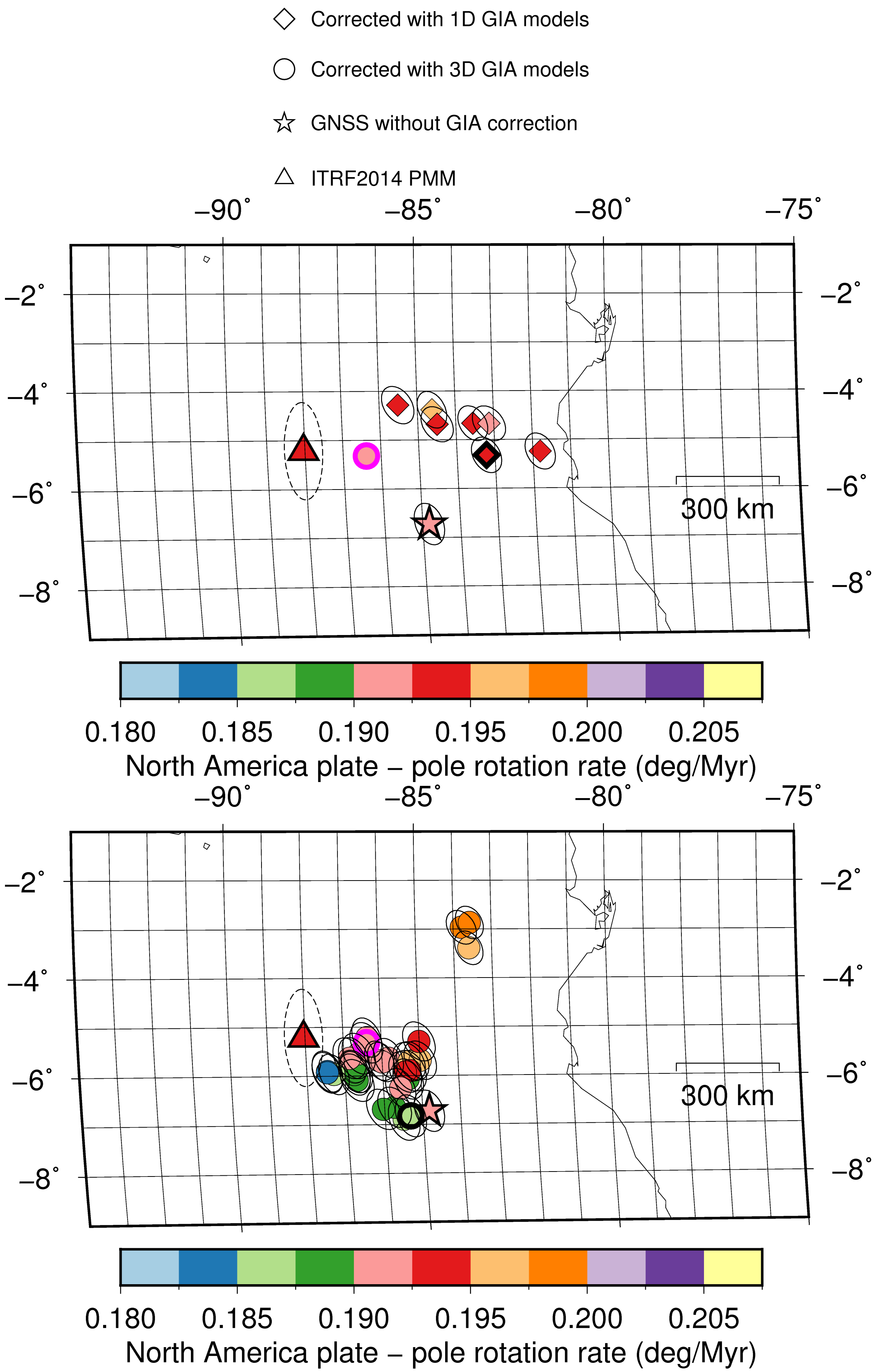

Figure 5.9: Euler pole locations for the North America tectonic plate for near-best GIA models. The error ellipse represents 99% probability of the pole location. The uncertainty of the rotation rate is 0.00046 °/Myr. The bold black outlined symbol represents the best models for North America among 1D GIA PMMs and 3D GIA PMMs. The magenta outlined symbol represents the globally best model.

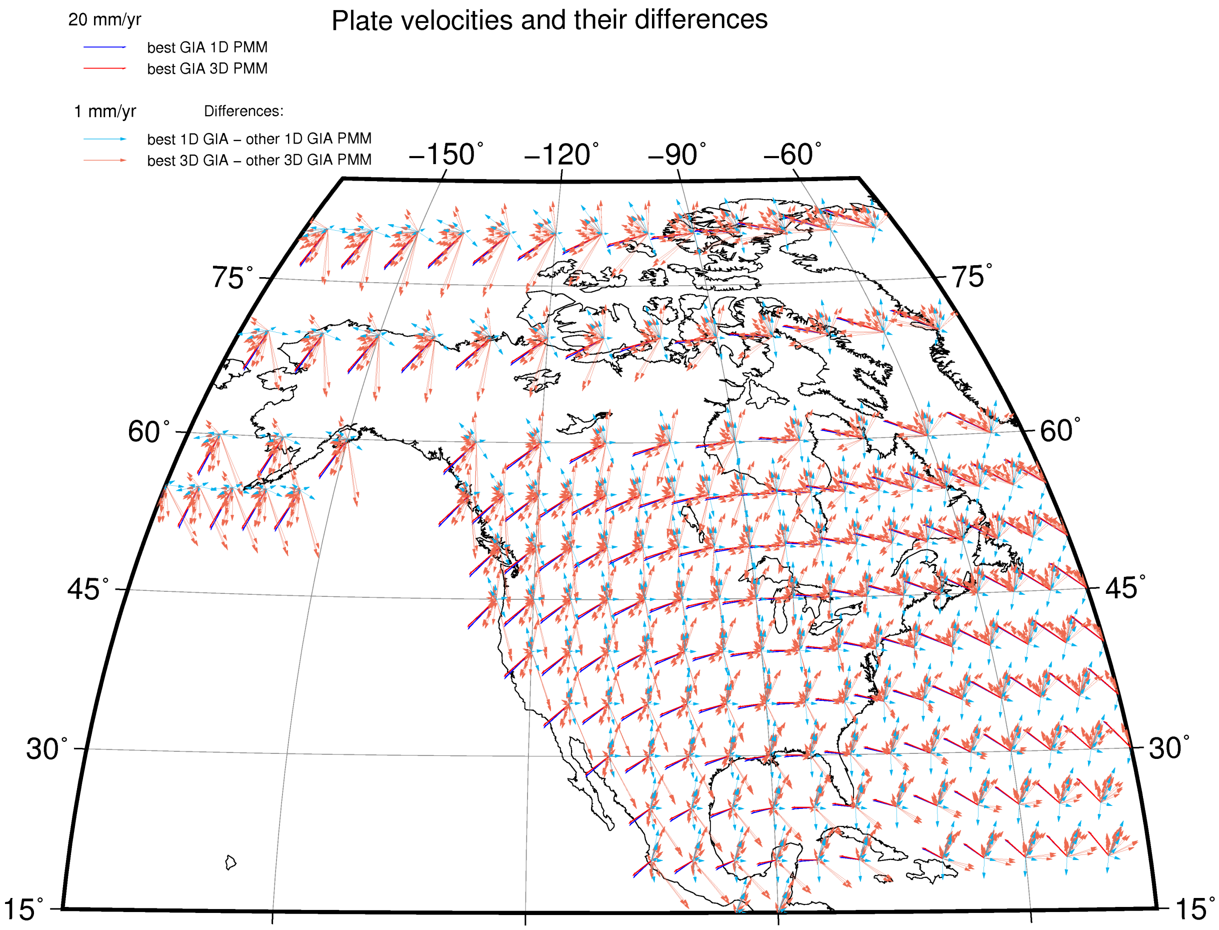

Figure 5.10: Plate velocities on North America plate estimated with best 1D and 3D GIA PMM and the differences between those and the ones estimated with near-best 1D and 3D GIA PMMs, respectively. Note the difference in scale.

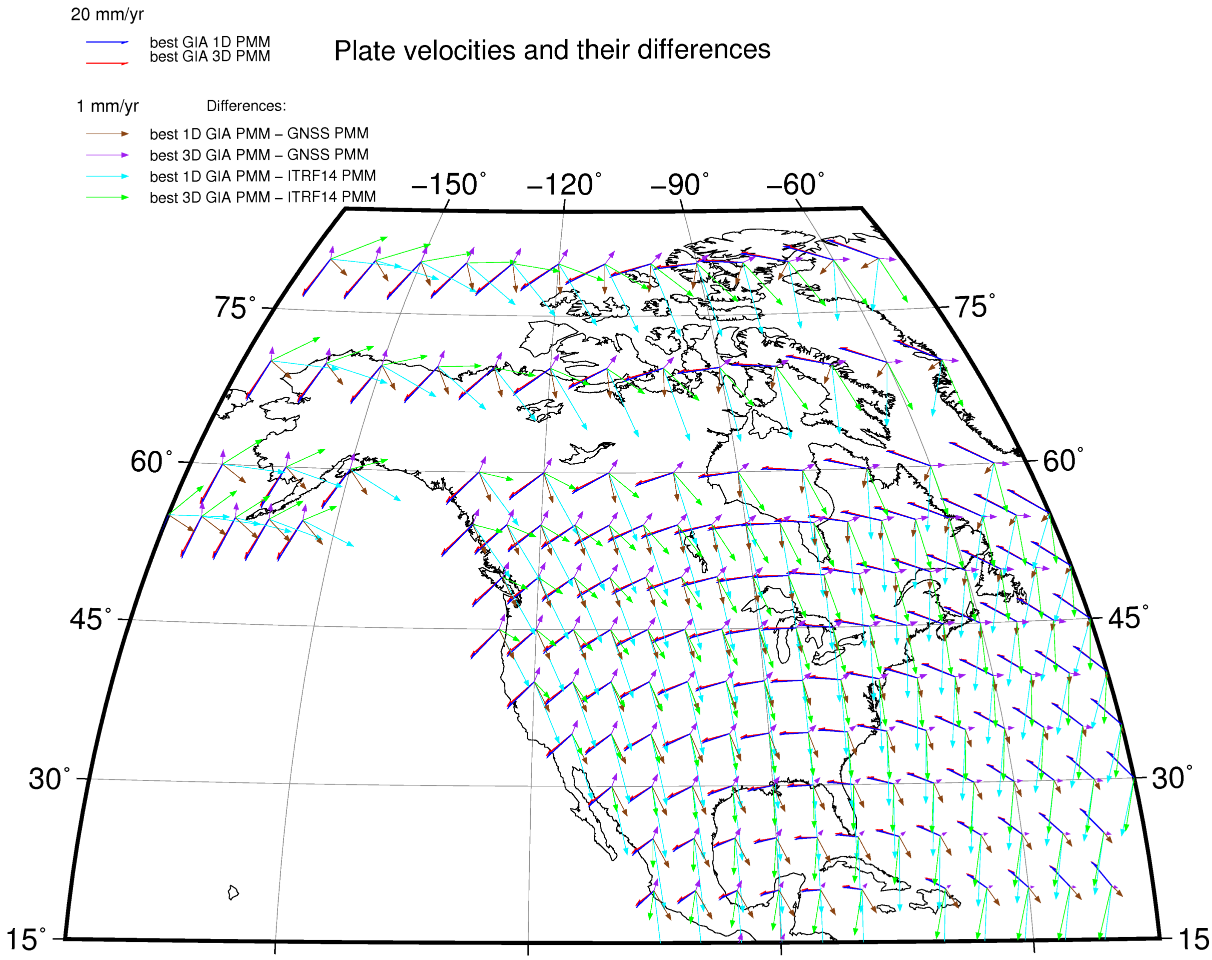

Figure 5.11: Plate velocities on North America plate estimated with best 1D and 3D GIA model and the differences between those and the ones estimated with a plate model estimated with GNSS-only PMM and the ITRF2014 PMM. Note the difference in scale.

Figs. 5.10 and 5.11 show plate velocities and differences of plate velocities in North America as it was presented above for Europe. They are shown on a 5×5° and 10×10° grid.

The North American tectonic plate is rotating anti-clockwise with plate velocities of on average ∼19 mm/yr. The differences of the plate velocities evaluated with the best 1D GIA PMM and the near-best 1D GIA PMMs are mostly up to ∼0.5 mm/yr with some differences up to 1 mm/yr. The larger differences are in the direction North-South. The plate velocity differences for the 3D GIA PMMs vary from those below 0.5 mm/yr to those of up to 1.9 mm/yr. The larger velocities pointing south are evaluated with the three models whose Euler poles are located far from the cluster of the majority of near-best 3D GIA PMMs (see Fig. 5.9). These were created using GIA models that combine each of the three ice models with the same 3D Earth model (SL seismic velocity model (Schaeffer and Lebedev, 2013), dry rheology and 10 mm grain size). The others with differences over 1 mm/yr are in the Northeast-Southwest direction.

The differences between the plate velocities from the best 1D GIA PMM and the GNSS-only PMM are on average 0.7 mm/yr, whereas the differences between the best 1D GIA PMM and ITRF2014 PMM are from 1 to 2 mm/yr, larger in the eastern part of the continent (Fig. 5.11). The differences between the best 3D GIA PMM and GNSS-only PMM are mostly just over 0.5 mm/yr (average 0.4 mm/yr) whereas for the best 3D PMM and ITRF2014 PMM the differences are on average 1.1 mm/yr, from 0.5 mm/yr in the west of the continent to over 1.5 mm/yr in the east of the continent. Comparing these plate velocity differences with Euler poles, the best 3D GIA model pole is 117 km closer to the ITRF2014 pole than the best 1D GIA model pole, and the velocities are more similar than 1D GIA - ITRF 2014 PMM.

5.4.3 Antarctica

Figs. 5.12 and 5.13 show Euler poles and rotation rates for the Antarctic tectonic plate for the 1D/3D GIA PMMs, GNSS-only PMM and ITRF2014 PMM. Fig. 5.12 shows Euler poles for all GIA models, and Fig. 5.13 for the PMMs from groups of near-best GIA models.

The GNSS-only PMM and 3D GIA PMM poles are located SW of the poles estimated with the 1D GIA models and ITRF2014 PMM. The poles are more widely spread in the East-West direction than in North-South (1D GIA PMMs spanning 410 km East-West/230 km North-South; 3D GIA PMMs 500 km East-West/120 km North-South). The rotation rates among most PMMs are similar to each other, compared to the variety of rotation rates for Eurasia and North America plates.

When considering the near-best models only, the 1D GIA PMM Euler poles are all located N and NE of the ITRF2014 PMM Euler pole. The 3D GIA PMMs Euler poles are more spread in the East-West direction, and some are very close in rotation rate and Euler pole location to the GNSS-only PMM. This could be because the GIA corrections for these models are so small that the resulting PMMs are similar to the GNSS-only PMM. The best 3D GIA PMM is closer to the GNSS-only PMM Euler pole than the best 1D GIA PMM (232 km for 1D and 151 km for 3D GIA PMM). The best 1D GIA PMM is 94 km from the ITRF2014 PMM Euler pole. The best 3D GIA PMM is 45 km from the ITRF2014 PMM Euler pole. However, the best 1D GIA PMM has a rotation rate closer to the ITRF2014 PMM rotation rate, than does the best 3D GIA PMM. Note that the uncertainty of the ITRF2014 PMM Euler pole location for Antarctica is larger than the uncertainty of any of the GIA PMM poles. Both the best 1D/3D GIA PMMs poles are located within the ITRF2014 PMM pole location uncertainty, making the difference in the distances between them and ITRF 2014 PMM less significant.

The rotation rate for all GIA corrected PMMs has a range of 0.015°/Myr where the near-best 1D GIA PMMs have rotation rates 0.217-0.228°/Myr and near-best 3D GIA PMMs

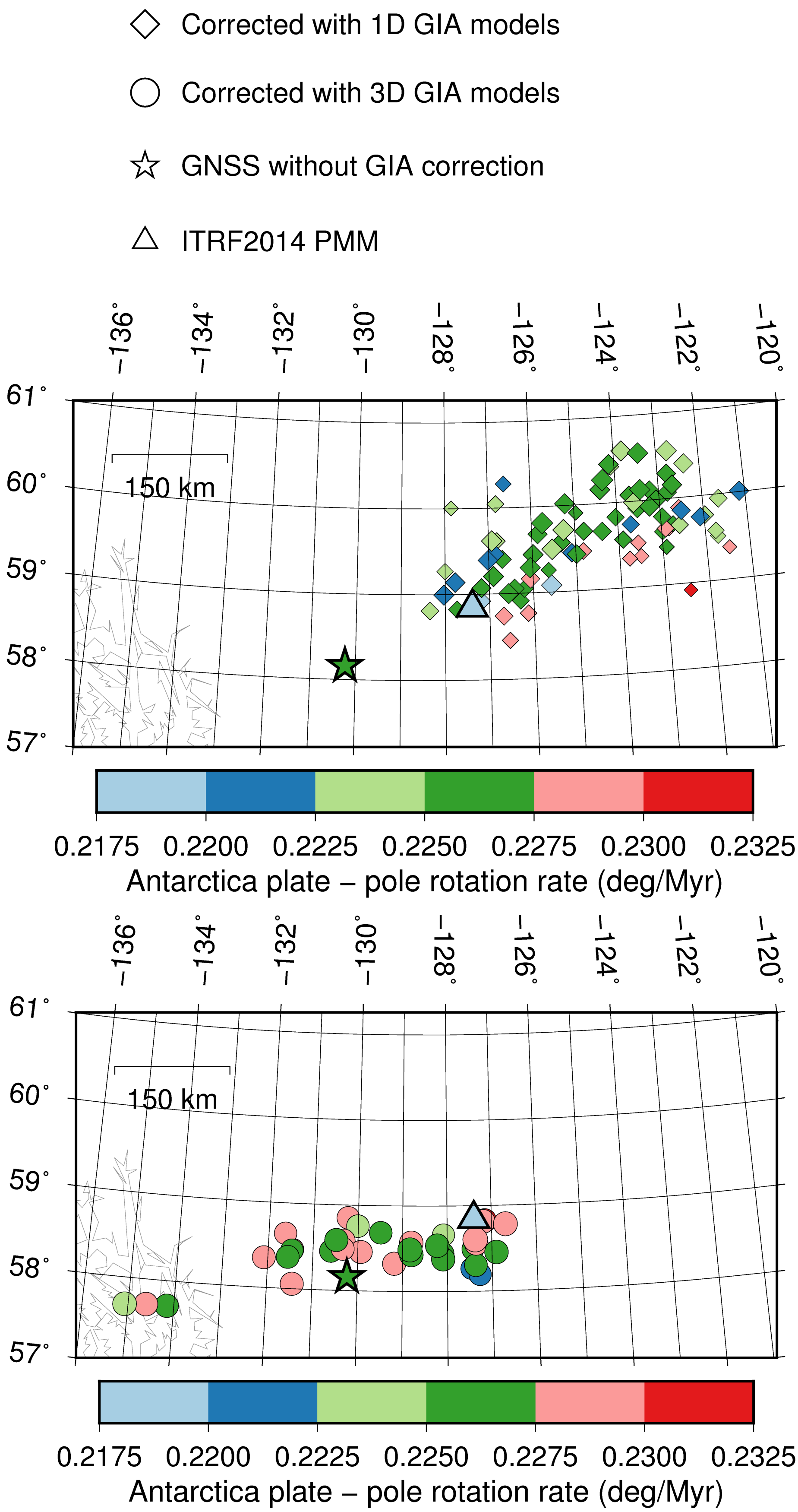

Figure 5.12: Euler pole locations for Antarctica tectonic plate. See Fig. 5.3 for location in world map.

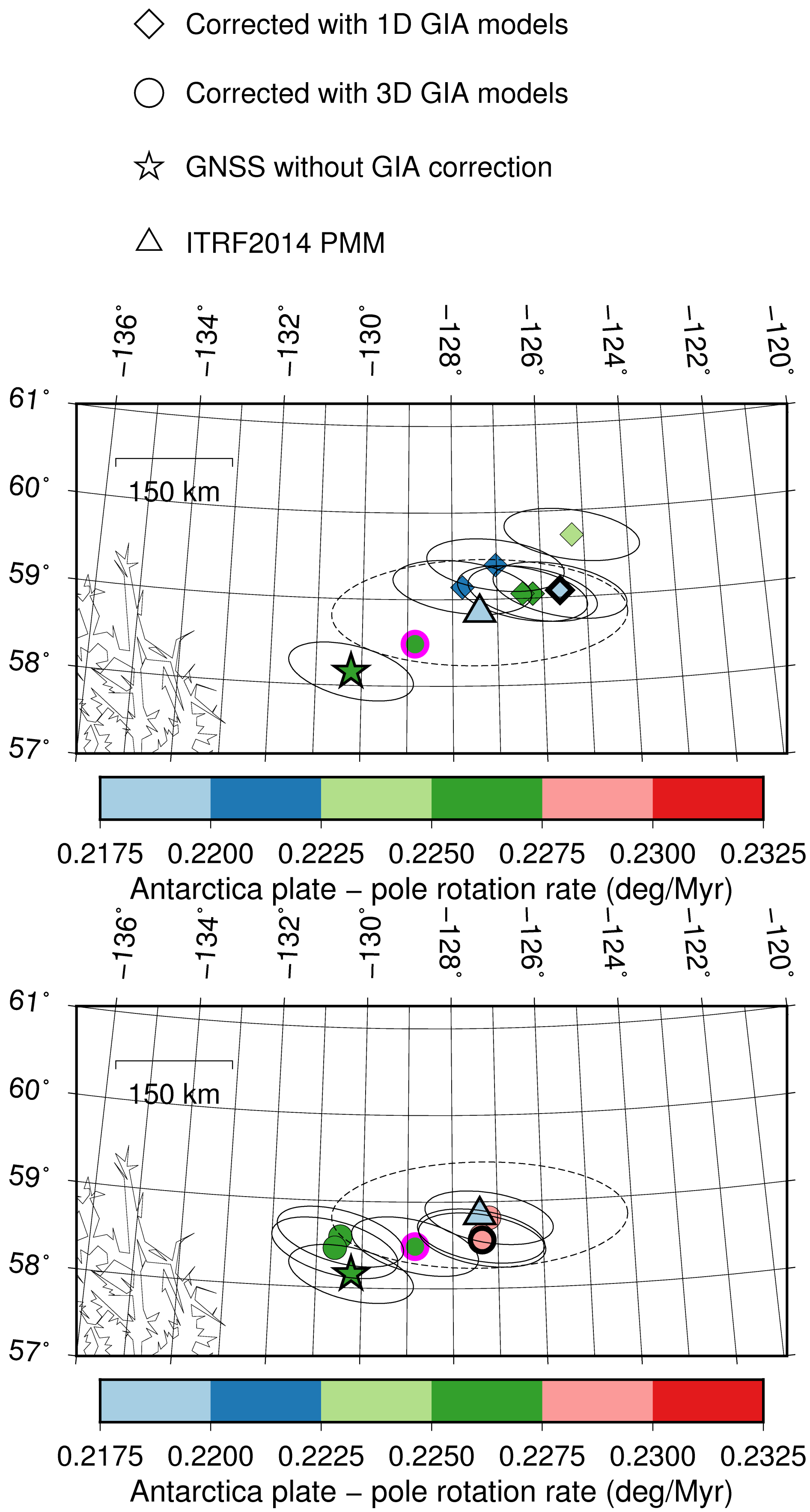

Figure 5.13: Euler pole locations for the Antarctica tectonic plate for near-best GIA models. The error ellipse represents 99% probability of the pole location. The uncertainty of the rotation rate is 0.001 °/Myr. The bold black outlined symbol represents the best models for Antarctica among 1D GIA PMMs and 3D GIA PMMs. The magenta outlined symbol represents the globally best model.

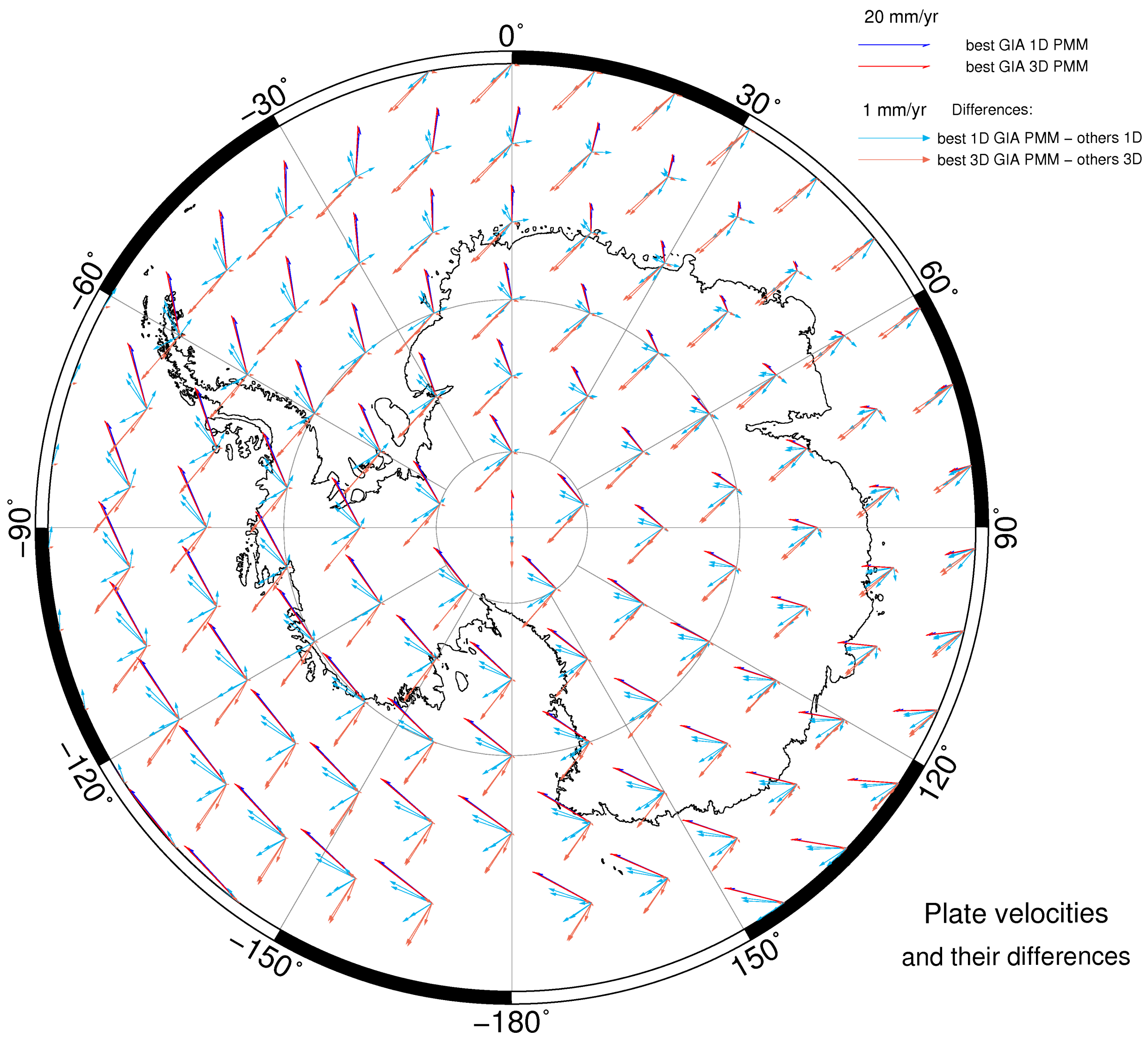

Figure 5.14: Plate velocities on Antarctica plate estimated with best 1D and 3D GIA model and the differences between those and the ones estimated with models from groups of near-best 1D and 3D models, respectively. Note the difference in scale.

0.225-0.230°/Myr. The rotation rate for the GNSS-only PMM is 0.226°/Myr and for the ITRF2014 PMM it is 0.219°/Myr. The uncertainties of the rotation rate in Antarctica are larger than in the other two analysed plates, it is 0.001°/Myr for the best GIA PMMs and 0.002°/Myr for ITRF2014 PMM.

Figures 5.14 and 5.15 show plate velocities and the differences in Antarctica as above for Europe and North America. The velocities are shown on an equidistant Reuter grid (Reuter, 1982). The Antarctic tectonic plate is rotating clockwise. The plate velocities in Antarctica are from ~20 mm/yr in the West and central part of the Antarctic continent and ~5 mm/yr in the East.

The differences between plate velocities evaluated with the best 1D GIA PMM and near-best 1D GIA PMMs are on average 0.4 mm/yr and pointing in various directions. The differences among the 3D models are also on average 0.4 mm/yr but pointing mostly in

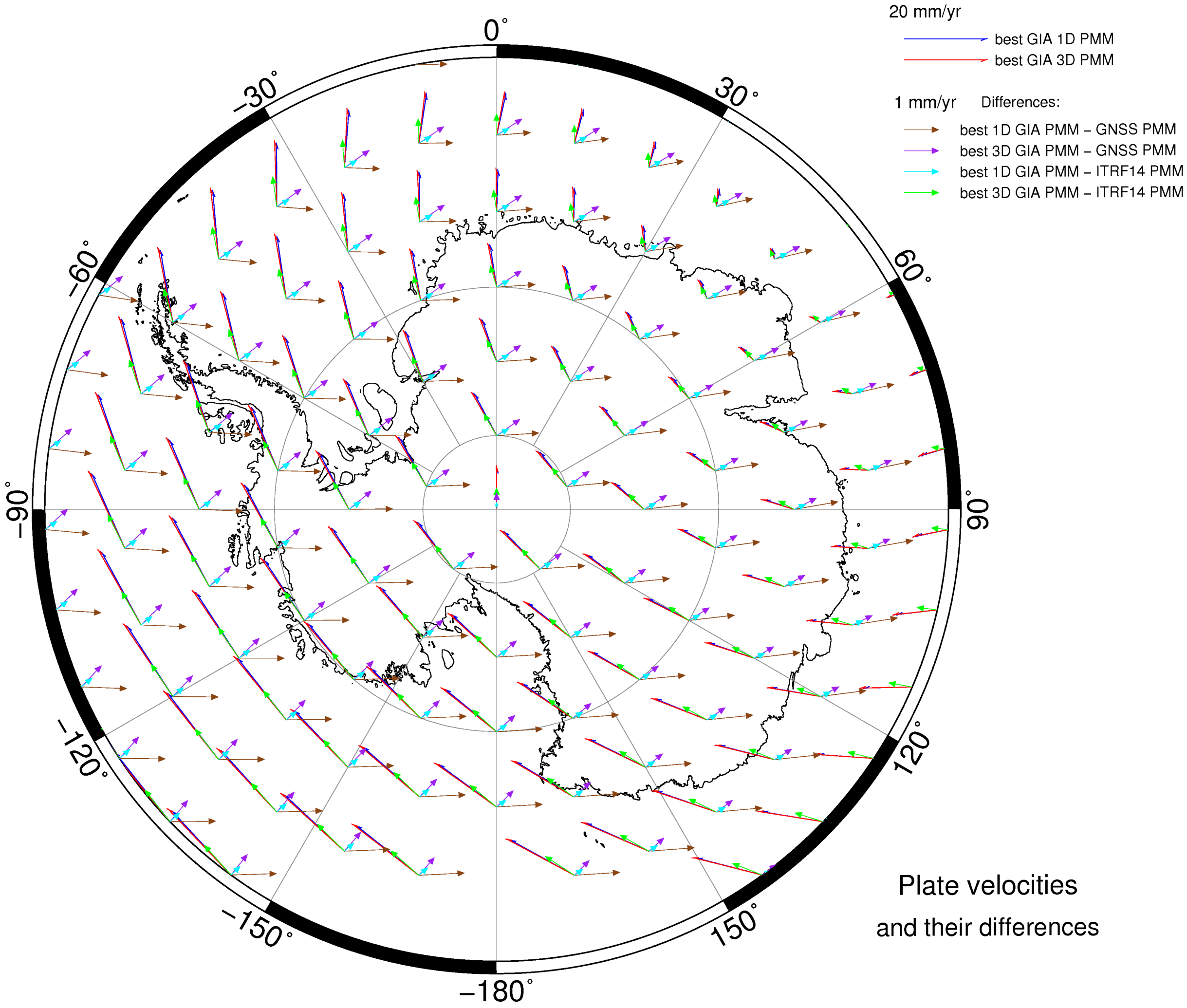

Figure 5.15: Plate velocities on Antarctica plate estimated with best 1D and 3D GIA PMM and the differences between those and the ones estimated with GNSS-only PMM and ITRF2014 PMM. Note the difference in scale.

the same direction, near to perpendicular to the single best 3D GIA PMM.

The differences between the plate velocities with the best 1D GIA PMM and GNSS-only PMM are on average 1.2 mm/yr. The differences between the best 3D GIA PMM plate velocities and the GNSS-only PMM plate velocities are smaller, on average 0.6 mm/yr. The latter are pointing in a similar direction as the differences between 1D GIA PMM-ITRF2014 PMM which are on average 0.4 mm/yr. The differences in plate velocities estimated with the best 3D GIA PMM and ITRF2014 PMM are on average 0.6 mm/yr. They are pointing in a similar direction as the plate velocities estimated with the best 1D/3D GIA PMM, meaning that the velocity vectors differ mostly just in magnitude. Similar plate velocity direction and different velocity magnitude indicate similar pole location and different rotation rate. This indeed is the case for Euler poles of the best 3D GIA PMM and ITRF2014 PMM in Fig. 5.13.

The ITRF2014 PMM Euler pole is, as mentioned above, closer to the best 1D GIA PMM in the value of rotation rate, but closer to the best 3D GIA PMM in the pole location. The plate velocities estimated with ITRF2014 PMM are more similar to the plate velocities from the best 1D GIA PMM. This suggests that in Antarctica, the change in rotation rate has a larger influence on the plate velocity than the change in pole location. However, these differences may also be due to the fact that the Euler poles of the best 1D GIA PMM and 3D GIA PMM are located close to each other, ∼50 km. The Euler pole for the Antarctic plate is located very far from the plate itself (see Fig. 5.3), so the change in its location has less of an influence on the plate velocities of the sites.

5.4.4 Global

As mentioned above, the globally best fitting GIA model is chosen according to its MAD. A globally best fitting model is chosen in two ways, by weighting the MADs by plate area or without any weighting. The best global PMM is chosen accordingly, by choosing the PMM corrected with the best fitting GIA model. Globally the best PMM, when weighting the MAD by plate area is the PMM estimated correcting with the GIA model 6G_SL_wet_10 mm (MAD = 0.58 mm/yr). Globally the best PMM, when applying no weighting, is the PMM estimated correcting the GNSS velocity field with the GIA model 6G_S_dry_4 mm (MAD = 0.56 mm/yr). The weighted case is the one that should be more realistic, since weighting the global MAD by plate area reduces the bias of small areas with a large density of sites (see Chapter 6, section 6.2). Therefore, the PMM with 6G_SL_wet10mm is the one that should be used when investigating global plate motion. Table 5.1 lists this PMM.

Fig. 5.16 shows Euler pole locations for all the plates estimated within this project, as well as the MORVEL56 PMM as an example of a geological model and the ITRF2014

PMM as a model from space-geodetic techniques (see Fig. 5.3 for locations on a global map). The figures show all 1D GIA PMMs, 3D GIA PMMs, GNSS-only PMM as well as emphasizing the location of the two globally best GIA corrected PMMs and their error ellipses. The error ellipses of the two GIA PMMs and ITRF2014 PMM show the pole locations with 95% confidence. MORVEL56 PMM does not publish uncertainty information. The MORVEL56 PMM shows only a loose agreement with Euler pole locations from ITRF2014 PMM and the PMMs estimated herein in the majority of plates. ITRF2014 PMM and MORVEL56 PMM do not estimate all of the plates estimated herein (see in Fig. 5.16 plates where the triangle or pentagon symbol is missing).

It can be seen that the globally best model with and without weighting are not located in the same place which confirms the choice of weighting. The globally (weighted) best PMM is based on a 3D GIA model and is therefore located among the 3D GIA PMMs. The ITRF2014 PMM poles are for most plates closer to the 3D GIA PMMs or equally far from the 1D GIA PMMs and the 3D GIA PMMs, only closer to the 1D GIA PMMs in the case of Australia and South America plate. South America plate shows large variations in Euler pole locations with different GIA models of up to $\sim$530 km East-West and up to $\sim$800 km North-South. Aside from South America, North America, Eurasia and Antarctica, the Euler pole locations for other plates vary for up to 300 - 400 km.

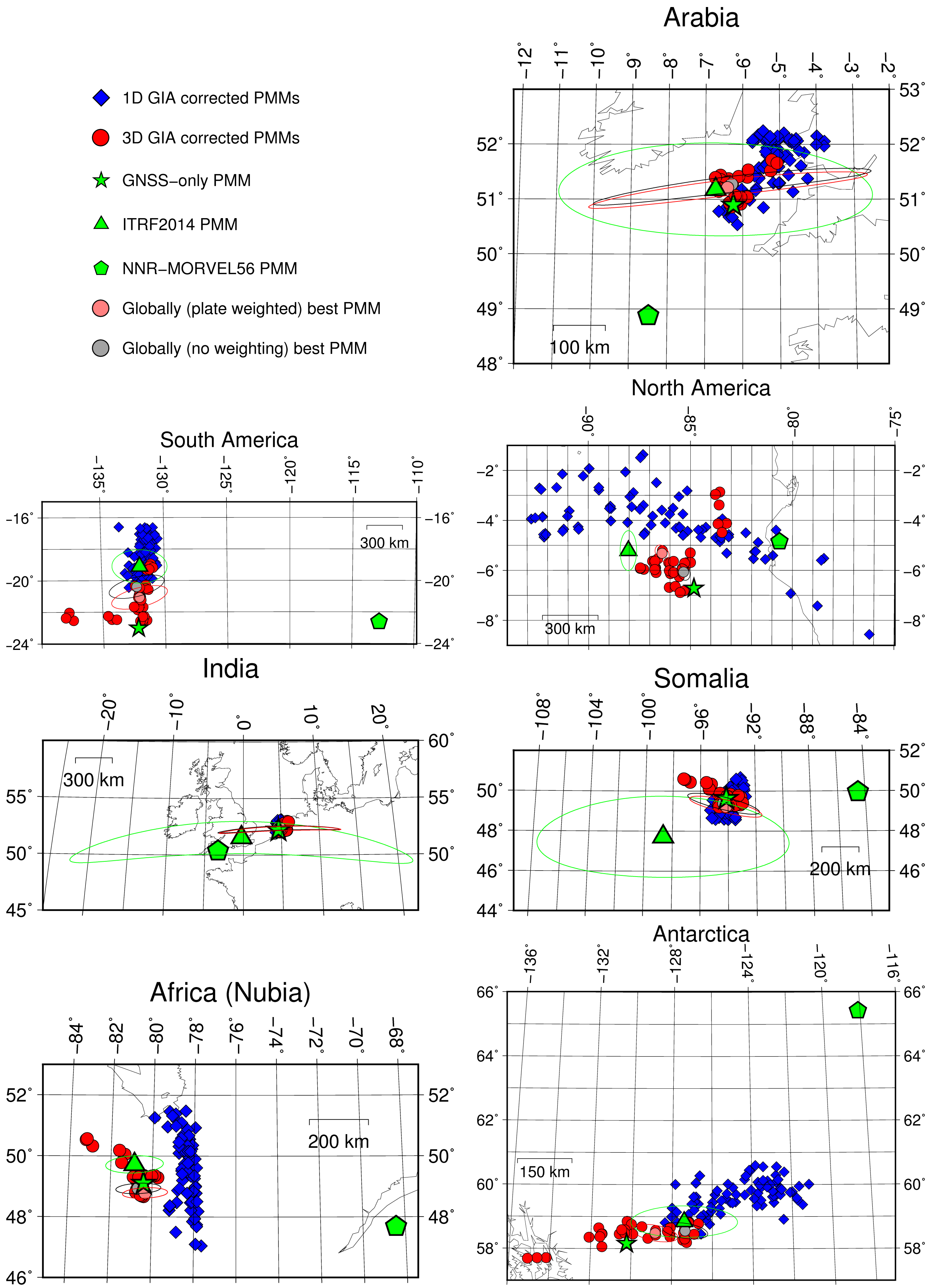
1D GIA corrected PMMs
3D GIA corrected PMMs
GNSS−only PMM
ITRF2014 PMM
NNR−MORVEL56 PMM
Globally (plate weighted) best PMM
Globally (no weighting) best PMM
Arabia
100 km
North America
300 km
South America
300 km
India
300 km
Somalia
200 km
Africa (Nubia)
200 km
Antarctica
150 km

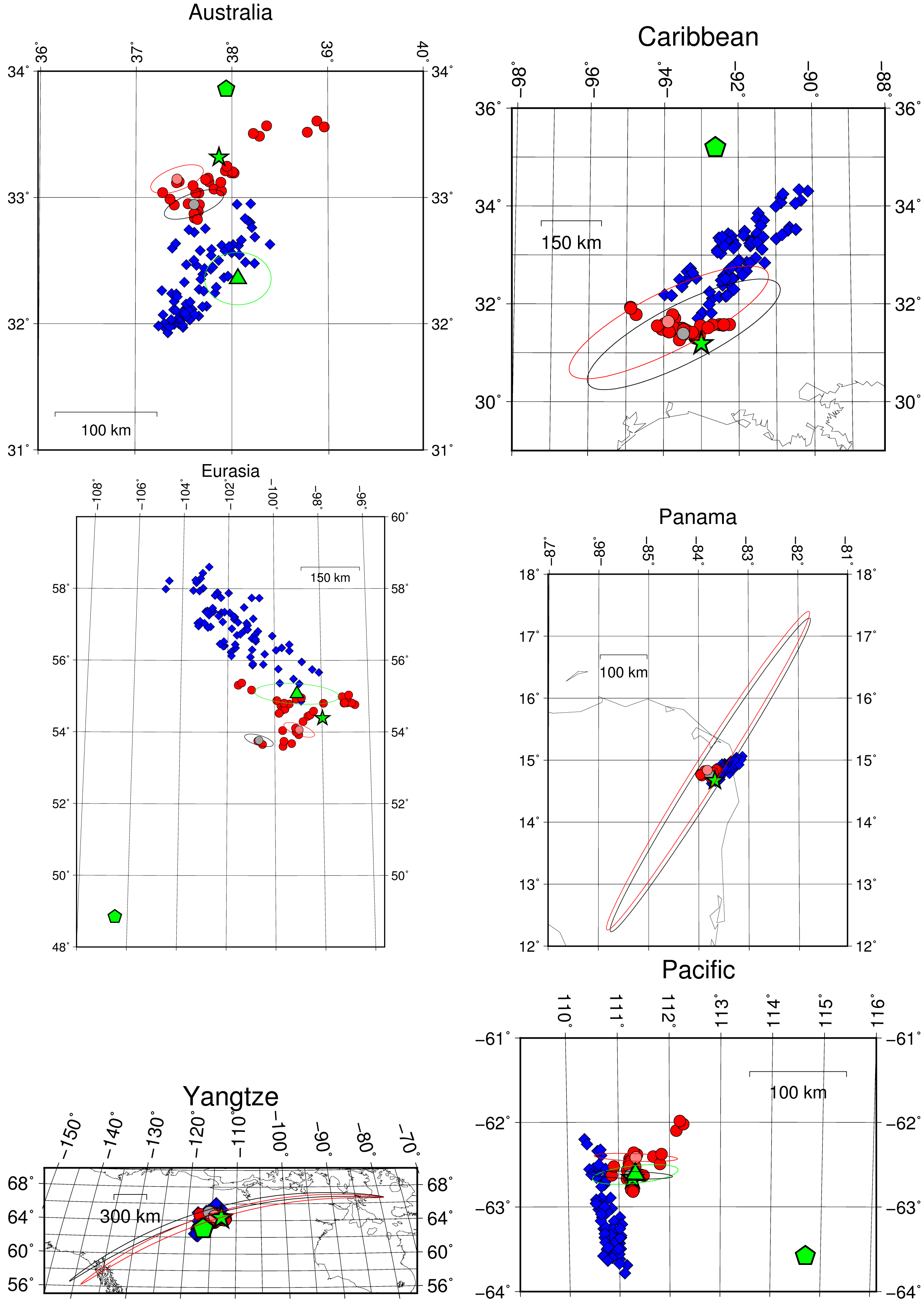

Figure 5.16: Euler poles of different PMMs for all estimated tectonic plates. The error ellipses show the positions of the Euler poles with 95% confidence. Red ellipse for globally best PMM when weighting by plate area is applied, black ellipse for globally best PMM chosen without weighting and green ellipse for ITRF2014 PMM. No error information is available for NNR-MORVEL56.

Plate	ω_x	ω_y	ω_z	Longitude	Latitude	ω	NS*	NS-ITRF14*
		[°/Myr]			[°]	[°/Myr]		
Africa (Nubia)	0.0286	-0.1678	0.1944	-80.33	48.79	0.2584	23	24
±	0.0009	0.0006	0.0006	0.29	0.11	0.0007		
Antarctica	-0.0741	-0.0921	0.1928	-128.83	58.49	0.2262	55	7
±	0.0006	0.0006	0.0012	0.25	0.18	0.0011		
Somalia	-0.0139	-0.1919	0.2232	-94.15	49.24	0.2947	7	3
±	0.0026	0.0025	0.0017	0.72	0.26	0.0029		
India	0.3178	0.0268	0.4134	4.82	52.35	0.5221	7	3
±	0.0026	0.0115	0.0036	2.02	0.14	0.0049		
Australia	0.4203	0.3217	0.3457	37.43	33.15	0.6322	26	36
±	0.0008	0.0007	0.0007	0.10	0.05	0.0007		
Eurasia	-0.0228	-0.1445	0.2018	-98.97	54.06	0.2492	229	97
±	0.0004	0.0005	0.0005	0.17	0.11	0.0005		
North America	0.0120	-0.1895	-0.0177	-86.39	-5.32	0.1907	461	72
±	0.0005	0.0005	0.0004	0.14	0.14	0.0005		
South America	-0.0744	-0.0826	-0.0428	-132.02	-21.08	0.1191	35	30
±	0.0012	0.0013	0.0007	0.86	0.32	0.0007		
Pacific	-0.1132	0.2898	-0.5955	111.34	-62.42	0.6719	21	18
±	0.0008	0.0005	0.0006	0.16	0.04	0.0006		
Arabia	0.3147	-0.0353	0.3940	-6.41	51.21	0.5054	6	5
±	0.0043	0.0049	0.0030	0.97	0.15	0.0046		
Caribbean	-0.0176	-0.2593	0.1601	-93.88	31.64	0.3053	10	∅
±	0.0037	0.0091	0.0032	0.95	0.50	0.0091		
Yangtze	-0.0578	-0.1272	0.2933	-114.45	64.53	0.3249	3	∅
±	0.0084	0.0161	0.0108	5.84	2.60	0.0050		
Panama	0.1597	-1.4765	0.3935	-83.83	14.84	1.5363	5	∅
±	0.0516	0.2796	0.0454	0.82	1.08	0.2856		

Table 5.1: Plate motion model estimated after correcting the GNSS velocity field with the globally best-fitting model, when applying weighting by plate. GIA corrections using model 6G_SL_wet_10mm. NS stands for the number of sites on each plate in this PMM, and NS-ITRF14 stands for the number of sites on each plate in ITRF2014 PMM. ∅ denotes plates which were not estimated in ITRF2014 PMM.

Geocentre motion

The variation of CG (reference frame origin of a GIA model, cf. section 5.1) with respect to CM and the geocentre origin rate bias are obtained in the PMM estimate for each GIA model according to Eq. (5.8). Each GIA model is expressed in a reference frame with an origin in its own realization of CE (1D GIA models) or its own realization of CFEM (3D GIA models) and it is therefore expected that β' will vary depending on the GIA model. The CG-CM (i.e. CE-CM or CFEM-CM) translations and the origin bias for each GIA PMM are listed in Table E.1 in Appendix E. The uncertainty of β for GNSS-only PMM is σ_{β_X}=0.002 mm/yr, σ_{β_Y}=0.002 mm/yr and σ_{β_Z}=0.001 mm/yr.

Schumacher et al. (2018) and King et al. (2012) estimate the origin translation between their developed GPS data set and the GIA models, and use it to correct vertical GIA velocities following the approach of King et al. (2012). These studies include only vertical GNSS and GIA velocities. In this thesis where horizontal velocities are also taken into consideration, the CG-CM and origin rate bias are estimated together for each PMM estimate and used to correct the vertical and horizontal observed velocities when computing the residual velocity fields (cf. Chapter 6). It is inconsequential that the term β' is estimated as a single value since the geocentre origin rate bias and CG-CM are not needed separately, but as a sum the term β' is relevant for accurate computation of residual velocities. Taking into consideration the differences between reference frame origins of the model and data velocities and taking into consideration the rate of the centre around which the plates rotate, the residuals are ultimately expressed in the desired reference frame of GNSS velocities.

5.5 Summary and discussion

It is common to estimate PMMs with an empirical surface velocity field. However, the horizontal surface velocities observed by GNSS are not only due to plate motion, with the second-most influential contributor being GIA. Ideally, after correcting the GNSS surface velocity field using modelled horizontal GIA velocity predictions, we should obtain a PMM free of GIA. In reality, however, GIA model imperfections will affect the PMM estimate which is why the analysis was narrowed to the near-best models (cf. Chapter 6).

Considering the locations and frequency of outliers and noting how the velocities at GNSS sites fit the PMMs, it seems that some sites in the northernmost part of North America had to be excluded in nearly all the different PMM estimates. This is unfortunate because it is an area sparsely covered by GNSS sites and it means that across a large portion of the tectonic plate, the PMM estimate is not well constrained. This indicates that these sites show velocities that are unlikely to be primarily due to plate motion. The most likely reason is that they are excluded because the GIA models do a poor job of estimating GIA-related motion in this region. Even after correcting for GIA, they are biased by a GIA signal and hence are flagged as outliers when seeking to fit a PMM. This may be either because the plate model cannot fit the horizontal velocities well or because the vertical motion is too large.

After analysing the differences in pole locations and rotation rates, and plate velocities in the regions of interest, it can be concluded that the differences in Euler pole locations between the presented PMMs have a larger influence on the site velocity than the differences in rotation rate. The only exception was in case of the differences in velocities of ITRF2014 PMM to 1D GIA and 3D GIA PMMs in Antarctica. However, this may be an exception due to the fact that the Euler poles of the best 1D GIA PMM and 3D GIA PMM for Antarctica are located close to each other. Additionally, the Euler pole for the Antarctic plate is located very far from the plate itself, so the change in its location has less influence on the plate velocities.

Taking the published ITRF2014 PMM (Altamimi et al., 2017) as a reference, the 3D GIA PMMs result in Euler poles closer to it than the 1D GIA PMMs. The ITRF2014 PMM approach excluded sites in GIA regions by excluding sites which showed vertical velocities $\geq$0.75 mm/yr. The fact that 3D GIA PMMs Euler pole estimates (including sites in GIA regions) are closer to ITRF2014 PMM Euler pole estimates which do not include GIA regions, indicate that the 3D models may be better at absorbing GIA motion that can contaminate the PMM estimate.

Both GIA PMMs and ITRF2014 PMM may be considered to be affected by errors related to GIA, the former due to the choice of GIA model, the latter due to the process of excluding sites in GIA regions. Thus, while an agreement of the GIA PMMs with ITRF2014 PMM can be taken as a quality measure, the GIA PMMs are preferred as the GIA effect is treated more rigorously.

In Antarctica, the plate velocities from ITRF2014 PMM are more similar to the ones of the 1D GIA PMMs than the ones of the 3D GIA PMMs. However, Altamimi et al. (2017) kept the sites in Antarctica regardless of whether they are in GIA regions, and did not correct them with any GIA model in the PMM estimate. In Antarctica, this project uses far more observation sites than ITRF2014 PMM (here 54-55 sites, ITRF2014 PMM 7 sites) and the uncertainty of the Euler vector for Antarctica is much smaller.

The results of this project indicate that using a new suite of GIA models to correct for GIA, allows us to use a larger data set when estimating PMMs, including sites in GIA areas that previously had to be omitted from the analysis because they were insufficiently described by GIA models.

The results show that there can be significant GIA-related horizontal motion which might be modelled into the plate motion model if left uncorrected, even in areas that could be considered to be outside of GIA regions, since the maximum GIA horizontal signal is in the peripheral bulge of the former ice sheet. A similar result was found by Klemann et al. (2008). They create a GIA model with a laterally homogeneous Earth and a GIA model with a laterally varying Earth which takes into consideration the role of plate boundaries. Unlike this project, where I estimate absolute PMMs from three-dimensional GNSS velocity fields where GIA has been removed, they calculate the incremental rotation of tectonic plates induced by GIA horizontal velocities. Klemann et al. (2008) estimate the rotation model with a least-squares fit of the GIA horizontal velocities at sites from the ITRF2005 PMM (Altamimi et al., 2007). Their results indicate that GIA is not negligible in the interpretation of GNSS time series of sites far away from the formerly glaciated areas for modelling plate motion.

The PMMs obtained in the present project follow a similar approach as in Booker et al. (2014) where they create a GNSS velocity field aligned to ITRF2005 from repro1 GNSS solutions and correct it with two GIA models. Besides using a more accurate and more dense GNSS velocity field, the results obtained here are superior to the ones from Booker et al. (2014) in terms of the uncertainty of the Euler pole estimate and the number of GIA models. They correct the GNSS velocity field with only two GIA models and find that there is very little variation in Euler poles due to the choice of a priori or null-GIA model, corresponding to less than ± 1 mm/yr in computed plate velocities at the sites. However, their GIA models predicted relatively small horizontal magnitudes. They find that the goodness of fit at GNSS sites improves with the introduction of both of the GIA models in the vertical component, but not in the horizontal. They suggest to extend the analysis to include 3D GIA models. The analysis of the vertical and horizontal fit of the 1D and 3D GIA models and respective PMMs at GNSS sites is the topic of the next chapter.

Chapter 6

GIA model analysis

6.1 Residual velocity field

In Chapter 5 PMMs were estimated using a suite of GIA models. In the present chapter, the suite of GIA models is tested by investigating how well the combination of a GIA model and (the solved-for) plate motion describe the observed velocity field. I start by defining a residual velocity field as the velocity field which remains after the GIA effect and plate motion have been removed from the GNSS velocity field. It is not expected that the GIA effect will be equivalent to the GNSS displacement at every site. However, since the plate motion is removed and the tectonically active sites and outliers are excluded, it is expected that the GIA predicted velocities should be as close as possible to the GNSS observed displacement at the majority of sites.

To estimate the residual horizontal velocity of a site, I remove the horizontal component of GIA and the plate velocity of that site, as well as the term β' which stands for the variations in frame origins. The advantage of the approach taken in this thesis is that the PMM used here is estimated taking GIA into account, instead of using a pre-existing PMM which may be biased by GIA. Additionally, this approach of computing residuals includes the variations in frame origins of the GIA models, GNSS network and the centre around which the tectonic plates rotate, thus further improving the residuals.

The plate velocity $\dot{X}_i^{pm_j}$ of site i with coordinates X_i is calculated using an equivalent of Eq. (5.2), where Ω_p^j is the Euler vector of plate p estimated after correcting the GNSS velocity with GIA model j, according to:

$$\dot{X}_i^{pm_j} = \Omega_p^j \times X_i \qquad (6.1)$$

I convert $\dot{X}_i^{pm_j}$ from the Cartesian XYZ system to the topocentric ENU system where

$\dot{E}_i^{pm_j}$ and $\dot{N}_i^{pm_j}$ are Easting and Northing components of the plate velocity of the site. Following Eq. (5.8) (Chapter 5), the residual horizontal velocity of the site is:

$$\dot{E}_i^{res_j} = \dot{E}_i^{GNSS} - \dot{E}_i^{pm_j} - \dot{E}_i^{GIA_j} - \beta'_E \tag{6.2}$$

$$\dot{N}_i^{res_j} = \dot{N}_i^{GNSS} - \dot{N}_i^{pm_j} - \dot{N}_i^{GIA_j} - \beta'_N \tag{6.3}$$

where $\dot{E}_i^{GNSS_j}$ and $\dot{N}_i^{GNSS_j}$ are the estimated GNSS velocities in East and North component respectively, $\dot{E}_i^{GIA_j}$ and $\dot{N}_i^{GIA_j}$ are the modelled GIA velocities in the East and North components and β'_E and β'_N are the local topocentric components of geocentre motion β' from Eq. (5.8).

The vertical residual velocity for each GIA model j is computed by removing the Up component of the predicted GIA velocity and the Up component of β' from the GNSS velocity:

$$\dot{U}_i^{res_j} = \dot{U}_i^{GNSS} - \dot{U}_i^{GIA_j} - \beta'_U \tag{6.4}$$

The plate motion is horizontal only, such that the Up component of plate motion $\dot{U}_i^{pm_j}$ is zero. In practice, the Up component of the estimated plate motion can be different from zero due to errors. For example, it can be nearly zero if the PMM is estimated with a velocity field which is contaminated by a GIA signal when not correcting for GIA at all, or using an unsuitable GIA model.

6.2 Median Absolute Deviations

To compare the GIA models, MADs are used as a measure of goodness of fit for each GIA model. The models with the smaller MADs are considered to be better models. The MAD is computed as follows:

$$MAD = \text{median}|X_{obs} - X_{modelled}| \tag{6.5}$$

where $X_{obs} - X_{modelled}$ are the residuals $\dot{E}_i^{res_j}, \dot{N}_i^{res_j}, \dot{U}_i^{res_j}$. We compute the MAD for the horizontal component,

$$MAD_{hor}^j = \text{median}\left(\sqrt{\left(\dot{E}_i^{res_j}\right)^2 + \left(\dot{N}_i^{res_j}\right)^2}\right), \tag{6.6}$$

and for the vertical component:

$$MAD_{up}^j = \text{median}|\dot{U}_i^{res_j}|. \tag{6.7}$$

where j is the GIA model number, and i is the site number which covers all the sites in a selected region. To assess whether the GIA models improve the goodness of fit, the MADs for the GNSS velocity field without any GIA corrections are also computed, which I denote as the null-GIA case. The MAD for the horizontal component in this case is computed as

$$MAD_{hor}^{GNSS} = \text{median}\left(\sqrt{\left(\dot{E}_i^{GNSS}\right)^2 + \left(\dot{N}_i^{GNSS}\right)^2}\right), \tag{6.8}$$

and the vertical component as

$$MAD_{up}^{GNSS} = \text{median}|\dot{U}_i^{GNSS}|. \tag{6.9}$$

The MADs are computed globally and for the following regions: Europe, North America and Antarctica.

Computing the global MAD is biased by the significantly higher density of GNSS sites in the United States network, on the North America plate. Therefore, to mitigate the bias, the global MAD is determined by computing the MAD of each plate and weighting by plate area:

$$MAD_{weighted}^{j} = \frac{\sum\limits_{p=1}^{n} A_p \times MAD_p^j}{\sum\limits_{p=1}^{n} A_p} \tag{6.10}$$

MAD_p^j and A_p are the MAD and area of each estimated plate p and $MAD_{weighted}^j$ is the global plate weighted MAD.

6.2.1 MAD comparison

I compute the MADs for all GIA models in categories which are combinations of the following:

1. Region - global, Europe, North America or Antarctica
2. GIA model Earth structure - 1D or 3D
3. Horizontal or vertical component

The MAD values for each region and component are compared, and the models with the smaller MAD are considered better models. As mentioned in section 6.1, it is not expected that the GIA effect will be equivalent to the GNSS displacement at every site. The residual motion at the majority of GNSS sites should be close to zero but large residuals can only unequivocally indicate that the observed motion is not in agreement with the modelled GIA prediction. The misfit between the GIA model and the GNSS observed motion can be due to the fact that the GIA model predicts too much or too little GIA motion compared to the true values, which are unknown. This disagreement can also be due to the action of processes not related to GIA that cause uplift, subsidence or horizontal motion, such as local tectonics or present-day ice mass changes. Antarctica and Greenland are examples of areas affected by GIA and the solid Earth response to present-day ice mass changes. In Antarctica, which is one of the areas of interest of this project, the effect of present-day ice mass changes has been removed when evaluating the residual velocity field by subtracting the elastic deformation in equations (6.2), (6.3) and (6.4), see section 6.6 for details. Greenland is not a study area in this project due to the lack of sufficient high-quality GNSS data. The effect of not correcting the existing Greenland sites for the effect of present-day ice mass changes on the global MAD fit is insignificant due to it being a part of the North American plate which has a very high number of sites outside of Greenland. However, it can be challenging to fit the data on a regional level if the spatial density of GNSS sites is uneven (cf. section 6.5.3).

The model with the smallest MAD in each category is selected as the best model. Table 6.2 lists the best 1D GIA model in each region and for each component, as well as the null-GIA case for comparison. Table 6.3 is similar to Table 6.2, but for the 3D GIA models. Among the 1D GIA models, the best model in most of the categories is based on the ICE-6G ice model whereas this is not the case within the 3D GIA models. The majority of the best 3D GIA models are based on dry rheology, except the global (plate weighted) in the horizontal component and the Antarctica vertical component.

The features of GIA models corresponding to better MAD fits are summarized in Table 6.1. Figs. D.1 - D.16 in Appendix D show the MAD fits for all GIA models and regions. For the 1D GIA models (hereafter referred to as 1D models) each figure is composed of nine sub-figures. The rows in the figures show different lithosphere thicknesses (71 km, 96 km and 120 km) and the columns show different ice models. The horizontal axis of each sub-figure shows upper mantle viscosities (η_{UM} of 0.3×10^{21}Pa s, 0.5×10^{21}Pa s and 0.8×10^{21}Pa s) and the vertical axis of each sub-figure shows lower mantle viscosities (η_{LM} of 5×10^{21}Pa s, 10×10^{21}Pa s and 20×10^{21}Pa s). For the 3D GIA models (hereafter referred to as 3D models) each figure consists of six sub-figures where the rows show different seismic velocity models (S40RTS for Ritsema et al. (2011) and SL for Schaeffer and Lebedev (2013)) and the columns show different ice models. The horizontal axis of each sub-figure shows the water content of the mantle and the vertical axis of each sub-figure shows the grain size.

Within the 1D models, in the vertical component, there is a preference for smaller η_{UM} in all studied regions except North America. In North America the vertical observations suggest larger η_{LM} with ICE-6G, and smaller η_{LM} with ICE-5G and W12 (Fig. D.9). The ice load in ICE-6G is thinner than in ICE-5G/W12 west of Hudson Bay and extending

		Global	Europe	North America	Antarctica
1D Vertical	Lithosphere	∅	∅	∅	∅
	Upper mantle η (0.3, 0.5 or 0.8 $\times 10^{21}$Pa s)	mostly smaller	smaller	∅	smaller
	Lower mantle η (5, 10 or 20 $\times 10^{21}$Pa s)	∅	mostly smaller	mostly smaller	∅
	Ice model	ICE-6G	ICE-6G	ICE-6G	ICE-6G
1D Horizontal	Lithosphere	120 km	120 and 96 km	weak preference for 120 km	∅
	Upper mantle η (0.3, 0.5 or 0.8 $\times 10^{21}$Pa s)	∅	smaller	larger	mostly larger
	Lower mantle η (5, 10 or 20 $\times 10^{21}$Pa s)	smaller	mostly small	∅	∅
	Ice model	∅	ICE-6G	weak preference for ICE-6G	∅
3D Vertical	Grain size	1 and 4 mm	4 and 10 mm	10 mm	1 mm
	Water content	∅	dry	dry	wet
	Mantle model	∅	∅	∅	∅
	Ice model	∅	∅	∅	∅
3D Horizontal	Grain size	1 and 4 mm	∅	weak preference for 4 mm	1 or 4
	Water content	∅	dry	∅	mostly dry
	Mantle model	∅	S40RTS	SL	∅
	Ice model	∅	∅	∅	∅

Table 6.1: Comparison of MADs and selected features of GIA models in each category. ∅ denotes no preference.

down into northern USA, which could explain the preference for more rigid η_{LM} than for ICE-5G/W12. The ice load in ICE-6G is thicker than ICE-5G/W12 in the Canadian Arctic Archipelago and the Cordilleran ice sheet in the west of the continent, but there are few or no sites in this area compared to the previously mentioned areas. Note, however, that besides the mentioned η_{LM} , η_{UM} plays an important role in the predicted uplift and subsidence rates. In Antarctica in the vertical component 1D models with ICE-6G give better fits than with ICE-5G and W12, but none of the 1D GIA models give an improvement on the null-GIA case. There is a preference for the ICE-6G ice model in all regions in the vertical component. In the horizontal component, there is a preference for ICE-6G only in Europe and North America (Figs. D.6 and D.10). In the horizontal component the models show a better fit with thicker lithosphere in all regions besides Antarctica. In Antarctica there is a preference for thicker lithosphere in the horizontal component only in combination with ICE-5G (Fig. D.14).

Among the 3D models, there is no preference for a particular ice model or seismic velocity model. In the horizontal component, there is a weak preference for S40RTS in Europe and for SL in North America (Figs. D.8 and D.12). The largest difference in MAD fits between using S40RTS or SL is found in Antarctica, in both the horizontal and the vertical component, but there is no preference for either of them (Figs. D.15 and D.16). In other regions, there is not much difference in the MAD fit depending on the choice of the seismic velocity model.

In the horizontal component, none of the 3D GIA models show preference for the largest grain size of 10 mm. Globally in the vertical component among the 3D models, there is no strong preference for a single parameter but the best MAD fits are obtained with a combination of 1 mm grain size and dry rheology or 4 mm grain size with wet rheology. These combinations indicate middle-range viscosities among the 3D GIA models (cf. Table 2.1) which are still small when compared to the regional 1D models. The top row in Fig. 6.1 shows examples of global mantle viscosity maps for two 3D GIA models with these combinations of rheological properties and the same seismic velocity model (S40RTS) and ice model (ICE-5G), 5G_S_dry_1mm and 5G_S_wet_4mm. The viscosities are averaged over mantle layer of 170-230 km depth.

In both the vertical and the horizontal component globally (global plate weighted), the best fitting models are 3D GIA models. The bottom row in Fig. 6.1 shows the mantle viscosities in the same mantle layer for the globally best fitting GIA model in the horizontal component (6G_SL_wet_10mm) and vertical component (W12_SL_dry_1mm). The globally best fitting GIA model in the vertical component W12_SL_dry_1mm gives average viscosities in 170 − 230 km depth of 5.2×10^{21} Pa s, 0.9×10^{21} Pa s and 1.9×10^{21} Pa s for the continental part of the regions of interest (Figs. A.1, A.2 and A.3) in Europe, North America and Antarctica, respectively. The globally best fitting 3D model in the horizontal component 6G_SL_wet_10mm gives higher average viscosities in 170 − 230 km depth of 87.3×10^{21} Pa s, 16.7×10^{21} Pa s and 34.7×10^{21} Pa s for the continental part of the regions of interest in Europe, North America and Antarctica, respectively. The layer 170 − 230 km can be interpreted as the closest compatible comparison with the upper mantle viscosities from the 1D models. However, the averaged values of viscosities from 3D models cannot be straightforwardly compared with the value of the uniform viscosities from the 1D models. The 1D and 3D GIA models used in this thesis are produced using very different algorithms. The 1D models use spherical harmonics to determine solid Earth deformation and perturbations to the gravity field. The 3D models use finite element methods to determine the solid Earth deformation. Additionally, in the 3D GIA models, the viscosity depends on the stress, i.e. ice and ocean load (cf. section 2.2.3). Therefore, a 3D GIA model with an averaged viscosity (globally or for a certain region) will not necessarily give the same GIA predictions as a 1D model with the uniform viscosity equal to the averaged viscosity of the 3D model.

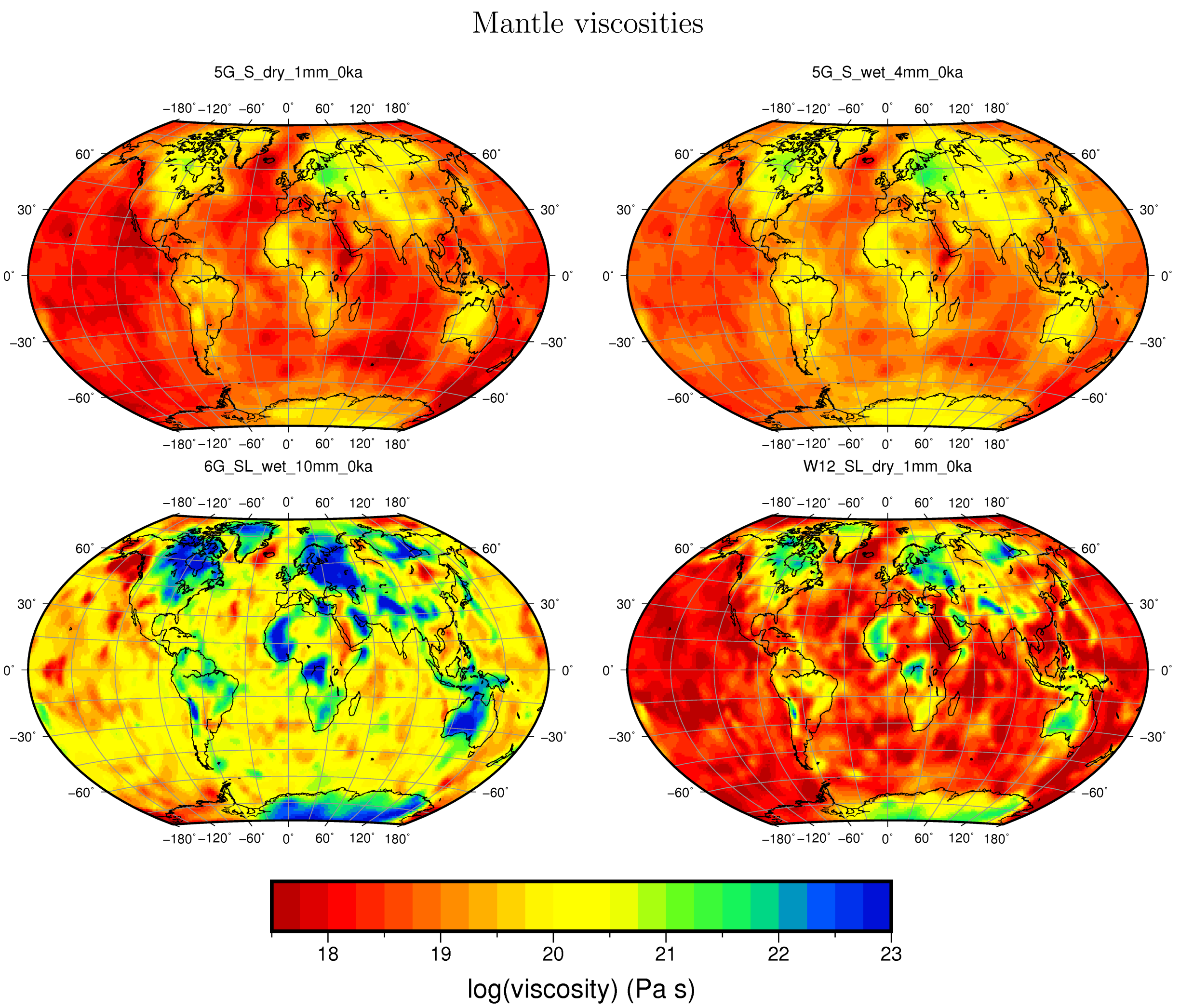

Figure 6.1: Mantle viscosity maps for four 3D GIA models. The viscosities are averaged for layer of 170–230 km depth.

Region		Best 1D GIA model (features)					Null-GIA MAD [mm/yr]
		Ice model	Lithosphere thickness [km]	Upper mantle viscosity [10^{21}Pa s]	Lower mantle viscosity [10^{21} Pa s]	MAD [mm/yr]	
Europe	hor	ICE-6G	96	0.3	10	0.40	0.44
	ver.	ICE-6G	71	0.3	20	0.55	1.29
North America	hor.	ICE-6G	120	0.8	10	0.60	0.68
	ver.	ICE-6G	120	0.8	20	0.75	1.07
Antarctica	hor.	ICE-6G	71	0.8	5	0.86	1.07
	ver.	ICE-6G	120	0.3	20	1.84	1.31
Global (plate weighted)	hor.	ICE-6G	120	0.3	5	0.66	0.60
	ver.	ICE-6G	120	0.8	20	0.98	1.02
Global (no weighting)	hor.	ICE-6G	71	0.3	20	0.57	0.60
	ver.	ICE-6G	120	0.8	20	0.78	1.12

Table 6.2: The best 1D GIA model for every category according to MADs, as well as MAD for the null-GIA case, when no GIA correction is applied. In the case of Antarctica in the vertical component and globally (plate weighted) in the horizontal component, no GIA model gives a smaller MAD than the null-GIA case.

Region		Best 3D GIA model (features)					Null-GIA MAD [mm/yr]
		Ice model	Mantle viscosities model	Rheology water content	Mantle grain size factor	MAD [mm yr]	
Europe	hor	ICE-6G	S	dry	4 mm	0.40	0.44
	ver.	W12	SL	dry	4 mm	0.71	1.29
North America	hor.	ICE-5G	S	dry	4 mm	0.62	0.68
	ver.	ICE-6G	SL	dry	10 mm	0.87	1.07
Antarctica	hor.	ICE-6G	S	dry	4 mm	1.01	1.07
	ver.	ICE-5G	S	wet	1 mm	1.22	1.31
Global (plate weighted)	hor.	ICE-6G	SL	wet	10 mm	0.58	0.60
	ver.	W12	SL	dry	1 mm	0.88	1.02
Global (no weighting)	hor.	ICE-6G	S	dry	4 mm	0.56	0.60
	ver.	ICE-6G	S	dry	10 mm	0.91	1.12

Table 6.3: Best 3D GIA model for every category according to MADs, as well as MAD for the null-GIA case, when no GIA correction is applied. In all cases applying a GIA correction is better than the null-GIA case.

6.3 Best and near-best GIA models

The best model is chosen by ranking the MAD in each category, i.e. horizontal and vertical component of each region (Tables 6.2 and 6.3). Next, groups of near-best models in each category were formed using an MAD criterion, i.e. by considering all models with MADs better than the null-GIA case and within a threshold of 0.1 mm/yr and 0.2 mm/yr of the best model for the horizontal and the vertical component, respectively. These thresholds were chosen based on the spread of MADs as well as the GNSS uncertainties for each component. The GNSS velocity uncertainties are mostly up to 0.5 mm/yr in the horizontal component and mostly up to 1 mm/yr in the vertical component (cf. Chapter 4). The MADs vary within 0.4-1.7 mm/yr in the horizontal component and 0.5-2.2 mm/yr in the vertical component in all regions except Antarctica, where they vary within 0.9-1.9 mm/yr in the horizontal and 1.2-4.1 mm/yr in the vertical component (cf. Table 6.5).

The groups of near-best models represent the models that are nearly as good as the best model according to the MAD criterion above, i.e. any of them could be the best model if a different observation dataset were used, considering the number of sites and their uncertainties. Tables E.2, E.3 and E.4 in Appendix E list the models in the groups of near-best models. Table 6.4 shows the number of GIA models assigned to each group of near-best models. The groups marked with ∅ are the ones where even the best fitting GIA model was not better than the null-GIA case. This is the case for the global (plate weighted) horizontal residuals using 1D GIA models, which suggests it is not possible to replicate the global horizontal velocity field by combining a 1D Earth model with the global ice models being tested here.

	Global	Europe	North America	Antarctica	Total N° models
Horizontal 1D	∅	6	7	6	81
Horizontal 3D	13	9	30	6	36
Vertical 1D	3	25	6	∅	81
Vertical 3D	18	18	16	4	36

Table 6.4: Number of GIA models in the groups of near-best GIA models for every observed category.

Since the group of near-best models is close to the best model in terms of the MAD value for each region, studying the differences in GIA predictions among the near-best models can provide information about the uncertainty of the GIA models. For each group of near-best GIA models, the range of GIA model predictions is computed for each grid point of the interest region. The range of GIA models tells us where the predictions of credible GIA models differ the most and reveals the areas that are more sensitive to a change in Earth and ice model parameters. For the vertical component, the range is defined to be

	Median Absolute Deviation [mm/yr]			
	Horizontal 1D	Horizontal 3D	Vertical 1D	Vertical 3D
Europe	0.40-0.78	0.40-0.49	0.55-1.31	0.71-1.25
North America	0.60-1.66	0.62-0.78	0.75-2.19	0.87-1.26
Antarctica	0.86-1.86	1.01-1.28	1.84-4.09	1.22-2.61
Far field	0.63-1.12	0.56-0.69	0.79-1.80	0.77-0.96
Global plate weighted	0.66-1.01	0.58-0.64	0.98-1.64	0.88-1.14
Global no weighting	0.57-1.21	0.56-0.68	0.78-1.76	0.91-1.22

Table 6.5: Minimum and maximum MAD values for all GIA models in each category.

the difference between maximum and minimum GIA prediction at each point. For the horizontal component, the range is defined to be the difference between the largest and smallest magnitude at each point. In the horizontal component, a range of directions of the horizontal velocities is also computed. It is shown as the maximum and minimum azimuths of the GIA horizontal velocities.

Finally, for each category, a residual velocity field is presented in terms of residual vertical and horizontal velocities, as well as residual horizontal magnitudes.

When discussing the vertical residual velocities, the term over-predict and under-predict is used in areas where GIA uplift is expected. The term over-predict is used when correcting the GNSS vertical velocities with the GIA model gives negative residuals, i.e. the predicted GIA signal is greater than the observed one. Conversely, the term under-predicting is used for cases when correcting with the GIA model gives a positive residual, i.e. the predicted GIA signal is smaller than the observed one. When correcting for GIA in areas where we do not know whether to expect uplift or subsidence, the terms residual uplift and residual subsidence are used to describe the positive and negative sign of the vertical residual velocities. Similarly when describing horizontal magnitudes, the term overpredict is used when the GIA model predicts more horizontal motion than the one that is at a site after removing plate motion. In the following sections I use the residual velocity fields and the ranges of near-best models to analyse and compare GIA models in each region of interest.

6.4 Europe

6.4.1 Range of GIA model predictions Europe

In Chapter 2, Figure 2.6 shows the vertical GIA predictions in Europe using the best 1D and the best 3D GIA model. The region of maximum vertical GIA deformation is in the centre of the former ice sheet, in the Gulf of Bothnia (Steffen and Wu, 2011). The uplift rates reduce radially from the centre of the Fennoscandian uplift area, which is shifted slightly westwards with the best 3D model compared to the best 1D model, where the centre of the uplift is inside the Gulf of Bothnia. The uplift rates in Fennoscandia are larger with the 1D model; the maximum uplift with the 1D model is 10 mm/yr and with the 3D model it is 6 mm/yr. The centre of the uplift with the 3D model coincides well with the one from the NKG2016LU empirical land uplift model (Vestøl et al., 2019), which is largely based on GNSS and levelling observations and a 1D GIA model for interpolation (and extrapolation) between the observation points. However, the magnitudes of uplift with the 1D model coincide better with NKG2016LU than the magnitudes of the 3D model. Continental Europe and the British Isles show small GIA vertical deformations of ± 1 mm/yr for both models, which is expected since they are further from the location of the former ice sheet.

Fig. 6.2 shows the range of vertical GIA predictions for the groups of 25 near-best 1D models and 18 near-best 3D models (Table 6.4) in Europe in the vertical component. It can be first noted that the 1D models show larger ranges than the 3D models, the former reaching values of 5.5 mm/yr, with the latter reaching values of 3 mm/yr. However, both 1D and 3D models show the largest ranges in the area with a strong GIA signal, i.e., Fennoscandia.

The 1D models show a concentration of larger ranges of 4-6 mm/yr around the Gulf of Bothnia. The maximum range in Fennoscandia spreads radially from the centre of the Gulf of Bothnia, with the lowest values in western Norway and southern Sweden of up to 2 mm/yr, and towards continental eastern Europe. The area around the Gulf of Finland is an anomaly in the southeast part of the radial spread from the Gulf of Bothnia, with maximum range up to 2 mm/yr. The northern coast of Norway towards the Barents Sea shows $\sim$1 mm larger maximum range than the continental areas surrounding it, up to 4 mm/yr of uncertainty in GIA predictions from Lofoten peninsula and along the coast to the east. This might reflect the uncertainty over the position of the transition from uplift to subsidence.

With the group of 3D models, the largest range in vertical predictions is in central Norway and central Sweden, of 2-3 mm/yr. Surrounding that area and around the Gulf of Bothnia there are ranges of 1.5-2 mm/yr. The rest of Fennoscandia and the Baltic states show maximum ranges of 1.5 mm/yr. The range reduces radially around the area with the maximum range, which is slightly shifted westwards as compared to the 1D models.

The 1D range is the strongest in the area the largest uplift is expected, and reduces around it. This could be because changing Earth model parameters (viscosity) changes the speed of the uplift. The 3D models show the largest range far from the central area of the former ice sheet. This indicates that the largest vertical uncertainty in the near-best 3D models in Fennoscandia is not due to the location of the ice sheet, but due to 3D Earth rheology. The groups of near-best 1D and 3D models contain models combined with all three ice models, although among the 1D near-best groups they are mostly based on ICE-6G. The near-best 1D models show larger uncertainties in the vertical model predictions than the 3D models. However, the 1D models vertical predictions also have larger magnitudes.

In continental Europe and the British Isles, well outside the Fennoscandian uplift area, the ranges are smaller for both 1D and 3D models, with values of up to 2 mm/yr and 1 mm/yr, respectively. With the 1D models, there is a region to the north of the Caspian Sea with large uncertainty in GIA models, which is likely due to water loading in the Caspian Sea when solving the sea-level equation although there is no ice loading in that area.

In Chapter 2, Fig. 2.7 shows the horizontal GIA predictions in Europe for the best 1D and best 3D GIA model. The magnitudes of horizontal velocities are smaller for the 3D model. For both the models, the velocities in continental Europe are pointing northwards and in Fennoscandia they mostly point outwards from the centre of the maximum uplift. Velocities in the part of Fennoscandia south of 60°N should be pointing southwards considering the maximum uplift area in the vertical component but they point more northwards with the 1D model and in an East-West direction with the best 3D model. One reason for this could be the influence of the former Laurentide ice sheet on Europe. This is because of the vast size of the former Laurentide ice sheet and because the stresses are not taken in the plate boundary when the latter are not considered in GIA modelling (Whitehouse et al., 2006; Klemann et al., 2008), which is the case for the GIA models in this thesis. Another reason could be that the direction of the velocities has been found to be a function of the viscosity (Hermans et al., 2018, which is discussed in 6.6.2). For both the best 1D GIA model and the best 3D GIA model, predicted velocities are smaller south of 60°N than for the rest of Fennoscandia. The model predictions disagree in direction west of 0° longitude and in the north of Fennoscandia where 3D models predict significantly smaller magnitudes.

Figs. 6.3 and 6.4 show the range of horizontal magnitudes and azimuths of horizontal velocity predictions in Europe for the groups of 6 near-best 1D models and 9 near-best 3D models. The 1D models show the largest magnitude range of 0.8-1.0 mm/yr in the area East of the Lofoten archipelago. The majority of Fennoscandia and the British Isles show ranges of 0.5-0.8 mm/yr. The rest of Fennoscandia and continental Europe shows smaller magnitude ranges below 0.5 mm/yr. The range is the smallest around the Gulf of Finland, similar to the vertical component range, less than 0.3 mm/yr. The maximum range reduces gradually for the 1D models, from NW to SW. With the 1D models, there is not a large range in velocity directions in Fennoscandia, mostly below $\sim 30°$ with the largest range in directions east of the Gulf of Bothnia. This is due to Earth properties of the different models in the near-best horizontal 1D models group since all of them are created using the same ice model.

The near-best 3D models range reaches a maximum of 0.75 mm/yr in the northern Norway. Smaller ranges up to 0.5 mm/yr are found in the rest of Fennoscandia. The range is also below 0.5 mm/yr in continental Europe south of 55°N and the British Isles. Similar to the vertical component, the 3D models show a smaller range in horizontal magnitude than the 1D models. However, the 3D models show a larger range in velocity directions than the 1D models. The directions of horizontal velocities with the near-best 3D models range over 180° in most of Fennoscandia. The range of azimuths is smaller east of the Gulf of Bothnia than in the rest of Europe. In this area the range of azimuths among 3D models is smaller than among the 1D models. In the rest of Europe, the range of azimuths is significantly smaller among the 1D models. The reason for the larger range of azimuths for the near-best 3D models than the near-best 1D models could be that the former contains models based on all three ice models, while the latter models are based on the same ice model.

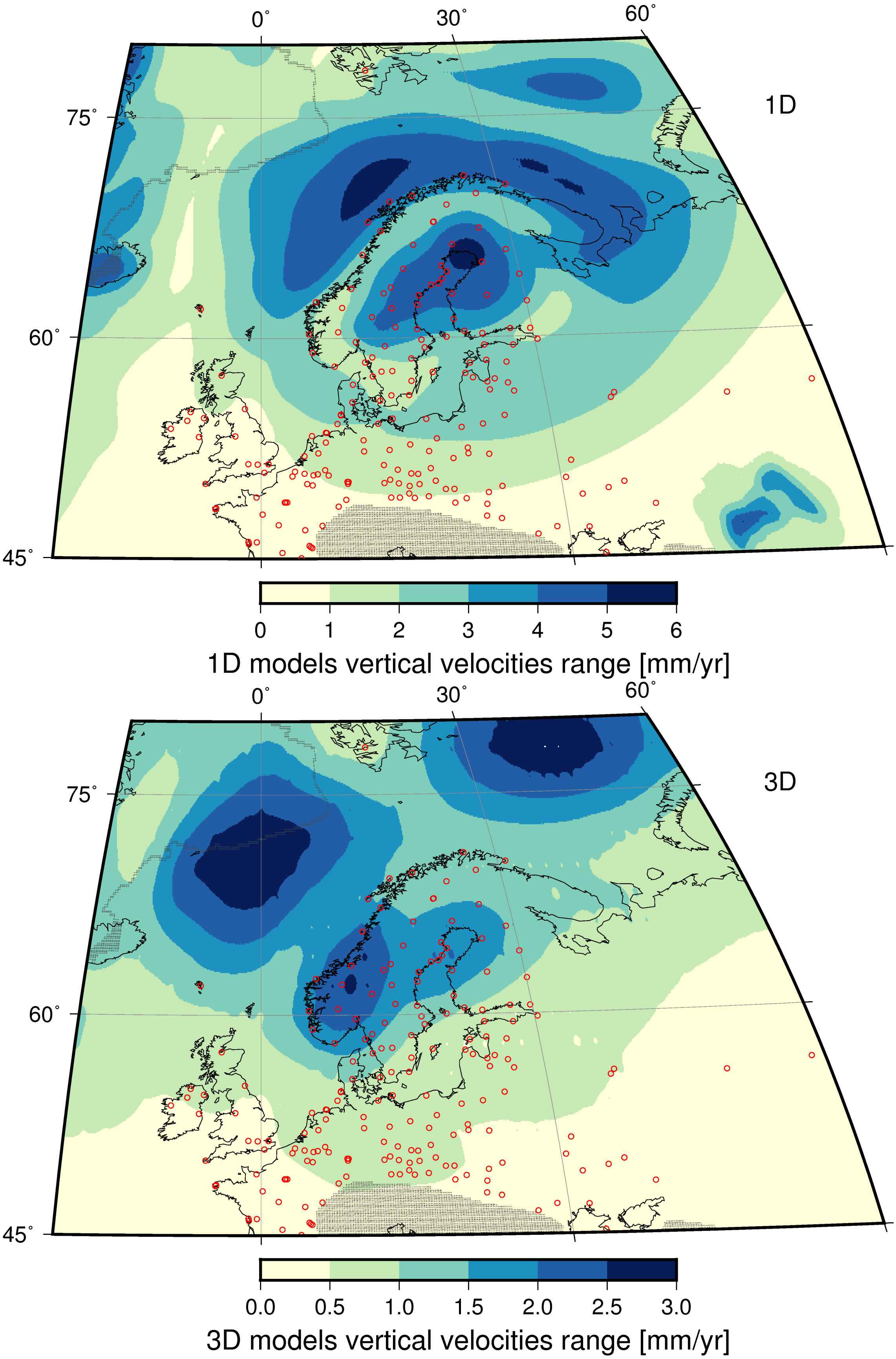

Figure 6.2: The maximum difference between vertical GIA velocity predictions for models in the group of near-best 1D GIA models (top) and near-best 3D GIA models (bottom) for Europe, cf. Table 6.4. The colourbar saturates at 9 mm, the largest value is 10 mm in the centre of the coast of the Gulf of Bothnia. The shaded areas cover high tectonic strain regions where the GNSS sites have been disregarded. The red circles represent the network GNSS sites.

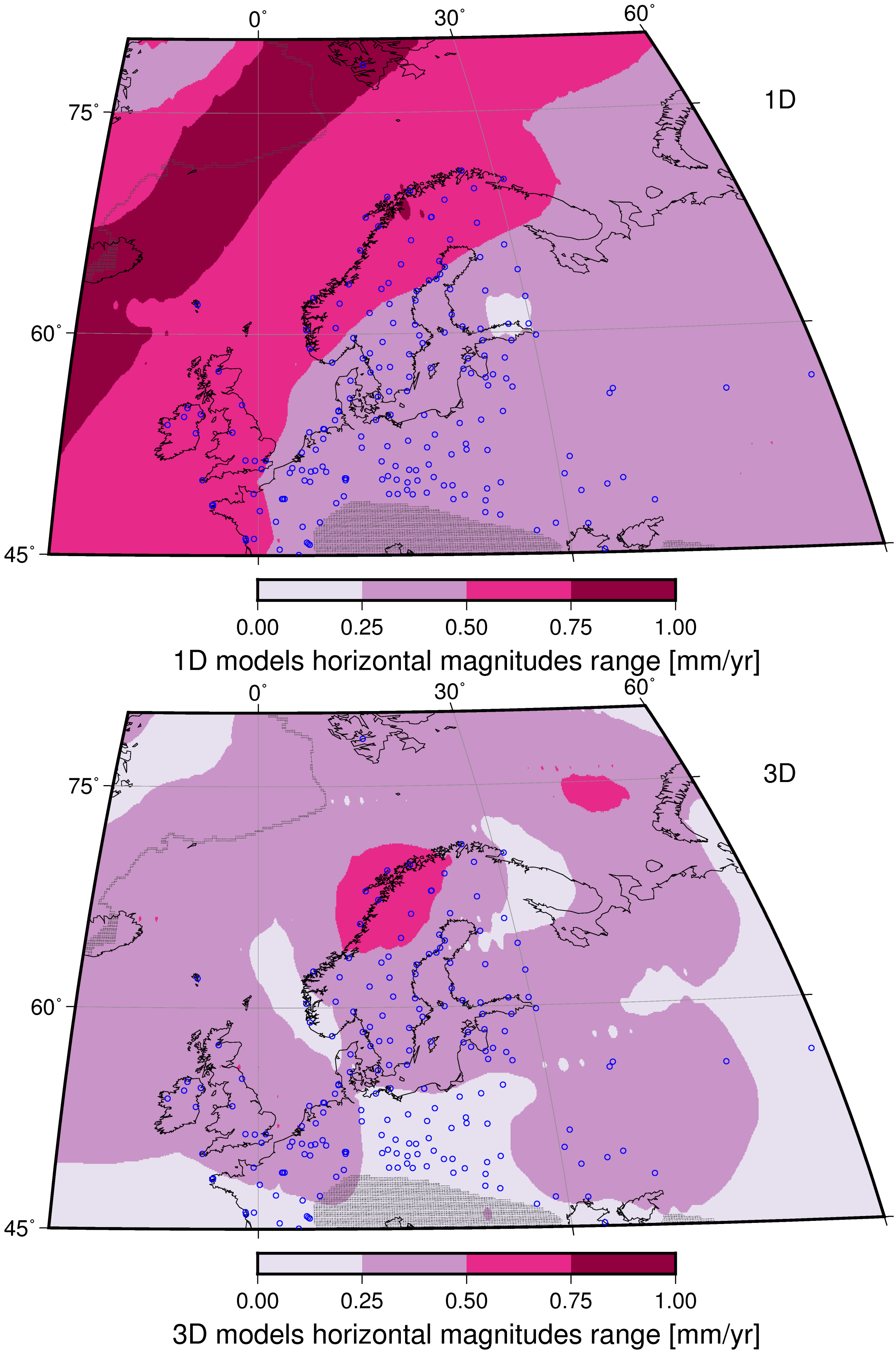

Figure 6.3: The maximum difference between horizontal magnitudes of GIA predictions for models in the group of near-best 1D GIA models (top) and near-best 3D GIA models (bottom) for Europe, cf. Table 6.4. The shaded areas cover high tectonic strain regions where the GNSS sites have been disregarded. Circles represent network GNSS sites.

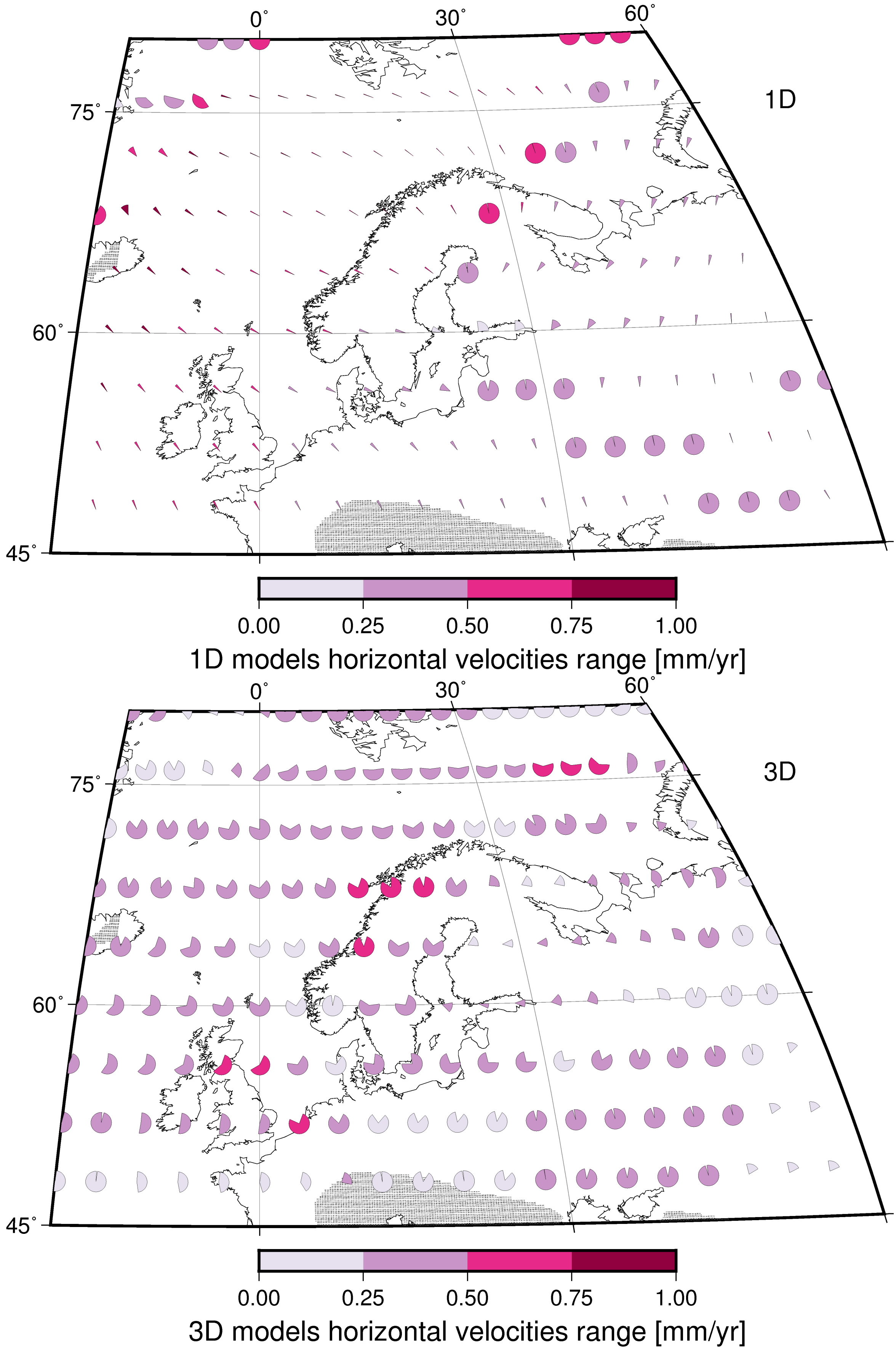

Figure 6.4: The maximum difference between magnitudes and azimuths of horizontal GIA predictions for models in the group of near-best 1D GIA models (top) and near-best 3D GIA models (bottom) for Europe, cf. Table 6.4. The shaded areas cover high tectonic strain area where the GNSS sites have been disregarded.

6.4.2 Residual velocity field Europe

Vertical

I compute the residual vertical velocity field for Europe using the best 1D and 3D GIA model, which is defined by the MAD fit. The best 1D GIA model in the vertical component for Europe is 6G_71p320 (see Table 2.2 in Chapter 2 for naming convention) and the best 3D GIA model in the vertical component is W12_SL_dry_4mm (Table 2.3). Fig. 6.5 shows residual vertical velocity fields in northern Europe after removing the GIA effect using the best 1D and 3D GIA model. The GNSS sites are indicated with circles of varying sizes, where the symbol size reflects the vertical GNSS uncertainty. A larger circle indicates lower uncertainty. The majority of the sites show uncertainties below 1 mm/yr.

In continental Europe south of 55° and the British Isles, both the 1D and the 3D model give similar residual velocities, within ±0.7 mm/yr at most sites, while they tend to disagree in Fennoscandia.

In Fennoscandia, the best 1D model underpredicts GIA along the Scandinavian mountains in Sweden and in parts of the western coast of the Gulf of Bothnia. The model overpredicts GIA to the north and east of the Gulf of Bothnia, though these values are within the GNSS uncertainty. To the north and NE of the Gulf of Bothnia we find negative residuals up to -0.7 mm/yr. The largest positive residuals of 2.3-2.7 mm/yr are in a small area in Sweden in the centre of the Scandinavian peninsula. South of the Gulf of Finland, in Estonia and Latvia, we find the largest negative residuals, -1 to -2 mm/yr, but some of these sites have vertical uncertainties 1-2 mm/yr and are not significant.

The best 3D model in Fennoscandia generally underpredicts GIA in the region of expected maximum uplift, with the largest residuals on the west coast of the Gulf of Bothnia, maximum 5.1 mm/yr at one site and otherwise 3.3-4.1 mm/yr. Along the Scandinavian mountains in Sweden, we find residuals of 1.7-3.3 mm/yr.

On the Northern coast of Norway, the residuals are varying within -0.3 to +0.8 mm/yr with the 1D model. The residuals are similar in magnitude with the 3D model in that area, with more sites showing residual subsidence than residual uplift than with the 1D model, from -1.1 to +0.3 mm/yr with the 3D model. An exception in both cases is a site that has high GNSS uncertainty.

The best 3D model shows more variation in the residual field than the best 1D model since it gives larger residual uplift in the Gulf of Bothnia and more subsidence on the west coast of Norway than the best 1D model. East of the former ice sheet, some sites show that observed rates are smaller and on some larger than the ones predicted by the models. West of the former ice sheet, observed uplift rates are greater than predicted by both models. This suggests that the area west of the ice sheet should be investigated more. The 1D model gives significantly smaller residuals on the coast of the Gulf of Bothnia and along the mountain range in the Scandinavian peninsula, where the 3D model strongly underpredicts GIA. This shows that the best 1D model outperforms the best 3D model in Europe, as the 3D model underpredicts GIA in Fennoscandia, the area covered by the former ice sheet. The difference in fit may be due to the fact that the ice models are created to fit GNSS velocities and relative sea-level records using 1D Earth models.

Horizontal

The best 1D GIA model in the horizontal component for Europe is 6G_96p310 and the best 3D GIA model in the horizontal component is 6G_S_dry_4mm. Residual horizontal magnitudes for the best horizontal GIA models are shown in Fig. 6.6. Fig. 6.7 shows the directions of the horizontal velocities of the residual velocity field at GNSS sites calculated using the best 1D and 3D model. The colours of the arrows in the figure denote the uncertainties of the horizontal component of the GNSS velocities. For both models, the small number of sites with large residual horizontal velocities of over 1.5 mm/yr are the ones with larger uncertainties. The horizontal uncertainty of GNSS velocities in Europe is mostly <0.5 mm/yr or 0.5-1 mm/yr.

In Fennoscandia, the best 1D model gives residual magnitudes below 0.8 mm/yr at most sites, with a few sites showing values between 1-1.3 mm/yr. The residual velocities on the west coast of Norway are pointing northwards, but their magnitudes are ∼0.5 mm/yr. This is close to the level of uncertainty of GNSS velocities so these values are hardly significant and should be interpreted with care. Similarly, residual velocities of 0.5-0.6 mm/yr are found on the west coast of the Gulf of Bothnia pointing SE, inwards to the Gulf of Bothnia. This indicates that the 1D GIA model overpredicts horizontal motion in this area, or that the location of the former ice sheet in the ice model is not correct and therefore predicting horizontal velocities in the wrong direction.

Correcting for GIA using the best 3D GIA model in northern Europe leaves residual magnitudes of mostly up to 0.9 mm/yr except for several sites with magnitudes 1-1.9 mm/yr. The magnitudes just north of the Gulf of Bothnia are smaller than with the 1D model. However, the magnitudes with the best 3D model are larger than the 1D model along the coast of Norway and the border with Sweden, 0.8-1.1 mm/yr (1.54 mm/yr on a site with high GNSS uncertainty). These residual velocities are pointing NW, outwards from the centre of uplift in Fennoscandia. The 3D model gives residuals of 0.2-0.6 mm/yr on the west coast of the Gulf of Bothnia and 0.4.-0.8 mm/yr east of the Gulf of Bothnia, pointing southwards.

Both models give small residual velocities in continental Europe and the UK, mostly up to

0.5 mm/yr with the best 3D model and mostly up to 0.7 mm/yr with the best 1D model. The main difference in performance between the 1D and 3D models in the horizontal component is on the coast of Norway and in the centre of the Scandinavian peninsula, where the 3D model shows larger residuals, all in NW direction. Since the large residuals on the west coast of Norway for the 3D model are all pointing in the same direction, this could be due to a bias of the PMM or the ice model.

6.4.3 Europe summary

Among the 1D GIA models, there is a preference for smaller η_{UM} and smaller η_{LM} for both the horizontal and vertical component (Figs. D.5 and D.6 and Table 6.1). Among 1D and also 3D GIA models, the near-best model groups for the vertical and horizontal component contain several of the same models (Table E.2). The above indicates that it is possible to find a GIA model that fits the observed vertical and horizontal (when plate motion is removed) surface velocity field well.

The largest GIA uplift signal is expected to be found in the central area of the former ice sheet (Milne et al., 2001; Steffen and Wu, 2011). The area of the maximum uplift and the direction of the horizontal velocities in Fennoscandia with the best models are as expected regarding the area of the former ice sheet.

Considering the 1D models, looking at the residual velocity fields of the best model (Figs. 6.5 and 6.6) and the range of the groups of near-best GIA models (Figs. 6.2 and 6.4), the largest vertical range in the group of near-best models is in the centre of the Gulf of Bothnia, and the largest negative residuals are just west of it. With the 3D models, the largest range is shifted SW towards the central latitude of the Scandinavian peninsula, whereas the largest residuals with the best 3D model are on the west coast of the Gulf of Bothnia. This indicates that the ongoing response to past ice load change is estimated to be different in the two sets of models. The two best models are created using different ice models, the best 1D GIA model is 6G_71p320, and the best 3D model is W12_SL_dry_4mm (the northern hemisphere ice sheets for W12 are from ICE-5G, cf. Chapter 2). The location of the maximum uplift with W12_SL_dry_4mm coincides with the one shown in e.g. Vestøl et al. (2019); Milne et al. (2001) although the magnitudes of the uplift do not coincide, and this is ambiguous for 6G_71p320.

When it comes to the difference in the residuals of the best 1D and 3D models, in the horizontal component the difference is the largest in the centre of the Scandinavian peninsula along the mountain range and along the coast of Norway. In the vertical component, the difference is the largest in the centre of the Scandinavian peninsula and on the coast of the Gulf of Bothnia.

In the vertical component, the 1D model outperforms the 3D model. In the horizontal component, the MADs of the best 1D and the best 3D GIA model are the same, but from visual inspection of the residuals in Norway, the 1D model seems to slightly outperform the 3D model. The latter residual velocities are all in the same direction which may indicate a bias of the plate model, when seeking to fit the velocities in the rest of the plate (it may be that the model is chosen to be the best one due to the fit in other areas, while it performs poorly along the Norwegian coast). However, on the west coast of the Gulf of Bothnia, near the centre of the uplift area, the 1D model overpredicts horizontal velocities.

The vertical residual velocity field on the coast of northern Norway for the best 1D and in particular the best 3D GIA model are in broad agreement with the vertical residual velocity field from Kierulf (2017) for their best fitting GIA model, in that uplift is over-predicted at the outer coastal sites (see their Fig. 6). Kierulf (2017) point to several possible causes for this, such as suboptimal rheological properties of the GIA model, error in the ice loading history, other neo-tectonic processes or errors in the GNSS observations. The present work confirms the tendency of over-prediction of uplift along these coastal sites, even when using models with laterally varying Earth models, which could point towards the topic of ice loading history (see section 6.7).

The best 3D GIA model underpredicts GIA in Fennoscandia, most prominently in the centre of the former ice sheet. This is in accordance with van der Wal et al. (2013) and Li et al. (2018), who investigate 3D GIA models in Fennoscandia and find that the 3D GIA predictions are not large enough to match the observed uplift.

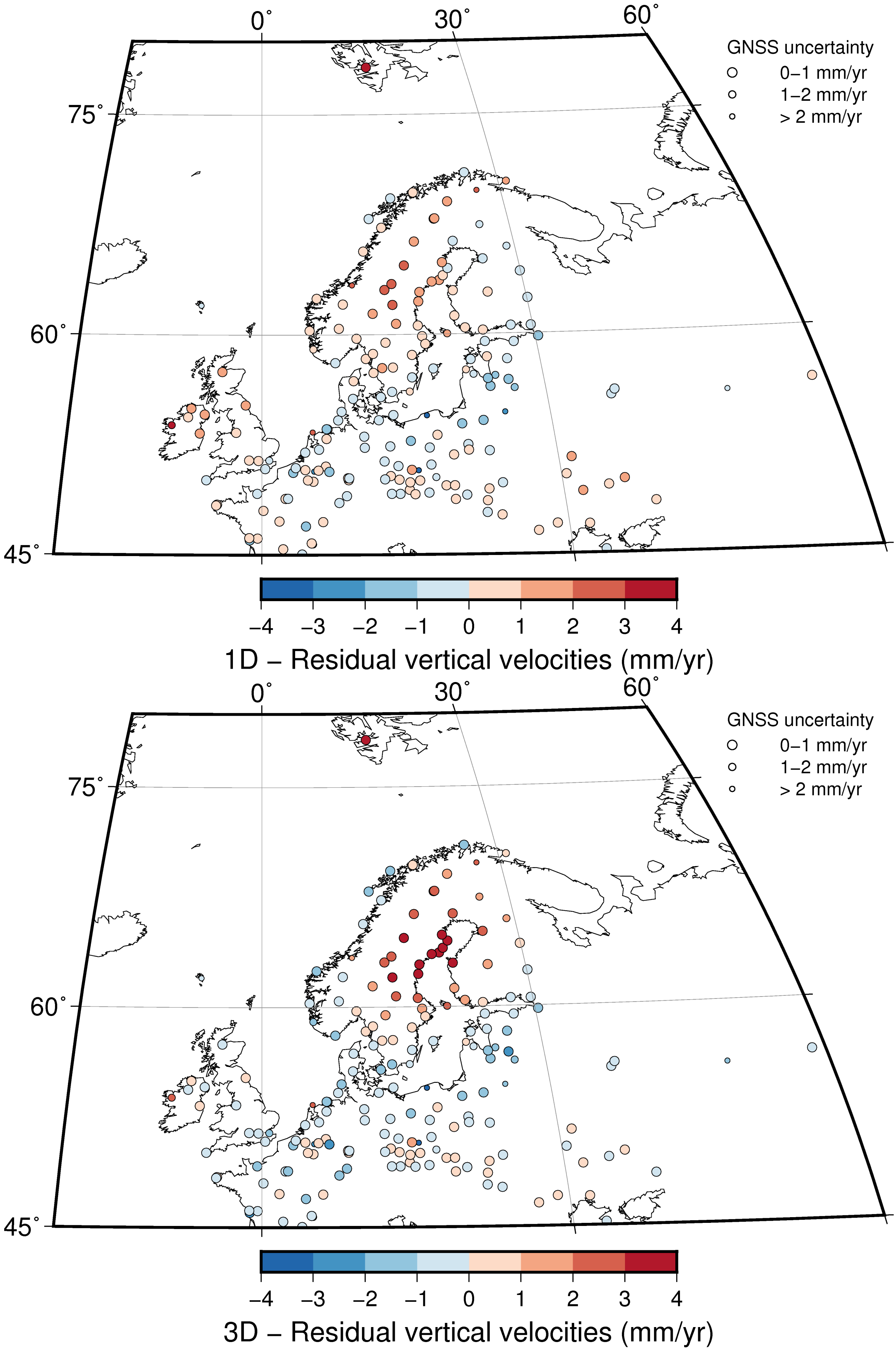

Figure 6.5: Residual vertical velocities at GNSS sites in Europe after removing the GIA signal using the best GIA model for Europe according to MADs in the vertical component: the best 1D GIA model (top) and the best 3D GIA model (bottom). The colourbar saturates at +4mm/yr with the largest residual uplift of 10 mm/yr on the west coast of the Gulf of Bothnia using the 3D GIA model.

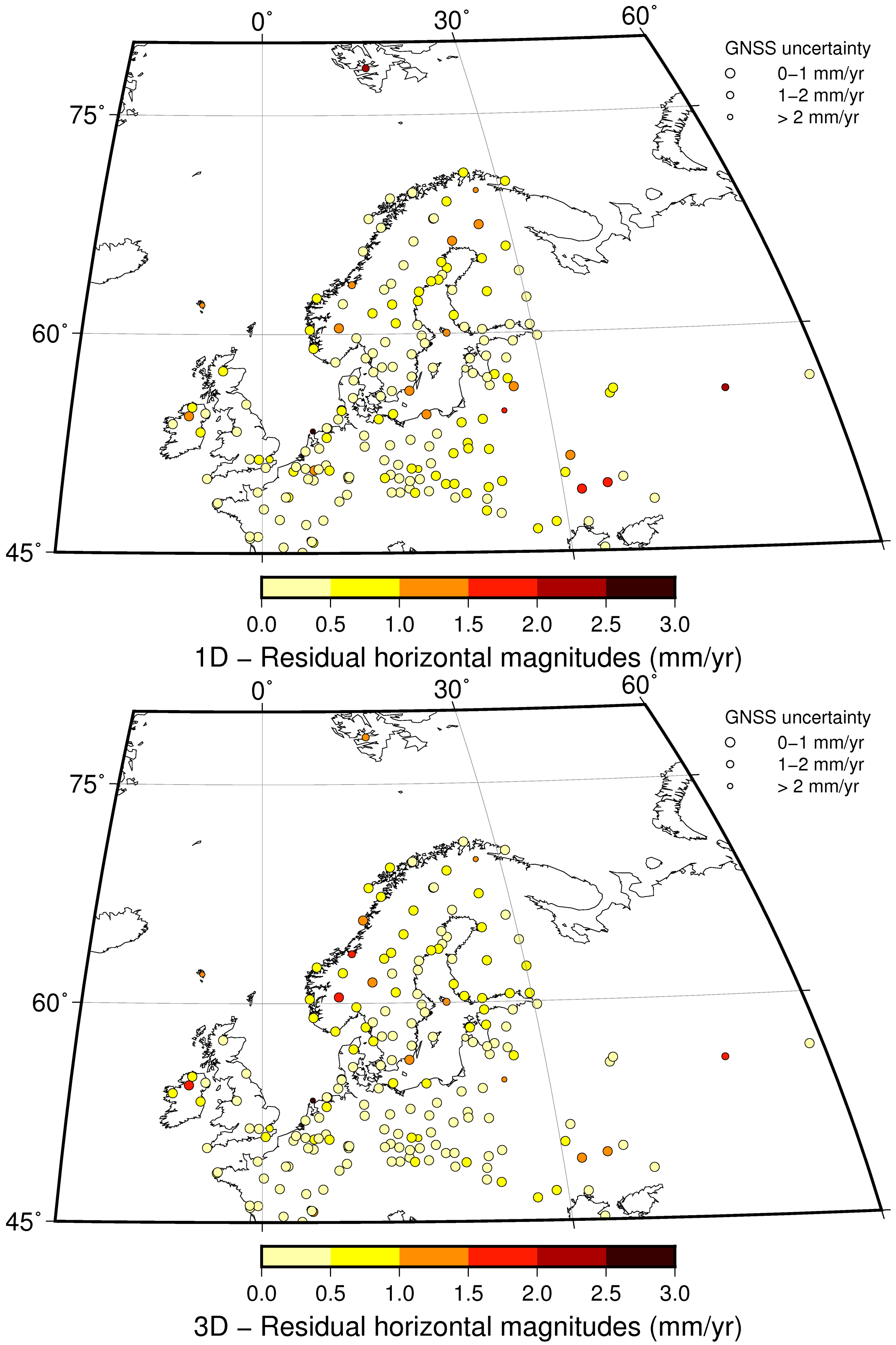

Figure 6.6: Magnitudes of the residual horizontal velocity field at GNSS sites after removing plate motion and GIA using the best GIA model for Europe according to MADs in the horizontal component: the best 1D GIA model (top) and the best 3D GIA model (bottom).

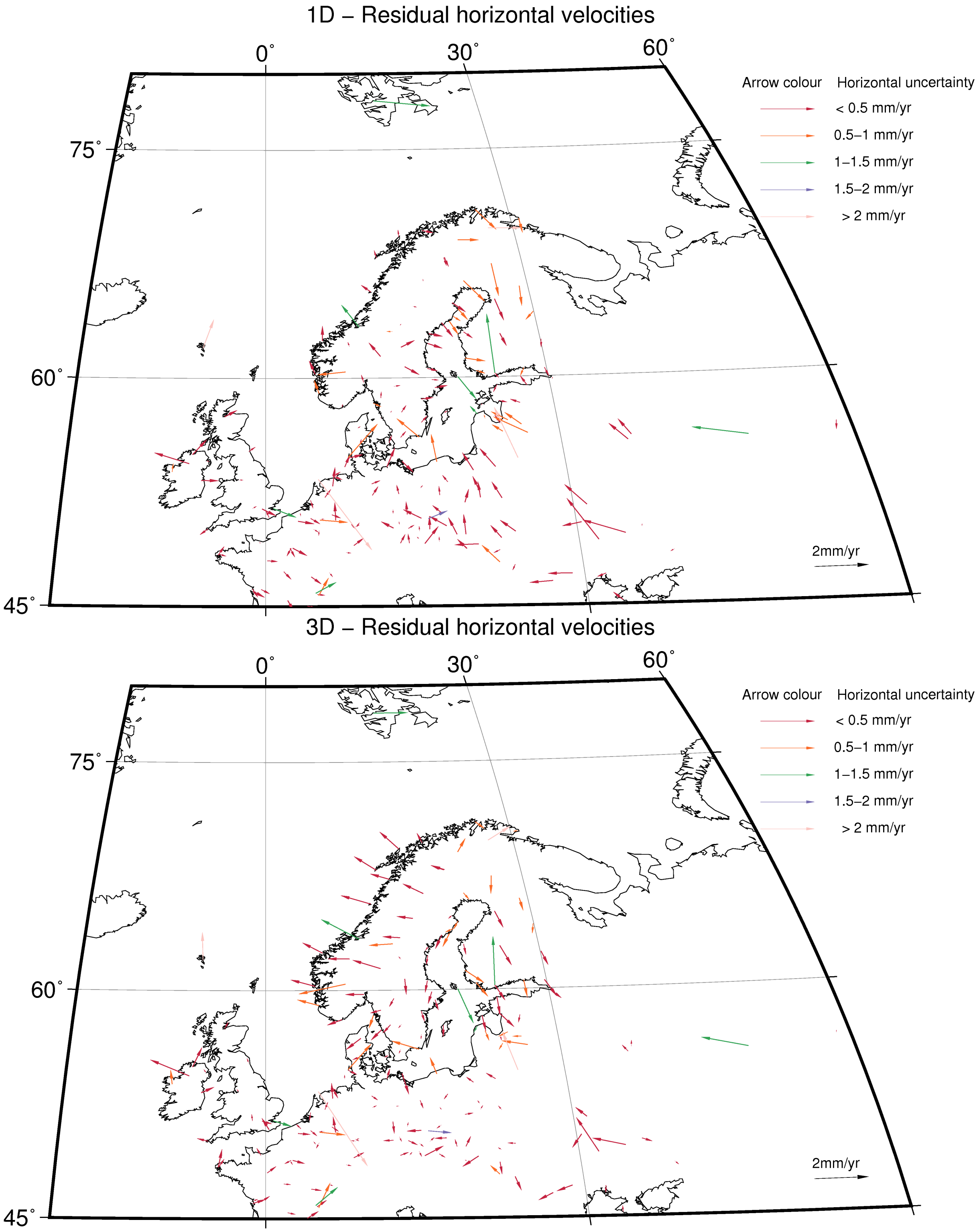

Figure 6.7: Residual horizontal velocity field at GNSS sites after removing plate motion and GIA using the best GIA model for Europe according to MADs in the horizontal component. The GNSS horizontal uncertainties are colour coded according to the legends: the best 1D GIA model (top) and the best 3D GIA model (bottom).

6.5 North America

6.5.1 Range of GIA model predictions North America

In Chapter 2, Fig. 2.8 shows the vertical GIA predictions in North America using the best 1D and the best 3D GIA model. With the best 1D model there are three distinct areas of maximum uplift around which the uplift rates reduce radially: one in the Canadian shield, SE of Great Slave Lake, another in the Laurentian Plateau SE of Hudson Bay and a third with lower uplift rates in the Northwestern Passages. Uplift rates reduce radially towards the centre of Hudson Bay. For the best 3D model, the uplift rates are lower than with the 1D model. There are again two centres of uplift, one to the NW and one to the SE of Hudson Bay. Both GIA models predict GIA uplift down to the Canadian-American border on the west coast of the continent and down to the Great Lakes on the East. South of this area, both models predict subsidence.

Fig. 6.8 shows the range of vertical GIA velocities in North America for the groups of near-best models in the vertical component, 6 1D GIA models and 16 3D GIA models. The grey shaded areas represent high tectonic strain regions where the GNSS sites are excluded since they are not considered suitable for testing GIA models.

The largest range in predictions in the group of 1D models is along the Northwestern passages and on the coast near Labrador sea where range reaches up to 5 mm/yr. The range is up to 3 mm/yr along Hudson Bay and reduces radially from it. Notably, the areas near or covering larger lakes show a bigger maximum range than surrounding areas, such as the region just south of Lake Winnipeg, the area of the Great Bear Lake in the NW of Canada and Lake Melville by the coast of Labrador Sea.

In the group of 3D models, the largest range is 4.5 mm/yr, over Lake Winnipeg and reducing radially. The range is mostly up to 3 mm/yr east of Hudson Bay and the rest of North America has a smaller range of mostly up to 2 mm/yr.

The range of the 3D models is smaller than the range of the 1D models, and their areas of the maximum ranges differ. South of 45°N, the maximum range is mostly up to 1 mm/yr with both groups of models, reaching larger values particularly west of the Rocky Mountains, at ∼45°N. For North America, the large vertical range, i.e. the uncertainties of GIA models in the vertical component, does not coincide exactly with the maximum uplift area, as it did for the near-best 1D models in Europe.

The northern parts of Canada have a sparse coverage of GNSS sites. Given that these areas show a large range, and are thus sensitive to the choice of modelling parameters, expanding the GNSS network in these areas is important for assessing GIA in North America.

In Chapter 2, Fig. 2.9 shows the horizontal GIA predictions in North America for the best 1D and the best 3D GIA model. Note the different scale, as the magnitudes predicted by the best 1D model are larger.

For the best 1D GIA model, the velocities below 45°N are ∼2 mm/yr and pointing North. The velocities are the smallest, up to 0.5 mm/yr, in the Laurentian plateau and around Lake Winnipeg from where they increase radially. The surrounding velocities are pointing outwards from the Laurentian plateau. They are pointing inwards around Lake Winnipeg with magnitudes up to 1 mm/yr. We find horizontal velocities of over 1.5 mm/yr surrounding Hudson Bay and in Labrador, as well as in the most northern regions.

The 3D model predicts very small magnitudes, up to 1-2 mm/yr, pointing mostly westwards and reaching maximum magnitudes of 0.8-1.0 mm/yr in the eastern part of Hudson Bay and NW Passages followed by the area surrounding it with magnitudes 0.5-0.8 mm/yr. The predicted horizontal GIA velocities are negligibly small south of 45°N.

Fig. 6.9 shows the range of horizontal magnitudes and Fig. 6.10 the range of directions of GIA velocity predictions in North America for the group of near-best models. There are 7 GIA models in the group of near-best 1D models in the horizontal component and 30 GIA models in the group of near-best 3D models according to the MAD fit criterion.

The range of near-best 1D models is up to 1.5 mm/yr with a part of Baffin Island in Northern Canada experiencing the maximum range up to 2 mm/yr. The 1D models generally show the highest uncertainty in the central part of the United States, spanning latitudes between 30°N-45°N. The highest uncertainty in direction (cf. Fig. 6.10) of horizontal velocities is however in the northern half of the continent. West of the Great Lakes and on the east coast, south of Nova Scotia, we find an area with high uncertainty in both direction and magnitude of GIA predictions. There is a similar situation in the northernmost part of Canada by the Northwestern Passages. The rest of the northern part of the continent shows smaller ranges of less than 1 mm/yr.

The range of the near-best 3D GIA models shows values up to 2 mm/yr towards the west coast, where the GNSS sites have been excluded due to high tectonic activity. The western half of the continent shows a larger uncertainty in GIA models of mostly 1.25-1.75 mm/yr, whereas the eastern half shows ranges of up to 1.25 mm/yr. Similar to the situation in Europe, the 3D models show a larger range in velocity directions than the 1D models. The range in velocity directions for the 3D models is over 270° for the most of the continent. The smallest range in directions is west of Lake Winnipeg and in the Laurentian Plateau, which is the area where the best 1D model predicts the smallest horizontal velocities.

Both groups of near-best models show different locations of the maximum and minimum ranges in the horizontal and the vertical component, similar to what was shown before for Europe.

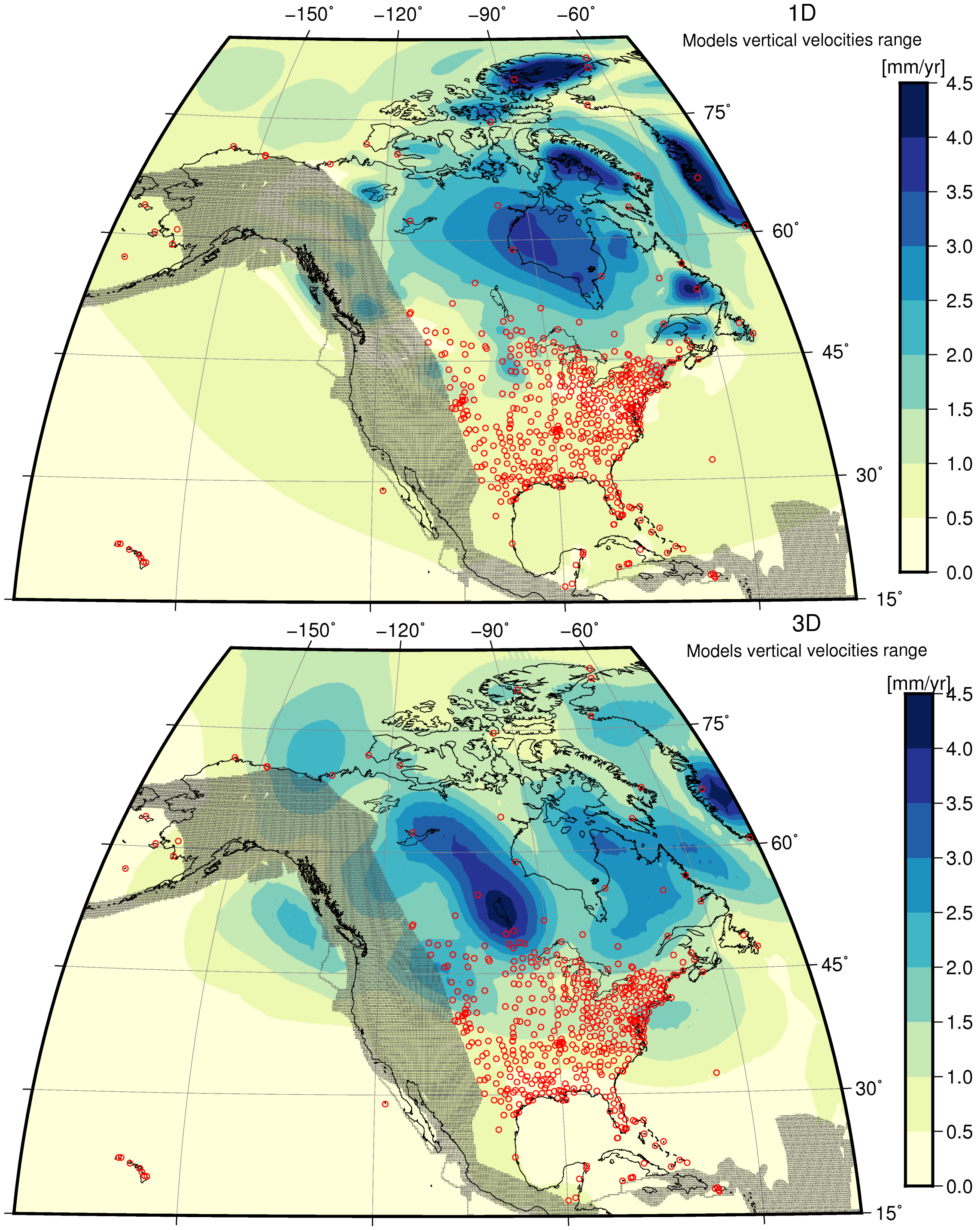

Figure 6.8: The maximum difference between vertical velocity predictions for models in the group of near-best 1D GIA models (top) and near-best 3D GIA models (bottom) for North America. Shaded area represents the high tectonic strain area where the GNSS sites have been disregarded. The circles represent the network GNSS sites.

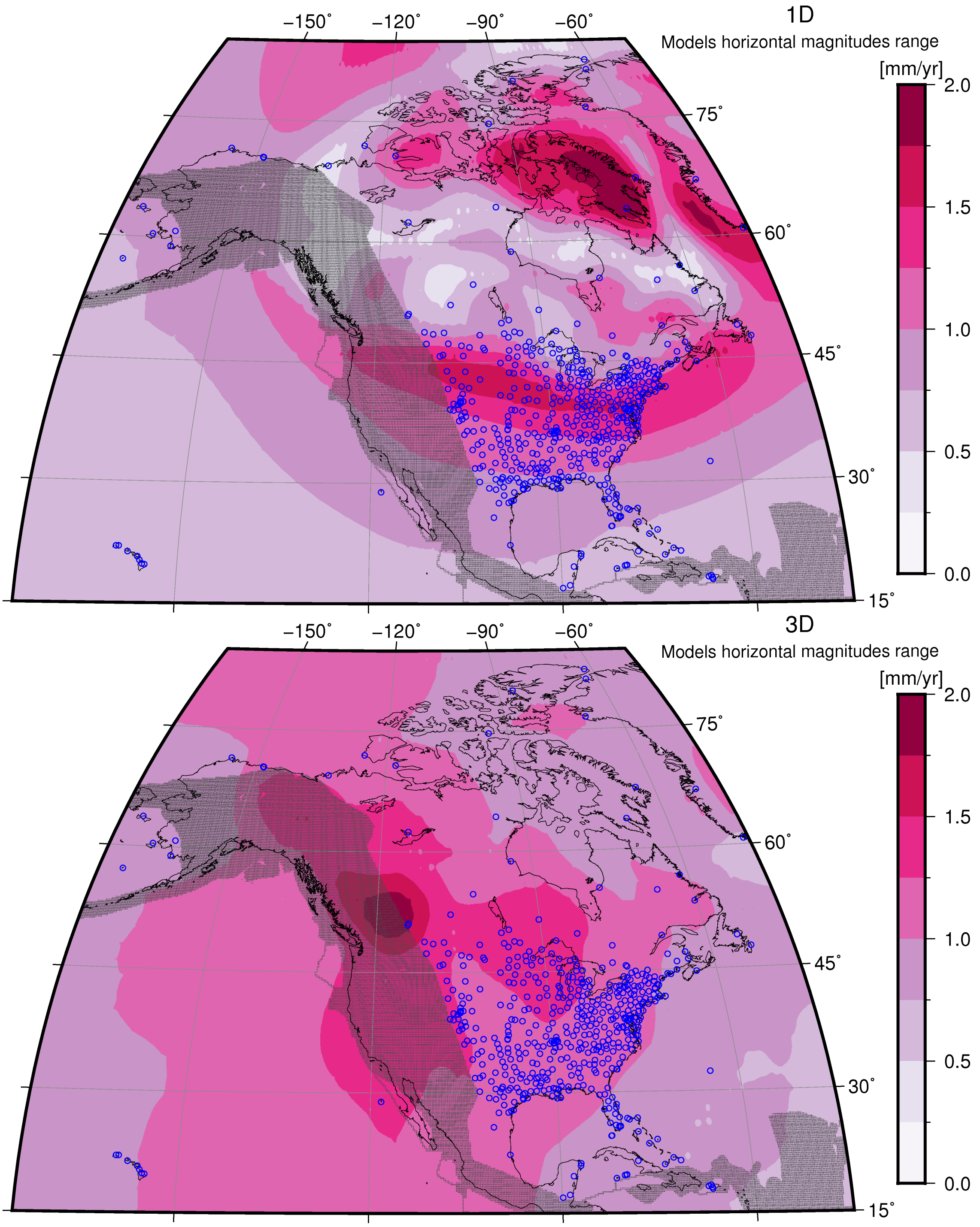

Figure 6.9: The maximum difference between horizontal magnitudes of GIA predictions for models in the group of near-best 1D GIA models (top) and near-best 3D GIA models (bottom) for North America. Shaded area represents the high tectonic strain area where the GNSS sites have been disregarded. The circles represent the network GNSS sites.

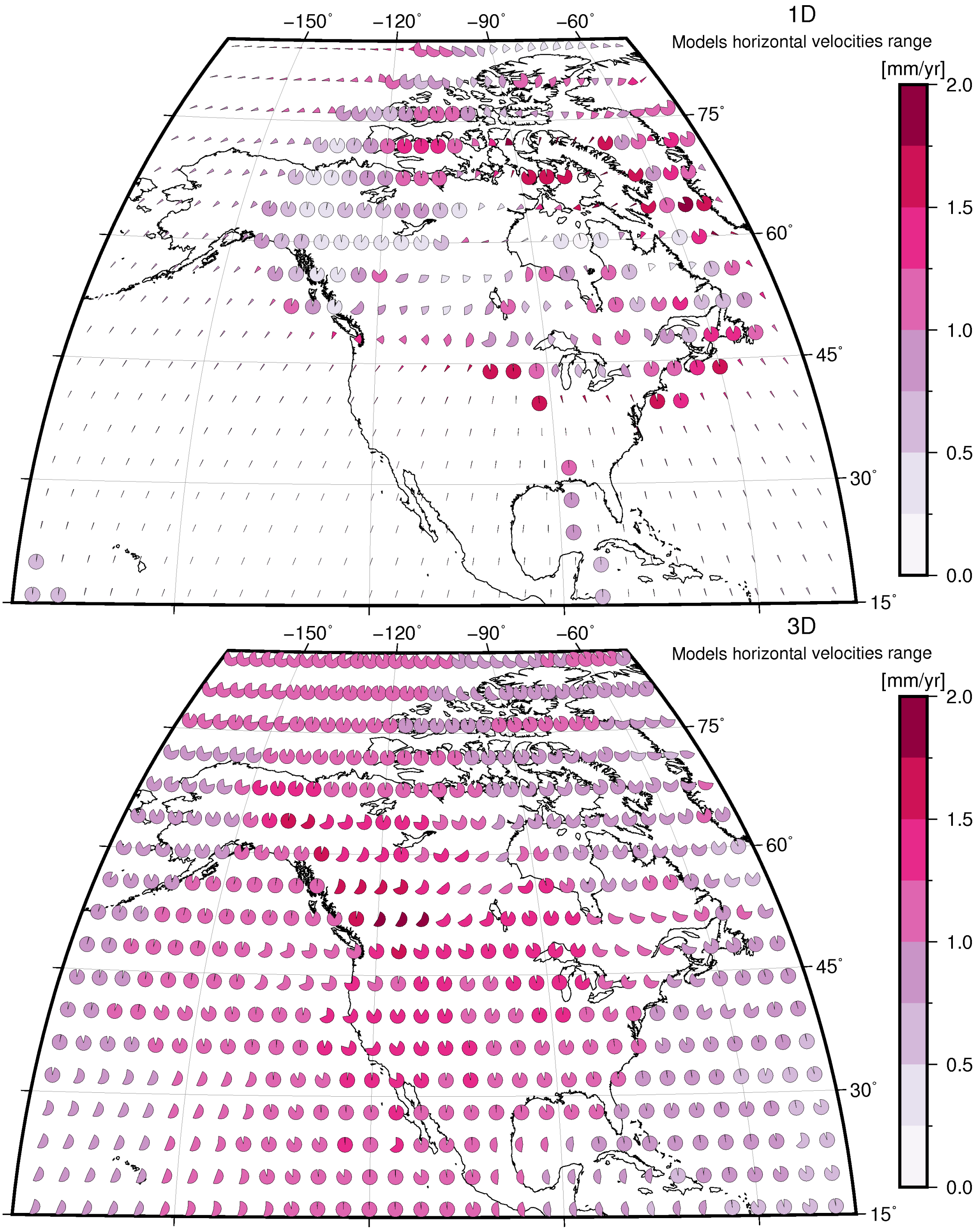

Figure 6.10: The maximum difference between magnitudes and azimuths of horizontal GIA predictions for models in the group of near-best 1D GIA models (top) and near-best 3D GIA models (bottom) for North America.

6.5.2 Residual velocity field North America

Vertical

In the vertical component, according to the MAD fit, the best 1D GIA model for North America is 6G_120p820 and the best 3D GIA model is 6G_SL_dry_10mm (cf. Tables 2.2 and 2.3). Fig. 6.11 shows the residual vertical velocity field in North America for the best 1D and 3D GIA model, as in Europe above. The uncertainties of the vertical GNSS velocity field in North America are up to 1 mm/yr for the majority of sites.

South of ∼45°N, both models show residuals mostly within ±1 mm/yr, with the 3D model showing more residual subsidence and the 1D model showing more residual uplift. The residuals are larger in the area of the Great Lakes, with residuals of up to -2.5 mm/yr for the best 1D model and up to -3.4 mm/yr for the best 3D model. For both models, the negative residual vertical velocities are the largest on the coast of and around the Gulf of Mexico, where they show a subsidence of over -4 mm/yr which is likely due to local effects (e.g. Wolstencroft et al. (2014), Kolker et al. (2011)).

Both of the best models underpredict GIA in the North of Canada and on the coast of Hudson Bay with residuals over 2 mm/yr, with maximum of 4 mm/yr on the west coast of Hudson Bay for the best 1D model and 6.5 mm/yr for the best 3D model on the east coast of Hudson Bay. On the Baffin Island east coast the 1D model residuals reach up to 5.4 mm/yr whereas the 3D residuals are smaller, up to 3.3 mm/yr. Hudson Bay and Baffin Island are however very sparsely covered with GNSS sites. Just north of the Great Lakes, the 1D model shows residuals of 0.2 to -1.2 mm/yr, and the 3D model shows residual uplift of 0.4 to 3.1 mm/yr. In Alaska, both models give small residuals of -1.6 to 0.6 mm/yr for the best 1D model and -2.0 to 0.2 mm/yr for the best 3D model.

Horizontal

In the horizontal component, the best 1D GIA model is 6G_120p810 and the best 3D GIA model is 5G_S_dry_4mm. Fig. 6.12 shows residual horizontal magnitudes for North America using the best 1D and 3D GIA model. The uncertainties are up to 0.5 mm/yr in the horizontal component for the majority of sites. Fig. 6.13 shows residual horizontal velocities at GNSS sites when using the best 1D and 3D GIA model. The horizontal GNSS uncertainties are expressed as colour variations of the velocity arrows. There is a small number of sites with large residual velocities which at the same time show small uncertainties. They are almost exclusively found in the Caribbean islands and around the Gulf of Mexico. The velocities in this area are large in the vertical component as well. The residual velocities in the Caribbean islands are over 3 mm/yr in the direction of NE for both GIA models. However, the Gulf of Mexico and the Caribbean islands are outside of the GIA affected area and the large residuals are likely due to local effects which are not within the scope of this study.

For the remaining sites south of 45°N, the residual magnitudes are well below 1 mm/yr, except in the Gulf of Mexico area which was an exception in the vertical component as well. North of 45°N, the residual magnitudes are mostly between 1-2 mm/yr with a number of sites with magnitudes up to 3 mm/yr. The 1D model gives ∼0.5 mm/yr smaller horizontal residual magnitudes than the 3D model in the most of North America, which is hardly significant given the horizontal GNSS uncertainty.

Along the Hudson Bay coast, the residual velocities are 1.3-1.6 mm/yr for the best 1D model and 0.4-1.0 mm/yr for the best 3D model, and pointing southwards. In NW Canada, for both models the residuals are pointing south with magnitudes of 1.4-2.3 mm/yr. In Newfoundland by the Labrador Sea, the 3D model gives residuals pointing North, and the 1D model West and SW. However, these areas have a very sparse density of sites so the mentioned values might not be significant.

For the 1D model in the United States east of the Rocky Mountains and west of 105°W, the residuals are pointing westwards, whereas between 105°W and the East Coast, residuals are pointing in various directions. Between them though there is an area without any GNSS sites. In Alaska we find the largest horizontal residuals of up to 4.9 mm/yr for the 1D model and up to 4.4 mm/yr for the 3D model.

6.5.3 North America summary

Unlike in Europe, where the best 1D GIA models for the vertical and horizontal components have different lithosphere thicknesses and η_{UM} , the best fitting 1D GIA models in North America in both components are the ones with ICE-6G ice model, 120 km lithosphere thickness and 0.8×10^{21} Pa s η_{UM} . As for η_{LM} , in the vertical component the best model prefers 20×10^{21} Pa s and in the horizontal component a smaller 10×10^{21} Pa s.

In the vertical component, both the best 1D model and the best 3D model underpredict GIA in the north of Canada and on the coast of Hudson Bay, albeit less for the 1D model. The reason for underpredictions may be linked to the way the best model is chosen, as the best models are chosen according to the MAD of all the sites in the considered region. In North America, there is a high density of sites in central United States, and rather sparse density of sites in the northern parts of the continent. Consequently, the best model fit could be biased towards the area with more GNSS sites, resulting in less weight put on, e.g., the area of observed maximum uplift rates around Hudson Bay. A possibility to overcome this could be to weight the GNSS sites by area when computing the MAD.

In the horizontal component, larger magnitudes of the residuals are observed in certain areas due to, e.g., GIA model imperfections or other geophysical processes, where the differences in residual magnitudes between the best 1D model and the best 3D model are close to 1 mm/yr. There is a tendency for smaller horizontal residuals with the best 3D model around Hudson Bay and east of the Rocky Mountains, and a tendency for smaller horizontal residuals with the best 1D model around the Great Lakes. However, the differences in residual magnitudes between the best 1D and best 3D models remain insignificant for the rest of the continent.

The large range of directions of GIA horizontal velocities within the group of near-best 3D models may indicate high uncertainty of the 3D Earth models in North America when predicting horizontal motion. However, there are 30 models in this group, which comprises 83% of all 3D GIA models, so it might be that the MAD criterion fit for choosing the near-best group needs to be stricter in North America.

Sella et al. (2007) performed one of the first validations of GIA models in both horizontal and vertical component for North America using the then available GIA models. They were able to find mantle viscosities that fit the vertical data well, but they were not able to find viscosities that simultaneously fit all the horizontal data well. In particular, they find that the GIA models with larger upper mantle viscosities (10^{21} Pa s) show horizontal velocities over most of the USA pointing radially inwards towards the former ice sheets, which is not seen in their observed velocity field nor in the observed velocity field in this project (cf. Fig. C.2). The best 1D GIA model selected here (6G_120p810) shows larger upper mantle viscosity and the velocities are pointing inwards towards the former ice sheets (Fig. 2.9). Looking at the MAD fits (Figures in Appendix D), both 1D and 3D models show better MAD fits with higher viscosities (for example best 3D GIA model, 5G_S_dry_4mm, averaged viscosity on land in North America 6.9 $\times 10^{21}$ Pa s).

Ding et al. (2019) compared vertical and horizontal GNSS velocities in eastern United States to GIA models, and estimated rigid plate motion for North America using the GNSS velocities as well as the GNSS velocities from which GIA had been removed, similar to what was done here. They used GIA predictions from ICE6G_D VM5a (Peltier et al., 2015, 2018). Besides their solution being regional, their approach differs to the present one also regarding the GNSS time series, which they obtained using precise point positioning, whereas the ones here are network solutions. The residual vertical velocities from Ding et al. (2019) for eastern United States show a general agreement with the ones obtained in this thesis for the best 1D and 3D GIA models, although more with the best 1D GIA model. Their residual horizontal velocities are small and pointing in various directions. In this thesis, the residual horizontal velocities with both best models in eastern United States are also small (below 1 mm/yr) and pointing in various directions, but do not agree with the ones from Ding et al. (2019). A more detailed comparison of the directions is not considered reasonable, given the uncertainty of GNSS and the small magnitudes of residual horizontal velocities, as well as a different method of estimating rigid plate motion.

The results from the work mentioned above, as well as those of Kreemer et al. (2018) and the ones obtained here, all agree that there is intraplate deformation over the North America plate. In Chapter 5, the range of Euler vectors depending on the GIA models is shown. Further, Figs. 6.10 and 2.9 show the GIA velocities from the best GIA models, which are a significant contribution to the intraplate deformation.

A large range in GIA predictions in the northern parts of the continent confirms that there is a need for more GNSS sites to better constrain GIA.

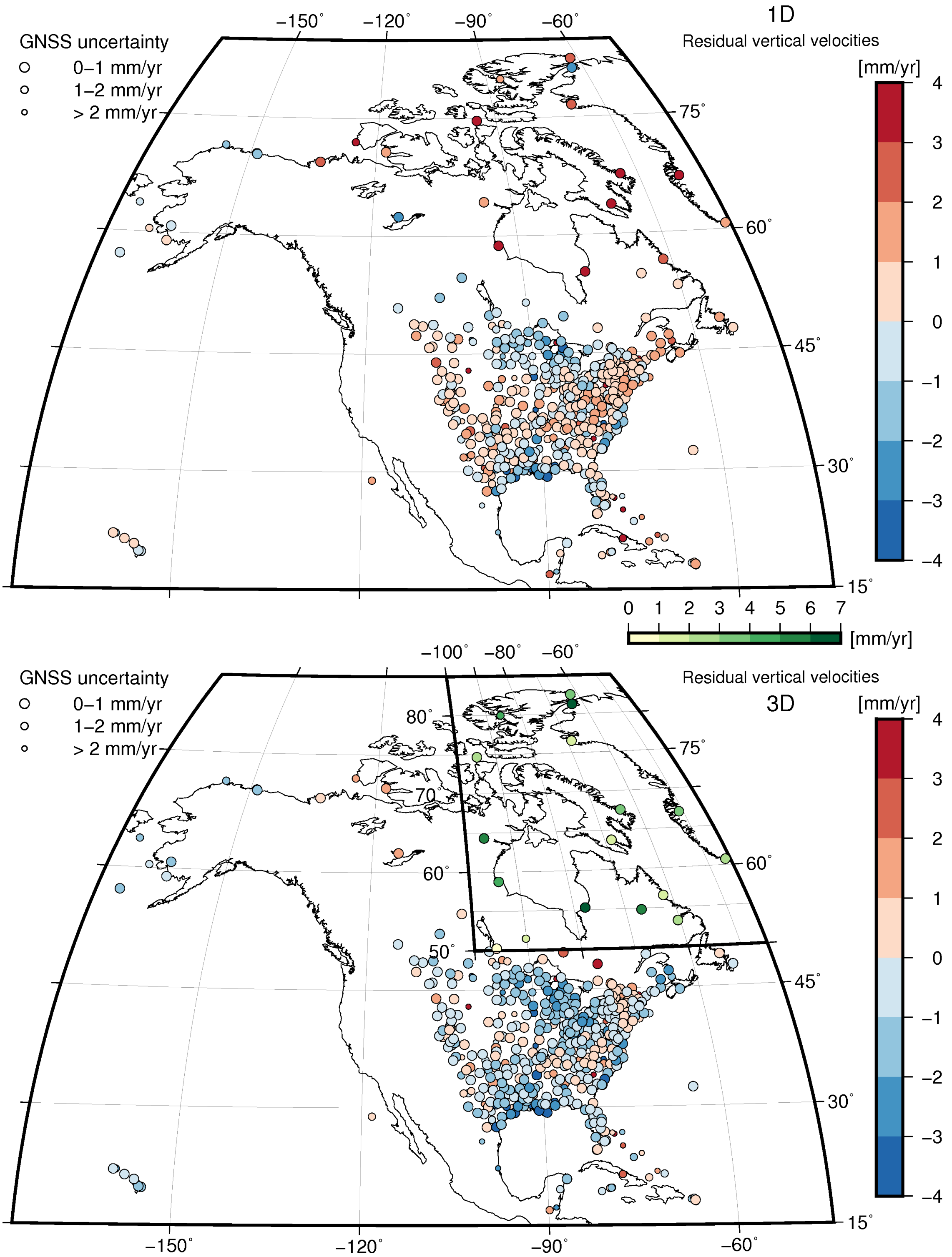

Figure 6.11: Vertical velocities in North America at GNSS sites after removing GIA using the best GIA model for North America according to MADs in the vertical component: the best 1D GIA model (top) and the best 3D GIA model (bottom). The colourbar saturates at 4.5 mm/yr.

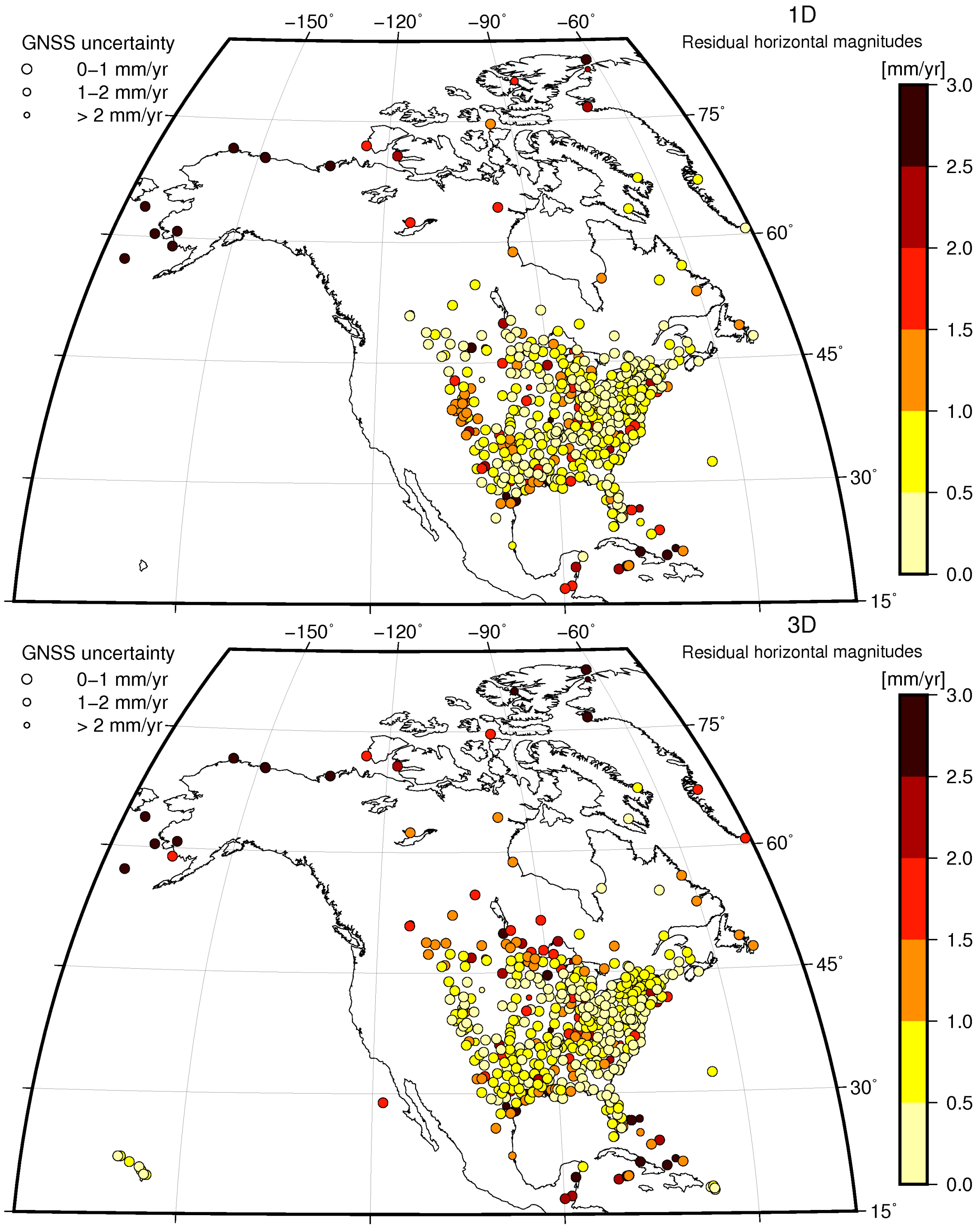

Figure 6.12: Magnitudes of residual horizontal velocity field at GNSS sites after removing plate motion and GIA using corrections from the best GIA model for North America according to MADs in horizontal sense. Best 1D GIA model (top) and best 3D GIA model (bottom)

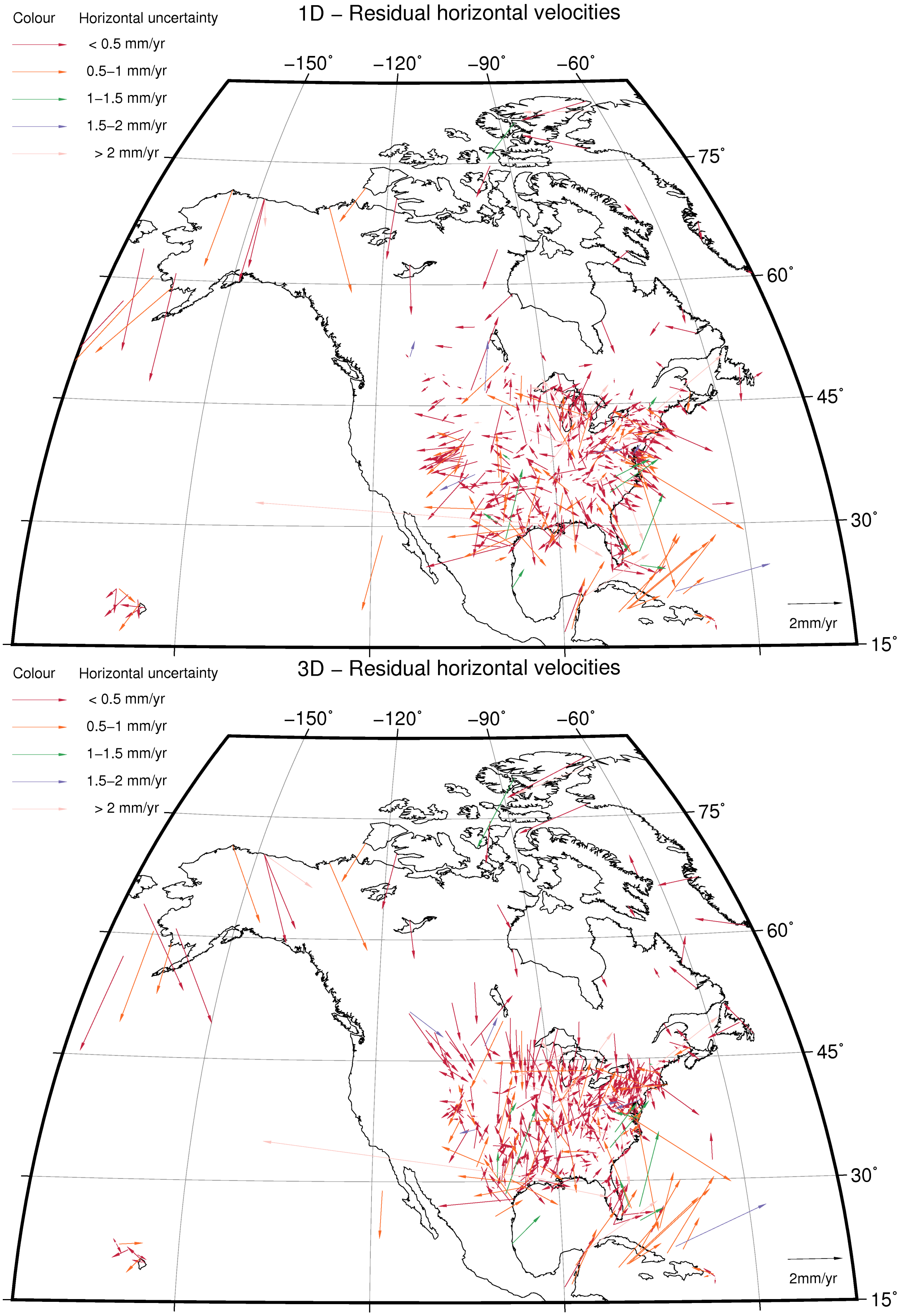

Figure 6.13: Residual horizontal velocity field at GNSS sites after removing plate motion and GIA using corrections from the best GIA model for North America according to MADs in horizontal sense. Best 1D GIA model (top) and best 3D GIA model (bottom)

6.6 Antarctica

Antarctica is, unlike the other two of the selected regions of interest, still covered with ice sheets at present. Thus, the residual velocity field was corrected for the elastic rebound due to present-day ice mass changes (e.g. Bevis et al. (2009); Thomas et al. (2011); Whitehouse (2018); Schumacher et al. (2018)). The corrections were applied in both the horizontal and the vertical component. The corrections were provided by A. Koulali (personal communication, 2020). They were determined closely following Shepherd et al. (2019). The approach exploits ice sheet surface elevation changes as determined from multi-mission satellite altimetry, where the elevation changes due to mass fluctuations of the ice sheet are isolated from the altimetry observations by correcting for a firn densification model and adding the surface mass balance anomaly output from a regional climate model, giving an overall ice sheet mass trend. In turn, the present-day elastic rebound was computed using the ice sheet mass trends using the Regional ElAstic Rebound (REAR) calculator (Melini et al., 2014).

The elastic deformation due to present-day ice mass changes at the Antarctic GNSS sites is shown in Fig. 6.14 and listed in Table E.6. The vertical elastic deformation is mostly positive, with negative rates along the East Antarctica coast only. The vertical elastic deformation is the largest in Marie Byrd Land, 3.0-9.3 mm/yr (note the alternative colour palette in Fig. 6.14). The horizontal elastic deformation is also the largest in West Antarctica, around Marie Byrd Land, and negligibly small in the rest of Antarctica.

6.6.1 Range of GIA model predictions Antarctica

In Antarctica in the vertical component none of the 1D GIA models give a better MAD fit than the null-GIA case and thus no group of near-best 1D GIA models in the vertical component was formed. However, the selected group of 3D GIA models do improve the vertical MAD fit. Fig. 6.15 shows the range of predictions of four near-best 3D GIA models in the vertical component in Antarctica. The group of near-best 3D GIA models shows the largest uncertainties in vertical predictions across the Ronne Ice Shelf, $\sim$4 mm/yr. The other two areas with large uncertainties are near Coats Land and east of Ross Ice Shelf with the range of GIA predictions of up to 3.5 mm/yr and 3 mm/yr, respectively. The three areas with large ranges have the maximum range in the centre of the area, reducing radially from the centre points. The range is below 0.5 mm/yr along the coast of East Antartica, and up to 1 mm/yr on the Antarctic peninsula.

Most of Antarctica is not sampled by GNSS, due to its inaccessibility and being covered in ice without access to stable bedrock. The maximum range for the 3D models is in an area with almost no GNSS coverage which means that the models are poorly constrained

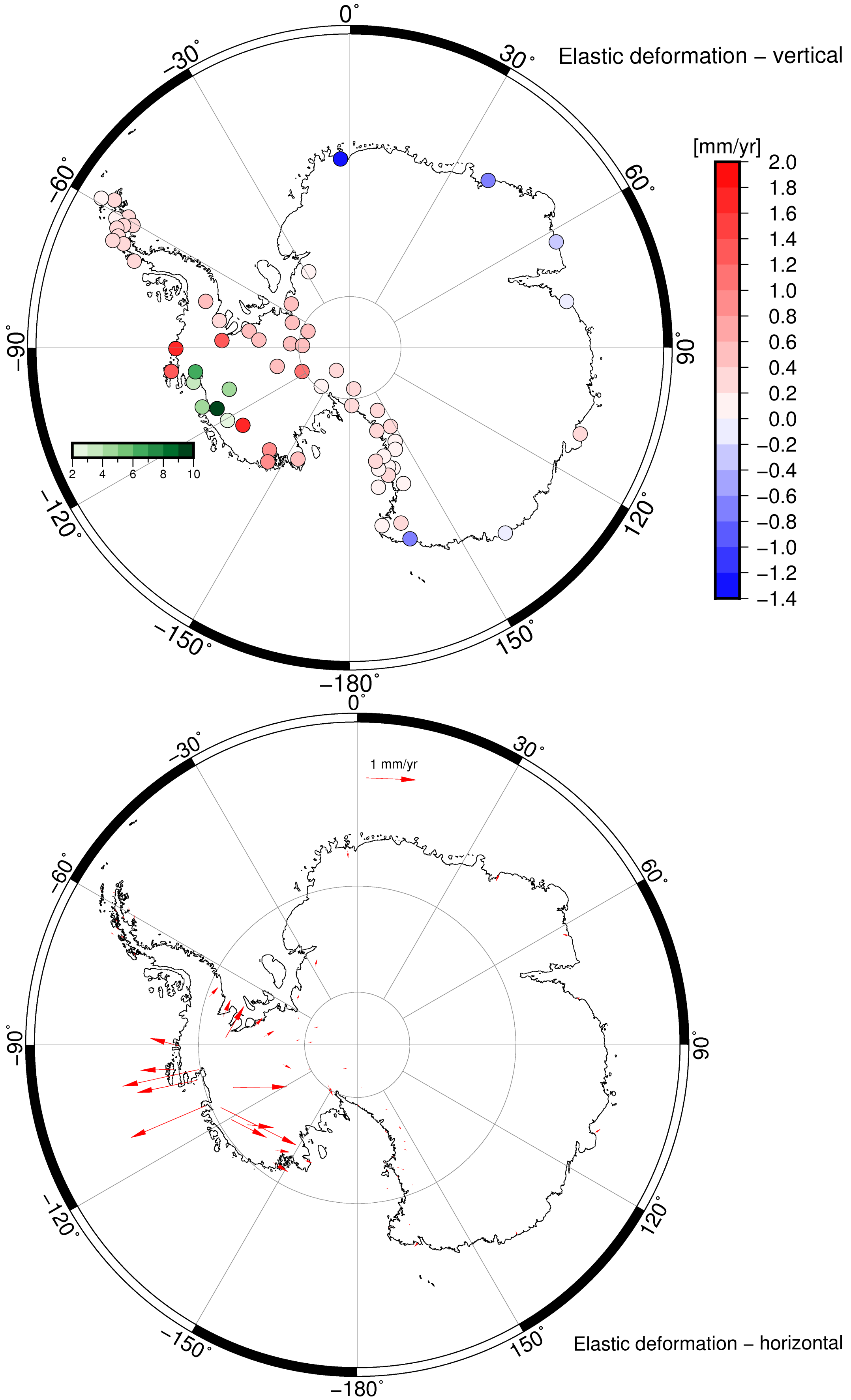

Figure 6.14: Vertical (top) and horizontal (bottom) elastic rebound due to present-day ice mass changes at GNSS sites in Antarctica.

by GNSS data there.

In Chapter 2, Figure 2.10 shows the vertical GIA predictions in Antarctica using the best 3D GIA model. It also shows the 1D GIA model that is the best fitting compared to the other 1D GIA models. The vertical velocities with the 1D model reach up to 6.7 mm/yr of uplift and -1.5 mm/yr of subsidence. The maximum uplift with the 1D model is in West Antarctica, near the Ronne Ice Shelf and East of the Ross Ice Shelf. The 1D model predicts subsidence up to 2 mm/yr in parts of East Antarctica. For the best 3D model, the predicted velocities are much smaller than with the best 1D model, reaching from -1 mm/yr to 2 mm/yr. Most of the continent shows GIA uplift of 0-1 mm/yr with the best 3D model, besides a few areas in West Antarctica. The two models also differ in the ice model, the best fitting 1D GIA model is a combination of a 1D Earth model with ICE-6G, and the best 3D GIA model is a combination of a 3D Earth model with ICE-5G. The best 3D model has wet rheology and 1 mm grain size which translates into very low viscosities (cf. 2.2.6). This could explain why there is very little ongoing GIA deformation, the rebound has decayed (see Fig. 2.4).

Fig. 6.16 shows the range in horizontal magnitudes of GIA predictions for the group of near-best models in the horizontal component in Antarctica. The groups of 1D and 3D near-best models contain six models each. The range is up to ~1.2 mm/yr for the 1D models and up to ~1.4 mm/yr for the 3D models.

The 1D models range is the largest in West Antarctica in the coastal area near Pine Island Glacier and in the Weddell Sea. The 3D models range is the largest south of Ronne Ice Shelf and on the coast east of Ross Ice Shelf. These areas have more GNSS sites coverage compared to the areas with large ranges in the vertical component of GIA models. In most of Antarctica, the uncertainty of GIA model horizontal magnitudes is of the same order of magnitude as the horizontal uncertainty of the GNSS velocities (or rather the combined uncertainty of the elastic component and GNSS).

Unlike in the vertical component, correcting for GIA in Antarctica in the horizontal component with both a group of 1D and 3D GIA models does reduce the MAD. In Chapter 2, Fig. 2.11 shows the horizontal GIA predictions in Antarctica using the best 3D GIA model and the best 1D GIA model. For the best 1D model, the largest horizontal magnitudes are up to 2.0-2.4 mm/yr in West Antarctica south of Marie Byrd Land. The magnitudes of horizontal velocities in the Antarctic peninsula are ~0.0-0.8 mm/yr and in East Antarctica 0.8-1.8 mm/yr. For the best 3D model, the magnitudes of horizontal velocity predictions are smaller than with the 1D model. They are larger in West Antarctica than in East Antarctica, reaching up to 1 mm/yr in West Antarctica and ~0.3-0.8 mm/yr in East Antarctica. The directions of the velocities for the best 1D and the best 3D model differ the most between 90°W and ±180° longitude. These two GIA models have the ice model in common, both are based on ICE-6G.

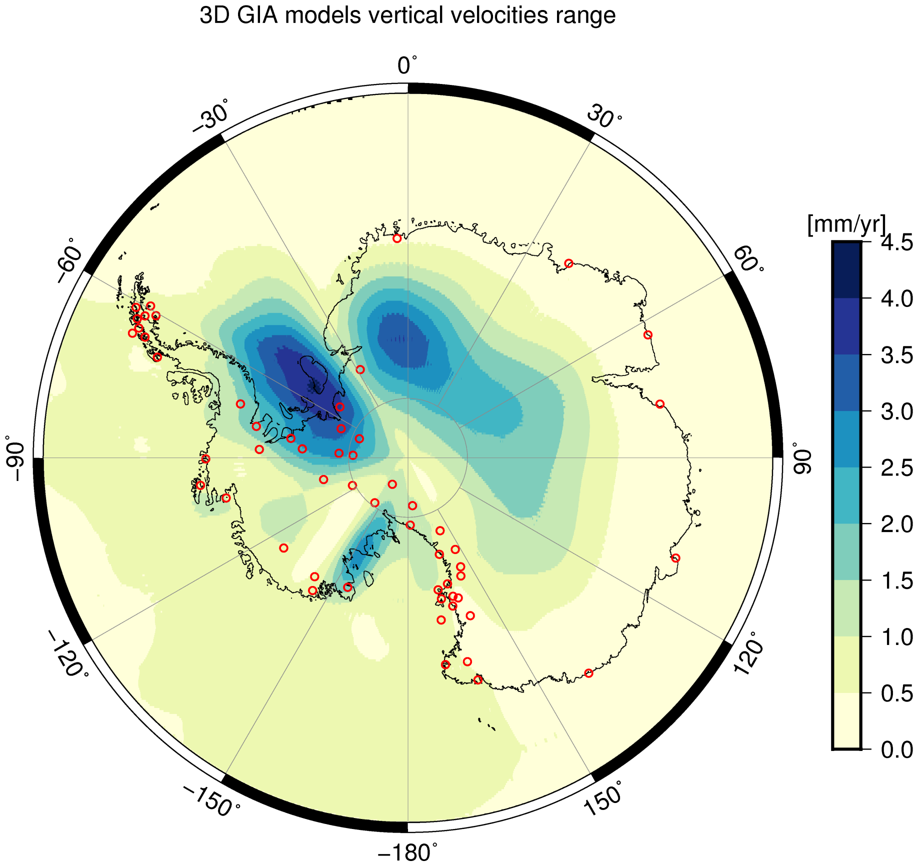

Figure 6.15: The maximum difference between vertical velocity predictions for models in the group of near-best 3D GIA models for Antarctica. The circles represent the GNSS sites.

Fig. 6.17 shows the range of directions of horizontal velocities for the groups of near-best models in Antarctica. Among the 1D models, the directions of the velocities in East Antarctica do not differ significantly. The range of directions is larger in West Antarctica, with the largest along the coast of Amundsen Sea, as well as on the Ronne Ice Shelf. As for Europe and North America, the 3D models show much larger range in directions than the near-best 1D models. In certain areas of East Antarctica and around the Ross Ice Shelf, the range of azimuths is well over 180°. Therefore, the group of near-best 3D GIA models has larger uncertainty in both magnitude and directions of horizontal GIA predictions when compared with the near-best 1D GIA models. It is worth noting that the GIA predictions magnitudes of the 3D GIA models in the near-best group are smaller than those of the 1D GIA models near-best group. Among the group of near-best 1D models, all of them are based on ICE-6G, whereas among the near-best 3D models, they are based on ICE-6G (4 models) and W12 (2 models).

Because of the uncertainty associated with correcting for the elastic component due to present-day ice melting, I also performed the analysis of MAD fits without correcting for it. Without removing the elastic component, the MAD for the null-GIA case and for the GIA models was lower in all cases except for the vertical component when using 3D GIA models. Without removing the elastic correction, the group of near-best 3D models in the vertical component in Antarctica includes 13 GIA models and the uncertainty is up to 6 mm/yr. For the 1D GIA models, similar to when the elastic component is removed, none of the models show a better fit in the vertical component than the null-GIA case. In the horizontal component, applying the elastic correction increases the number of models in the near-best groups (without elastic correction near-best horizontal 1D models - 5, 3D models - 4). It is worth mentioning that the Antarctic velocities corrected for the elastic component are a part of the global MAD estimate, where the MAD has only slightly (<0.05 mm/yr) increased compared to not applying the correction in Antarctica.

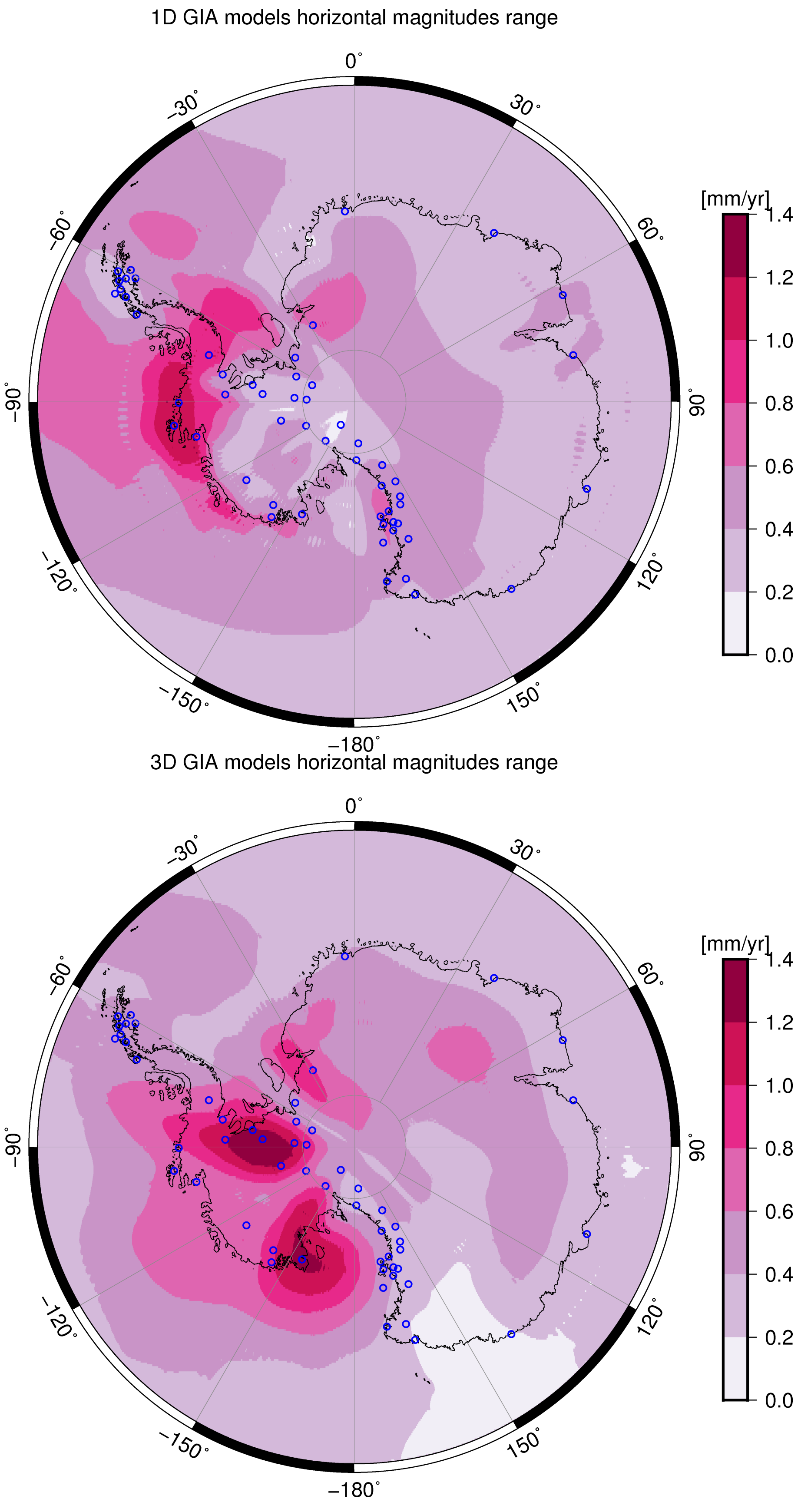

Figure 6.16: The maximum difference between horizontal magnitudes of GIA predictions for models in the group of best 1D GIA models (top) and best 3D GIA models (bottom) for Antarctica.

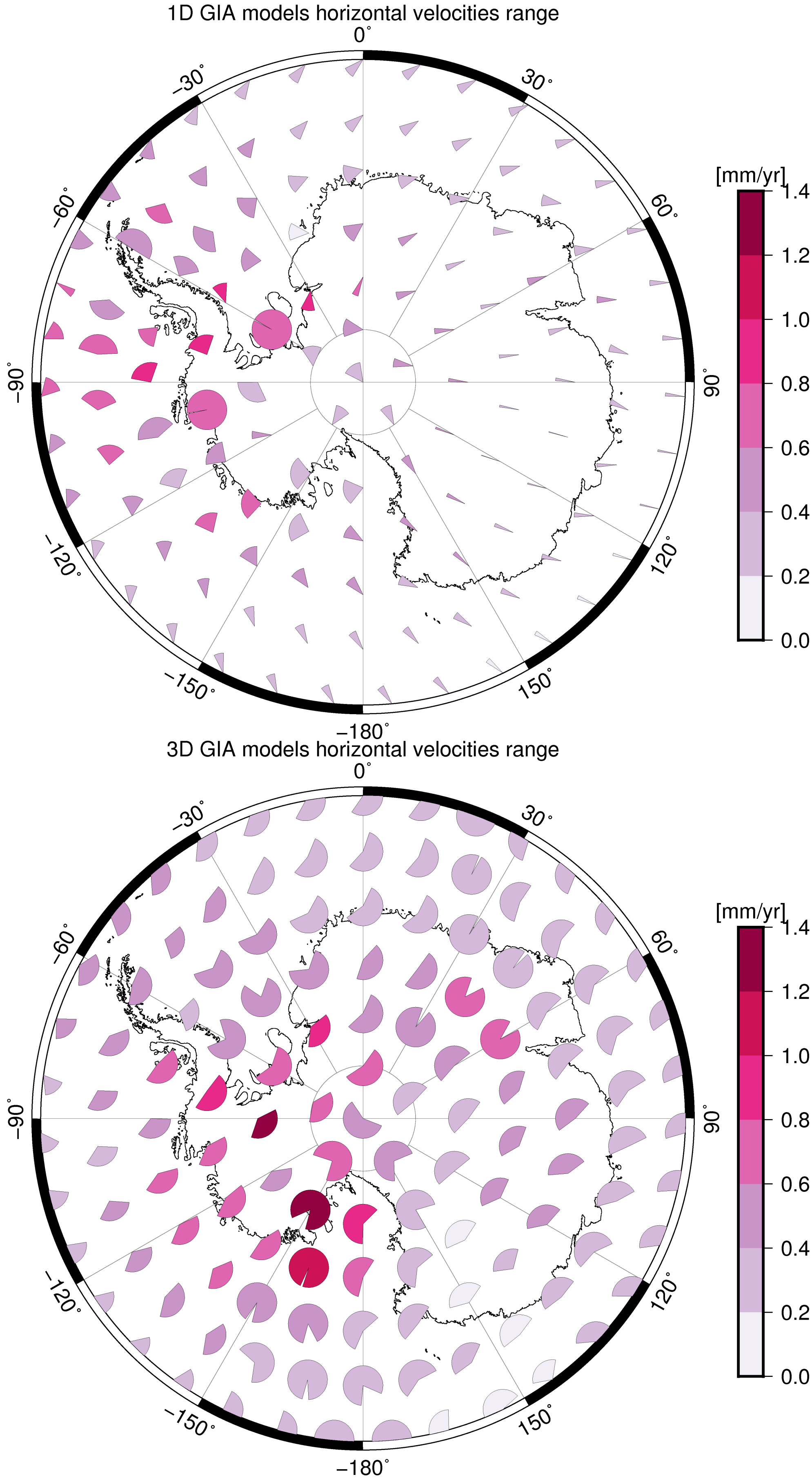

Figure 6.17: The maximum difference between magnitudes and azimuths of horizontal GIA predictions for models in the group of near-best 1D GIA models (top) and near-best 3D GIA models (bottom) for Antarctica.

6.6.2 Residual velocity field Antarctica

Vertical

The residuals in Antarctica are larger than in other regions, as shown in Figs. 6.18 and 6.19, which prompts different colour palettes than in the other regions. The best 1D GIA model in the vertical component for Antarctica, which is still a poorer fit than the null-GIA case, is 6G_120p320. The best 3D GIA model in the vertical component is 5G_S_wet_1mm. Fig. 6.18 shows the residual vertical velocity field with these two GIA models. The uncertainty of the vertical GNSS velocities is larger in Antarctica than in the other two observed regions. Note that the uncertainty as represented by symbol size is the combined uncertainty of the GNSS velocity and the elastic deformation component.

Using the 1D model, the residuals are mostly negative, apart from along the tip of the Antarctic Peninsula where the residuals are mostly positive and between 0.0-7.8 mm/yr (one site with high uncertainty 9.7 mm/yr). There are two sites with negative residuals -0.3 to -0.8 mm/yr near the tip of the peninsula. In the rest of West Antarctica, the residuals are between -8.2 and 1.7 mm/yr. The smallest residuals can be found along the coast of East Antarctica, -0.9 to 0.7 mm/yr. The residuals are small also in Victoria Land off the Ross Sea coast, -1.8 to +0.3. This area shows the smallest GNSS velocity uncertainties in all of Antarctica. The larger residuals indicate that the 1D GIA model is not predicting strong enough GIA uplift in the Antarctic peninsula and predicting too much GIA uplift or too little GIA subsidence in the rest of Antarctica. However, the large negative residuals could also be due to the error in the correction for present-day ice melting.

With the best 3D model, there are both positive and negative residuals over the entire continent. In the Antarctic peninsula, the best 3D model shows only positive residual velocities of 0.7-9.2 mm/yr (one site with high uncertainty 11.1 mm/yr). The residuals are significantly smaller in East Antarctica than in West Antarctica, being the smallest in Victoria Land off the coast of Ross Sea, between -0.6 and 1 mm/yr. This area shows smaller residuals with the 3D GIA model than with the 1D GIA model. The east coast of Antarctica shows residuals of -0.1 to 1.8 mm/yr. Both the 1D and the 3D model give a large residual of 6.2 mm/yr and 11.0 mm/yr, respectively, at the “BACK” site on the coast of the Amundsen Sea. The positive residuals with both models along the tip of the Antarctic peninsula are likely to be because of recent ice loss from the last few decades that has triggered viscoelastic rebound (Nield et al., 2014), which is not accounted for in the GIA models, and not removed by the elastic correction.

Horizontal

The best 1D GIA model in the horizontal component for Antarctica is 6G_71p85 and the best 3D GIA model in the horizontal component is 6G_S_dry_4mm. Fig. 6.19 shows residual horizontal magnitudes in Antarctica for the best 1D and 3D GIA model and Fig. 6.20 shows residual horizontal velocity vectors for the best 1D and 3D GIA model. The 1D and 3D models residual magnitudes generally agree in the horizontal component, showing values mostly below 1 mm/yr in East Antarctica and up to 4.1 mm/yr in West Antarctica. Around 80°S, some sites show significantly larger residual magnitudes with the 3D model and some with the 1D model. Both models show the largest residuals at the tip of the Antarctic peninsula and on the coast by the Amundsen Sea.

Among the residuals at the tip of the Antarctic peninsula (0.5-4.0 mm/yr), the larger residuals also have larger horizontal GNSS uncertainties, and these sites are moving in the same direction for both the 1D and the 3D model. The directions of the residual velocities are similar considering their magnitudes and GNSS velocity uncertainties.

Along the Transantarctic Mountains, on the Ross Sea coast, we find the smallest horizontal GNSS uncertainties in Antarctica but also the smallest residuals, with magnitudes of mostly up to 0.6 mm/yr and 0.4 mm/yr for the best 1D and 3D model, respectively. There is a tendency that in this area, the residuals are slightly smaller with the best 3D model. The best 3D model GIA horizontal predictions (6G_S_dry_4mm, Fig. 2.11), shows horizontal velocities pointing towards the Ross Sea, opposite of the best 1D model (6G_71p85, Fig. 2.11) and the expected direction (which is outwards from the centre of the LGM ice sheet). However, as mentioned, Hermans et al. (2018) find that the direction of the horizontal GIA velocities may point inward or outward of the previously glaciated region, depending on the mantle viscosity.

6.6.3 Antarctica summary

In the vertical component, none of the 1D GIA models improves the MAD as compared to the null-GIA case, whereas the near-best 3D GIA models do. This can indicate that none of the 1D GIA models are well suited for Antarctica.

The best model among the 1D models exhibits relatively low η_{UM} of 0.3 $\times 10^{21}$Pa s and relatively high η_{LM} of 20×10^{21}Pa s with the thickest lithosphere among those tested here, 120 km. In the vertical component among the 3D GIA models there is a preference for wet rheology and 1 mm grain size (cf. Tables 6.1, E.4 and Fig. D.15), which leads to very low viscosities. These low viscosities are lower than the low viscosities found by Nield et al. (2014) and Barletta et al. (2018). However, both of these studies concentrate on smaller Antarctic regions (Antarctic peninsula and West Antarctic Ice Sheet, respectively), whereas the present project computes the model fit based on the whole of Antarctica, and the sparsity of GNSS data coverage in East Antarctica leads to a large spread of well-fitting viscosities. Thus, if the present project would compute the model fit based on smaller regions in western Antarctica, one cannot rule out the possibility that a different model could be identified as the best model, with viscosities in better agreement with the previously published ones.

In the horizontal component, the greatest uncertainty within near-best GIA models is in different parts of the continent for the 1D and the 3D models. This could indicate a larger sensitivity of the GIA model predictions to the change in rheology or differences in the ice sheet reconstructions used in the near-best models. The near-best 1D GIA models in Antarctica are all models based on ICE-6G, whereas the 3D models are made in combinations with different ice models.

The uncertainty of GNSS measurements in both horizontal and vertical component in Antarctica varies, from the lowest below 0.5 mm/yr up to over 2 mm/yr. Given that the overall number of sites in my network in Antarctica is only 54, it is challenging to use GNSS for testing GIA models. Unlike the other analysed regions, Antarctica is still covered by ice sheets. The MADs and estimate of uncertainty of GIA models differs depending on whether an elastic correction is used or not. Since the elastic correction is subject to uncertainty too, a larger number of elastic component models could be used to better interpret the results. The uncertainties of the elastic correction used here are obtained through Monte Carlo simulations and they are propagated with the GNSS uncertainty to obtain the final uncertainty of the GNSS residuals in Antarctica.

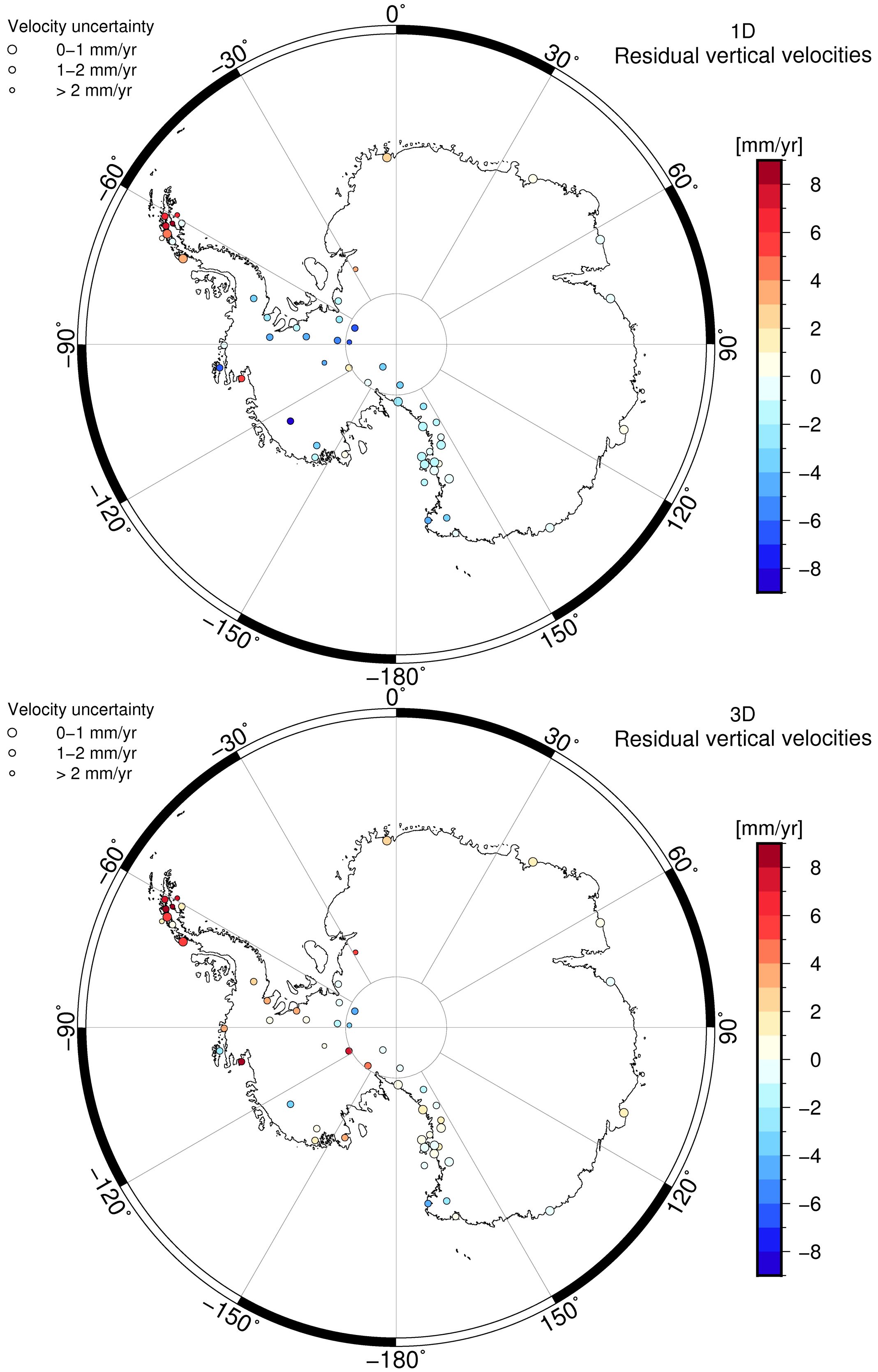

Figure 6.18: Vertical velocities in Antarctica at GNSS sites after removing GIA using the best GIA model for Antarctica in the vertical component. Best 1D GIA model (top) and best 3D GIA model (bottom). The colourbar saturates at 9 mm/yr, above which value are a few residual velocities that are not significant. E.g. site FONP on the Antarctic peninsula has a large residual velocity of 9.7 mm/yr with the 1D model and 11.1 mm/yr with the best 3D model, however the GNSS velocity uncertainty of the site Up component is 4.2 mm/yr.

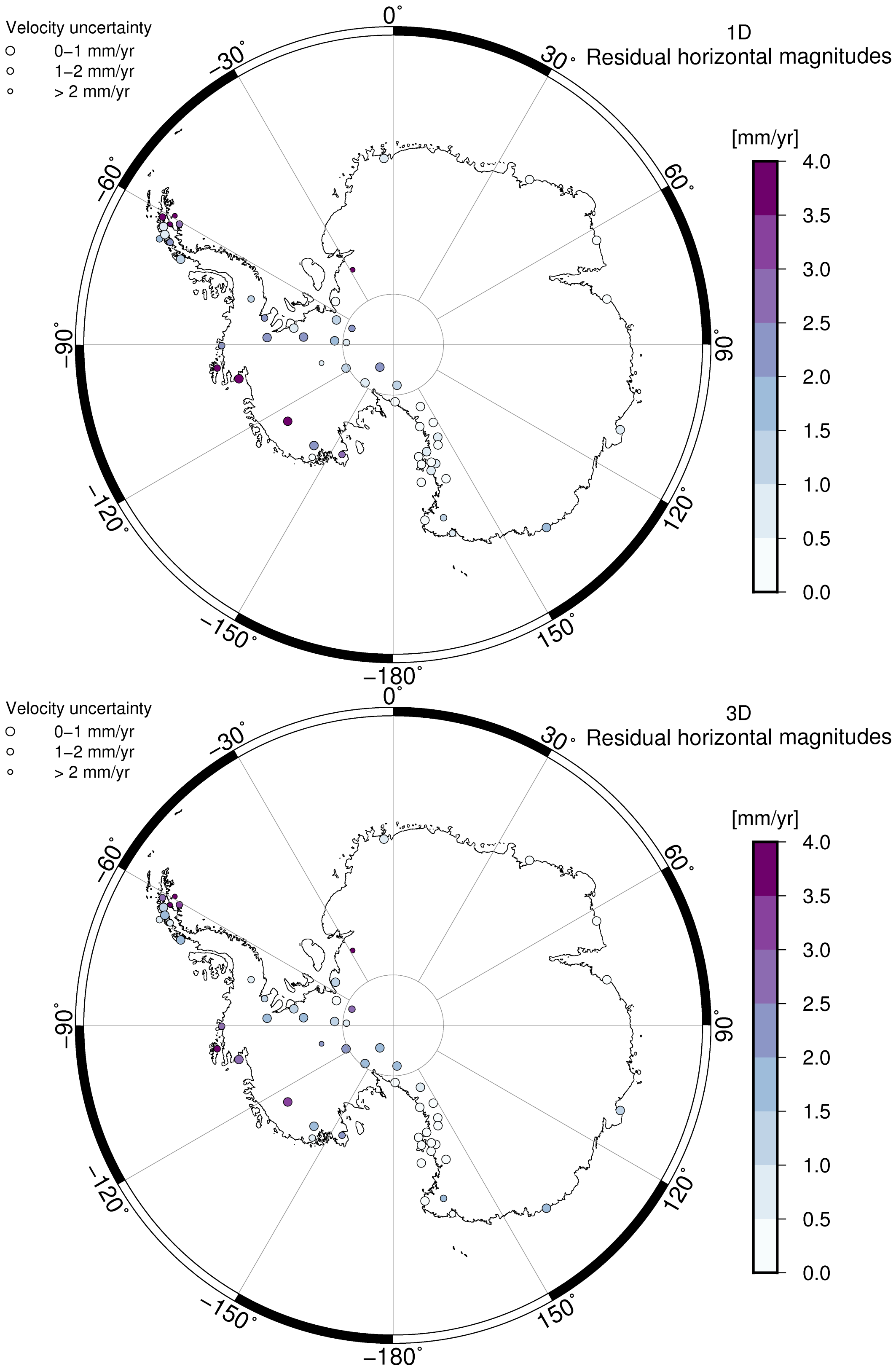

Figure 6.19: Magnitudes of residual horizontal velocity field at GNSS sites after removing plate motion and GIA using corrections from the best GIA model for Antarctica in the horizontal component. Best 1D GIA model (top) and best 3D GIA model (bottom)

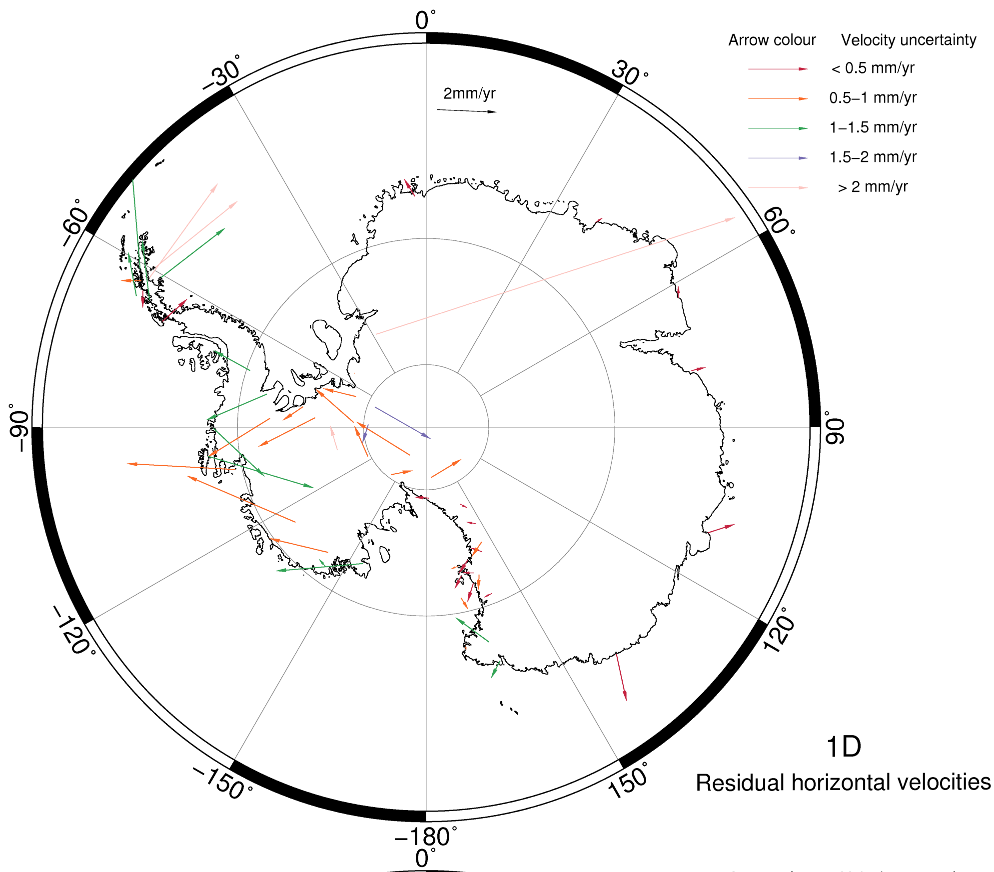

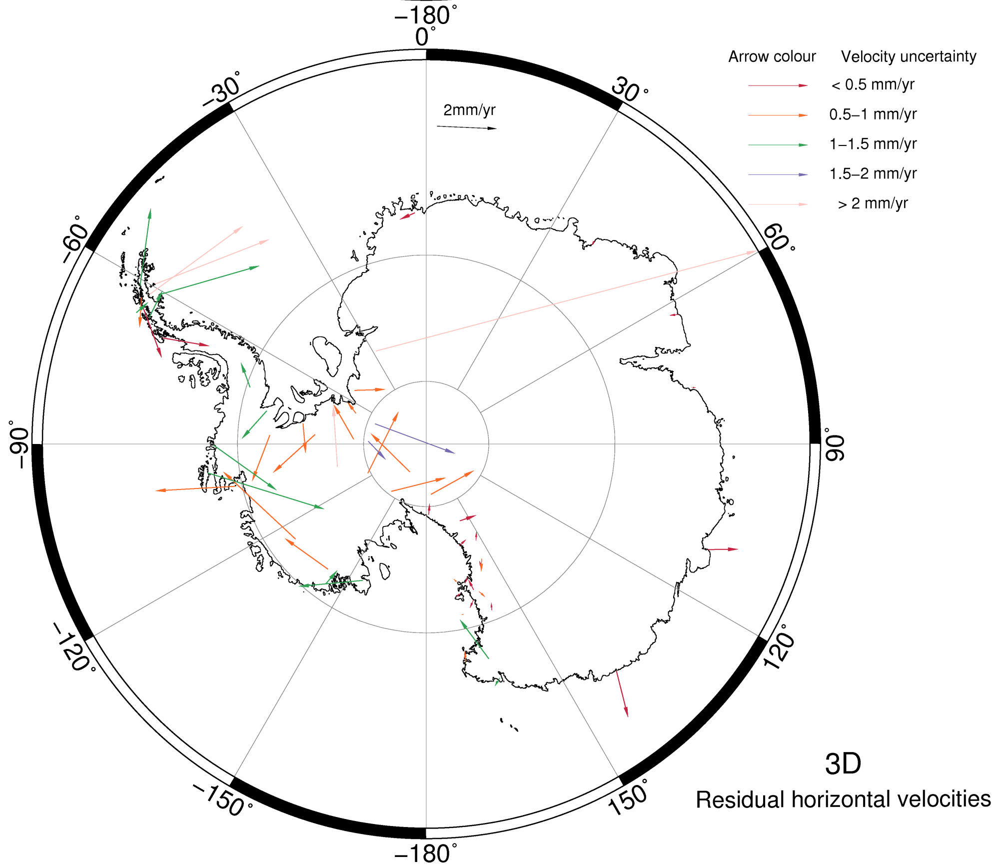

Figure 6.20: Residual horizontal velocity field at GNSS sites after removing plate motion and GIA using the best GIA model for Antarctica in the horizontal component. Best 1D GIA model (top) and best 3D GIA model (bottom)

6.7 Discussion

There is no general agreement on how to quantify the uncertainty of GIA models. It is typically done with external validation, by considering misfits between the GIA model and observations. This thesis is an example of such an assessment. The misfits, however, might be due to a number of errors, such as errors in the GIA model's underlying ice model or Earth rheology, errors in the observations (in this case GNSS), and other geophysical processes contributing to vertical and horizontal deformation. Deriving reliable formal uncertainties for the GIA models is a challenging task. Tarasov et al. (2012) attempt to quantify the uncertainty in ice models in particular. They suspect that the most critical unquantified uncertainties are related to climate forcing, deglacial ice margin chronology and Earth rheology.

Vestøl et al. (2019) quantify their GIA model uncertainty by comparing 11,025 different GIA models to their observations, and computing the standard deviation of a subset of 21 good GIA models, based on seven different ice models and 14 different Earth models. They define a total GIA modelling uncertainty as the square root of the squared sum of the standard deviation and an uncertainty factor accommodating remaining errors (non-modelled effects, non-GIA effects), which they estimate using the differences between the GNSS observations and the GIA model.

In a recent publication, Simon and Riva (2020) investigate four methods of estimating GIA uncertainties that have been discussed in previous GIA studies:

1. parameter variation - considering various Earth-ice model combinations and using the standard deviation of them as a measure of uncertainty
2. residual analysis - considering the fit of the GIA model predictions to a set of constraining data
3. canonical $\pm 20\%$ value - assumption that in general the uncertainty associated with GIA is within $\sim \pm 20\%$ of the GIA signal
4. (semi) empirical estimation - inversion of constraining datasets, i.e. inverse GIA models

The methods are applied to selected 1D GIA model vertical predictions and compared with vertical land motion data from GPS measurements and sea-level data across Fennoscandia and North America. They find that all four methods perform in a consistent manner making them all potentially suitable for uncertainty estimation. However, they find that the $\pm 20\%$ rule may underestimate uncertainties in the centres of former ice sheets and be inappropriate for application in farther-field regions and regional studies. They also find that the parameter variation method may be overly pessimistic for 1D GIA models. However, they note that there are various formulations for parameter variation, other than those applied in their study. Simon and Riva (2020) add that the use of 3D Earth models may further complicate this with the introduction of more free parameters and extrapolation from laboratory to natural scales.

In this project, the range of GIA predictions from the near-best models may be seen as a measure of uncertainty of GIA models. This is comparable to a combination of the above mentioned methods of (1) parameter variation and (2) residual analysis. Here the parameter variation is considered only for groups of GIA models selected by validation with GNSS observations. The groups of near-best models are formed separately for 1D and 3D GIA models, as well as vertical and horizontal component (Table 6.4, E.2, E.3, E.4). The near-best models are chosen based on their MAD fit, and the variation of models within these groups is considered as an indication of uncertainty in the GIA estimate. Simon and Riva (2020) state that the disadvantage of the parameter variation approach is that it may give unrealistically large uncertainty estimates, particularly in load centres, and that the selection of which parameters to vary is itself subject to uncertainty. The advantage of the approach taken in the present project is that the group of GIA models is also validated against empirical data. It is important to stress, however, that it is not a formal statistical measure of GIA modelling uncertainty.

When studying surface mass change estimates from satellite gravity missions, such as GRACE and GRACE Follow-On, the GIA signal component must be accounted for. The range of GIA models can be interpreted as the uncertainty which is introduced when correcting surface mass change estimates for GIA. Mass density change can be expressed in units of mass per unit of area. A commonly used and more intuitive unit can be obtained by dividing the surface mass density estimate by the density of water ρ_w, which gives density changes in units of equivalent water height (EWH).

This is particularly interesting for Antarctica, which is still covered in ice. In order to study deformation due to present-day ice mass changes from gravity, the GIA deformation must be corrected for. The range of vertical GIA predictions from Fig. 6.15 in Chapter 6 can be interpreted as the uncertainty of GIA predictions in Antarctica and Fig. 6.21 shows these uncertainties expressed in mm/yr EWH. In this estimate, the rock density is taken to be 3700 kg/m^3 (Wahr et al. (2000), Riva et al. (2009)). The uncertainty caused by GIA reaches up to 10 mm/yr in most of Antarctica. The largest uncertainty is up to 18 mm/yr EWH in the area of the Ronne Ice Shelf, up to 14 mm/yr in East Antarctica south of Dronning Maud Land and up to 12 mm/yr on the coast by Ross Ice Shelf.

The GIA vertical predictions can also be expressed as annual mass change. Thus, they can be taken as the GIA contribution to the observed annual mass change from GRACE (and Follow-On) missions. Antarctica can be divided into three regions with respect to

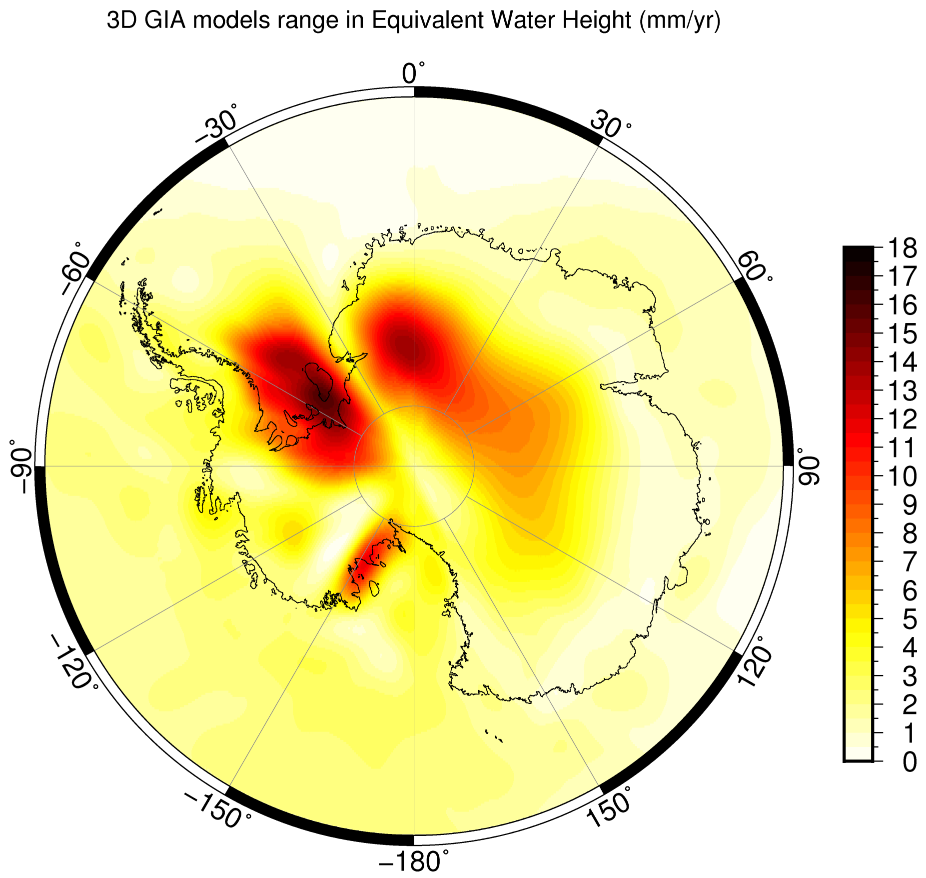

Figure 6.21: The uncertainty of GIA models in Antarctica in terms of mass density in mm/yr of equivalent water height (EWH).

major ice sheets: West Antarctic Ice Sheet (WAIS), East Antarctic Ice Sheet (EAIS) and Antarctic Peninsula (AP) (Zwally et al., 2012). For EAIS, Shepherd et al. (2018) find an ice-mass change rate of $+5 \pm 46$ Gt/yr, for WAIS they find -94 ± 27 Gt/yr, and for AP they find -20 ± 15 Gt/yr. For the whole of Antarctica, they find -109 ± 56 Gt/yr.

In Antarctica, depending on which GIA model from the group of near-best models is used, the predicted GIA contribution to observed annual mass change ranges from 5.27 Gt/yr to 45.10 Gt/yr (cf. Table 6.6). This indicates that the uncertainty in ice-mass change from gravity missions caused by GIA is $\sim$40 Gt/yr in Antarctica. Shepherd et al. (2018) analyse the mass balance of Antarctica for the 1992-2017 period using satellite observations. For ten models that cover all of Antarctica, they find that the GIA-induced mass change estimates are in relatively good agreement, ranging from +12 Gt/yr to +81 Gt/yr, with a mean value of +56 Gt/yr. They report uncertainties (one standard deviation) of different average GIA-induced mass change estimates across Antarctica between ± 13 to ± 27 Gt/yr.

I quantify the contribution of GIA to annual mass change as above for each ice sheet area from Zwally et al. (2012). The results are listed in Table 6.6. Columns 2-5 show the GIA contribution to annual mass change with each of the near-best 3D GIA models. There is no group of near-best 1D GIA models since none of the 1D GIA models showed better MAD fits than null-GIA. Column 6 shows the range of these mass changes, which may

Gt/yr	5G_S_wet_1mm	W12_SL_dry_1mm	W12_SL_wet_1mm	6G_SL_wet_1mm	Range of mass change estimates
WAIS	2.32	30.40	7.58	2.62	28.09
EAIS	1.36	6.37	1.23	0.79	5.58
AP	1.60	8.33	1.54	1.11	7.22
Antarctica	5.27	45.10	10.35	4.52	40.58

Table 6.6: GIA contribution to annual mass change in Antarctica using each of the near-best GIA models and the uncertainty (range) in mass change estimate in connection to GIA.

be used as the GIA contribution to uncertainty in mass change estimates for each area (EAIS, WAIS, AP or Antarctica as a whole).

With the exception of W12_SL_dry_1mm, the GIA-induced mass change estimates in Table 6.6 are on the lower end of the estimates of Shepherd et al. (2018). However, their relatively low +12 Gt/yr estimate is based on the only model which accounts for lateral variations in Earth's rheology, and thus more comparable to the estimates in Table 6.6, which are also based on 3D GIA model outputs.

The range of azimuths of horizontal GIA predictions (Figs. 6.4, 6.10, 6.17) may be seen as the uncertainty in directions of GIA models horizontal predictions. In each of the three earlier discussed regions of interest (Europe, North America and Antarctica), the range of azimuths of near-best 3D GIA models is larger than the range of azimuths of near-best 1D GIA models. The groups of near-best 1D GIA models in the horizontal component are in all three regions of interest based on ICE-6G, whereas among the near-best 3D GIA models, there is a larger variety in ice models. To investigate whether the larger variations in horizontal directions among the 3D GIA models than the 1D GIA models are due to different ice models, the azimuths were also inspected for the near-best 3D GIA models created with the same ice model. A large range of azimuths was still observed, suggesting that the predicted horizontal velocities are very sensitive to the lateral variations in mantle viscosity.

Finding ice sheet models that fit different study areas well is an ongoing research topic. Ice sheet models are traditionally created assuming a 1D Earth structure. This could be one of the reasons why 3D GIA models do not perform as well as 1D GIA models in some regions. Huang et al. (2019) find an ice sheet model based on ICE-6G, which simultaneously fits the observations in North America and northern Europe when combined with an Earth model with composite rheology, where the effective viscosity is laterally heterogeneous. The observations that they seek to fit are historical RSL data, present day uplift rates from GNSS and gravity rates from the GRACE satellite gravity mission. They denote their ice model ICE-C.

Compared to ICE-6G, in Fennoscandia ICE-C assumes a thicker former ice sheet near the centre of uplift to the west of the Gulf of Bothnia, and a thinner former ice sheet near the margin of the ice sheet along the western and northern coast of Norway, southern Sweden and part of Finland. Their model also increases the ice thickness in the northern part of the British Isles compared to ICE-6G. The best 3D GIA model for Europe in the vertical component in this thesis is W12_SL_dry_4mm. As mentioned, the northern hemisphere of ice sheet history in W12 is equivalent to ICE-5G. In Europe, ICE-5G and ICE-6G are relatively similar. Therefore, if the ice sheet in W12_SL_dry_4mm was adapted according to Huang et al. (2019), this might reduce larger residuals obtained here for the best 3D GIA model (Fig. 6.5). Large positive residuals are found to the west of the Gulf of Bothnia, which indicate that uplift rates due to GIA are underpredicted in that area. Assuming the same Earth properties, the residuals would be less positive if a thicker ice sheet were assumed in that area. Similarly, the negative residuals along the coast of Norway and southern Sweden indicate that the GIA model overpredicts the uplift. If the ice sheet were thinner in this area, the predicted GIA uplift would be smaller and the residuals less negative.

In North America, ICE-C assumes more ice in the SE of Hudson Bay, west of Newfoundland and the edge of Greenland, as compared to ICE-6G. In the Northeastern part of Hudson Bay and along the east coast of northern USA, the ice thickness was reduced in ICE-C. The best 3D GIA model for North America in the vertical component in this thesis is 6G_SL_dry_10mm. Similarly as above for Europe, the ice sheet history from ICE-C may explain some of the larger residuals in Fig. 6.11. The large (4.9-6.5 mm/yr) positive residuals in the SE of Hudson Bay would be reduced if a thicker ice sheet in that area were combined with the same Earth model. The negative residuals along the east coast of USA would also be less negative if a thinner ice sheet were assumed in that area. We find large (2.0-3.9 mm/yr) positive residuals along the coast of Hudson Bay with the best 1D GIA model (6G_120p820) as well. Still, these residuals are not as large as with the best 3D GIA model. However, large positive residuals for both the best 1D and 3D GIA models, may support the findings of Huang et al. (2019) that the former ice sheet was thicker in that area.

Kierulf et al. (2014) investigate the fit of vertical and horizontal GIA model predictions in Fennoscandia using an alternative approach where they express the GNSS velocities in a so-called "GIA reference frame". They transform the GNSS velocities to a GIA reference frame for each GIA model with a four-parameter similarity transformation, where only the three elements of the rotation matrix and the scale rate parameter are estimated. The disadvantage of their method is that it introduces more degrees of freedom, might increase uncertainty and mask potential large scale systematic GIA model biases. Compared to a traditional approach, where the reference frame is fixed and the rigid plate motion is removed, their method avoids the influence of errors in scale, rotation and geocentre of the reference frame and bias from plate motion on the comparison between the GNSS velocity field and the GIA model. This approach can only be applied in regional studies within one tectonic plate since it would otherwise be contaminated by rigid plate motion. In the present project, the residual velocities for each GIA model are compared without contamination by an external PMM and by correcting for frame origin differences. A set of PMMs is estimated from a bespoke GNSS surface velocity field corrected with a set of GIA models. With such global PMM estimates, the differences in reference frame origins of GIA, rigid plate motion and GNSS network are taken into consideration. Therefore, it is an alternative to the "GIA reference frame" approach and is likely able to better constrain GIA models.

Chapter 7

Conclusions

The main goal of this project was to compare a set of recent 1D and 3D GIA models and investigate tectonic plate motion by creating a bespoke GNSS velocity field. Three objectives were defined to reach this goal: (1) derive a global surface velocity field from GNSS measurements, (2) estimate plate motion models and investigate the effect of GIA on these, and (3) investigate and compare a set of 1D and 3D GIA models, validating them against present-day surface velocities in both horizontal and vertical components.

A global surface velocity field was determined using time series of GNSS measurements. The GNSS velocity field was corrected for GIA using a suite of GIA models and used to estimate global plate motion. Each global plate motion model was applied and the respective GIA model predictions removed from the GNSS velocity field to obtain a residual velocity field. The residual velocity field was used to validate the GIA models. Fig. 4.6 summarises the approach. Obtaining the velocity field and estimating plate models has been done with thorough attention to error sources and excluding outliers. Unlike some regional model-data comparisons where relatively simple methods can be applied to remove the errors due to the reference frame, this thesis offers a global approach. The GNSS networks are well-aligned to the ITRF2014 reference frame and the variations of reference frame origins between the different velocities (GIA, GNSS and plate velocities) are taken into account in the estimate and the computation of the residuals.

In particular, time series of several ACs' daily global GNSS networks were combined into a time series of daily unique global network solutions. The unique combined daily solutions were then aligned to the most recent ITRF2014. The daily time series of regional solutions were aligned to the global network, indirectly aligning them as well to the ITRF2014 reference frame. Using the MIDAS trend estimator, the velocities of the sites in the network were estimated. Each of the steps included quality control and finally resulted in a global surface velocity field from GNSS with horizontal velocity uncertainty of mostly up to 0.5 mm/yr and vertical velocity uncertainty of mostly up to 1 mm/yr.

A recent publication by Métivier et al. (2020) makes a comparison of vertical GNSS velocities from the last four ITRF solutions (ITRF2000 to ITRF2014) with some of the recent 1D GIA models. They state that they do not make a comparison of horizontal velocities and GIA because the difference between ITRF GNSS observations and PMMs is probably polluted by a GIA signal that is poorly known. They state that it would be interesting to develop joint inversions of plate tectonics and GIA models from GNSS horizontal velocities. In this thesis, horizontal velocities are investigated as well as the vertical, and the GIA models are used jointly with GNSS velocities for plate model inversions. This work builds on the work of Booker (2012), but with a higher density of GNSS sites in GIA regions, facilitating the first comprehensive global assessment of horizontal GIA velocities and their effect on plate motion from GNSS network solutions.

GNSS velocity field

The GNSS velocity field is an improvement to the previously published ones due to the combination of several reasons:

- The GNSS data used was IGS repro2 and following operational data, and other datasets which are processed in a similar way as repro2. Repro2 GNSS processing standards are the most accurate and to date most recent IGS standards.
- The combined networks are aligned to ITRF2014, which is the most recent ITRF solution, and includes features that did not exist in earlier ITRF realizations (seasonal variations and PSD models). The alignment to ITRF2014 was improved with an update of the in-house software Tanya and ITRF2014 to work with discontinuity SINEX files and PSD models.
- The network combination algorithm was changed compared to the Newcastle University GNAAC combination algorithm to include sites that were estimated by minimum one AC. This resulted in a combined network with larger number of sites while still giving good post fit residuals. The WRMS of the post fit residuals of the daily network alignments to the ITRF2014 reference frame is a measure of quality which shows how well the combined network fits the reference frame. The WRMS is 2.5 mm on average for the entire combined network time series from May 1995 to January 2017.
- The daily WRMS values were compared and found superior to weekly WRMS values from a similar previous network combination (Booker et al., 2014). Compared to the previous version of Tanya using ITRF2008, when using the present version of Tanya using ITRF2014 there is a reduction in WRMS from 8.0 mm to 3.5 mm on average for their overlapping time period (15^{th} February 2015 – 28^{th}January 2017).

- Using the adaptation of the MIDAS algorithm with a tolerance value of four weeks (when matching the pairs, cf. section 4.3.1) gives negligibly different results than using a strict 1-year difference, while increasing the amount of usable data.

- The extended number of sites resulted in a dense global velocity field which improved coverage in GIA affected regions in North America, Europe and Antarctica (compared to, e.g. Booker et al. (2014), the IGS network (Rebischung et al., 2016) or the ITRF network (Altamimi et al., 2016)).

PMM estimate

A set of PMMs was created using the GNSS velocity field (GNSS-only PMM) and the surface velocity field corrected with GIA predictions (1D GIA PMMs and 3D GIA PMMs). From these, a subset of PMMs created with near-best GIA models was further analysed. The best and near-best GIA models are chosen according to their MADs, and the ranking of the PMM is based on the ranking of the GIA model that was used in estimating that PMM. The PMM estimates resulted in the following conclusions:

- It is shown that using an extensive set of 1D and 3D GIA models facilitates the estimation of a PMM from a larger data set than in previous global PMM estimates where sites in GIA regions had to be removed.

- There can be GIA related horizontal motion which may be incorporated into the plate motion if left uncorrected. This can significantly influence the plate velocities on the millimetre level. This is important for North America and Europe which have areas that are affected by GIA, and especially for Antarctica where almost the entire plate is affected by GIA.

- 3D GIA PMMs Euler poles are located closer to ITRF2014 PMM Euler poles (which excludes sites in GIA regions) than the 1D GIA PMMs, which indicates that 3D GIA models may be better at correcting for the horizontal GIA motion which can bias the PMM estimate.

  It is important to note that while ITRF2014 PMM is chosen as a reference, it does not mean that it is considered to be less biased by GIA than the GIA PMMs. This is due to the possible errors in the process of excluding GIA-affected regions in ITRF2014 PMM (cf. section 5.3). An advantage of the GIA PMMs is that the GIA effect is treated more rigorously.

- The PMM estimates for Antarctica in this thesis include ∼8 times more sites than ITRF2014 PMM and also result in a significant reduction of the Euler vector uncertainty (formal error) for that plate.

- Using GIA models in PMM estimation is favourable when validating GIA with GNSS observations because it reduces the risk of using a (pre-existing) PMM which can be contaminated by GIA. Additionally, the joint estimation takes into consideration the difference in frame origin of the GIA models, GNSS network and rigid plate motion further improving the residuals.

- The globally best-fitting PMM estimated here (Table 5.1), is a state-of-the-art geodetic PMM which may be used in other studies involving tectonic plate motion or requiring correcting for it.

Comparison and validation of GIA models

In this project a set of 1D and 3D GIA models was used which had not yet been investigated globally or in the horizontal component. The GIA model predictions and their ranges were investigated as well as validated against the GNSS surface velocity field. On the whole, it was not possible to identify whether 1D or 3D GIA models are better. However, the following conclusions can be drawn:

- While it is not possible to select a universally best GIA model, it is possible to identify the ice models and features of Earth models which are common to the better fitting GIA models. Table 6.1 summarizes the analysis of MADs from Figures D.1-D.16. Unlike the 3D GIA models, the 1D GIA models show a preference for ICE-6G in all regions. Due to the different input parameters of 1D and 3D Earth models, it is not straightforward to identify matching properties of 1D and 3D GIA models in each region. Using Table 2.1 as a rough guide, however, it can be noted that in North America, the 1D and 3D GIA models show a preference for larger mantle viscosities, and in Antarctica, both show a preference for smaller mantle viscosities. In the horizontal component, no similar agreement could be identified for the 1D and 3D GIA models in any of the regions.

- Global: When seeking to find one GIA model for the entire Earth, the best 3D GIA model for each component gives a better fit than the best 1D GIA model for each component (cf. Tables 6.2 and 6.3). In the horizontal component, none of the 1D GIA models are better than null-GIA, whereas the 3D GIA models are better than null-GIA in both horizontal and vertical components. This suggests that 3D Earth structure is important when seeking to replicate the global horizontal velocity field.

- Regional: In Antarctica, none of the 1D GIA models fit the GNSS vertical velocity field better than null-GIA, whereas the near-best 3D GIA models show an improvement of the fit. In North America and Europe, the 1D GIA models give a better fit in the vertical component than the 3D GIA models. One of the reasons for this could be the fact that the ice models are developed assuming 1D Earth structure.

- The subsets of suitable GIA models, i.e. near-best models (cf. Tables E.2, E.3, E.4 and E.5), may be used in crustal deformation studies where a correction for GIA is required. Furthermore, the ranges of GIA model predictions selected here may be interpreted as a measure of uncertainty of GIA models, and can contribute to error budgeting.

Recommendations for future work

The GNSS velocity field obtained here is a state-of-the-art product which can be used in future studies constraining or validating GIA models. As ever, there are aspects of this project which could be further improved and extended.

Regarding the GNSS network combination, the issue with discontinuity SINEX block mentioned in section B.1 required developing a method for matching SINEX blocks and an alternative way of creating the SINEX catalogue. This had been raised as an issue in the SINEX and IGS community prior to the start of this project. When this is resolved, the matching of the discontinuity information should be simplified and would not require a tolerance value for epoch start and end times. Furthermore, future improved GNSS processing methods and/or availability of longer GNSS time series, could improve the GNSS velocity field.

The GNSS velocities in this project were estimated using the MIDAS trend estimator. MIDAS does not take into consideration the correlation between the position coordinate components and positions of the sites in the network. The Tanya software has potential for estimating velocities from a time series of networks. However, within the scope of this project it was not possible to implement this. A recommendation for future work could be to exploit this aspect of the Tanya software. Importantly, this may offer more realistic estimates of PMM uncertainties.

The GIA model fits were in this project analysed separately in the horizontal and vertical component. This resulted in different best models in the horizontal and the vertical component. The groups of near-best models in the two components partially overlap, offering models that may be used for both horizontal and vertical studies. However, an additional consideration of a three-dimensional MAD fit may be beneficial in choosing a best fitting model for both components.

A more in depth analysis of the GIA models can be done by analysing the residual velocity fields of each model in the near-best group. This would permit inspecting how the residual velocity field pattern of the best model agrees with the other well fitting (near-best) models in the group, adding more robustness to the interpretation.

The analysis of GIA models indicates that there is large uncertainty in GIA model predictions in parts of Canada which are sparsely covered by GNSS sites. More GNSS site coverage in these areas would improve the constraints and validation of GIA models. Also in Antarctica, which is sparsely covered by GNSS sites, establishing more continuously operated GNSS sites would improve the constraints and validation on GIA models and PMM estimate.

The ice models used in this thesis are created assuming a 1D Earth structure, which is not consistent when used together with 3D Earth models to form a GIA model. Should new ice models created assuming a 3D Earth structure become available, new GIA models based on these could be created and the validation using the GNSS velocity field could be revisited. The 3D GIA models can additionally be improved by including compressibility and rotational feedback which would further improve the model-data comparison.

Unlike North America and Europe, Antarctica is still covered by ice sheets, and therefore experiences crustal deformation due to present-day ice mass change in addition to GIA. Thus, a correction for the elastic deformation caused by present-day ice mass change was applied. This elastic correction presents just one approach of determining the elastic deformation. Comparing the results with a number of different elastic corrections would help clarify the uncertainty caused by the elastic correction in validating GIA models.

A main application of observations from GRACE and GRACE Follow-On satellite gravity missions is the determination of surface mass redistribution associated with the hydrosphere. This includes, e.g. studies of changes in ocean mass content, the studies of steric sea level, studies of global and regional hydrological variations, and studies of mass changes of large ice sheets. The GNSS velocity field can also be used to infer present-day surface mass loading (e.g. following the approach from Booker et al. (2014)) in studies of the global hydrological cycle as mentioned above. Common for the mentioned studies is the necessity to correct for mass change due to GIA, and the resulting uncertainties of the studies are influenced by the relatively large uncertainty of the GIA correction. As mentioned above, the range of GIA models from this project may be used as a measure of GIA uncertainty for such studies. The continued improvement of GIA models and realistic uncertainties will narrow the error bars of these studies.

Appendix A

Geographical maps

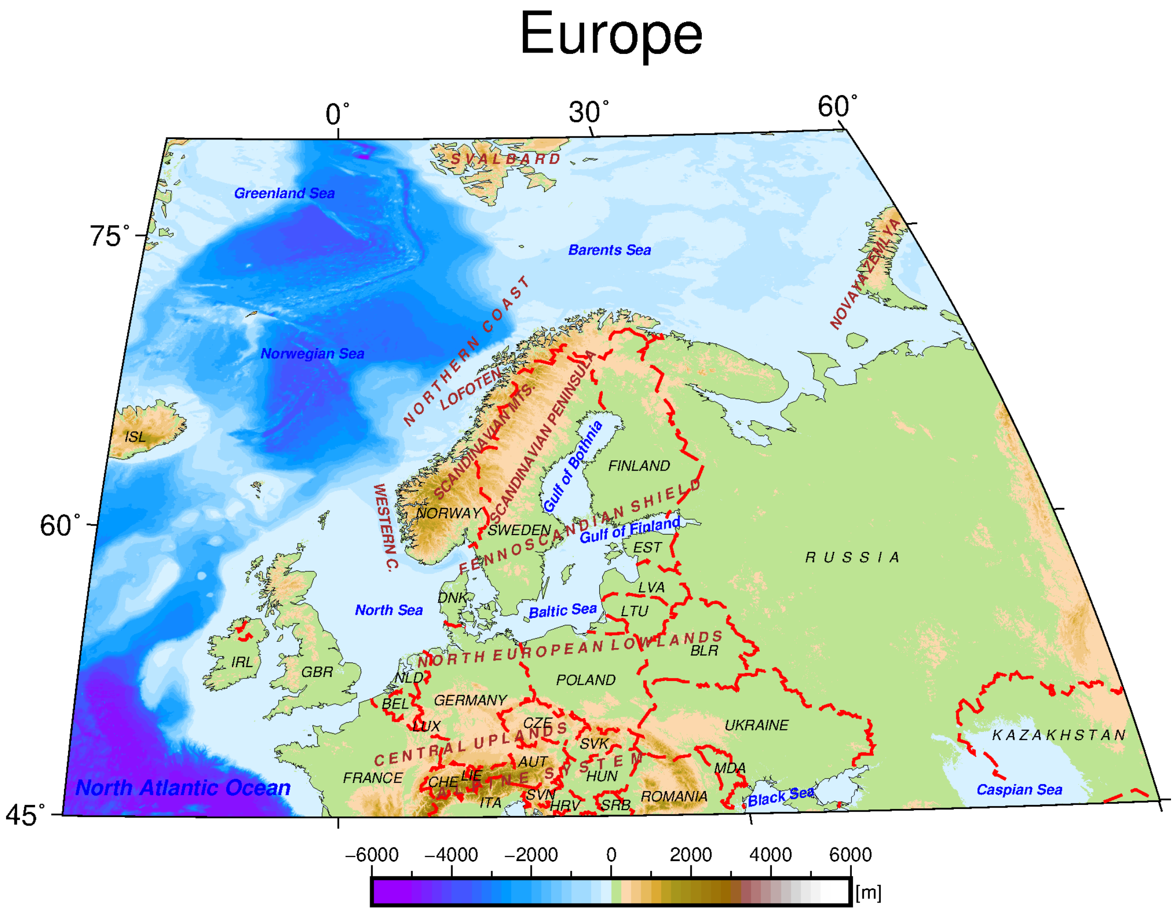

Figure A.1: Reference map for Europe with topography and geographical names of features described in the thesis. The map is created using GMT software (Wessel et al., 2013). Topography and bathymetry information from GEBCO (2020).

Figure A.2: Reference map for North America with topography and geographical names of features described in the thesis. The map is created using GMT software (Wessel et al., 2013). Topography and bathymetry information from GEBCO (2020).

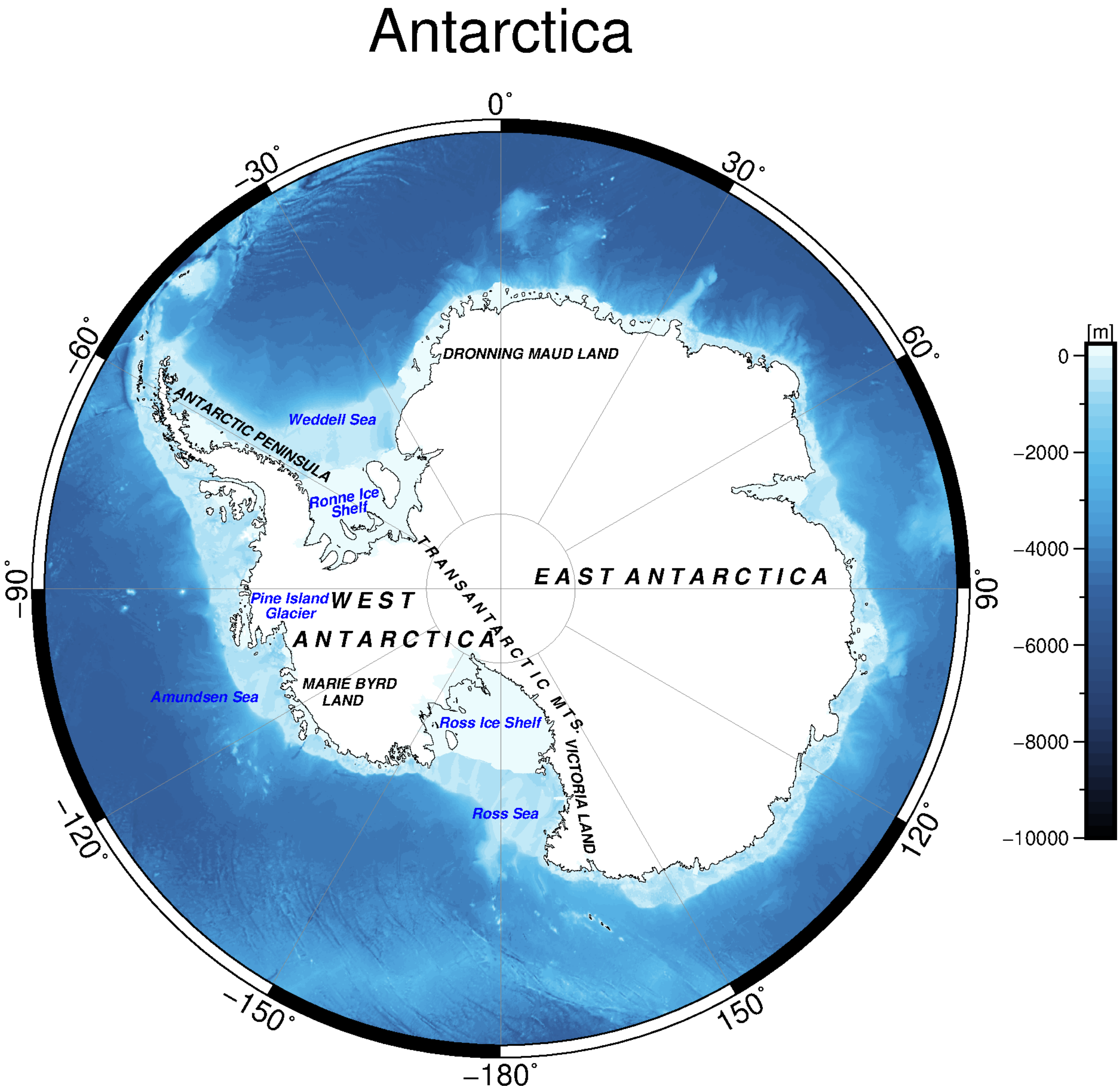

Figure A.3: Reference map for Antarctica with topography and geographical names of features described in the thesis. The map is created using GMT software (Wessel et al., 2013). Topography and bathymetry information from GEBCO (2020).

Appendix B

Tanya software modifications

This appendix describes the Tanya software-specific procedures related to network combination and contains supporting information for sections 4.1 and 4.2 of Chapter 4. The first section of the appendix describes the way Tanya extracts information from network solution files and discontinuity files and the updates implemented in the software for this process. The second section deals with the implementation of ITRF2014 PSD models.

B.1 Extracting a network solution from a SINEX file

After reading SINEX files, Tanya stores them in its own data block format for all further processing. This data block format is called Tanya block and should not be mistaken for a SINEX block. A Tanya block consists of a set of files with the same root file name but with different three-character extensions (Davies, 1997). These blocks contain standardised information from the SINEX file in a file format that can further be efficiently processed. The blocks used in this thesis are listed in Table B.1.

Extension	Content	Format	Optional
.hed (header)	agency, timestamp, number of stations in catalogue, number of stations in this block, number of parameters per station, covariance scaling factor, reference epoch	single line	no
.sib (site in block)	list of station reference numbers	list of integers	no
.vec (vector)	vectors of parameters	list of floating point numbers	no
.cov (covariance)	upper triangular VCM of the vector in .vec	list of floating point numbers	yes
.wgt (weight)	upper triangular inverse VCM of the vector in .vec, or information matrix of normal equation system	list of floating point numbers	yes

Table B.1: Standard file types defined in the Tanya block format. Adapted from Davies (1997).

Before storing the SINEX blocks in its own file format, Tanya reads the SINEX file, checks the internal integrity of it, and cross-references the SINEX blocks with each other.

Tanya uses a catalogue SINEX file to identify and cross-reference parameters. It is a standard SINEX format file but with the SOLUTION/ESTIMATE and other estimate blocks removed. Without the estimate blocks, the file reads more efficiently (Lavallée, 2006). The catalogue can list all sites that have been processed in Tanya, sites from a specific AC, or sites chosen for a specific project. It is an indirect link between SINEX files processed at different times, as well as a link between the solution SINEX file and the discontinuity file. The order number of the station solution from the catalogue SOLUTION/EPOCHS block is a unique identifier of the station and it is called `catalogue number`. They identify parameters in the Tanya block "site in block" file (`*.sib`)

To align the daily epoch solutions to the kinematic solution, the latter has to be propagated to each of these epochs and to do so, appropriate sets of positions, velocities and VCMs valid for the respective epoch need to be chosen. For each propagation epoch, only the kinematic solution parameters related to that epoch are written into Tanya blocks. When it comes to epoch solutions, there is only one station solution for each site and that one is chosen for the Tanya block.

The previous version of Tanya could not choose the sets of parameters for kinematic solutions according to the propagation epoch, or read the discontinuity file and cross reference it with the other SINEX blocks. Tanya had always chosen the first station solution given, so the input SINEX file had to be edited manually beforehand for all epochs. Therefore, a part of the software development in this thesis was modifying this process, and the new process is described in detail below and illustrated in Fig. B.1.

B.1.1 Reading and internal checking of SINEX files in Tanya

The following text describes the way Tanya software reads and handles SINEX files, choosing the appropriate information to be written into Tanya block format. Reading the SINEX files into Tanya, checking the internal integrity of each SINEX block and matching the information from different SINEX blocks concluded with writing the relevant information into Tanya block format is controlled by the module `sbuild`.

`sbuild` first initialises a SINEX-contents C structure, which depends on the SINEX version. It is possible to add new SINEX version features to the software, and here the type of data related to ITRF2014 PSD models was added (see section B.2). The `rsinex` function reads the SINEX file into the SINEX-contents structure copying the data from SINEX blocks into appropriate structure members. From here on, when talking about SINEX blocks, it is referred to the SINEX-contents structure members containing SINEX block data.

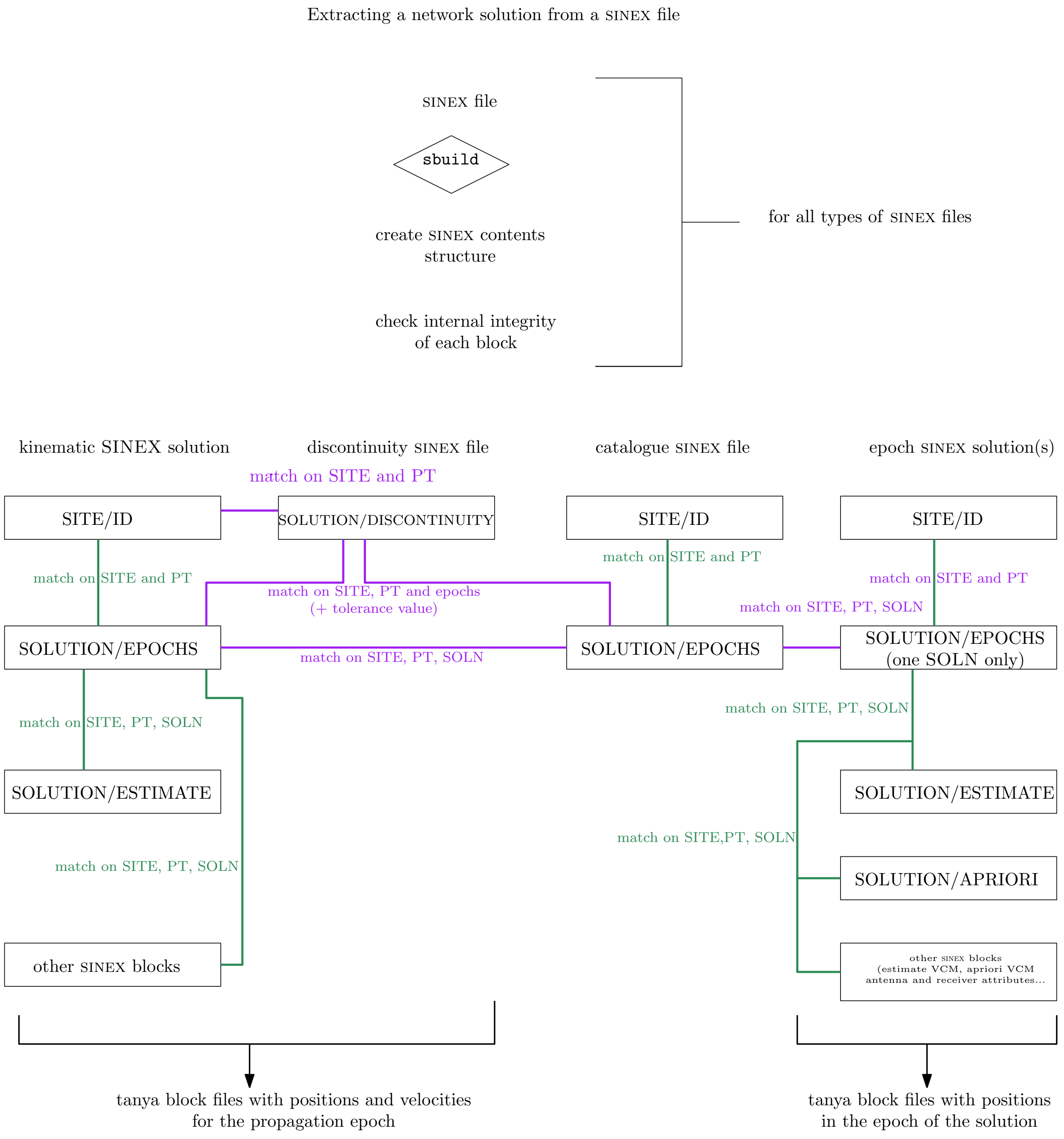

Figure B.1: Extracting the network solution from a SINEX file: After checking the internal integrity of SINEX blocks, the blocks containing different information are matched to each other, both within the file (green) and between different files (purple).

The sint function then checks if the syntax of the SINEX file is satisfied, checks for missing blocks and missing or incorrect record inputs and finally matches the SINEX blocks with each other. The functions sint and rsinex are called for solution SINEX (the main file containing the network solution), catalogue SINEX and, if it exists, discontinuity SINEX, separately. Depending on the type of SINEX file being read, all or some of the following are executed.

The order of the SITE/ID block data in the structure allows identifying each site with a unique site number while reading the SINEX files. Based on SITE and PT codes, the function connects the SOLUTION/EPOCHS and SITE/ID blocks and gives each station solution (station) in SOLUTION/EPOCHS the respective site number. Similarly, using the SITE and PT codes and, if given, SOLNs, the module then matches the records in SOLUTION/EPOCHS blocks with the records in blocks containing information about receivers, antennas and eccentricity, as well as phase centre observation. The function also matches the SOLUTION/DISCONTINUITY block with the SITE/ID block based on their PT and SITE codes. Each discontinuity record then gets a site number of the matching SITE/ID record.

To choose which pairs of parameters are used for the propagation of the kinematic solution, we need to compare the propagation epoch with the epochs in the SOLUTION/DISCONTINUITY and match the parameter vector with the SOLUTION/DISCONTINUITY block. The two can only be matched indirectly through the SOLUTION/EPOCHS block. Therefore, the next step is to match the SOLUTION/DISCONTINUITY to the SOLUTION/EPOCHS block.

The records in different blocks are usually matched on their unique identifiers. As mentioned before, a station solution is identified by SITE, PT and SOLN. When matching a SOLUTION/DISCONTINUITY record to a SOLUTION/EPOCHS record, Tanya first checks if the SITE and PT codes match. After having done that, it was intended to match on SOLNs. However, the discontinuity block has a different way of numbering the solutions. This makes it impossible to match the block entries based on SOLNs, which is an issue that has been raised in the SINEX and IGS community (e.g. IGS message ACS-599 September 2011) but up to the time of this project, it has not been resolved. Therefore, the matching of the SOLUTION/EPOCHS and SOLUTION/DISCONTINUITY blocks is done based on their time epochs.

An issue in the implementation of epochs as a matching criterion were the epochs themselves. The epochs in the discontinuity file and the epochs in the SOLUTION/EPOCHS block do not always correspond exactly. According to the IGN (www.itrf.ensg.ign.fr/ITRF_Solutions/2014/computation_strategy.php), each coordinate is identified by the SOLN and is valid for the period supplied in the discontinuity files. In other words, the information about the exact times when the discontinuities occur (T_1, T_2 and T_3 in Fig. 3.1) is contained in the SOLUTION/DISCONTINUITY block. The information about the epochs used for parameter estimation is contained in the SOLUTION/EPOCHS block.

Due to this, when matching the mentioned epochs, a tolerance value was introduced for comparing start and end times which allows for a small difference between epochs from the two blocks. The tolerance value can be decided by the user through the command line when running the main script. For the purpose of testing the software modifications, tolerance periods of 10 to 12 days were used and after a manual check on a sample ITRF SINEX file, the time period of 10 days proved to be reasonable.

This means that the propagation epoch of the kinematic solution is compared to the epochs in the SOLUTION/DISCONTINUITY block. A record in the SOLUTION/DISCONTINUITY block is therefore chosen and its epoch is compared to the epoch from the SOLUTION/EPOCHS block to find the SOLNs matching the propagation epoch. Finally, the SOLN that is chosen for the propagation epoch is used to select the appropriate parameters in the SOLUTION/ESTIMATE block (pairs (P_1, v_1), (P_2, v_1) and (P_3, v_3) in Fig. 3.1). The SITE ID, PT and SOLN allow the SOLUTION/ESTIMATE block to be matched to any other blocks, such as the SOLUTION/MATRIX_ESTIMATE block and any of the SITE/* blocks. For the blocks containing VCMs, each entry is matched with the pair of observations it is valid for. In case of an apriori solution (SOLUTION/APRIORI and SOLUTION/MATRIX_APRIORI blocks), the matching is analogous to the one with the estimate blocks.

B.1.2 Matching with the catalogue and creating Tanya blocks

The next step is to establish links with the catalogue. The `catreffix` function sets up and checks cross-reference lists (`smat` lists) between input SINEX and the catalogue. In the case of epoch SINEX, there are no solution numbers.

To match the stations from the main SINEX file SOLUTION/EPOCHS block with the catalogue SOLUTION/EPOCHS block, the site identification (SITE and PT code), SOLNs and epochs are checked. It has not been a custom in Tanya to contain updated epochs in the catalogue file since the catalogue is primarily used as a summary of sites. In the catalogue, each site was presented as only one station solution without a SOLN and the epochs in the SOLUTION/EPOCHS block given as $\pm\infty$, to ensure they would be valid whenever the catalogue might be used in the future. With no SOLNs and the catalogue epochs as $\pm\infty$, the station matching was based effectively only on SITE and PT codes. However, when using a kinematic solution with a discontinuity file, the catalogue must always have the updated epochs and SOLNs in order to allow block information matching through epochs in a way similar to the one described above for the `sint` function. Therefore, the catalogue file for this project contains epochs and SOLNs for all sites that are a part of the ITRF2014-IGS network.

In the case of an epoch SINEX solution which usually contains a daily or weekly solution, the epoch can be far earlier or later than any of the solution epochs of the ITRF, so this type of matching does not work. Therefore the updated Tanya version checks if the input file is an epoch or a kinematic solution by checking if it contains only position estimates or both position and velocity estimates. In case of an epoch SINEX solution where the epoch is before, or after, any of the catalogue epochs (for catalogue sites from ITRF2014-IGS network), it matches the record with the first or last given solution in the catalogue, respectively. The catalogue can also contain information about the attributes such as receiver type, antenna type, antenna eccentricity, GPS phase centre etc. The function also checks if the pair of records (record in the catalogue SINEX file and record in the main SINEX file) match on these attributes, which can be allowed to fail by the user.

If after all these checks, the matches for one solution SINEX station are down to a single catalogue station, an attachment is made and it is recorded as an entry in the station match list `smat`.

The function `catreffix2` cross-references the SOLUTION/DISCONTINUITY block with the catalogue through SITE ID, PT and epochs. Again as in the function `sint` above, for the epoch matching, there is a tolerance value. The output is written in another station match list, `smatd`.

At many sites there is a position discontinuity, but not a velocity discontinuity. For such sites, in the SINEX discontinuity file, there are entries marked as velocities with epochs $\pm\infty$. Since the velocity time span in that case is written in SINEX as infinity, when matching with catalogue based on epochs, such entries get matched with multiple catalogue station solutions because an infinite epoch contains all other epochs. Generally, in case that any one discontinuity entry is matched with more than one catalogue entry, that match is not accepted and does not get written into the station match list. That is resolved in the next subroutine by forcing the velocity parameter to match the corresponding position parameter.

The subroutine `mblock` uses the catalogue matched lists from the previous routines (`smat` and `smatd`) to construct a tanya block for a chosen epoch. This means that not all the parameters, VCMs, attributes etc. are copied into the Tanya block, but only the ones that were accepted through the procedures described above.

The end product of reading a SINEX file is a list of catalogue SINEX serial numbers for each station in the Tanya block (*.sib file), a list of floating-point elements of the vector of parameters (*.vec file), an upper triangular VCM of .vec vector, an upper triangular inverse VCM of .vec vector (*.wgt) and a header file with information about the SINEX file (*.hed) and by preference, some additional block files.

B.2 Post-seismic deformation model corrections

An important novelty in the published ITRF2014 solution are the PSD corrections (Altamimi et al., 2016). They published, in SINEX format, parameters of equations of the PSD models and their VCMs for sites affected by earthquakes. The propagation of the position of a site through a post-seismic trajectory can be computed with Eq. (4.4) where the last term can be computed for each component using Eq. (4.5).

For each site with provided parameters of the PSD model, there is an unspecified number of parameters in Eq. (4.5). All or only some of the components E, N and U of a site may be affected. For each of the affected components, there is an unlimited number of exponential and logarithmic terms. Again, there can be only an exponential or only a logarithmic pair of terms, or both. Each pair of terms for the PSD corrections consists of the amplitude of that term and the relaxation time (A and τ), together with the time when the earthquake related to that parameter occurred. The terms constituting the vector of parameters of the PSD model θ for each site are:

$$\theta = [A_1^l, \tau_1^l, ...A_n^l, \tau_n^l, A_1^e, \tau_1^e, ..., A_n^e, \tau_n^e] \tag{B.1}$$

The PSD models are provided per component, independently, so there are no correlations between E, N or U component. However, there is a correlation between the amplitude and relaxation time for each logarithmic or exponential term. Thus, the VCM matrix of δL_t^{PSD} is given by (Altamimi et al., 2016):

$$C_{\delta L} = C \cdot C_\theta \cdot C^T \tag{B.2}$$

where C_θ is the VCM of the parameters of the PSD model whose elements are given in the SOLUTION/MATRIX_ESTIMATE block of the PSD SINEX file, and C is the design matrix whose elements are computed by the following formulae:

$$\frac{\partial \delta L}{\partial A_i^l} = \log(1 + \frac{t - t_i^l}{\tau_i^l}) \tag{B.3}$$

$$\frac{\partial \delta L}{\partial \tau_i^l} = -\frac{A_i^l(t - t_i^l)}{(\tau_i^l)^2(1 + \frac{t-t_i^l}{\tau_i^l})} \tag{B.4}$$

$$\frac{\partial \delta L}{\partial A_i^e} = 1 - e^{(-\frac{t-t_i^e}{\tau_i^e})} \tag{B.5}$$

$$\frac{\partial \delta L}{\partial \tau_i^e} = -\frac{A_i^e(t-t_i^e)e^{(-\frac{t-t_i^e}{\tau_i^e})}}{(\tau_i^e)^2} \tag{B.6}$$

To implement this into Tanya, new subroutines for reading in a new type of block and working with it were created. A script for reading in PSD SINEX was written which creates a new structure type specific to PSD and copies the necessary values into it. A significant difference between the PSD corrections SINEX and standard SINEX observations is that any site can have an unlimited number of parameters which are not given in a specific order. This made the scripting of the routines related to PSD different from the usual subroutines.

Using the equations (4.5) and (B.1) – (B.6), corrections per component (E, N or U) and the VCM of direction components of all sites are computed. The corrections and the VCM are then transformed into the Cartesian XYZ coordinates. The corrections and the VCM are then combined with all the catalogue sites and added to the coordinates/VCM obtained from the kinematic solution SINEX file analogous to Eq. (4.4). This gives the final coordinates of the ITRF2014-IGS sites in each epoch of propagation, to which the combined network is aligned.

Appendix C

Observed velocities

Table C.1: GNSS site velocities used in this thesis. The GNSS velocities are obtained using the Tanya software and MIDAS algorithm, realised in ITRF2014. The velocities and the corresponding uncertainties are for the North, East and Up components, respectively. All the results are in mm/yr.

Site code	φ [°]	λ [°]	$\dot{N}$	$\pm\,\sigma_{\dot{N}}$	$\dot{E}$	$\pm\,\sigma_{\dot{E}}$	$\dot{U}$	$\pm\,\sigma_{\dot{U}}$
1LSU	30.41	-91.18	-0.36	0.27	-11.93	0.36	-3.02	0.76
1NSU	31.75	-93.10	0.13	0.18	-13.23	0.20	-0.67	0.68
1ULM	32.53	-92.08	-0.98	0.18	-12.91	0.21	-3.01	0.67
AB04	63.66	-170.57	-23.58	0.32	-0.36	0.29	-0.78	1.06
AB08	60.38	-166.20	-23.51	0.39	-4.70	0.65	0.12	1.11
AB12	58.95	-161.75	-21.55	0.43	-5.99	0.40	0.71	0.95
AC58	57.16	-170.22	-23.88	0.33	-3.80	0.35	-1.55	0.86
ACOR	43.36	-8.40	16.52	0.19	20.98	0.18	-2.78	0.56
ACP1	9.37	-79.95	12.10	0.53	16.77	0.53	2.61	1.41
ACP6	9.24	-79.41	12.48	0.44	16.82	0.40	-0.41	1.20
ACSO	40.23	-82.98	2.20	0.18	-15.31	0.19	-1.25	0.71
ACUM	41.74	-70.89	6.08	0.13	-15.37	0.15	-1.68	0.48
ADE1	-34.73	138.65	58.39	0.15	24.68	0.18	-0.93	0.50
ADIS	9.04	38.77	18.91	0.24	24.73	0.34	-1.34	0.71
ADRI	41.92	-84.02	1.58	0.14	-15.86	0.16	-1.34	0.55
AJAC	41.93	8.76	15.94	0.14	21.21	0.15	0.19	0.45
AL30	33.53	-86.85	0.57	0.21	-13.05	0.25	-0.96	0.91
AL40	32.96	-86.01	0.53	0.26	-12.89	0.32	0.76	1.18
AL50	33.17	-87.50	-1.20	0.41	-13.12	0.46	-1.27	0.96
AL60	32.41	-86.27	0.63	0.25	-12.55	0.27	-2.80	1.07
AL70	31.78	-85.97	0.82	0.23	-12.41	0.28	-1.58	0.99
AL90	30.69	-88.03	0.37	0.27	-12.27	0.33	-3.86	1.05

continued . . .

. . . continued

Site code	φ [°]	λ [°]	$\dot{N}$	$\pm\,\sigma_{\dot{N}}$	$\dot{E}$	$\pm\,\sigma_{\dot{E}}$	$\dot{U}$	$\pm\,\sigma_{\dot{U}}$
ALCI	48.46	38.91	11.03	0.26	24.46	0.24	0.20	0.79
ALES	62.48	6.20	16.43	0.26	13.87	0.20	1.97	0.45
ALGO	45.96	-78.07	2.51	0.11	-16.45	0.11	3.13	0.37
ALIC	-23.67	133.89	59.14	0.10	32.10	0.12	-0.36	0.37
ALRT	82.49	-62.34	6.87	0.37	-22.48	0.31	6.33	0.44
AMC2	38.80	-104.52	-5.70	0.11	-14.38	0.10	-0.67	0.38
ANDO	69.28	16.01	15.66	0.27	14.05	0.26	1.49	0.57
ANG1	29.30	-95.49	-3.17	0.59	-13.81	0.72	1.06	1.46
ANP5	39.01	-76.61	4.41	0.25	-14.45	0.24	-2.75	0.70
ANTO	29.49	-98.58	-3.62	0.30	-11.90	0.30	-0.36	1.28
AOML	25.73	-80.16	2.76	0.27	-9.76	0.30	-0.28	0.82
AOPR	18.35	-66.75	14.05	0.41	8.34	0.58	-0.53	1.38
ARBT	35.71	-91.63	-0.62	0.25	-14.23	0.24	-1.55	1.01
ARCM	33.54	-92.88	-1.03	0.17	-13.21	0.20	-1.29	0.74
ARFY	36.12	-94.18	-1.78	0.18	-13.93	0.19	-1.90	0.71
ARGI	62.00	-6.78	17.49	1.46	11.85	1.93	-1.11	5.19
ARHP	33.70	-93.60	-2.02	0.25	-12.74	0.24	-0.08	0.90
ARHR	36.18	-93.03	-0.63	0.28	-13.94	0.26	-1.45	0.99
ARJM	66.32	18.12	15.21	0.42	15.47	0.23	7.98	0.64
ARP3	27.84	-97.06	-3.68	0.25	-14.26	0.29	-1.42	0.72
ARPG	36.06	-90.52	-0.26	0.18	-13.93	0.19	-1.35	0.72
ARTU	56.43	58.56	6.15	0.11	25.21	0.12	0.34	0.49
ASC1	-7.95	-14.41	11.09	0.36	-5.29	0.41	-1.15	1.03
ASCG	-7.92	-14.33	12.29	1.02	-5.38	2.03	1.45	3.34
ASHV	35.60	-82.55	2.82	0.49	-13.71	0.52	-0.00	1.77
ASUB	36.21	-81.68	2.61	0.21	-14.09	0.27	-0.63	0.76
AUCK	-36.60	174.83	39.48	0.12	4.34	0.13	-0.62	0.32
AUDR	58.42	24.31	12.93	0.27	20.61	0.32	3.21	0.98
AUS5	30.31	-97.76	-4.59	0.56	-10.42	0.45	-3.56	1.99
AUTN	46.95	4.29	15.99	0.15	19.32	0.12	-1.51	0.43
AVCA	43.06	-82.69	1.80	0.14	-16.42	0.19	-1.43	0.63
AXPV	43.49	5.33	16.49	0.15	20.06	0.14	0.02	0.56
BACA	46.56	26.91	13.27	0.13	22.38	0.14	0.26	0.52
BACK	-74.43	-102.48	9.58	0.45	17.39	0.54	12.94	1.25
BACO	39.40	-76.61	4.08	0.27	-14.77	0.23	-1.70	0.82
BADH	50.23	8.61	15.72	0.12	19.06	0.14	0.54	0.52
BAHR	26.21	50.61	29.90	0.19	31.16	0.18	-0.36	0.44

continued . . .

...continued

Site code	φ [°]	λ [°]	$\dot{N}$	$\pm\,\sigma_{\dot{N}}$	$\dot{E}$	$\pm\,\sigma_{\dot{E}}$	$\dot{U}$	$\pm\,\sigma_{\dot{U}}$
BAIA	47.65	23.56	13.58	0.13	22.36	0.15	0.09	0.55
BAIE	49.19	-68.26	6.13	0.21	-16.23	0.21	3.88	0.75
BAKE	64.32	-96.00	-4.44	0.17	-18.75	0.16	11.48	0.58
BAN2	13.03	77.51	34.83	0.29	42.89	0.41	0.28	0.78
BARH	44.40	-68.22	7.13	0.12	-15.14	0.12	0.43	0.37
BARN	44.10	-71.16	7.76	5.77	-12.83	3.15	13.16	21.79
BAUS	56.41	24.19	13.37	0.46	20.34	0.33	0.77	0.97
BAYR	43.45	-83.89	0.78	1.85	-16.87	3.82	-3.00	34.07
BBYS	48.75	19.15	14.72	0.20	21.13	0.18	0.26	0.63
BCLN	41.41	2.00	16.66	0.71	19.93	0.72	3.74	2.63
BELE	-1.41	-48.46	14.29	1.37	-3.46	0.86	4.01	4.55
BELF	54.58	-5.93	16.55	0.14	14.44	0.24	1.17	0.54
BELL	41.60	1.40	16.25	0.16	19.86	0.15	0.27	0.44
BENN	-84.79	-116.46	0.40	0.36	16.26	0.55	7.31	1.30
BET1	60.79	-161.84	-23.18	0.29	-3.51	0.33	-0.82	0.98
BIAZ	43.47	-1.54	15.85	1.18	19.87	1.15	-0.25	6.96
BIL5	45.97	-108.00	-7.86	0.19	-15.07	0.17	-2.43	0.62
BISK	50.26	17.43	14.87	0.31	20.13	0.23	-0.68	1.05
BJCO	6.38	2.45	19.01	0.21	21.93	0.20	-0.76	0.60
BJU0	64.48	21.57	13.78	0.49	17.62	0.44	9.84	0.78
BLA1	37.21	-80.42	3.26	0.20	-14.21	0.22	-0.28	0.73
BNDY	-24.91	152.32	53.58	0.36	23.67	0.27	-1.12	0.78
BNFY	30.85	-85.60	1.09	0.22	-12.42	0.26	-0.98	0.90
BOD3	67.29	14.43	15.51	0.20	14.22	0.18	3.56	0.56
BOGI	52.47	21.04	14.40	0.13	20.74	0.12	0.14	0.53
BOMJ	-13.26	-43.42	12.79	0.37	-4.55	0.41	2.64	1.28
BOR1	52.28	17.07	14.75	0.09	20.13	0.09	-0.22	0.39
BORJ	53.58	6.67	15.51	0.12	17.75	0.10	-1.17	0.55
BORK	53.56	6.75	15.80	0.25	17.67	0.23	0.16	0.75
BORR	39.91	-0.08	16.33	0.15	20.12	0.14	-0.59	0.51
BPDL	52.04	23.13	14.15	0.18	21.17	0.22	-0.47	0.65
BRAZ	-15.95	-47.88	12.58	0.17	-4.04	0.16	-0.16	0.52
BRFT	-3.88	-38.43	13.57	0.29	-4.23	0.20	-0.42	0.67
BRGS	60.29	5.27	16.27	0.29	14.28	0.23	2.67	0.53
BRIP	-75.80	158.47	-12.73	0.28	8.26	0.26	-0.94	0.88
BRMF	45.73	4.94	16.91	0.41	19.81	0.50	1.21	1.88
BRMU	32.37	-64.70	8.97	0.11	-11.94	0.13	-0.72	0.37

continued ...

. . . continued

Site code	φ [°]	λ [°]	$\dot{N}$	$\pm\,\sigma_{\dot{N}}$	$\dot{E}$	$\pm\,\sigma_{\dot{E}}$	$\dot{U}$	$\pm\,\sigma_{\dot{U}}$
BRST	48.38	-4.50	17.10	0.14	16.91	0.15	-0.14	0.41
BRTW	27.95	-81.78	1.60	0.28	-11.71	0.26	-1.09	0.78
BRU5	43.89	-69.95	6.27	0.26	-15.73	0.29	0.28	0.80
BRUS	50.80	4.36	15.88	0.12	18.16	0.13	0.46	0.41
BSCN	47.25	5.99	15.91	0.14	19.34	0.14	0.51	0.42
BSMK	46.82	-100.82	-3.46	1.32	-15.71	1.07	-4.65	5.22
BUDP	55.74	12.50	15.07	0.12	18.09	0.13	0.97	0.54
BUE1	-34.57	-58.52	12.34	0.29	-0.75	0.28	1.84	0.76
BUMS	-85.96	174.50	-12.06	0.51	6.46	0.69	-1.50	1.66
BURI	-79.15	155.89	-12.88	0.25	6.51	0.24	-0.52	0.88
BVHS	29.34	-89.41	-0.69	0.22	-12.38	0.25	-4.46	0.73
BYDG	53.13	17.99	14.46	0.15	19.93	0.14	1.30	0.77
CACE	39.48	-6.34	17.16	0.15	18.29	0.14	-0.14	0.42
CAEN	49.18	-0.46	16.55	0.10	17.24	0.12	-1.23	0.41
CAGL	39.14	8.97	15.98	0.13	21.86	0.15	-0.13	0.43
CAGS	45.59	-75.81	3.41	0.16	-16.25	0.17	3.43	0.53
CALU	41.73	-87.54	0.33	0.19	-15.47	0.22	-2.63	0.73
CANT	43.47	-3.80	16.86	0.37	18.22	0.27	0.32	0.65
CAPF	-66.01	-60.56	9.54	0.80	16.34	0.83	0.56	1.78
CARM	46.87	-68.01	6.62	0.22	-15.07	0.31	0.82	0.70
CAS1	-66.28	110.52	-9.62	0.16	1.42	0.13	1.70	0.39
CASB	53.85	-9.29	17.00	0.47	13.89	0.52	3.07	1.54
CASC	38.69	-9.42	16.98	0.16	17.94	0.18	0.07	0.50
CASP	42.82	-106.38	-6.01	0.22	-15.43	0.17	-1.35	0.66
CAYU	42.94	-76.54	3.68	0.21	-15.98	0.23	-1.96	0.89
CBMD	19.74	-79.76	5.42	0.55	-5.82	0.59	-0.76	1.46
CBSB	19.71	-79.83	3.42	0.39	-7.72	0.39	-2.05	1.03
CCV5	28.46	-80.55	3.22	0.22	-11.74	0.25	-2.14	0.73
CEBR	40.45	-4.37	16.51	0.16	18.73	0.17	-0.65	0.73
CEDU	-31.87	133.81	58.92	0.11	28.89	0.13	-0.44	0.36
CEFE	-20.31	-40.32	13.57	0.41	-3.77	0.42	2.39	1.55
CFRM	49.68	18.35	15.04	0.16	20.81	0.18	0.54	0.75
CGGN	10.12	9.12	17.67	1.48	24.68	1.30	0.19	1.32
CHA1	32.76	-79.84	3.37	0.26	-12.39	0.34	-1.93	0.95
CHAN	43.79	125.44	-12.12	0.22	27.00	0.22	-0.41	0.51
CHAT	-43.96	-176.57	33.03	0.15	-40.60	0.16	-0.14	0.42
CHB5	45.65	-84.47	1.13	0.24	-16.36	0.21	-1.14	0.78

continued . . .

...continued

Site code	φ [°]	λ [°]	$\dot{N}$	$\pm\,\sigma_{\dot{N}}$	$\dot{E}$	$\pm\,\sigma_{\dot{E}}$	$\dot{U}$	$\pm\,\sigma_{\dot{U}}$
CHIZ	46.13	-0.41	16.51	0.12	18.52	0.13	0.19	0.38
CHL1	38.78	-75.09	4.24	0.33	-14.49	0.52	-0.55	1.18
CHPI	-22.68	-45.00	12.57	0.21	-3.94	0.15	0.54	0.58
CHR1	36.93	-76.01	0.45	0.49	-13.65	0.47	0.35	1.24
CHT1	41.67	-69.95	6.29	0.46	-16.52	0.50	-0.31	1.14
CHTI	-43.74	-176.62	32.81	0.16	-40.83	0.17	-1.93	0.45
CHUR	58.76	-94.09	-3.73	0.14	-18.63	0.12	10.68	0.40
CJTR	34.82	-92.27	-1.11	0.17	-14.27	0.20	-0.86	0.68
CKIS	-21.20	-159.80	35.30	0.19	-62.60	0.24	-0.81	0.76
CLIB	50.77	15.06	15.12	0.20	19.46	0.17	1.40	0.82
CLK5	44.94	-97.96	-5.73	0.33	-16.23	0.25	-1.78	0.80
CLRK	-77.34	-141.87	-2.88	0.38	18.26	0.37	0.07	1.19
CN13	24.07	-74.53	6.63	0.65	-9.56	0.72	-0.01	2.34
CN14	20.98	-73.68	7.62	0.56	-7.32	0.57	0.39	1.75
CN15	26.56	-78.69	5.70	0.55	-11.89	0.45	3.79	2.59
CN16	21.42	-77.85	5.94	0.56	-7.84	0.63	2.13	1.89
CN23	17.26	-88.78	1.50	0.67	-7.28	0.73	-2.09	2.16
CN24	19.58	-88.05	1.82	0.51	-7.46	0.53	-0.27	1.47
CN28	8.63	-79.03	15.36	0.59	18.97	0.65	-0.40	1.91
CN29	14.05	-83.37	10.07	2.88	12.07	3.80	2.07	26.41
CN33	8.49	-80.33	10.69	0.99	18.15	1.20	2.50	2.50
CN34	8.55	-78.01	14.89	11.94	21.29	7.63	-17.45	15.04
CN35	13.38	-81.36	8.03	0.84	11.33	0.71	3.31	2.09
CN41	8.94	-68.04	11.37	0.91	-2.87	1.03	-7.59	3.30
CN46	12.49	-61.43	15.55	0.73	12.33	1.01	0.57	2.17
CN53	21.78	-72.25	6.84	1.39	-6.03	1.36	1.52	4.88
CNC0	21.17	-86.82	2.14	2.28	-6.70	4.97	0.92	4.58
CNIV	51.52	31.31	13.04	0.18	22.36	0.18	1.20	0.66
CNMR	15.23	145.74	12.89	0.25	-17.54	0.32	-1.44	0.75
COLA	34.08	-81.12	4.29	0.77	-11.64	0.68	2.63	3.18
CONO	35.70	-81.23	2.95	3.81	-14.74	1.70	-7.90	11.15
CORB	38.20	-77.37	4.30	0.45	-14.02	0.58	-0.16	1.70
CORC	27.74	-97.44	-2.05	0.43	-12.40	0.39	-4.00	1.95
COTE	-77.81	162.00	-12.55	0.27	8.50	0.25	-0.65	0.90
COVG	30.48	-90.10	-0.54	0.23	-12.17	0.21	-1.65	0.66
COVX	36.90	-75.71	4.20	0.37	-14.18	0.42	-1.10	1.21
CPAR	50.04	15.78	15.23	0.16	20.49	0.14	0.74	0.77

continued ...

. . . continued

Site code	φ [°]	λ [°]	$\dot{N}$	$\pm\,\sigma_{\dot{N}}$	$\dot{E}$	$\pm\,\sigma_{\dot{E}}$	$\dot{U}$	$\pm\,\sigma_{\dot{U}}$
CRAK	50.10	13.73	15.14	0.16	20.24	0.17	0.58	0.76
CRAO	44.41	33.99	12.14	0.19	24.26	0.19	0.05	0.63
CRDI	-82.86	-53.20	11.31	0.73	7.03	0.49	0.82	1.25
CRST	30.73	-86.51	0.20	0.22	-12.63	0.25	-0.64	0.85
CTAB	49.41	14.68	15.01	0.17	20.33	0.15	0.79	0.74
CTBR	41.50	-73.42	4.84	0.17	-14.92	0.27	-1.20	0.75
CTGU	41.29	-72.67	5.23	0.16	-15.02	0.23	-1.75	0.71
CTPU	41.90	-71.89	5.46	0.17	-14.78	0.26	-1.38	0.77
CTWN	-33.95	18.47	19.38	0.56	17.61	0.31	1.80	1.69
CUIB	-15.56	-56.07	12.27	1.42	-4.00	0.86	6.15	4.06
CUSV	13.74	100.53	-9.60	0.57	23.35	0.37	-2.66	0.99
CVMS	35.54	-89.64	-0.13	0.21	-13.89	0.22	0.21	0.91
DAKR	14.72	-17.44	17.51	0.48	19.92	0.33	-1.35	1.41
DANE	74.31	-20.20	20.33	0.17	-11.07	0.23	3.75	0.73
DARE	53.34	-2.64	16.42	0.12	15.65	0.14	0.36	0.43
DAVM	-68.58	77.97	-5.01	0.15	-3.18	0.11	-0.72	0.32
DEAR	-30.67	23.99	19.08	0.52	15.91	0.54	1.38	1.18
DEFI	41.28	-84.41	3.23	5.27	-16.82	2.04	-2.80	15.37
DEGE	60.03	20.38	12.72	0.88	19.33	0.67	6.93	1.07
DELM	51.99	4.39	15.76	0.11	17.54	0.09	-0.50	0.34
DENE	39.68	-75.74	4.35	0.22	-15.04	0.29	-1.50	0.86
DENT	50.93	3.40	16.29	0.11	17.54	0.15	-0.78	0.34
DEVI	-81.48	161.98	-12.38	0.28	6.83	0.28	0.37	0.93
DGLS	60.42	8.50	15.35	0.45	14.14	0.34	3.91	0.85
DNRC	39.16	-75.52	4.44	0.27	-14.44	0.50	-2.65	0.95
DOBS	36.43	-80.72	2.93	0.20	-13.88	0.19	-0.46	0.68
DOMS	62.07	9.11	15.73	0.29	14.63	0.24	4.23	0.66
DOUR	50.09	4.59	15.96	0.12	18.26	0.11	0.52	0.37
DREM	51.03	13.73	15.43	0.14	19.75	0.14	-0.16	0.43
DRV5	36.96	-76.56	5.87	0.26	-13.48	0.22	-2.35	0.64
DSL1	70.33	-148.47	-21.04	0.36	-7.94	0.27	-4.76	0.85
DUBO	50.26	-95.87	-4.35	0.12	-17.44	0.10	0.95	0.51
DUM1	-66.67	140.00	-11.59	0.20	8.24	0.19	-0.72	0.45
DUPT	-64.80	-62.82	11.35	0.56	13.60	0.48	8.40	1.32
EBRE	40.82	0.49	16.14	0.20	20.07	0.19	-0.47	0.59
ECSD	43.73	-96.61	-3.13	0.16	-15.63	0.16	-1.98	0.61
EDOC	70.31	-148.32	-18.86	2.19	-7.73	1.81	-3.80	5.33

continued . . .

. . . continued

Site code	φ [°]	λ [°]	$\dot{N}$	$\pm\,\sigma_{\dot{N}}$	$\dot{E}$	$\pm\,\sigma_{\dot{E}}$	$\dot{U}$	$\pm\,\sigma_{\dot{U}}$
EGLT	45.40	2.05	16.11	0.14	19.17	0.13	0.36	0.44
EIJS	50.76	5.68	15.97	0.10	18.01	0.10	0.45	0.37
ELEN	16.92	-89.87	0.89	0.31	-7.04	0.33	1.65	1.03
ENG1	29.88	-89.94	-0.94	0.40	-12.42	0.38	-1.72	1.08
ENIS	54.40	-7.64	17.03	0.16	12.70	0.21	0.35	0.55
ENTZ	48.55	7.64	15.81	0.10	19.37	0.11	-1.12	0.49
EPRT	44.91	-66.99	7.15	0.14	-15.33	0.17	-0.17	0.59
ESCO	42.69	0.98	16.50	0.15	19.44	0.14	-0.07	0.43
ESCU	47.07	-64.80	8.33	0.22	-15.85	0.23	-0.57	0.79
EUR2	79.99	-85.94	-2.47	0.51	-22.62	0.88	7.19	1.52
EUSK	50.67	6.76	16.52	0.12	18.36	0.12	-1.90	0.45
EVPA	45.22	33.16	12.59	0.18	24.08	0.16	-0.56	0.77
EXU0	23.56	-75.87	5.09	0.30	-9.62	0.38	-2.03	1.04
FALL	-85.31	-143.63	-5.29	0.34	12.70	0.37	3.69	1.31
FFMJ	50.09	8.66	15.82	0.22	18.79	0.21	0.42	0.67
FIE0	-76.14	168.42	-11.58	0.43	10.33	0.36	-1.05	1.30
FLIN	54.73	-101.98	-6.81	0.12	-17.70	0.10	3.28	0.50
FLIU	25.75	-80.37	3.49	0.33	-10.27	0.38	-1.77	1.22
FLM5	-77.53	160.27	-12.08	0.39	8.01	0.38	0.89	1.45
FLRS	39.45	-31.13	20.21	0.21	-10.04	0.37	-0.88	1.03
FONP	-65.25	-61.65	10.23	1.73	17.74	1.41	10.38	4.23
FOYL	54.98	-7.34	17.18	0.17	14.36	0.19	1.97	0.51
FREE	26.70	-78.99	4.10	0.82	-11.43	0.76	-0.11	2.28
FREI	-62.19	-58.98	17.46	0.81	9.86	0.70	-2.88	1.34
FRKN	35.19	-83.39	1.88	0.21	-13.95	0.25	-0.97	0.76
FTP4	-78.93	162.56	-11.93	0.25	8.35	0.25	0.41	1.03
FUNC	32.65	-16.91	17.81	0.22	14.63	0.26	-0.42	0.96
GAAT	33.95	-83.33	1.85	0.25	-13.14	0.30	-0.63	0.88
GABR	34.86	-84.33	2.01	0.30	-13.44	0.30	-1.27	1.03
GACC	33.55	-82.13	3.25	0.18	-13.57	0.27	-0.68	0.73
GACL	33.63	-85.16	1.10	0.37	-14.14	0.43	-0.95	0.87
GACR	32.38	-83.35	2.08	0.27	-13.05	0.30	-0.08	0.90
GAIA	41.11	-8.59	17.04	0.15	17.93	0.15	-0.29	0.53
GAIT	39.13	-77.22	3.98	0.29	-14.83	0.35	0.31	1.25
GAL1	29.33	-94.74	-3.23	0.32	-11.41	0.27	-4.60	0.96
GANP	49.03	20.32	14.15	0.18	20.72	0.17	-0.65	0.54
GARF	41.42	-81.61	2.11	0.21	-15.46	0.20	-2.96	0.71

continued . . .

...continued

Site code	φ [°]	λ [°]	$\dot{N}$	$\pm\,\sigma_{\dot{N}}$	$\dot{E}$	$\pm\,\sigma_{\dot{E}}$	$\dot{U}$	$\pm\,\sigma_{\dot{U}}$
GAST	35.31	-81.19	2.55	0.19	-13.71	0.22	-0.46	0.67
GCEA	19.29	-81.38	3.82	0.74	-7.30	0.61	-1.00	1.97
GDMA	47.75	-90.34	-2.31	0.18	-17.44	0.20	0.19	0.62
GLPM	-0.74	-90.30	4.45	0.22	-14.14	0.21	-2.57	0.86
GLPS	-0.74	-90.30	10.47	0.17	50.83	0.18	-0.80	0.43
GLSV	50.36	30.50	12.36	0.15	22.40	0.13	0.20	0.43
GMSD	30.56	131.02	-22.57	0.30	30.05	0.33	-0.59	0.63
GNVL	29.69	-82.28	2.37	0.20	-11.91	0.22	-0.23	0.68
GODE	39.02	-76.83	4.13	0.11	-14.57	0.11	-1.21	0.41
GOGA	33.41	-83.47	1.81	0.24	-13.73	0.26	-0.51	0.92
GOPM	49.91	14.79	15.08	0.10	20.29	0.10	0.62	0.42
GOUG	-40.35	-9.88	18.46	0.45	21.16	0.59	-0.74	1.28
GRAS	43.75	6.92	16.10	0.10	20.59	0.11	0.11	0.28
GRE0	12.22	-61.64	15.69	0.34	13.40	0.45	-1.49	1.06
GRIS	29.27	-89.96	-1.23	2.41	-10.27	2.33	-0.74	4.18
GRN0	63.04	13.97	15.14	0.49	15.32	0.50	8.39	0.97
GRTN	38.86	-83.88	1.87	0.17	-14.27	0.20	-3.48	0.73
GTK0	21.43	-71.14	6.85	0.34	-8.63	0.40	-0.58	1.05
GUAM	13.59	144.87	4.75	0.20	-8.55	0.22	-0.31	0.64
GUAX	28.88	-118.29	25.33	0.46	-47.75	0.59	-0.01	1.59
GUIP	48.44	-4.41	16.70	0.11	16.96	0.13	0.36	0.46
GUUG	13.43	144.80	4.48	0.21	-7.59	0.25	-1.51	0.63
GWWL	52.74	15.21	14.74	0.15	19.69	0.14	-0.71	0.74
HAAG	-77.04	-78.29	10.34	0.63	12.03	0.88	2.77	1.43
HAC6	34.28	-87.86	1.44	0.55	-14.31	0.43	0.90	1.03
HAG6	39.55	-77.71	4.11	0.22	-15.21	0.22	-3.02	0.76
HALY	29.14	36.10	23.00	0.31	27.18	0.32	1.30	0.97
HAMM	30.51	-90.47	-0.02	0.26	-12.13	0.36	-1.53	1.24
HAMP	42.32	-72.64	4.18	0.17	-13.52	0.25	0.03	0.65
HARK	-25.89	27.69	18.61	0.16	17.81	0.13	0.87	0.45
HASM	56.09	13.72	14.84	0.26	18.37	0.17	1.32	0.63
HBCH	43.85	-82.64	1.77	0.18	-15.63	0.21	-1.45	0.79
HBRK	38.30	-97.29	-2.76	0.66	-14.16	0.87	-0.70	2.72
HCES	36.33	-89.17	-0.22	0.21	-13.98	0.30	-1.64	0.82
HDIL	40.56	-89.29	0.31	0.21	-15.49	0.24	-2.23	0.89
HELG	54.17	7.89	15.91	0.10	17.64	0.13	0.32	0.44
HERS	50.87	0.34	16.67	0.11	16.82	0.12	-0.45	0.41

continued ...

. . . continued

Site code	φ [°]	λ [°]	$\dot{N}$	$\pm\,\sigma_{\dot{N}}$	$\dot{E}$	$\pm\,\sigma_{\dot{E}}$	$\dot{U}$	$\pm\,\sigma_{\dot{U}}$
HILB	36.05	-79.10	1.37	9.68	-13.63	3.07	-5.54	5.39
HILO	19.72	-155.05	35.54	0.22	-62.98	0.26	-1.16	0.78
HIPT	35.97	-80.01	4.10	0.77	-12.79	0.67	-1.69	2.34
HJOR	63.42	-41.15	15.73	1.81	-15.49	2.60	-1.51	7.40
HKLO	35.68	-95.86	-2.47	0.35	-14.04	0.35	1.44	1.38
HLFX	44.68	-63.61	8.77	0.12	-15.28	0.13	-0.81	0.39
HNLC	21.30	-157.86	34.73	0.19	-62.80	0.18	-0.69	0.53
HNPT	38.59	-76.13	4.37	0.16	-14.45	0.16	-1.83	0.36
HNUS	-34.42	19.22	19.12	0.53	16.62	0.53	-0.07	1.26
HOB2	-42.80	147.44	55.32	0.14	14.00	0.16	-1.08	0.37
HOBU	53.05	10.48	15.40	0.10	18.72	0.12	0.21	0.42
HOE2	54.76	8.29	15.53	0.15	17.89	0.17	-0.32	0.59
HOLM	70.74	-117.76	-12.40	0.15	-17.46	0.14	2.73	0.40
HONS	70.98	25.96	13.13	0.40	16.89	0.39	2.56	0.70
HOS0	63.67	20.39	13.73	0.41	17.44	0.30	10.27	0.88
HOUM	29.59	-90.72	-1.42	0.27	-12.26	0.22	-3.90	0.71
HOUS	29.78	-95.43	-2.53	0.52	-14.52	0.58	-9.46	2.10
HOWE	-87.42	-149.43	-5.85	0.56	14.60	0.54	-1.61	1.29
HOWN	-77.53	-86.77	8.53	0.40	13.04	0.46	0.91	1.19
HRMM	51.45	-1.28	16.53	0.11	16.55	0.11	-0.22	0.40
HRST	49.67	-83.51	0.60	0.22	-17.56	0.20	7.45	0.67
HUGO	-64.96	-65.67	11.28	0.74	15.36	0.83	0.43	2.11
HYDE	17.42	78.55	34.93	0.19	40.55	0.18	-0.25	0.53
IBIZ	38.91	1.45	16.08	0.52	20.77	0.59	-3.03	1.95
ICT1	37.59	-97.31	-2.32	0.20	-14.28	0.21	0.48	0.88
IGEO	47.03	28.84	12.98	0.15	22.56	0.16	0.38	0.59
IGGY	-83.31	156.25	-12.76	0.28	4.47	0.31	-1.66	1.06
IISC	13.02	77.57	34.64	0.25	42.60	0.28	0.26	0.70
ILDX	46.01	-1.18	16.50	0.19	18.52	0.21	-1.65	0.85
ILHA	-20.43	-51.34	12.15	0.61	-2.89	0.43	-1.25	1.53
ILSA	39.78	-89.61	-0.23	0.20	-14.58	0.32	-2.39	0.62
ILUC	40.10	-88.22	0.93	0.38	-14.50	0.39	-1.97	0.92
IMBT	-28.23	-48.66	12.32	2.27	-4.58	2.96	-1.61	8.80
IMPZ	-5.49	-47.50	12.58	0.23	-4.70	0.21	-2.13	0.86
INAB	40.30	-85.21	1.94	0.24	-15.20	0.30	-1.61	0.91
INES	38.13	-87.55	0.97	0.25	-14.31	0.35	-1.22	0.94
INGG	39.36	-85.51	2.66	0.50	-14.33	0.37	-2.35	1.36

continued . . .

. . . continued

Site code	φ [°]	λ [°]	$\dot{N}$	$\pm\sigma_{\dot{N}}$	$\dot{E}$	$\pm\sigma_{\dot{E}}$	$\dot{U}$	$\pm\sigma_{\dot{U}}$
INVM	57.49	-4.22	16.73	0.14	14.12	0.14	1.58	0.50
INWN	41.08	-86.60	1.69	0.30	-15.38	0.26	-2.18	0.90
IQAL	63.76	-68.51	5.91	0.17	-18.71	0.15	5.04	0.53
IQUI	-3.77	-73.27	10.69	0.27	-4.11	0.34	-1.47	1.09
IRBE	57.55	21.85	13.64	0.78	19.67	0.74	3.19	1.98
IRKM	52.22	104.32	-6.71	0.10	25.34	0.08	0.49	0.30
ISCO	5.54	-87.06	77.15	0.79	50.04	0.81	-3.50	2.89
ISPA	-27.15	-109.38	-6.28	0.21	66.47	0.22	-0.87	0.64
IZAN	28.31	-16.50	16.84	0.22	15.33	0.22	-1.62	0.59
JAB2	-12.66	132.89	58.80	0.37	35.32	0.34	-3.24	1.09
JCT1	30.48	-99.80	-3.41	0.85	-12.07	1.11	1.80	3.42
JFNG	30.52	114.49	-10.61	0.47	32.78	0.42	0.37	1.65
JFWS	42.91	-90.25	-0.75	0.19	-15.74	0.20	-2.83	0.74
JOEN	62.39	30.10	11.91	0.12	20.55	0.11	3.98	0.48
JONM	57.75	14.06	14.75	0.23	17.87	0.15	3.71	0.48
JOZE	52.10	21.03	14.45	0.11	21.00	0.10	0.54	0.43
JXVL	30.48	-81.70	2.46	0.21	-12.18	0.22	-0.03	0.99
KAR0	59.44	13.51	14.70	0.24	17.10	0.20	5.92	0.62
KARL	49.01	8.41	15.99	0.25	19.59	0.31	-1.01	0.88
KARR	-20.98	117.10	58.80	0.13	38.66	0.13	0.11	0.36
KAT1	-14.38	132.15	59.20	0.22	35.43	0.22	-0.30	0.73
KAUS	69.02	23.02	14.57	0.36	16.96	0.36	6.18	0.79
KELY	66.99	-50.94	11.78	0.14	-18.16	0.16	4.38	0.54
KERM	-49.35	70.26	-2.74	0.20	4.63	0.18	0.10	0.50
KEVO	69.76	27.01	13.80	13.52	18.30	6.47	7.06	15.91
KEW5	47.23	-88.62	-2.06	0.20	-16.59	0.23	0.06	0.83
KHAJ	48.52	135.05	-13.71	0.21	21.98	0.21	0.18	0.69
KHAR	50.01	36.24	11.61	0.22	24.06	0.22	0.97	0.69
KIRI	1.35	172.92	31.09	0.21	-67.78	0.22	-0.17	0.78
KIRM	67.88	21.06	14.55	0.11	16.03	0.10	7.23	0.38
KIRU	67.86	20.97	14.61	0.13	15.97	0.11	7.02	0.49
KIVE	62.82	25.70	12.46	0.34	19.72	0.24	7.14	0.85
KJUN	30.22	-92.05	-0.09	1.97	-22.56	5.27	-8.56	4.42
KLOP	50.22	8.73	15.79	0.13	19.04	0.12	-0.36	0.40
KMOR	81.25	-63.53	6.91	11.76	-21.98	0.00	1.55	0.00
KNGS	44.22	-76.52	3.53	0.14	-15.70	0.17	0.49	0.58
KNS5	33.48	-79.34	3.52	0.33	-12.98	0.35	-3.80	0.85

continued . . .

. . . continued

Site code	φ [°]	λ [°]	$\dot{N}$	$\pm\,\sigma_{\dot{N}}$	$\dot{E}$	$\pm\,\sigma_{\dot{E}}$	$\dot{U}$	$\pm\,\sigma_{\dot{U}}$
KNTN	40.63	-83.61	1.73	0.16	-15.23	0.18	-2.02	0.75
KOK1	21.98	-159.76	35.23	0.28	-62.52	0.33	-0.70	0.89
KOKM	21.98	-159.76	34.68	0.12	-62.16	0.13	-0.46	0.38
KOSG	52.18	5.81	16.25	0.12	17.93	0.13	-0.59	0.41
KOUC	-20.56	164.29	47.69	0.17	23.09	0.25	-1.18	0.42
KOUG	5.10	-52.64	13.34	0.39	-4.00	0.41	2.29	1.35
KOUR	5.25	-52.81	13.02	0.18	-4.40	0.19	-0.13	0.61
KRA0	62.88	17.93	14.42	0.30	17.17	0.26	9.58	0.88
KRSS	58.08	7.91	15.49	0.37	15.99	0.26	1.62	0.45
KRTV	50.71	78.62	1.13	0.33	26.52	0.28	-0.43	1.32
KST5	39.04	-96.04	-2.23	0.21	-13.79	0.28	-0.99	0.82
KSTU	55.99	92.79	-4.45	0.44	24.87	0.41	1.44	1.11
KSU1	39.10	-96.61	-2.45	0.20	-14.85	0.24	-0.27	0.62
KULU	65.58	-37.15	15.90	0.40	-15.94	0.42	4.43	1.61
KUN0	56.10	15.59	15.05	0.75	17.86	0.44	2.25	1.05
KUNZ	49.11	15.20	15.52	0.16	21.13	0.14	0.08	0.60
KURE	58.26	22.51	13.15	0.14	19.87	0.14	2.75	0.67
KUUJ	55.28	-77.75	3.23	0.25	-18.50	0.21	13.95	0.68
KUUS	65.91	29.03	12.33	0.44	19.30	0.34	6.83	1.27
KUWT	29.32	47.97	29.79	0.30	27.63	0.51	0.89	1.36
KVTX	27.55	-97.89	-2.73	0.29	-12.05	0.24	-3.25	0.78
KWJ1	8.72	167.73	29.36	0.44	-69.25	0.54	-1.07	1.55
KWST	24.55	-81.75	2.87	0.24	-10.17	0.25	-0.94	0.79
KYBO	39.04	-84.72	1.52	0.20	-14.35	0.22	-1.71	0.79
KYMH	38.18	-83.44	2.22	0.21	-14.17	0.23	-1.24	0.72
KYTB	37.35	-87.50	1.86	0.27	-14.20	0.31	-2.13	1.00
KYTC	36.99	-86.47	1.68	0.24	-14.42	0.26	-0.48	0.77
KYTD	37.68	-85.85	2.26	0.35	-13.25	0.30	-2.60	0.88
KYTE	38.28	-85.60	1.36	0.27	-14.62	0.28	-2.09	0.93
KYTG	38.08	-84.49	2.05	0.26	-14.53	0.22	-1.31	0.73
KYTH	37.07	-84.62	2.40	0.29	-14.57	0.34	-2.43	0.88
KYTK	37.15	-83.76	3.61	0.62	-13.09	0.45	-0.34	1.12
KYTL	37.48	-82.54	2.29	0.23	-13.98	0.25	-2.80	0.79
KYW1	24.58	-81.65	2.43	0.27	-9.49	0.29	-0.22	0.77
KZN2	55.79	49.12	9.06	1.13	22.71	0.84	-0.69	3.83
LAMA	53.89	20.67	14.43	0.10	20.18	0.09	-0.29	0.42
LAMT	41.00	-73.91	4.79	5.01	-14.53	1.86	5.88	3.21

continued . . .

...continued

Site code	φ [°]	λ [°]	$\dot{N}$	$\pm\,\sigma_{\dot{N}}$	$\dot{E}$	$\pm\,\sigma_{\dot{E}}$	$\dot{U}$	$\pm\,\sigma_{\dot{U}}$
LANS	42.67	-84.66	1.06	0.15	-15.91	0.16	-1.27	0.61
LCDT	42.30	-87.96	0.36	0.14	-15.50	0.17	-2.19	0.57
LCHS	36.38	-89.47	0.19	0.20	-13.83	0.18	-0.51	0.81
LCKM	26.91	80.96	34.32	0.42	37.64	0.37	-2.91	1.04
LCSB	19.67	-80.08	5.02	0.63	-6.17	0.66	-0.16	1.87
LEBA	39.43	-84.28	1.88	0.16	-14.67	0.18	-2.30	0.62
LEES	28.83	-81.81	2.60	0.25	-11.90	0.28	-1.03	0.81
LEIJ	51.35	12.37	14.97	0.13	19.36	0.12	-0.22	0.46
LEK0	60.72	14.88	14.30	0.25	17.20	0.19	8.01	0.67
LEON	42.59	-5.65	16.71	0.20	17.65	0.21	-0.27	0.49
LESV	31.14	-93.27	-1.39	0.18	-12.52	0.20	-1.00	0.76
LHCL	-38.00	-65.60	11.34	0.39	-0.99	0.43	0.50	0.84
LHUE	21.98	-159.34	35.08	0.73	-61.42	0.54	-2.72	1.52
LIL2	50.61	3.14	16.10	0.15	18.19	0.17	-1.08	0.64
LKHU	29.91	-95.15	-0.21	0.38	-11.13	0.35	0.23	1.29
LLIV	42.48	1.97	16.18	0.17	19.82	0.15	-0.05	0.48
LMNO	36.69	-97.48	-3.37	0.39	-13.80	0.44	-0.15	1.32
LODZ	51.78	19.46	14.60	0.16	20.97	0.13	0.53	0.71
LOFS	67.89	13.04	15.96	0.26	13.60	0.25	1.65	0.71
LOVM	59.34	17.83	14.00	0.21	18.56	0.18	5.42	0.56
LPAL	28.76	-17.89	17.27	0.15	15.81	0.13	-0.65	0.33
LPGS	-34.91	-57.93	11.79	0.18	-1.73	0.19	0.42	0.60
LPIL	-20.92	167.26	47.26	0.46	22.86	1.45	-0.80	1.17
LPLY	-73.11	-90.30	6.56	1.02	14.67	1.00	4.82	1.65
LROC	46.16	-1.22	16.42	0.10	18.23	0.11	-0.31	0.31
LSBN	40.77	-80.81	2.59	0.17	-15.20	0.19	-3.44	0.73
LSUA	31.18	-92.41	-1.12	0.23	-12.25	0.20	-0.91	0.72
LWN0	-81.35	152.73	-13.06	0.32	4.86	0.32	-0.85	1.21
LWX1	38.97	-77.49	4.35	0.18	-15.02	0.22	-1.82	0.69
LYCO	41.24	-77.00	3.83	0.23	-14.92	0.26	-1.17	0.79
LYNS	64.43	-40.20	15.56	0.21	-15.79	0.25	6.65	0.80
LYRS	78.23	15.40	14.51	0.97	12.89	0.50	5.78	0.86
MACC	37.85	-90.48	2.38	2.02	-11.93	2.61	-6.25	3.75
MADM	40.43	-4.25	16.60	0.10	18.59	0.10	0.09	0.40
MADO	56.85	26.22	13.27	0.41	20.48	0.42	-0.01	0.96
MAG0	59.58	150.77	-18.78	0.37	8.87	0.38	1.08	0.49
MAIR	36.85	-89.36	-0.19	0.16	-14.27	0.18	-1.01	0.75

continued ...

. . . continued

Site code	φ [°]	λ [°]	$\dot{N}$	$\pm\,\sigma_{\dot{N}}$	$\dot{E}$	$\pm\,\sigma_{\dot{E}}$	$\dot{U}$	$\pm\,\sigma_{\dot{U}}$
MAJU	7.12	171.36	30.43	0.42	-69.10	0.41	-1.19	1.09
MALD	4.19	73.53	35.59	0.63	45.33	0.89	0.40	2.14
MALL	39.55	2.62	16.72	0.27	18.48	0.53	0.50	0.80
MAN2	48.02	0.16	16.51	0.15	18.16	0.14	-0.14	0.46
MAPA	0.05	-51.10	14.01	1.46	-2.79	2.71	3.63	5.05
MAR6	60.60	17.26	14.08	0.10	17.78	0.11	7.72	0.45
MARJ	50.36	12.89	15.22	0.15	19.76	0.14	0.50	0.53
MARN	-46.88	37.86	2.57	1.37	1.06	2.40	-6.24	2.68
MARS	43.28	5.35	16.21	0.22	19.95	0.21	-0.88	0.62
MAS1	27.76	-15.63	17.57	0.11	16.53	0.12	-0.59	0.33
MAUI	20.71	-156.26	34.83	0.12	-61.83	0.13	-0.98	0.32
MAW1	-67.60	62.87	-2.07	0.16	-3.77	0.11	-0.45	0.32
MAYZ	18.22	-67.16	13.54	0.52	8.89	0.50	-1.51	1.40
MCAR	-76.32	-144.30	-3.98	0.76	16.51	0.87	1.37	1.43
MCD5	27.85	-82.53	2.27	0.27	-11.06	0.30	-1.97	0.80
MCIL	24.29	153.98	24.71	0.18	-71.38	0.16	0.55	0.51
MCM4	-77.85	166.67	-11.62	0.12	9.68	0.12	-0.75	0.50
MCN1	32.70	-83.56	1.78	0.60	-12.88	0.57	-0.77	2.12
MCNE	30.18	-93.22	-2.28	0.25	-11.08	0.26	-1.85	0.82
MCTY	36.12	-89.70	-0.43	0.19	-14.01	0.19	-1.10	0.72
MDOR	45.80	4.81	16.23	0.15	19.67	0.15	-0.29	0.56
MDR6	46.91	-103.27	-3.45	0.24	-14.43	0.28	-0.78	0.91
MDVJ	56.02	37.21	11.64	0.13	22.83	0.14	0.32	0.54
MET6	39.95	-105.19	-6.28	0.12	-14.67	0.12	-0.37	0.39
MET7	60.24	24.38	12.81	0.09	20.04	0.09	4.56	0.35
METG	60.24	24.38	15.22	0.95	20.01	0.71	5.68	2.46
MFLD	44.64	-90.13	-3.30	0.40	-15.58	0.42	-2.29	1.10
MIAR	43.98	-83.98	1.05	0.18	-16.34	0.25	-1.22	0.86
MICW	41.94	-84.98	1.24	0.16	-15.64	0.20	-1.72	0.65
MIDS	43.05	-83.52	1.52	0.18	-16.49	0.20	-1.56	0.66
MIGD	45.03	-84.64	0.69	0.19	-16.56	0.24	-1.28	0.87
MIHO	42.81	-86.08	0.61	0.17	-16.03	0.20	-2.34	0.76
MIHT	43.69	-86.36	0.81	0.20	-16.02	0.24	-1.97	0.82
MIIR	46.08	-88.63	-0.82	0.18	-16.77	0.21	-0.69	0.70
MIKL	46.97	31.97	12.31	0.14	23.59	0.12	0.28	0.47
MIL1	43.00	-87.89	0.56	0.60	-15.84	0.60	-4.10	2.11
MIMN	44.37	-86.16	0.35	0.18	-16.14	0.25	-2.19	0.83

continued . . .

. . . continued

Site code	φ [°]	λ [°]	$\dot{N}$	$\pm\,\sigma_{\dot{N}}$	$\dot{E}$	$\pm\,\sigma_{\dot{E}}$	$\dot{U}$	$\pm\,\sigma_{\dot{U}}$
MIMQ	46.55	-87.38	-0.61	0.23	-16.55	0.24	-0.24	0.93
MIN0	-78.65	167.16	-11.85	0.39	9.42	0.46	-0.46	0.92
MINI	41.81	-86.22	1.56	0.21	-14.09	0.26	-2.24	0.82
MIPR	17.89	-66.53	13.67	0.31	9.35	0.34	-0.83	1.04
MIST	45.42	-87.60	-1.54	0.24	-16.92	0.37	-0.33	0.79
MKEA	19.80	-155.46	35.07	0.12	-62.75	0.13	-1.91	0.38
MLF1	32.09	-87.39	1.61	0.33	-13.07	0.30	-1.01	0.83
MLVL	48.84	2.59	16.05	0.10	18.57	0.12	-0.86	0.37
MNBD	48.63	-94.07	-4.27	0.63	-17.14	0.33	0.74	1.25
MNBE	43.66	-94.12	-2.40	0.22	-15.47	0.25	-1.74	0.82
MNCA	43.63	-91.50	-1.59	0.27	-16.03	0.28	-1.99	0.94
MNDN	48.57	-96.91	-4.48	0.32	-16.71	0.31	0.27	1.16
MNGR	45.56	-96.49	-2.79	0.25	-15.81	0.23	-1.06	1.13
MNJC	46.98	-93.27	-2.94	0.20	-16.65	0.24	-1.42	0.82
MNP1	41.07	-71.86	6.68	0.63	-16.76	0.57	-0.42	1.26
MNPL	46.34	-93.26	-2.88	0.21	-15.98	0.45	-1.97	0.87
MNRM	43.64	-95.77	-3.18	0.22	-15.67	0.25	-3.00	0.80
MNRT	46.49	-96.29	-3.69	0.20	-16.34	0.22	-1.94	0.77
MNRV	48.79	-95.05	-3.56	0.29	-17.05	0.32	1.39	1.32
MNSC	45.71	-94.93	-3.03	0.23	-16.23	0.25	-2.71	0.94
MNTF	48.12	-96.21	-4.24	0.27	-16.88	0.34	-0.38	1.12
MNVI	47.52	-92.56	-3.34	0.29	-17.02	0.25	-0.86	0.78
MOAL	40.26	-94.30	-0.57	0.28	-14.90	0.26	-1.47	0.90
MOB1	30.23	-88.02	-0.47	0.21	-13.44	0.22	-2.82	0.70
MOBS	-37.83	144.98	57.30	0.17	19.55	0.17	-1.50	0.33
MOED	40.19	-92.18	-0.56	0.30	-14.79	0.26	-0.85	0.97
MOEL	38.35	-92.60	-0.78	0.25	-14.55	0.30	-0.05	0.89
MOGF	37.43	-93.85	-1.93	0.55	-13.54	0.38	-0.84	0.93
MOPN	40.42	-93.58	-1.72	0.26	-14.69	0.29	-1.25	0.93
MORP	55.21	-1.69	16.52	0.18	15.30	0.15	1.29	0.57
MOVB	36.96	-91.06	-0.18	0.29	-14.78	0.29	-0.62	0.96
MPLA	-38.04	-57.53	11.80	0.55	-0.29	0.39	2.56	1.73
MPLE	43.62	-84.76	1.25	0.15	-16.04	0.16	-1.37	0.65
MRO1	-26.70	116.64	59.76	2.08	35.74	2.38	6.67	6.75
MRRN	42.90	-101.70	-4.88	1.71	-15.02	2.54	5.32	13.18
MSB5	34.11	-90.69	-0.15	0.20	-13.81	0.22	-3.30	0.98
MSHT	31.33	-89.34	-0.76	0.30	-12.56	0.34	-0.29	0.91

continued . . .

...continued

Site code	φ [°]	λ [°]	$\dot{N}$	$\pm\sigma_{\dot{N}}$	$\dot{E}$	$\pm\sigma_{\dot{E}}$	$\dot{U}$	$\pm\sigma_{\dot{U}}$
MSKU	-1.63	13.55	20.88	0.83	20.71	1.61	6.20	2.58
MSNA	31.56	-91.40	-1.29	0.37	-12.74	0.47	0.30	1.83
MSPK	30.78	-89.14	-0.41	0.33	-12.30	0.34	-0.26	1.09
MSSC	30.38	-89.61	-0.31	0.22	-12.78	0.21	-1.09	0.64
MSYZ	32.85	-90.41	-0.81	0.29	-11.97	0.34	-1.13	1.05
MTMS	48.54	-109.69	-8.74	0.22	-15.21	0.20	-2.00	0.85
MTNT	25.87	-80.91	3.50	0.28	-10.50	0.32	0.38	0.98
MTY2	25.72	-100.31	-3.96	0.49	-9.74	0.61	-1.03	2.01
NAIN	56.54	-61.69	10.44	0.14	-16.38	0.13	4.43	0.40
NAMA	19.21	42.04	27.51	0.21	34.57	0.20	0.52	0.67
NAPL	26.15	-81.78	2.85	0.24	-10.59	0.28	-2.09	0.88
NAS0	25.05	-77.46	4.05	0.86	-9.75	0.59	2.29	2.78
NAUR	-0.55	166.93	29.49	0.25	-67.00	0.24	-1.71	0.74
NAUS	-3.02	-60.06	11.42	5.44	-6.02	0.69	10.30	5.12
NBR6	35.18	-77.05	4.38	0.26	-13.52	0.29	-1.81	0.78
NCDU	36.18	-75.75	4.41	0.23	-13.57	0.30	-2.77	0.82
NCGO	35.42	-78.06	4.23	0.27	-13.65	0.34	-0.42	0.86
NCJA	36.41	-77.44	3.43	0.20	-13.08	0.22	-1.34	0.72
NCPO	34.99	-80.18	2.56	0.21	-13.37	0.25	-0.88	0.75
NCSW	35.60	-82.42	1.94	0.25	-13.89	0.28	-0.44	0.73
NCWH	34.28	-78.72	3.60	0.24	-13.00	0.31	-2.10	0.85
NCWI	35.83	-77.03	4.16	0.18	-13.36	0.23	-3.36	0.72
NDMB	48.42	-101.33	-5.80	0.20	-16.28	0.22	-2.00	0.83
NEDR	40.77	-96.70	-2.91	0.16	-14.98	0.17	-1.87	0.68
NEGI	40.92	-98.33	-3.45	0.15	-15.30	0.19	-0.33	0.75
NEIA	-25.02	-47.92	12.82	0.29	-2.60	0.26	1.31	0.87
NESC	41.83	-103.66	-6.23	0.23	-14.80	0.19	-1.69	0.71
NEWL	50.10	-5.54	16.51	0.18	15.65	0.17	-0.60	0.46
NHUN	43.14	-70.95	5.45	0.24	-15.28	0.28	-0.43	0.73
NIST	40.00	-105.26	-6.23	0.25	-14.34	0.22	-0.20	0.70
NIUM	-19.08	-169.93	35.50	0.21	-60.56	0.30	-1.41	0.67
NJCM	39.10	-74.80	4.70	0.20	-14.31	0.28	-1.85	0.80
NJHC	40.50	-74.90	4.61	0.20	-15.14	0.23	-0.31	0.71
NJI2	40.74	-74.18	4.88	1.91	-16.21	1.40	0.09	8.54
NJOC	39.95	-74.19	4.72	0.21	-14.82	0.27	-0.74	0.72
NJTW	39.94	-74.95	4.46	0.94	-15.55	1.21	-1.26	3.07
NKLG	0.35	9.67	19.41	0.14	22.24	0.14	0.11	0.45

continued ...

. . . continued

Site code	φ [°]	λ [°]	$\dot{N}$	$\pm\,\sigma_{\dot{N}}$	$\dot{E}$	$\pm\,\sigma_{\dot{E}}$	$\dot{U}$	$\pm\,\sigma_{\dot{U}}$
NLIB	41.77	-91.57	-0.95	0.12	-15.35	0.13	-1.87	0.52
NMKM	36.45	-89.40	0.30	0.20	-13.90	0.17	-0.42	0.77
NNOR	-31.05	116.19	58.05	0.13	38.13	0.16	-0.90	0.43
NOR0	58.59	16.25	14.21	0.25	18.36	0.17	4.75	0.54
NOR1	44.26	-85.44	0.44	0.14	-16.42	0.16	-1.10	0.60
NOR3	45.07	-83.57	0.61	0.14	-16.78	0.17	-0.04	0.62
NOUM	-22.26	166.44	46.02	0.22	21.12	0.34	-1.60	0.67
NPLD	51.42	-0.34	16.16	0.20	17.15	0.19	-0.01	0.65
NPRI	41.51	-71.33	5.99	0.40	-14.96	0.47	-0.13	1.72
NRCM	45.45	-75.62	3.94	0.13	-16.08	0.12	3.01	0.42
NRIL	69.36	88.36	-2.05	0.13	22.18	0.13	1.71	0.55
NRL1	38.82	-77.02	4.24	0.22	-14.40	0.19	-0.05	0.68
NRMD	-22.23	166.48	46.39	0.31	21.49	0.27	-0.36	0.56
NTUS	1.35	103.68	-6.25	0.35	26.73	0.57	-1.22	0.58
NYBH	42.11	-75.83	3.96	0.17	-15.69	0.25	-0.76	0.72
NYBT	42.99	-78.12	3.14	0.17	-15.90	0.24	-0.44	0.82
NYCL	42.58	-76.21	3.76	0.20	-16.14	0.26	0.01	0.70
NYCP	42.19	-77.14	3.43	0.20	-15.62	0.26	-0.73	0.71
NYDV	42.55	-77.70	3.35	0.24	-15.88	0.26	-0.82	0.79
NYFD	42.43	-79.34	2.90	0.19	-15.94	0.25	-1.41	0.80
NYFS	42.20	-78.14	3.12	0.18	-15.38	0.26	-0.98	0.74
NYFV	42.94	-74.35	4.34	0.18	-15.81	0.26	0.81	0.72
NYHC	41.96	-75.29	4.14	0.20	-15.61	0.26	0.08	0.80
NYHM	43.02	-75.00	3.56	0.22	-15.79	0.30	0.56	0.81
NYHS	42.25	-73.76	4.68	0.19	-15.54	0.29	0.46	0.80
NYIR	47.84	22.14	14.63	0.45	21.60	0.46	-0.27	0.92
NYLV	43.80	-75.49	3.98	0.18	-15.57	0.27	0.96	0.77
NYMD	41.41	-74.44	4.74	0.19	-15.00	0.26	-0.03	0.74
NYML	44.87	-74.29	4.31	0.17	-15.95	0.24	1.85	0.75
NYNS	43.12	-76.14	3.38	0.19	-15.93	0.28	0.50	0.74
NYON	42.44	-75.11	4.17	0.18	-15.35	0.26	0.14	0.72
NYPD	44.65	-75.04	3.72	0.17	-16.04	0.24	1.69	0.70
NYPF	43.09	-77.53	3.29	0.19	-15.84	0.23	-0.26	0.78
NYRB	44.30	-74.08	4.46	0.21	-16.01	0.25	2.36	0.89
NYST	43.06	-73.80	4.38	0.19	-15.68	0.27	0.91	0.79
NYWL	42.90	-76.85	3.36	0.18	-15.46	0.25	0.07	0.74
NYWT	44.03	-75.92	3.77	0.16	-15.88	0.23	1.29	0.70

continued . . .

. . . continued

Site code	φ [°]	λ [°]	$\dot{N}$	$\pm\,\sigma_{\dot{N}}$	$\dot{E}$	$\pm\,\sigma_{\dot{E}}$	$\dot{U}$	$\pm\,\sigma_{\dot{U}}$
OAKH	30.82	-92.66	-1.25	0.21	-12.22	0.20	-1.88	0.79
ODS5	31.87	-102.32	-6.32	0.36	-12.11	0.35	-0.26	1.33
OHAS	41.93	-80.55	2.62	0.19	-15.75	0.24	-1.28	0.88
OHFA	39.53	-83.48	2.21	0.27	-14.38	0.30	-2.03	0.72
OHHU	41.18	-82.56	2.11	0.21	-14.96	0.24	-2.28	0.79
OHLI	39.95	-82.41	2.29	0.18	-14.77	0.25	-1.99	0.86
OHMO	39.78	-81.10	2.43	0.20	-14.76	0.22	-1.01	0.76
OHMR	40.55	-84.63	1.36	0.21	-14.94	0.23	-1.72	0.79
OHPR	39.74	-84.57	1.19	0.20	-15.22	0.25	-2.22	0.75
OKAN	34.20	-95.62	-2.46	0.15	-13.46	0.19	-0.70	0.67
OKAR	34.17	-97.17	-3.12	0.21	-13.78	0.34	-0.56	0.79
OKBF	36.83	-99.64	-3.67	0.24	-13.71	0.18	-0.39	0.67
OKCB	27.27	-80.86	2.78	0.22	-11.18	0.23	-0.37	0.73
OKCL	35.48	-98.97	-3.47	0.18	-13.80	0.17	-0.32	0.64
OKDT	35.49	-97.51	-3.91	0.18	-14.13	0.18	-1.95	0.61
OKGM	36.67	-101.48	-4.98	0.27	-13.67	0.20	-0.23	0.60
OKHV	34.91	-94.62	-1.88	0.20	-13.81	0.20	-0.90	0.79
OKMA	34.93	-95.74	-1.82	0.20	-13.50	0.21	-0.24	0.71
OKOM	34.09	-88.86	-0.52	0.38	-13.50	0.39	-0.15	1.73
OLKI	61.24	21.47	13.39	0.48	19.50	0.36	7.07	0.90
OMH5	41.78	-95.91	-2.95	0.27	-15.76	0.28	-0.25	1.16
ONSM	57.40	11.92	14.79	0.08	17.22	0.09	2.52	0.32
OPMT	48.84	2.33	16.02	0.10	18.16	0.11	0.13	0.43
ORMD	29.30	-81.11	2.48	0.22	-11.69	0.23	-0.54	0.80
OSKM	57.07	16.00	14.46	0.23	18.64	0.17	2.54	0.57
OSLS	59.74	10.37	15.43	0.15	15.84	0.13	4.96	0.46
OSPA	43.46	-76.51	3.45	0.17	-15.82	0.18	0.60	0.55
OST0	63.44	14.86	15.14	0.34	15.64	0.24	8.62	0.59
OUAG	12.36	-1.51	19.64	0.79	21.57	1.55	-2.20	4.02
OULU	65.09	25.89	12.72	0.33	18.99	0.24	8.87	0.98
OVE0	66.32	22.77	13.79	0.53	17.67	0.39	8.38	0.80
P032	41.74	-107.26	-6.83	0.14	-14.48	0.15	-1.33	0.48
P033	43.95	-107.39	-7.10	0.19	-14.31	0.17	0.51	0.61
P037	38.42	-105.10	-5.82	0.15	-14.18	0.15	-0.44	0.51
P038	34.15	-103.41	-4.56	0.32	-12.85	0.37	-1.04	1.29
P039	36.45	-103.15	-5.51	1.29	-14.19	1.49	0.05	3.38
P040	38.07	-102.69	-5.08	0.17	-14.31	0.15	0.41	0.57

continued . . .

. . . continued

Site code	φ [°]	λ [°]	$\dot{N}$	$\pm\sigma_{\dot{N}}$	$\dot{E}$	$\pm\sigma_{\dot{E}}$	$\dot{U}$	$\pm\sigma_{\dot{U}}$
P042	42.05	-104.91	-6.13	0.14	-14.92	0.15	-1.28	0.51
P043	43.88	-104.19	-5.86	0.15	-15.09	0.15	-1.40	0.59
P044	40.17	-103.22	-5.26	0.15	-14.78	0.15	-0.87	0.56
P049	47.35	-110.91	-8.84	0.15	-14.55	0.15	-1.28	0.54
P050	48.81	-111.25	-9.08	0.16	-14.57	0.17	-1.25	0.57
P051	45.81	-108.55	-7.70	0.14	-14.71	0.13	-1.54	0.55
P052	47.37	-107.02	-7.21	0.15	-15.20	0.14	-2.30	0.61
P053	48.73	-107.73	-7.94	0.15	-15.23	0.15	-2.39	0.64
P054	45.85	-104.44	-6.23	0.16	-15.39	0.16	-2.18	0.62
P055	47.12	-104.69	-6.57	0.19	-15.54	0.19	-3.27	0.74
P070	36.04	-104.70	-5.29	0.16	-13.67	0.16	-0.07	0.57
P728	39.18	-106.97	-6.66	0.20	-14.17	0.20	-0.46	0.65
P775	40.48	-86.99	0.73	0.28	-14.85	0.38	-0.62	1.06
P776	43.54	-71.38	5.54	0.20	-15.74	0.25	1.14	0.78
P777	35.70	-92.55	-0.91	0.20	-13.86	0.21	-0.73	0.84
P778	35.24	-85.81	1.54	0.20	-13.54	0.21	-0.68	0.82
P779	35.20	-82.87	2.56	0.26	-13.88	0.30	-0.61	1.04
P780	18.08	-66.58	14.16	0.31	8.88	0.34	-0.29	0.96
P802	46.56	-100.62	-4.72	0.27	-15.67	0.26	-2.18	1.07
P803	46.33	-90.68	-1.57	0.26	-16.29	0.28	-2.06	1.09
P807	30.49	-98.82	-2.31	0.43	-11.52	0.32	-2.26	1.16
P817	40.15	-78.51	4.08	0.34	-15.06	0.39	-1.41	1.39
PAAP	40.44	-79.96	3.04	0.27	-15.18	0.31	-1.89	0.91
PAFU	39.93	-79.70	3.26	0.20	-15.03	0.22	-1.48	0.75
PALK	7.27	80.70	33.67	0.72	48.34	1.00	0.19	2.79
PAMS	41.00	-75.25	4.11	0.20	-14.71	0.26	-0.93	0.82
PAPC	41.76	-78.02	3.22	0.26	-15.59	0.32	-0.89	0.89
PARK	-33.00	148.26	54.55	0.27	20.42	0.24	-0.24	0.49
PARY	45.34	-80.04	1.89	0.16	-16.77	0.17	0.85	0.59
PASA	43.32	-1.93	17.60	1.10	19.46	1.30	2.20	2.63
PASS	40.64	-76.16	4.06	0.22	-14.97	0.25	-1.45	0.76
PATN	-78.03	-155.02	-4.51	0.77	17.19	0.94	2.86	1.69
PATT	31.78	-95.72	-2.49	0.21	-12.80	0.23	-0.29	0.96
PBCH	26.85	-80.22	3.17	0.26	-11.29	0.26	0.20	0.93
PBRM	11.64	92.71	18.70	0.29	6.87	0.28	20.39	0.80
PECE	-85.61	-68.56	8.00	1.28	8.65	1.23	-4.82	1.76
PICL	51.48	-90.16	-2.21	0.34	-18.07	0.35	5.10	1.04

continued . . .

. . . continued

Site code	φ [°]	λ [°]	$\dot{N}$	$\pm\,\sigma_{\dot{N}}$	$\dot{E}$	$\pm\,\sigma_{\dot{E}}$	$\dot{U}$	$\pm\,\sigma_{\dot{U}}$
PIGT	36.37	-90.18	-0.05	0.29	-12.66	0.39	-1.10	0.93
PIRT	-81.10	-85.14	9.65	0.65	11.34	0.49	-0.74	1.60
PKTN	39.05	-83.02	2.18	1.37	-13.87	1.35	-4.29	9.45
PLTC	40.18	-104.73	-6.71	0.42	-14.02	0.48	-0.60	1.40
PNBM	44.45	-68.77	6.83	0.17	-15.73	0.21	-0.05	0.51
PNGM	-2.04	147.37	24.33	0.28	-64.22	0.28	-1.18	0.81
PNR6	46.86	-94.72	-3.21	0.22	-16.56	0.28	-0.97	0.81
POAL	-30.07	-51.12	10.96	0.60	-0.79	0.91	-2.72	1.84
POHN	6.96	158.21	26.32	0.33	-69.55	0.36	0.07	1.17
POLV	49.60	34.54	12.37	0.13	22.36	0.11	-0.06	0.46
POR2	43.07	-70.71	6.38	0.50	-15.97	0.55	3.50	1.29
POTS	52.38	13.07	15.30	0.10	19.14	0.09	0.32	0.41
POUS	50.14	12.30	15.44	0.14	19.26	0.12	-0.18	0.52
POVE	-8.71	-63.90	12.36	0.28	-3.51	0.22	0.68	0.82
PRCO	34.98	-97.52	-3.87	0.36	-13.26	0.42	0.13	1.35
PRDS	50.87	-114.29	-10.35	0.17	-14.46	0.12	0.10	0.42
PREI	56.29	26.72	13.38	0.53	20.08	0.52	-0.02	1.04
PREM	-25.75	28.22	18.68	0.18	17.84	0.17	0.02	0.48
PRPT	-66.01	-65.34	11.54	0.88	15.45	0.68	-0.01	1.75
PSU1	40.81	-77.85	3.92	0.50	-14.99	0.53	1.51	2.30
PTBB	52.30	10.46	15.65	0.11	18.87	0.10	-0.10	0.54
PTGV	36.41	-89.70	-0.33	0.15	-14.25	0.17	-1.85	0.64
PTIR	46.48	-84.63	0.13	0.18	-17.02	0.19	1.64	0.67
PUB5	38.29	-104.35	-6.17	0.19	-13.51	0.19	-1.80	0.64
PUIN	3.85	-67.90	7.54	2.81	-0.57	3.31	-3.06	8.22
PULK	59.77	30.33	12.17	0.17	21.26	0.19	1.16	0.69
PUO1	70.26	-148.33	-20.44	0.27	-7.83	0.32	-2.34	0.77
PUYV	45.04	3.88	16.30	0.14	19.73	0.12	-0.32	0.46
PWEL	43.24	-79.22	2.86	0.16	-15.88	0.16	-1.00	0.66
QAQ1	60.72	-46.05	13.70	0.11	-16.58	0.11	3.27	0.41
QIKI	67.56	-64.03	8.59	0.20	-18.66	0.20	4.20	0.42
RAMG	-84.34	178.05	-11.15	0.28	9.31	0.24	-0.06	0.99
RAMO	30.60	34.76	19.59	0.14	23.43	0.14	1.45	0.41
RANT	54.81	8.29	16.63	0.54	18.47	0.61	-1.18	1.88
RAT0	63.99	20.90	14.03	0.42	17.50	0.33	9.80	0.86
RBAY	-28.80	32.08	17.87	0.26	16.20	0.24	1.05	0.78
RCMV	25.61	-80.38	2.85	0.21	-10.60	0.25	-0.97	0.78

continued . . .

. . . continued

Site code	φ [°]	λ [°]	$\dot{N}$	$\pm\,\sigma_{\dot{N}}$	$\dot{E}$	$\pm\,\sigma_{\dot{E}}$	$\dot{U}$	$\pm\,\sigma_{\dot{U}}$
RECF	-8.05	-34.95	12.91	0.29	-4.15	0.36	-1.76	0.71
REDU	50.00	5.14	15.83	0.11	18.20	0.13	0.45	0.46
REDZ	54.47	17.12	15.28	0.62	19.41	0.38	-2.59	11.03
RESO	74.69	-94.89	-4.97	0.16	-20.45	0.14	5.69	0.38
REUN	-21.21	55.57	11.86	0.18	17.11	0.21	-0.35	0.72
RG13	36.49	-104.21	-6.98	0.25	-14.33	0.22	-1.43	0.62
RG15	37.74	-105.50	-7.02	0.42	-14.25	0.40	-2.70	1.24
RG16	39.88	-106.35	-6.30	0.21	-14.76	0.24	-1.73	0.62
RG17	39.76	-105.67	-6.22	0.39	-14.36	0.38	-1.27	0.99
RG18	39.07	-106.40	-6.74	0.27	-14.51	0.28	0.20	0.97
RG19	39.19	-105.55	-6.49	0.25	-14.57	0.24	0.51	0.94
RG23	37.74	-105.50	-6.13	0.22	-14.05	0.24	-0.43	0.87
RG24	37.96	-104.97	-5.47	0.27	-14.35	0.30	-0.52	0.90
RIC1	37.54	-77.43	4.14	0.42	-13.54	0.56	-0.80	1.75
RIGA	56.95	24.06	13.39	0.12	20.41	0.13	1.01	0.52
RIO1	42.46	-2.43	16.30	0.25	18.64	0.22	0.27	0.87
RIOJ	42.46	-2.50	14.31	0.52	19.39	0.35	-0.83	0.87
RIS5	42.01	-90.23	-0.95	0.31	-15.54	0.30	-5.53	1.01
RLAP	36.47	-89.35	-0.47	0.22	-14.16	0.22	-0.15	0.77
RMBO	-83.87	-66.39	11.44	0.55	8.79	0.47	-0.08	1.57
ROB4	-77.03	163.19	-11.84	0.28	9.18	0.25	0.52	1.00
ROBN	-65.25	-59.44	9.51	1.34	17.16	2.40	6.88	2.94
ROMU	64.22	29.93	12.15	0.44	19.81	0.37	5.67	0.93
ROSS	48.83	-87.52	-1.81	0.23	-17.86	0.27	3.06	0.62
ROTH	-67.57	-68.13	9.71	0.33	14.76	0.29	4.84	0.98
RWSN	-43.30	-65.11	11.20	0.35	-1.75	0.27	0.49	0.99
SA62	40.59	-105.15	-5.45	0.48	-14.56	0.39	-0.93	1.03
SACH	71.99	-125.25	-14.01	0.57	-16.28	0.42	1.23	1.22
SAG1	43.63	-83.84	1.58	0.56	-18.75	0.63	-2.94	1.78
SAGA	-0.14	-67.06	11.64	0.84	-3.48	0.67	-2.91	3.78
SALA	40.95	-5.50	16.91	0.13	18.62	0.13	-0.10	0.50
SALU	-2.59	-44.21	13.46	0.25	-3.64	0.31	1.77	0.80
SAN0	12.58	-81.72	6.60	0.32	11.97	0.52	-0.57	0.94
SASK	52.20	-106.40	-8.03	0.19	-16.57	0.14	-0.87	0.79
SASS	54.51	13.64	14.32	0.25	19.04	0.17	0.72	0.86
SAV1	32.14	-81.70	2.35	0.26	-12.64	0.25	-0.50	0.78
SAVO	-12.94	-38.43	12.72	0.21	-4.46	0.20	0.34	0.58

continued . . .

. . . continued

Site code	φ [°]	λ [°]	$\dot{N}$	$\pm\,\sigma_{\dot{N}}$	$\dot{E}$	$\pm\,\sigma_{\dot{E}}$	$\dot{U}$	$\pm\,\sigma_{\dot{U}}$
SBOK	-29.67	17.88	19.65	0.46	17.27	0.48	1.02	1.15
SCCC	32.78	-79.94	3.16	0.24	-12.54	0.28	-1.87	0.79
SCGP	34.94	-82.23	2.89	0.21	-13.24	0.25	-2.50	0.88
SCH2	54.83	-66.83	7.94	0.15	-17.35	0.15	11.12	0.46
SCOA	43.40	-1.68	16.71	0.32	18.18	0.25	-2.14	0.78
SCOR	70.49	-21.95	19.84	0.11	-10.80	0.13	3.84	0.46
SCWT	32.90	-80.67	2.43	0.21	-13.16	0.26	-0.52	0.90
SDLY	-77.14	-125.97	0.97	0.38	20.16	0.37	-3.05	1.39
SETE	43.40	3.70	16.82	1.06	19.34	2.73	-0.66	8.25
SEY1	-4.67	55.48	11.67	0.34	24.41	0.36	-1.66	1.14
SG01	36.60	-97.48	-2.77	0.15	-13.90	0.16	-0.30	0.60
SG04	37.13	-97.27	-2.67	0.15	-14.29	0.17	-0.52	0.63
SG05	28.07	-80.62	2.94	0.18	-11.29	0.22	-0.84	0.65
SG27	71.32	-156.61	-21.92	0.72	-5.34	0.37	-1.85	1.14
SG32	30.60	-96.36	-2.99	0.21	-11.69	0.21	-1.29	0.70
SGOC	6.89	79.87	36.35	0.68	44.57	0.50	-2.00	1.23
SHAO	31.10	121.20	-12.33	0.18	32.19	0.19	-0.88	0.50
SHE2	46.22	-64.55	7.75	0.34	-16.02	0.41	0.30	1.07
SHEE	51.45	0.74	16.02	0.85	17.69	0.60	-1.10	1.85
SHRV	32.43	-93.70	-1.89	0.19	-12.17	0.20	-1.64	0.71
SIBY	42.17	-83.24	1.84	0.13	-15.67	0.17	-1.64	0.58
SIGU	57.15	24.89	13.29	0.38	20.13	0.34	0.68	1.02
SIHS	31.84	-91.66	-0.90	0.19	-12.86	0.18	-1.28	0.70
SIMO	-34.19	18.44	19.74	0.58	16.02	0.50	-0.37	1.44
SJDV	45.88	4.68	16.68	0.82	20.11	0.84	4.97	2.20
SKE0	64.88	21.05	14.10	0.19	17.36	0.19	11.47	0.64
SLAI	41.90	-93.70	-2.64	1.62	-13.71	1.21	-0.99	5.78
SMID	55.64	9.56	15.42	0.11	17.35	0.12	0.80	0.43
SMLA	49.20	31.87	13.91	0.34	22.63	0.23	1.04	0.95
SMNE	48.84	2.43	16.05	0.14	17.84	0.14	0.23	0.48
SMO0	58.35	11.22	14.78	0.52	16.97	0.35	4.15	0.65
SNEC	50.74	15.74	14.99	0.95	21.00	1.32	-4.49	2.94
SNFD	35.47	-79.16	3.52	0.47	-13.24	0.60	0.42	1.76
SODA	67.42	26.39	12.74	0.53	17.94	0.46	6.58	1.72
SOLA	24.91	46.40	29.33	0.18	31.75	0.17	-1.37	0.56
SOLM	38.32	-76.45	4.26	0.13	-14.51	0.14	-1.45	0.53
SONS	39.68	-3.96	16.53	0.18	18.96	0.17	-0.25	0.53

continued . . .

. . . continued

Site code	φ [°]	λ [°]	$\dot{N}$	$\pm\,\sigma_{\dot{N}}$	$\dot{E}$	$\pm\,\sigma_{\dot{E}}$	$\dot{U}$	$\pm\,\sigma_{\dot{U}}$
SPGT	-64.29	-61.05	12.87	0.85	16.88	0.69	6.90	1.74
SPT0	57.71	12.89	14.73	0.10	17.44	0.11	4.35	0.43
SSA1	-12.98	-38.52	13.50	2.28	-4.17	1.31	2.71	4.80
STAS	59.02	5.60	16.16	0.38	14.91	0.38	1.40	1.50
STBM	44.80	-87.31	-0.06	0.17	-16.35	0.20	-2.48	0.63
STEW	-84.19	-86.25	9.16	0.47	13.16	0.64	-1.91	1.64
STHL	-15.94	-5.67	18.75	0.22	22.54	0.28	-0.07	0.68
STJM	47.60	-52.68	13.04	0.10	-14.78	0.12	-0.16	0.33
STLE	36.09	-89.86	-0.32	0.17	-13.77	0.17	-0.84	0.73
STLM	38.61	-89.76	-0.17	0.20	-15.11	0.23	-0.59	0.74
STP6	44.30	-91.90	-1.25	0.21	-15.82	0.22	-2.36	0.82
STRM	-35.32	149.01	55.43	0.08	18.43	0.11	-0.44	0.33
SUGG	-75.28	-72.18	11.24	0.79	13.38	0.75	2.24	1.27
SULD	56.84	9.74	15.06	0.11	16.77	0.11	2.01	0.45
SULP	49.84	24.01	13.99	0.15	21.60	0.14	-0.02	0.55
SUM5	34.83	-102.51	-4.54	0.22	-12.87	0.29	0.25	0.65
SUN0	62.23	17.66	14.24	0.21	17.37	0.18	9.66	0.59
SUNM	-27.48	153.04	53.92	0.36	21.46	0.32	-2.02	1.23
SUP3	46.30	-85.51	-0.05	1.28	-18.69	5.20	8.42	8.51
SUTH	-32.38	20.81	19.45	0.15	16.89	0.14	0.00	0.37
SUUM	59.46	24.38	12.71	0.23	19.94	0.24	3.61	0.88
SVE0	62.02	14.70	15.11	0.26	16.63	0.26	9.00	0.61
SVGB	13.27	-61.25	13.83	3.00	13.50	3.65	5.33	8.27
SVTL	60.53	29.78	11.87	0.16	21.05	0.14	2.90	0.72
SWKI	54.10	22.93	14.13	0.18	20.46	0.17	-0.43	0.64
SYDN	-33.78	151.15	54.40	0.12	18.27	0.14	-0.99	0.41
SYOG	-69.01	39.58	2.98	0.16	-3.96	0.12	0.64	0.40
TAHM	-17.56	-149.61	34.30	0.14	-65.77	0.16	-1.50	0.55
TAKL	-36.84	174.77	40.09	0.46	5.10	0.52	-1.25	1.75
TALH	30.40	-84.36	1.64	0.21	-12.02	0.23	-0.78	0.74
TALL	32.40	-91.18	-1.13	0.28	-12.88	0.26	-1.56	0.83
TALS	57.25	22.59	13.41	0.40	20.14	0.40	1.92	1.11
TAMP	22.28	-97.86	-2.68	0.68	-8.70	0.91	-2.79	2.82
TCA0	26.74	-77.38	6.43	0.86	-10.16	1.15	-1.38	3.33
TDOU	-23.08	30.38	18.44	1.08	17.79	0.89	-0.14	1.71
TERS	53.36	5.22	13.20	1.93	19.09	1.46	2.78	4.16
TERU	40.35	-1.12	16.38	0.17	19.52	0.20	0.34	0.63

continued . . .

...continued

Site code	φ [°]	λ [°]	$\dot{N}$	$\pm\,\sigma_{\dot{N}}$	$\dot{E}$	$\pm\,\sigma_{\dot{E}}$	$\dot{U}$	$\pm\,\sigma_{\dot{U}}$
TGCV	16.73	-22.93	16.38	1.06	18.94	1.22	1.24	3.58
THU1	76.54	-68.79	4.81	0.30	-22.34	0.37	2.96	1.00
THUR	-72.53	-97.56	3.70	0.71	15.42	0.73	-2.63	1.55
TID2	-35.40	148.98	55.38	0.08	18.11	0.11	-0.95	0.27
TITZ	51.04	6.43	15.78	0.12	18.51	0.13	1.00	0.49
TLLG	53.29	-6.36	16.61	0.22	15.33	0.22	0.98	0.82
TLMF	43.57	1.38	16.38	0.12	19.34	0.16	0.51	0.46
TLSE	43.56	1.48	16.46	0.10	19.56	0.10	0.22	0.34
TMGO	40.13	-105.23	-6.88	0.43	-14.85	0.47	-1.17	1.73
TN13	35.94	-83.21	2.25	0.24	-14.19	0.35	0.85	1.02
TN16	35.90	-84.60	2.29	0.23	-13.68	0.29	-0.74	0.85
TN22	35.39	-85.38	1.31	0.15	-13.43	0.19	-0.16	0.57
TN24	36.13	-85.50	1.64	0.23	-13.60	0.30	-1.05	0.84
TN35	36.10	-87.62	0.74	0.25	-13.81	0.31	-0.26	0.93
TN37	35.60	-87.09	0.95	0.22	-13.50	0.25	-0.41	0.89
TN44	35.64	-88.92	0.45	0.23	-13.72	0.26	-0.04	0.72
TOIL	59.42	27.54	12.88	0.20	20.57	0.16	2.51	0.63
TONG	-21.14	-175.18	-6.95	0.31	91.28	0.58	-0.79	0.76
TOPL	-10.17	-48.33	14.34	0.62	-2.82	1.53	5.77	1.99
TOR2	58.26	26.46	12.85	0.20	20.45	0.22	1.53	0.80
TOW2	-19.27	147.06	56.27	0.15	29.08	0.16	-0.82	0.44
TRDS	63.37	10.32	16.42	0.76	13.89	0.65	6.51	2.60
TRO1	69.66	18.94	14.99	0.14	15.14	0.15	3.55	0.42
TRYS	61.42	12.38	15.60	0.25	15.37	0.20	7.55	0.57
TUBO	49.21	16.59	14.88	0.11	20.84	0.12	-0.35	0.46
TUC2	35.53	24.07	-14.29	1.83	-0.29	0.93	16.79	0.79
TUKT	69.44	-132.99	-17.68	0.36	-11.76	0.35	-0.01	0.82
TUOR	60.42	22.44	13.17	0.53	19.67	0.34	6.08	0.84
TUVA	-8.53	179.20	32.21	0.23	-64.45	0.22	-1.00	0.74
TXAB	32.50	-99.76	-3.70	0.19	-12.33	0.21	-0.04	0.70
TXAG	29.16	-95.42	-1.47	0.33	-11.70	0.31	-2.62	0.93
TXAM	35.15	-101.88	-4.57	0.16	-13.53	0.16	1.28	0.70
TXBM	30.16	-94.18	-2.81	0.27	-12.80	0.28	-2.10	0.79
TXC1	31.81	-94.16	-1.16	0.35	-11.99	0.33	-2.70	1.32
TXCH	34.46	-100.28	-4.45	0.18	-12.43	0.20	-0.14	0.66
TXCO	33.17	-96.63	-2.42	0.21	-13.04	0.23	-1.01	0.72
TXDR	29.36	-100.90	-4.80	0.21	-11.64	0.25	-0.88	0.68

continued ...

. . . continued

Site code	φ [°]	λ [°]	$\dot{N}$	$\pm\,\sigma_{\dot{N}}$	$\dot{E}$	$\pm\,\sigma_{\dot{E}}$	$\dot{U}$	$\pm\,\sigma_{\dot{U}}$
TXHE	30.10	-96.06	-2.53	0.29	-11.50	0.36	-5.93	1.01
TXJA	33.19	-98.15	-3.42	0.24	-13.29	0.22	1.21	0.79
TXKA	32.57	-96.31	-2.80	0.23	-12.48	0.23	-1.09	0.75
TXKM	31.84	-103.11	-4.33	0.38	-11.94	0.39	0.51	1.10
TXKR	30.06	-99.12	-3.26	0.25	-11.91	0.27	0.43	0.89
TXLF	31.36	-94.72	-2.24	0.20	-12.16	0.23	-0.75	0.79
TXLL	30.73	-98.68	-3.17	0.21	-12.12	0.22	-0.38	0.77
TXLR	27.51	-99.45	-3.68	0.21	-11.79	0.19	0.52	0.66
TXLU	33.54	-101.84	-5.23	0.16	-12.80	0.18	0.04	0.77
TXSA	31.41	-100.47	-3.97	0.21	-12.49	0.20	-0.43	0.65
TXSN	30.15	-102.41	-4.76	0.20	-11.74	0.20	-0.89	0.70
TXSO	32.14	-101.81	-4.36	0.41	-14.09	0.40	0.83	1.12
TXST	32.23	-98.18	-3.19	0.21	-12.45	0.23	-0.63	0.76
TXTA	30.56	-97.45	-2.53	0.28	-12.16	0.24	-1.38	0.71
TXTI	28.47	-98.56	-0.81	0.96	-10.35	0.39	-0.20	1.06
TXTY	32.25	-95.39	-2.21	0.18	-12.68	0.23	-1.37	0.75
TXUV	29.20	-99.83	-3.91	0.33	-11.65	0.23	0.13	0.89
TXVA	28.83	-96.91	-2.74	0.22	-10.96	0.24	-1.82	0.86
TXWA	31.58	-97.11	-2.92	0.19	-12.26	0.19	-1.49	0.73
TXWF	33.85	-98.51	-3.20	0.18	-13.29	0.19	-1.26	0.70
UCAG	39.23	9.11	17.00	0.79	20.72	0.64	0.81	2.18
UCAL	51.08	-114.13	-9.89	1.41	-14.24	0.69	-5.60	4.49
UEPP	-22.12	-51.41	12.91	0.35	-2.86	0.40	1.16	1.11
UFPR	-25.45	-49.23	12.77	0.23	-3.58	0.16	0.24	0.53
ULAB	47.87	107.05	-8.77	0.18	28.29	0.15	0.93	0.52
ULDI	-28.29	31.42	18.13	0.54	16.12	0.51	-1.04	1.45
UMEM	63.58	19.51	13.86	0.26	17.23	0.18	10.56	0.55
UNBJ	45.93	-66.66	7.54	0.13	-15.60	0.14	-0.59	0.52
UNPM	20.87	-86.87	0.91	0.26	-8.96	0.27	-1.73	0.72
UNX3	-33.92	151.23	53.57	1.56	19.70	1.20	7.26	5.16
UPO1	20.25	-155.88	34.46	0.48	-62.70	0.77	-2.29	1.20
UPP0	59.87	17.59	13.99	0.29	18.06	0.23	6.49	0.75
UPTC	41.63	-79.66	3.02	0.53	-15.49	0.21	-2.14	1.01
USDL	49.43	22.59	14.28	0.17	21.59	0.18	0.43	0.68
USNA	38.98	-76.48	3.33	0.27	-14.22	0.31	-0.62	0.65
USNO	38.98	-76.48	4.00	0.11	-14.65	0.12	-0.91	0.45
UVFM	37.88	-78.69	3.73	0.38	-14.24	0.36	-2.08	1.13

continued . . .

. . . continued

Site code	φ [°]	λ [°]	$\dot{N}$	$\pm\,\sigma_{\dot{N}}$	$\dot{E}$	$\pm\,\sigma_{\dot{E}}$	$\dot{U}$	$\pm\,\sigma_{\dot{U}}$
UZHL	48.63	22.30	13.80	0.14	21.81	0.11	0.42	0.58
VA01	38.02	-78.01	4.56	0.25	-14.54	0.29	-2.38	0.94
VA02	37.94	-77.99	4.50	0.30	-14.71	0.34	-5.79	1.26
VAAS	62.96	21.77	13.52	0.11	18.44	0.11	9.21	0.56
VABG	36.86	-82.76	2.42	0.22	-14.24	0.23	-1.80	0.74
VACO	49.13	13.72	15.44	0.16	20.25	0.15	-0.31	0.63
VACS	-20.30	57.50	11.32	0.24	17.09	0.28	-0.76	0.96
VALA	41.70	-4.71	16.58	0.14	18.45	0.16	0.74	0.64
VALD	48.10	-77.56	2.40	0.16	-16.99	0.18	7.85	0.48
VALE	39.48	-0.34	16.33	0.27	20.33	0.26	-0.58	0.72
VALY	37.38	-79.13	3.50	0.20	-14.45	0.21	-0.19	0.79
VAN0	58.69	12.04	15.06	0.29	16.82	0.25	4.75	0.53
VARI	37.29	-77.40	4.07	0.20	-13.78	0.28	-0.93	0.80
VARS	70.34	31.03	12.38	0.52	17.88	0.42	4.21	1.98
VAST	38.16	-79.05	3.61	0.18	-14.54	0.21	-0.37	0.74
VAWI	37.93	-75.47	4.93	0.18	-14.25	0.21	-3.15	0.75
VBCA	-38.70	-62.27	11.66	0.35	-1.40	0.54	-0.54	0.98
VCAP	44.26	-72.58	5.51	0.63	-15.45	0.80	1.81	2.32
VCIO	36.07	-99.22	-1.90	0.70	-13.15	0.52	-0.26	1.35
VEGS	65.67	11.96	15.91	0.27	13.75	0.26	3.40	0.88
VESL	-71.67	-2.84	10.49	0.20	-0.30	0.16	0.88	0.60
VFCH	47.29	1.72	16.17	0.09	18.59	0.10	0.52	0.46
VFDG	70.30	-29.82	19.24	0.18	-14.20	0.18	8.35	0.87
VIGO	42.18	-8.81	16.87	0.13	17.69	0.14	-0.28	0.42
VIL0	64.70	16.56	15.03	0.12	15.71	0.12	9.33	0.42
VILL	40.44	-3.95	16.55	0.11	18.58	0.13	-0.86	0.36
VIMS	37.61	-75.69	4.78	0.74	-14.86	1.03	-4.46	3.34
VIRO	60.54	27.55	12.23	0.51	20.32	0.30	3.64	0.77
VIS0	57.65	18.37	13.90	0.08	19.02	0.08	3.20	0.43
VL01	-72.45	169.73	-11.90	0.59	11.93	0.55	-5.24	1.59
VL12	-72.27	163.73	-13.68	1.07	11.32	0.53	-2.94	1.73
VL30	-70.60	162.53	-11.95	0.93	11.41	0.73	-1.23	1.73
VLNS	54.65	25.30	14.97	2.25	20.74	1.65	-0.83	10.86
VNAD	-65.25	-64.25	10.33	0.33	13.32	0.29	4.67	0.76
VTD9	44.95	-72.16	4.74	0.23	-15.87	0.33	3.05	0.91
VTOX	44.01	-72.11	5.24	0.22	-15.20	0.34	1.24	0.87
VTRU	43.61	-72.98	4.83	0.27	-15.67	0.37	0.82	0.85

continued . . .

. . . continued

Site code	φ [°]	λ [°]	$\dot{N}$	$\pm\,\sigma_{\dot{N}}$	$\dot{E}$	$\pm\,\sigma_{\dot{E}}$	$\dot{U}$	$\pm\,\sigma_{\dot{U}}$
VTSP	43.28	-72.48	5.05	0.15	-15.72	0.14	0.59	0.57
VTUV	44.47	-73.20	4.85	0.16	-16.07	0.20	1.11	0.61
WARE	50.69	5.25	15.92	0.57	19.08	0.70	-2.21	2.18
WARK	-36.43	174.66	39.61	0.25	4.22	0.27	-1.48	0.79
WARN	54.17	12.10	15.68	0.20	18.72	0.16	0.23	0.70
WDLM	44.67	-95.45	-2.60	0.69	-16.77	0.65	-2.99	2.25
WES2	42.61	-71.49	5.56	0.14	-15.20	0.13	0.02	0.42
WHN0	-79.85	154.22	-12.36	0.38	6.09	0.33	0.46	1.31
WHTM	-82.68	-104.39	4.58	2.15	16.74	1.57	0.38	4.79
WIL1	41.31	-76.02	3.73	0.21	-15.28	0.18	-1.36	0.79
WILN	-80.04	-80.56	8.83	0.77	11.32	0.53	3.37	1.49
WIMM	43.19	-88.06	0.53	0.18	-16.36	0.26	-2.32	0.56
WIND	-22.57	17.09	19.95	0.24	19.80	0.26	0.62	0.53
WIS5	46.71	-92.02	-2.36	0.15	-16.73	0.17	-0.90	0.58
WISN	45.82	-92.37	-2.88	0.21	-16.44	0.23	-2.85	0.88
WLCT	-85.37	-87.39	7.54	1.49	11.32	1.07	-4.05	3.40
WMOK	34.74	-98.78	-1.95	0.45	-12.82	0.35	-1.82	1.36
WNFL	31.90	-92.78	-2.33	0.39	-11.96	0.36	1.10	2.10
WOOS	40.80	-81.96	1.58	0.30	-14.80	0.13	-3.26	0.66
WROC	51.11	17.06	14.77	0.10	20.13	0.10	-0.17	0.43
WSRT	52.91	6.60	16.47	0.08	17.73	0.09	-0.23	0.37
WTZM	49.14	12.88	15.52	0.06	20.29	0.07	-0.31	0.29
WUHN	30.53	114.36	-11.29	0.17	32.72	0.18	0.61	0.58
WVBU	39.34	-78.91	3.33	0.27	-14.90	0.34	-1.90	1.08
WVCV	39.02	-79.46	0.45	0.31	-10.68	0.60	-1.79	1.00
WVHU	38.42	-82.42	2.82	0.23	-14.38	0.24	-1.21	0.69
WVNR	38.90	-79.86	3.59	0.30	-14.29	0.40	-0.99	0.93
WVOH	38.00	-81.13	2.80	0.24	-14.42	0.30	-2.17	0.90
WVRA	38.94	-81.75	2.30	0.19	-14.56	0.25	-0.66	0.74
WWAY	-81.58	-28.40	9.55	3.04	14.30	3.33	4.94	2.71
WYLC	41.10	-104.78	-6.03	0.18	-14.79	0.18	-1.45	0.61
XCTY	29.63	-83.11	1.93	0.25	-11.69	0.26	-1.45	0.83
YAKT	62.03	129.68	-12.22	0.20	18.90	0.17	-0.33	0.62
YAR2	-29.05	115.35	57.86	0.13	38.80	0.14	-0.74	0.35
YEBE	40.52	-3.09	16.47	0.10	18.89	0.10	0.32	0.34
YELL	62.48	-114.48	-10.90	0.14	-17.11	0.11	6.33	0.47
YIBL	22.19	56.11	31.99	0.16	33.63	0.20	-0.52	0.48

continued . . .

. . . continued

Site code	φ [°]	λ [°]	$\dot{N}$	$\pm\,\sigma_{\dot{N}}$	$\dot{E}$	$\pm\,\sigma_{\dot{E}}$	$\dot{U}$	$\pm\,\sigma_{\dot{U}}$
YKRO	6.87	-5.24	18.81	0.24	21.58	0.25	0.84	0.77
YORK	39.99	-76.74	4.36	0.14	-14.50	0.18	-1.30	0.60
YQX1	48.97	-54.60	10.76	0.38	-15.90	0.31	0.81	0.75
YWG1	49.90	-97.26	-5.84	0.41	-18.57	0.34	-0.16	0.88
YYR1	53.31	-60.42	10.57	0.23	-16.87	0.33	5.53	0.80
ZAMB	-15.43	28.31	18.58	0.24	20.00	0.22	0.42	0.68
ZARA	41.63	-0.88	16.23	0.12	19.14	0.12	-0.17	0.47
ZAU1	41.78	-88.33	0.43	0.19	-15.51	0.20	-1.67	0.66
ZBW1	42.74	-71.48	5.05	0.21	-14.94	0.24	-0.51	0.61
ZDC1	39.10	-77.54	3.63	0.17	-14.80	0.19	-0.91	0.66
ZDV1	40.19	-105.13	-6.40	0.17	-14.57	0.20	-0.85	0.63
ZKC1	38.88	-94.79	-2.24	0.18	-14.69	0.19	-0.81	0.71
ZME1	35.07	-89.96	-0.45	0.20	-13.52	0.21	-0.40	0.86
ZMP1	44.64	-93.15	-2.04	0.16	-16.00	0.21	-2.42	0.70
ZNY1	40.78	-73.10	4.75	0.16	-14.59	0.23	-0.25	0.66
ZTL4	33.38	-84.30	1.35	0.21	-13.34	0.22	-0.32	0.73
ZWE2	55.70	36.76	11.76	0.15	22.60	0.14	0.02	0.57
ZYWI	49.69	19.21	15.04	0.15	21.23	0.14	0.27	0.63

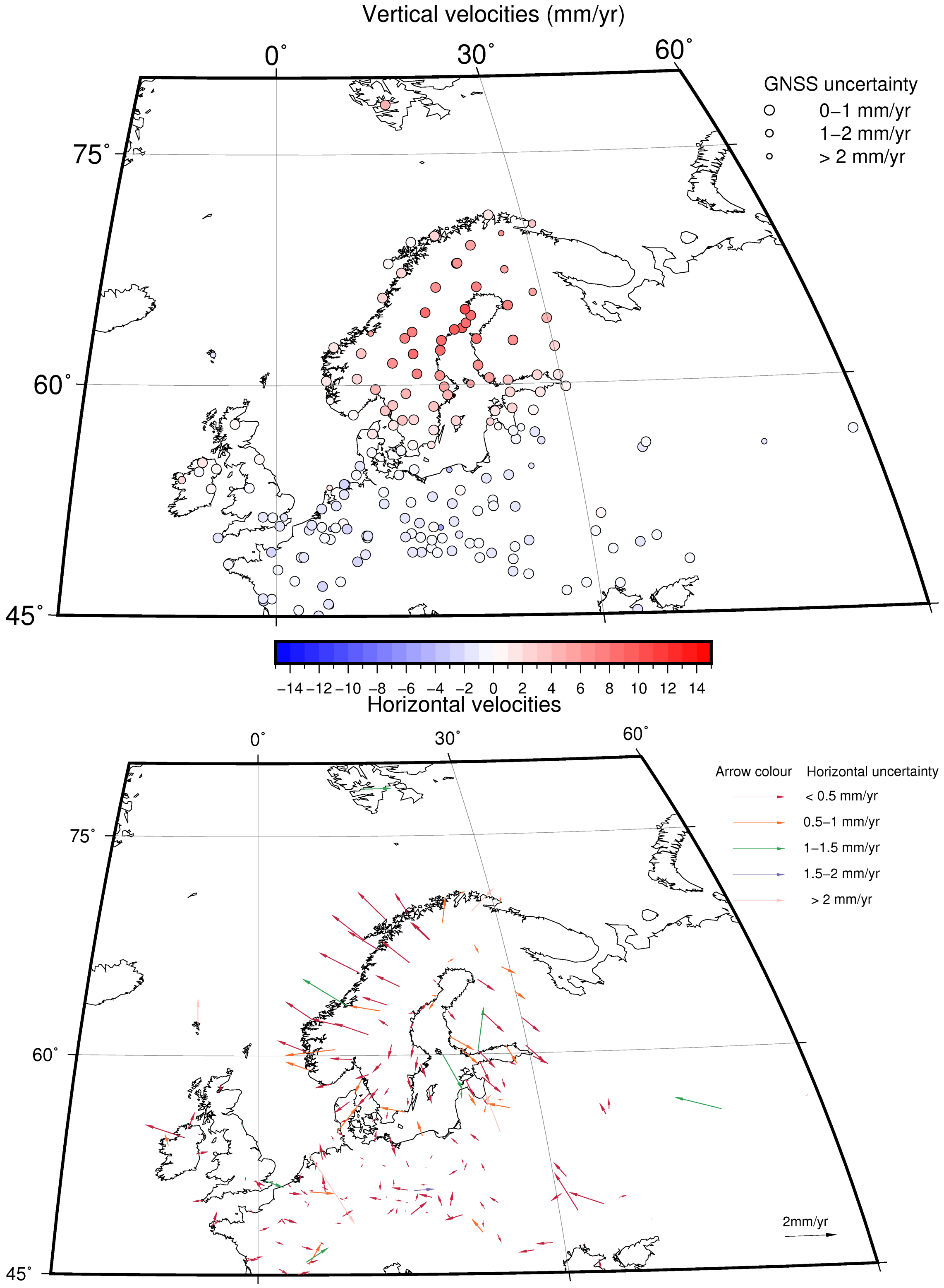

Figure C.1: Observed vertical velocities in Europe where β has been removed (top) and horizontal velocities in Europe where β and rigid plate motion has been removed (bottom) using GNSS-only PMM.

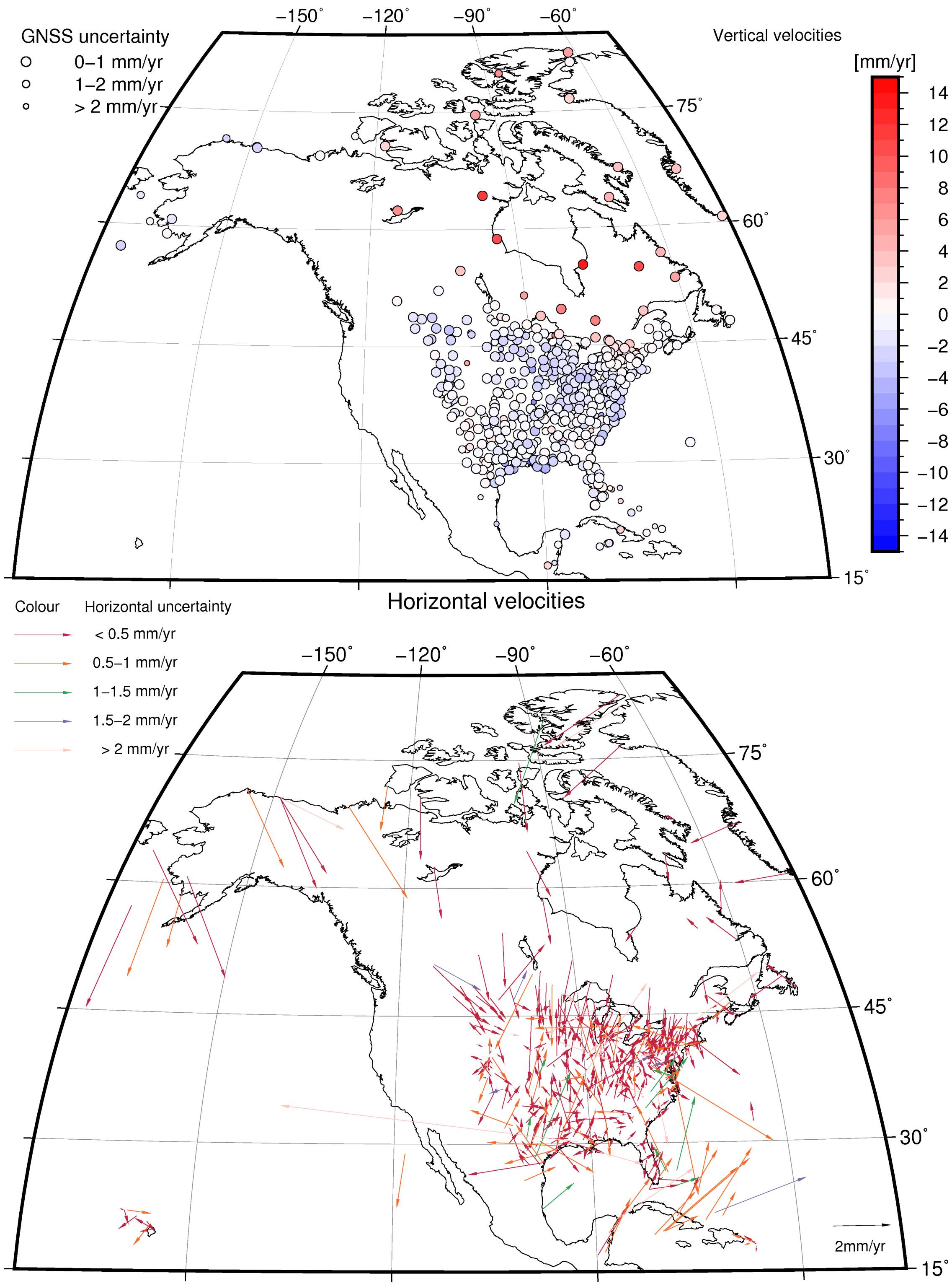

Figure C.2: Observed vertical velocities in North America where β has been removed (top) and horizontal velocities in North America where β and rigid plate motion has been removed (bottom) using GNSS-only PMM.

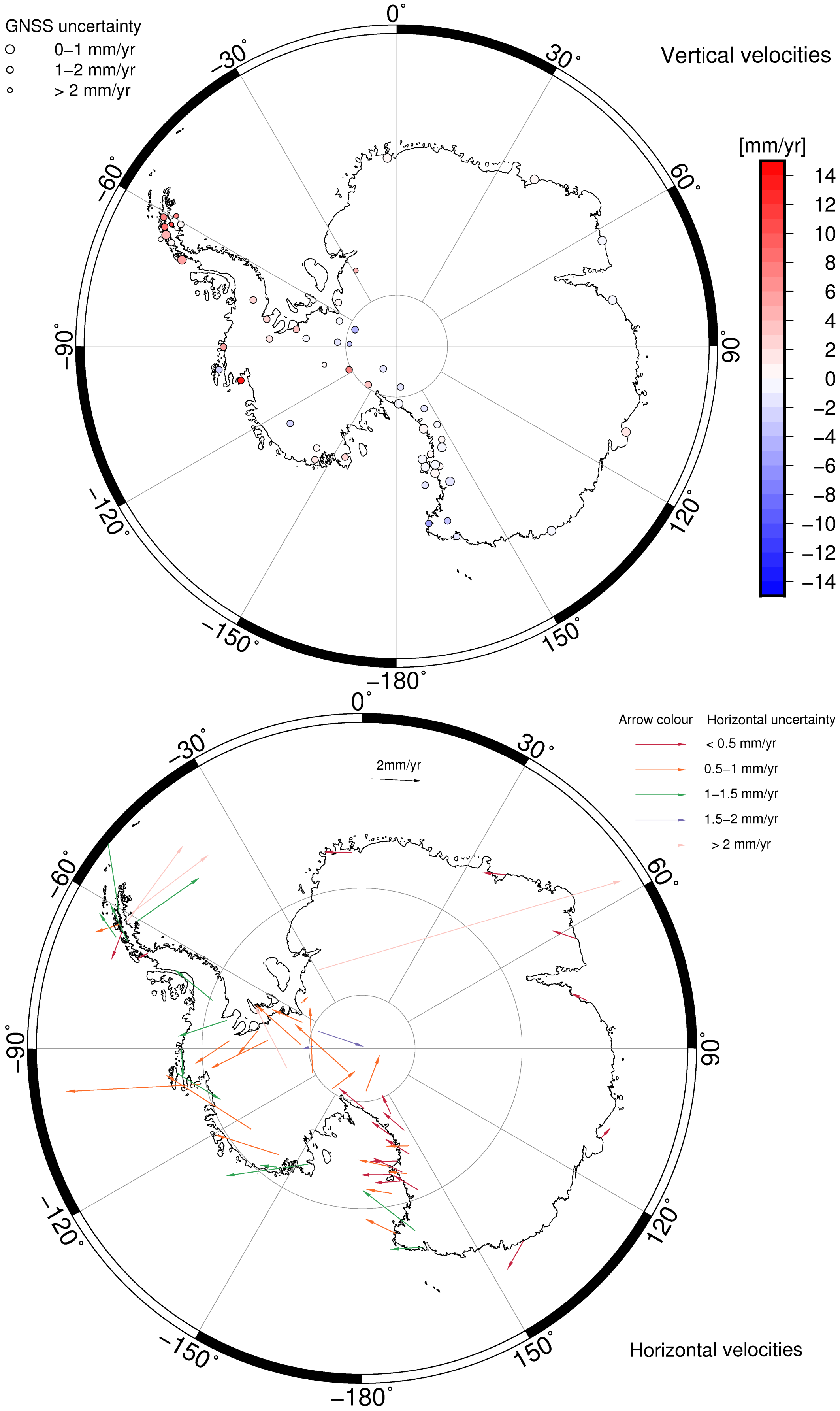

Figure C.3: Observed vertical velocities in Antarctica where β' has been removed (top) and horizontal velocities in Antarctica where β' and rigid plate motion has been removed (bottom) using 6G_71p85 GIA PMM.

Appendix D

MAD plots

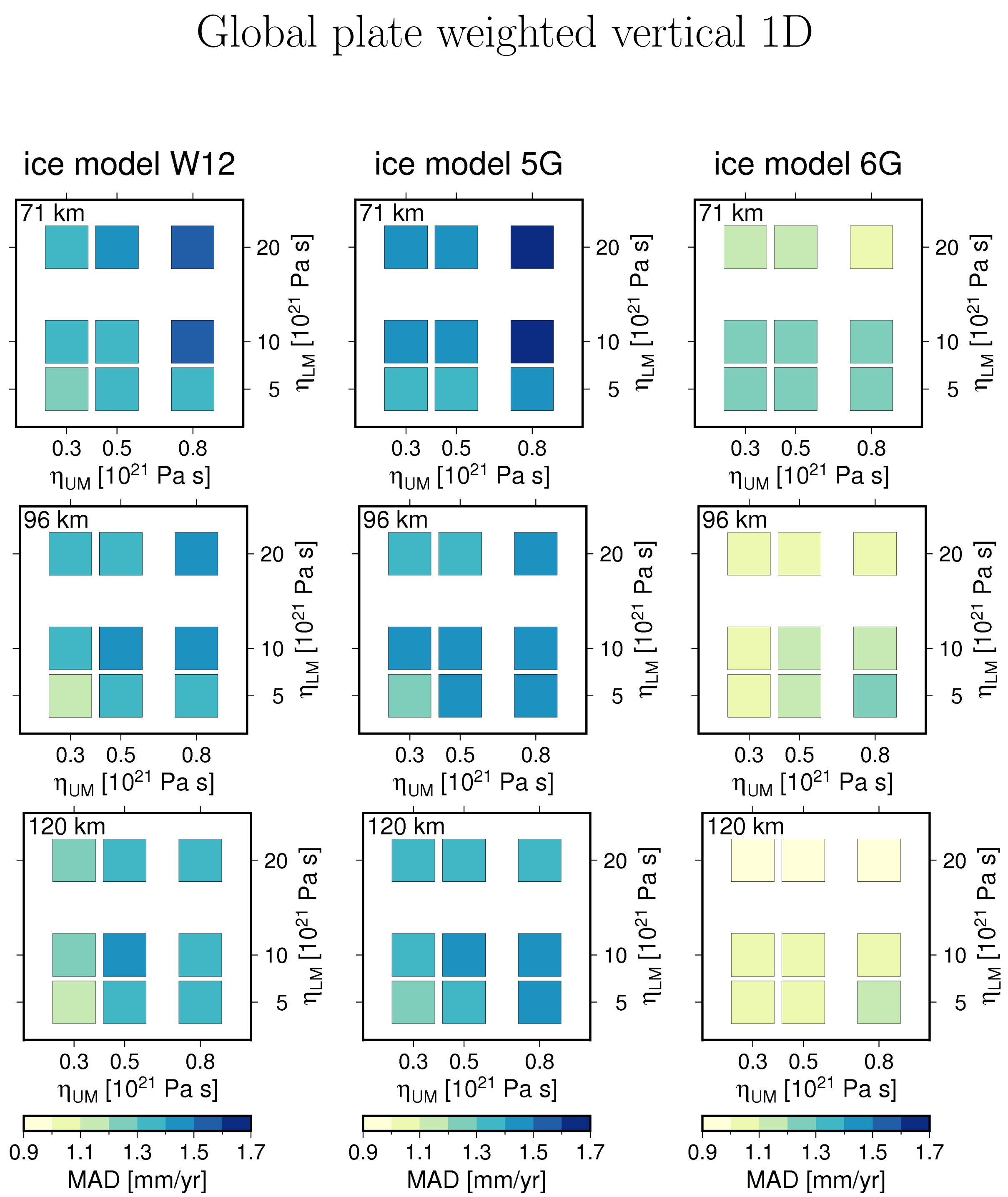

Figure D.1: Global (weighted by tectonic plates area) MAD values of the vertical component for each 1D GIA model

Global plate weighted horizontal 1D

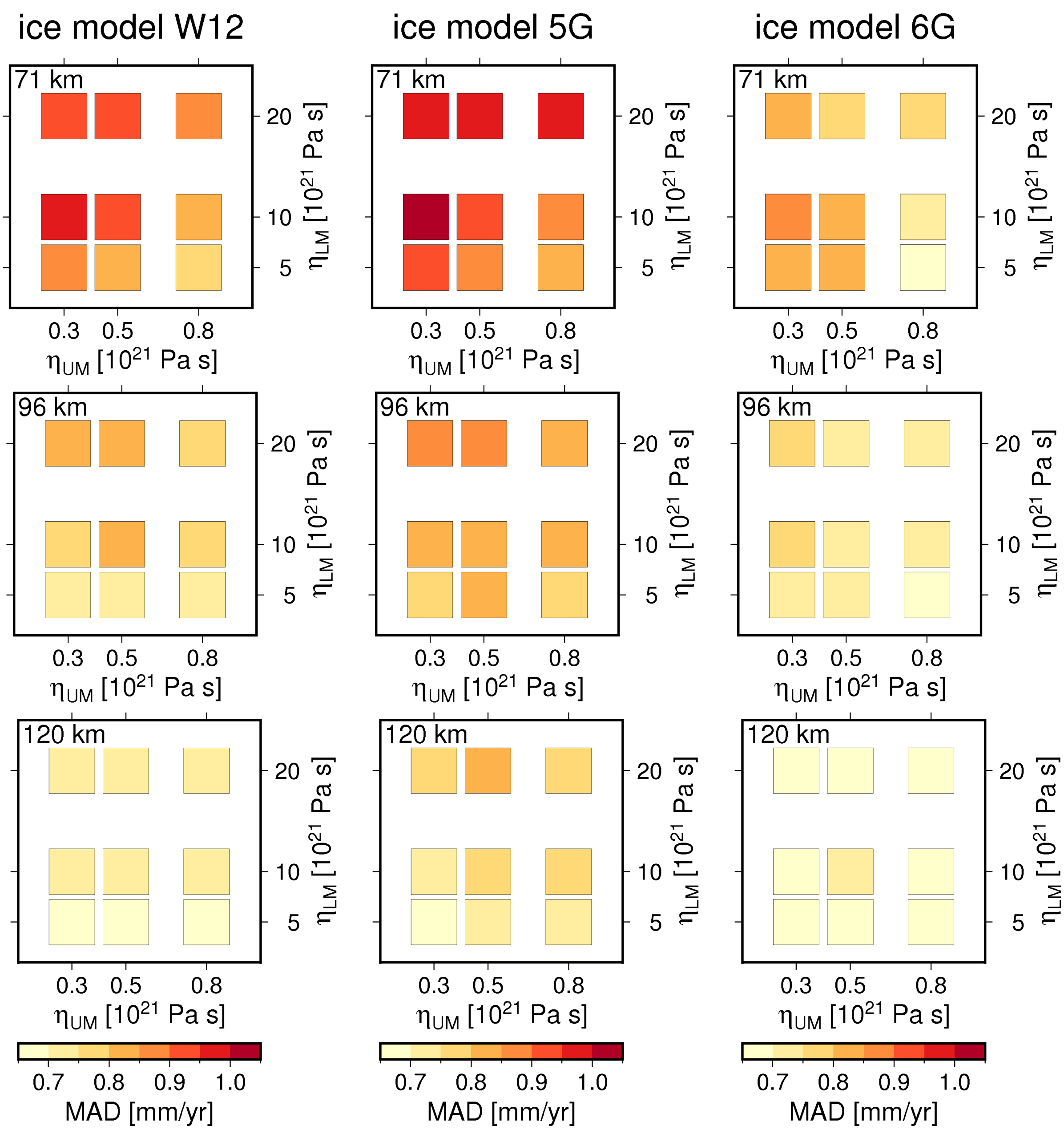

Figure D.2: Global (weighted by tectonic plates area) MAD values of the horizontal component for each 1D GIA model

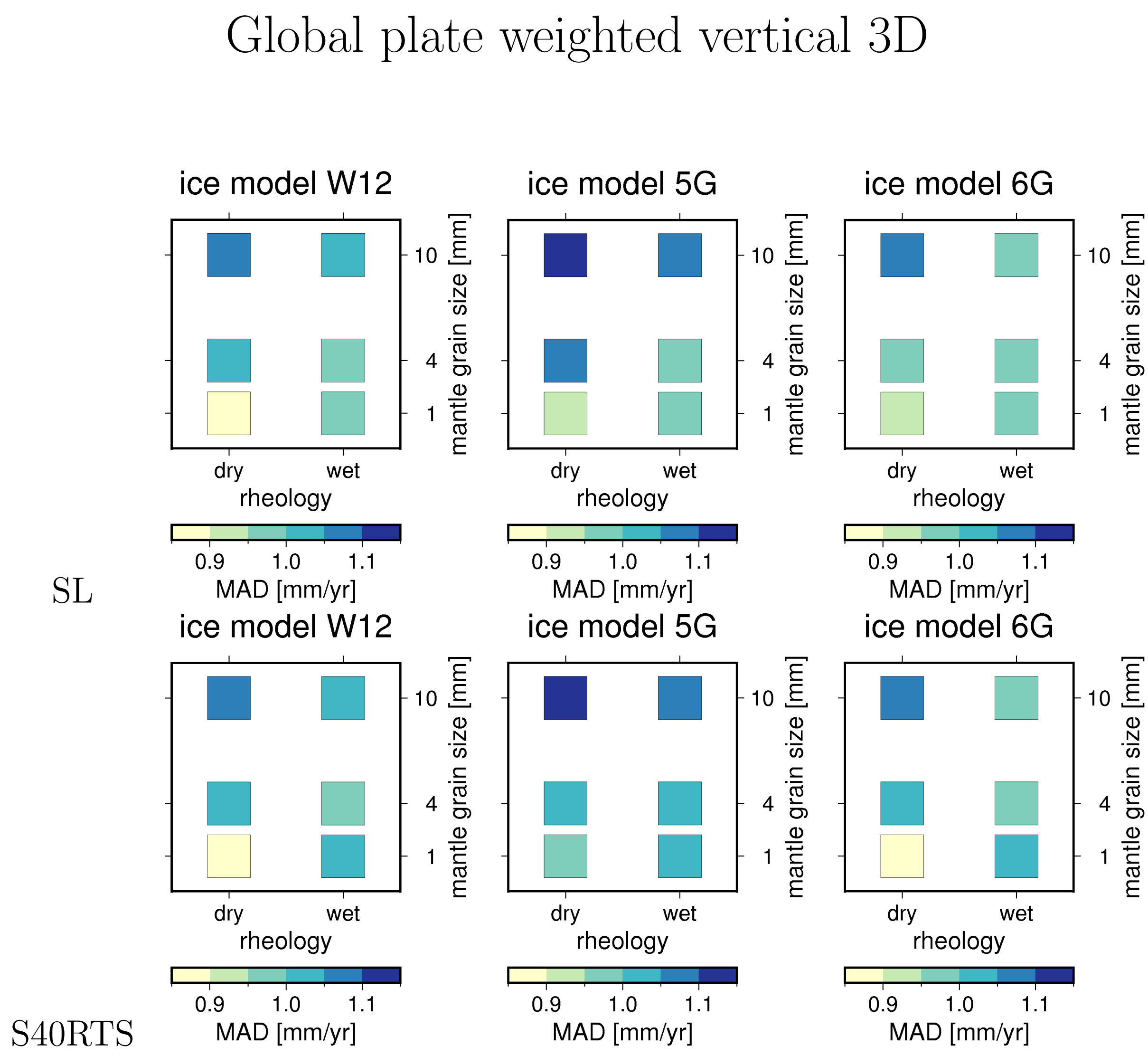

Figure D.3: Global (weighted by tectonic plates area) MAD values of the vertical component for each 3D GIA model. Top row with SL Earth model, bottom row with S40RTS Earth model

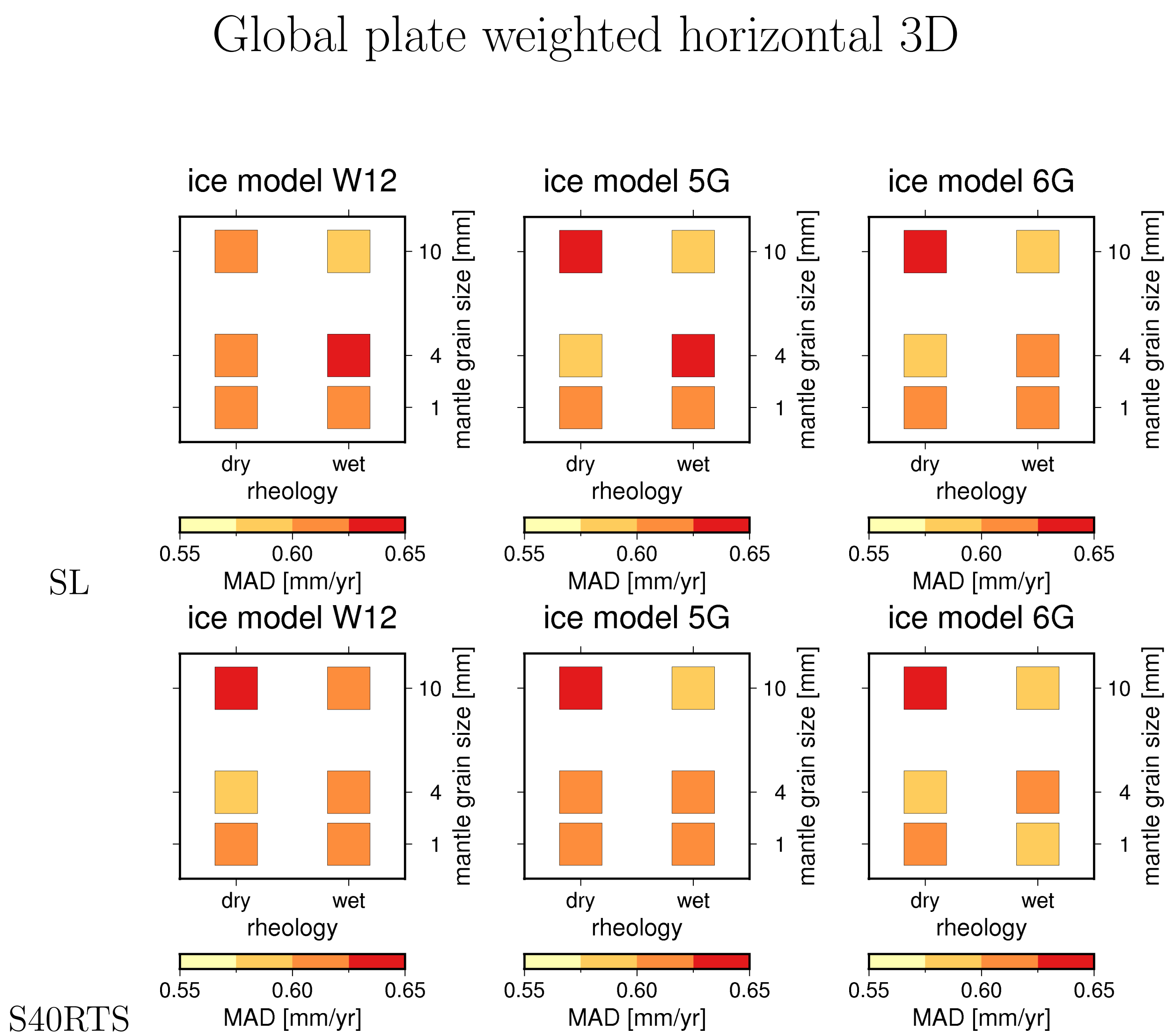

Figure D.4: Global (weighted by tectonic plates area) MAD values of the horizontal component for each 3D GIA model. Top row with SL Earth model, bottom row with S40RTS Earth model.

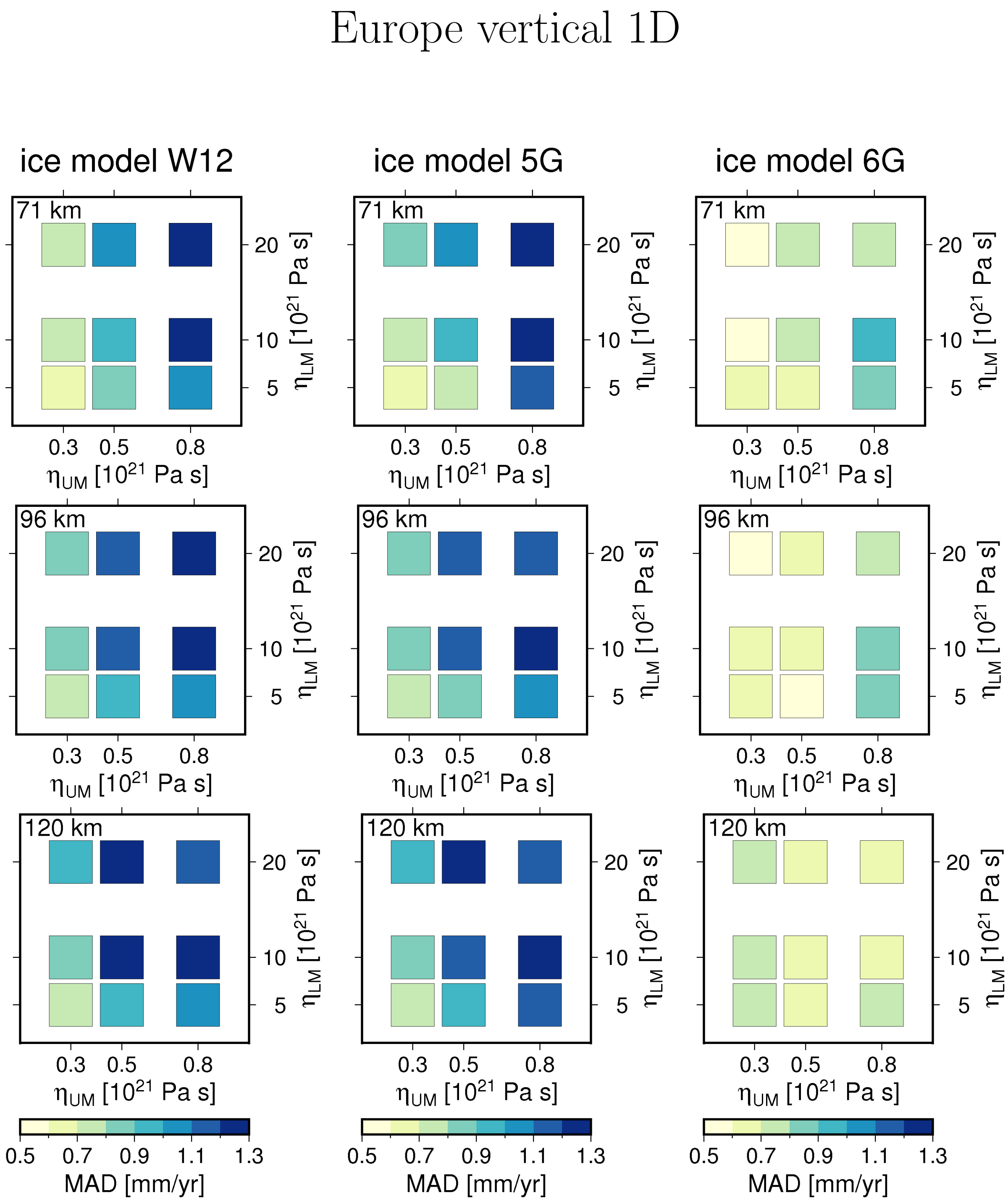

Figure D.5: MAD values in the vertical component in Europe for each 1D GIA model

Europe horizontal 1D

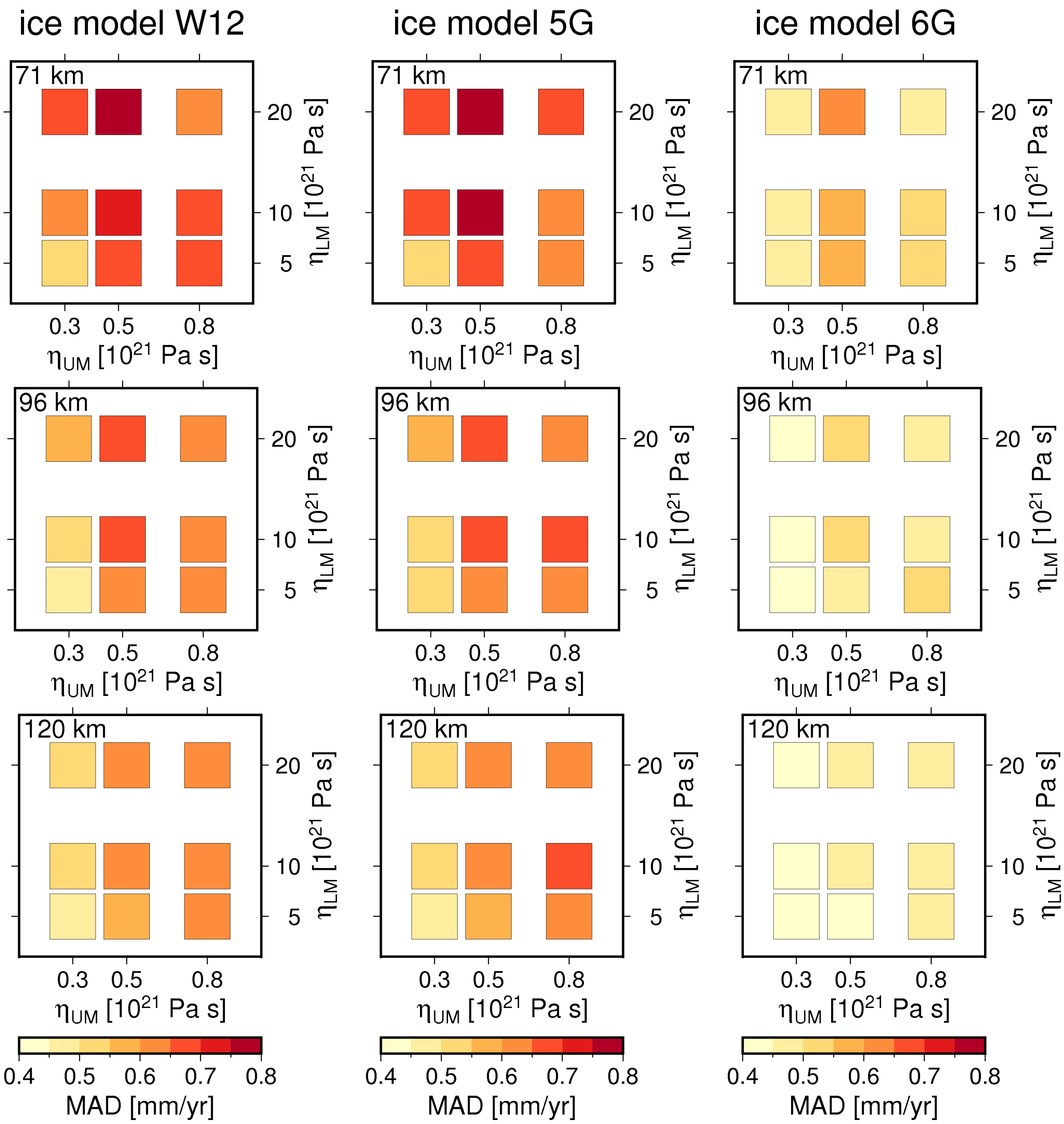

Figure D.6: MAD values in the horizontal component in Europe for each 1D GIA model

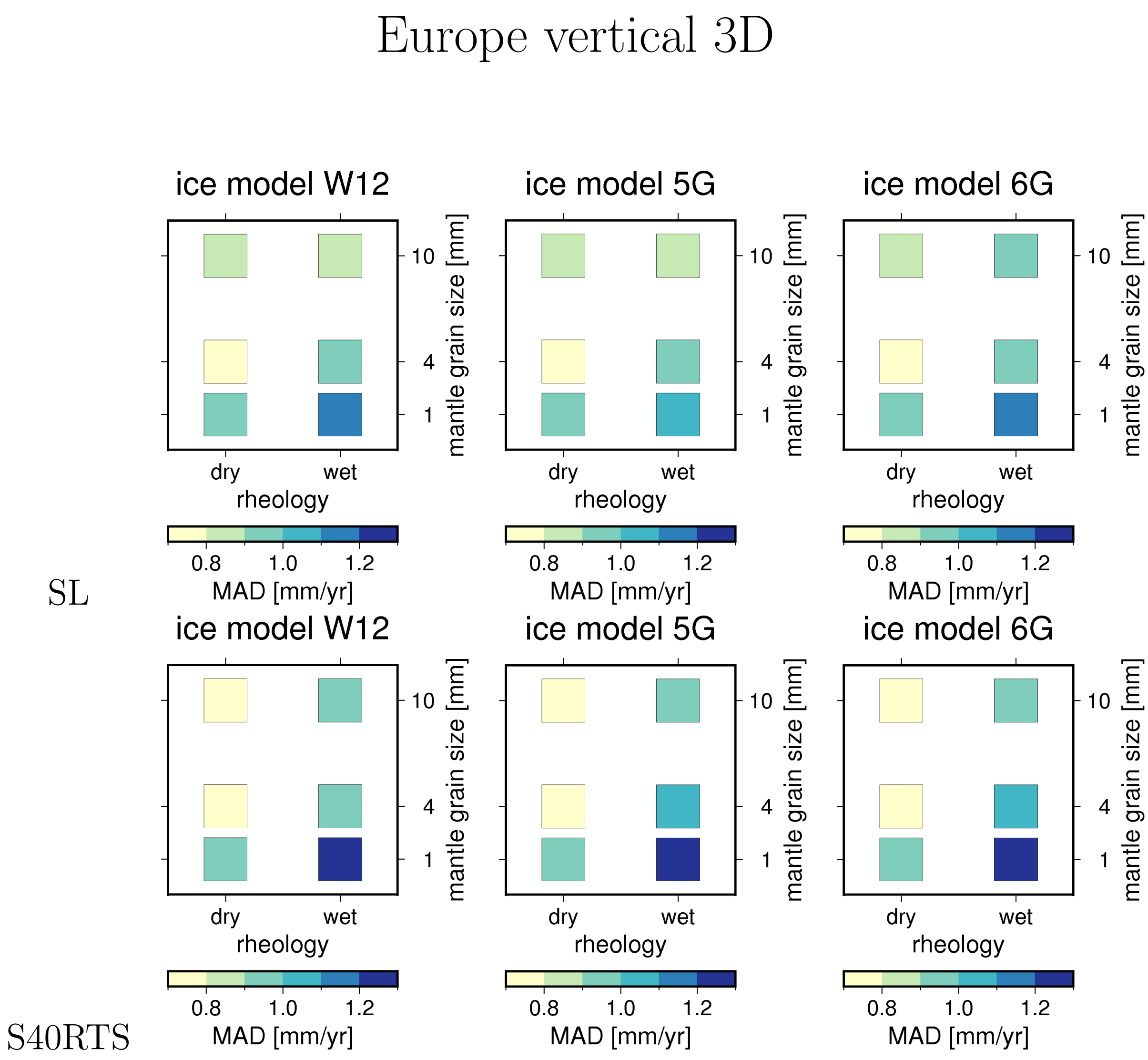

Figure D.7: MAD values in the vertical component in Europe for each 3D GIA model. Top row with SL Earth model, bottom row with S40RTS Earth model

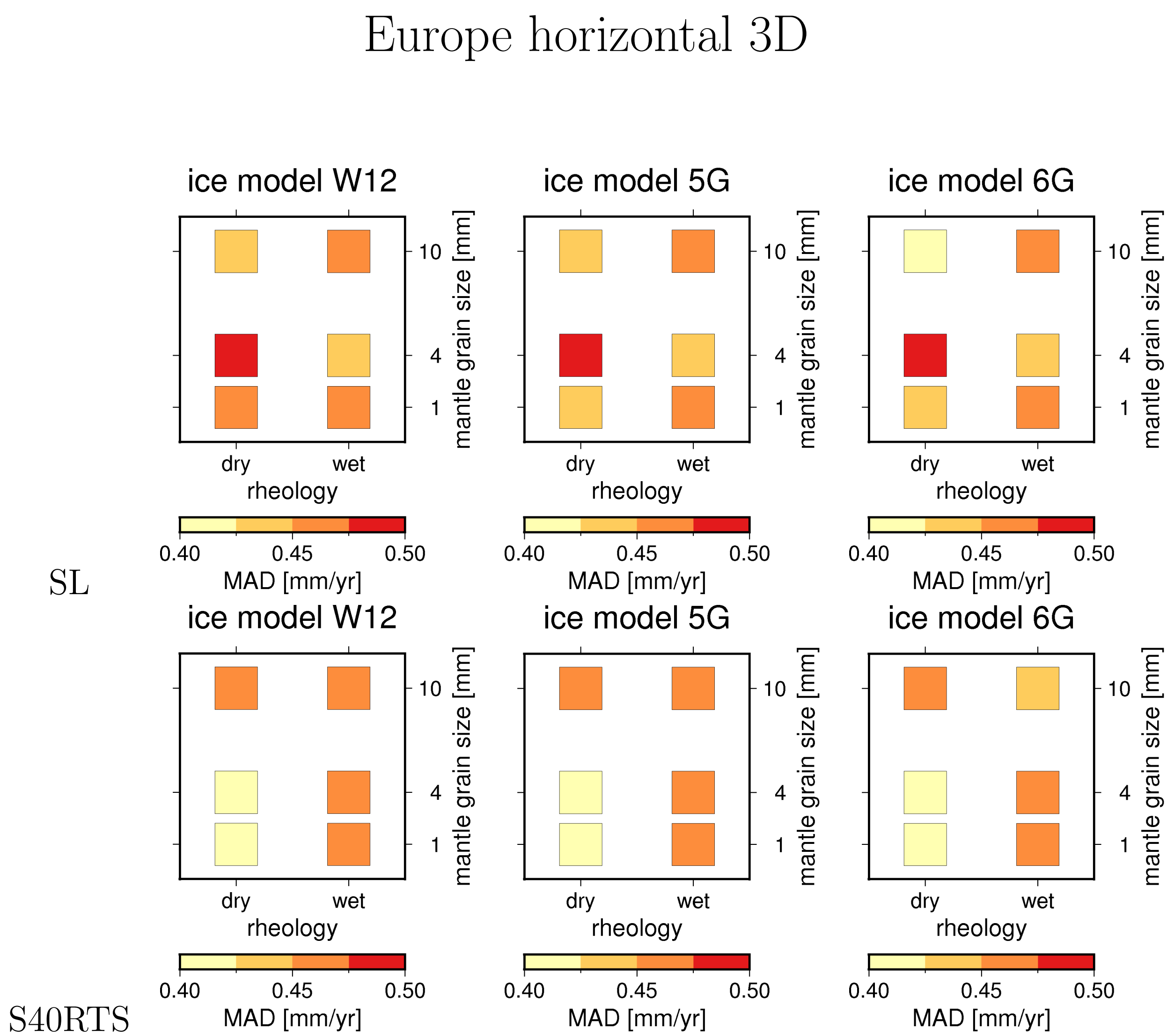

Figure D.8: MAD values in the horizontal component in Europe for each 3D GIA model. Top row with SL Earth model, bottom row with S40RTS Earth model.

North America vertical 1D

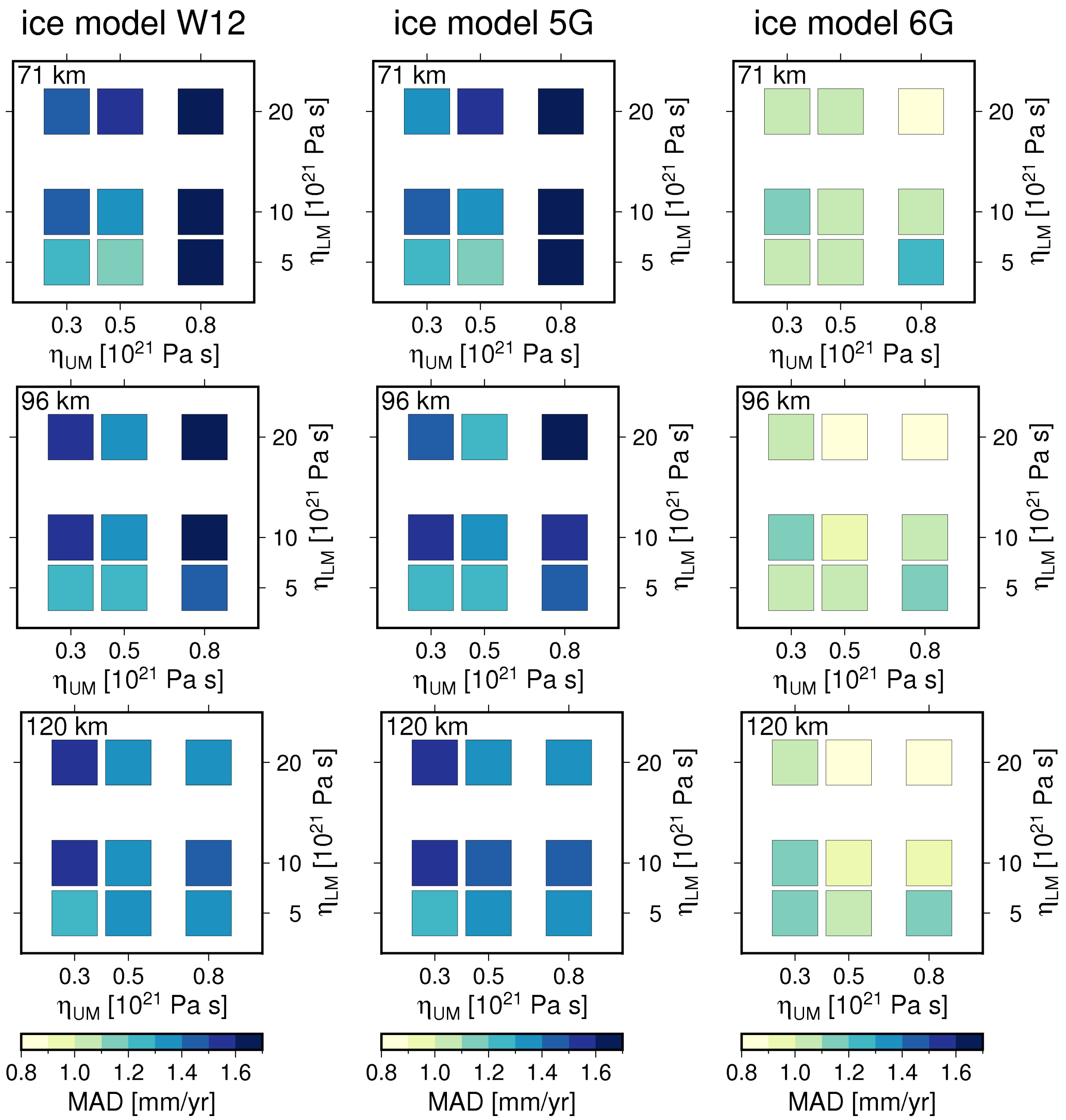

Figure D.9: MAD values in the vertical component in North America for each 1D GIA model. Colour scale saturates at 1.7 mm/yr, maximum value is 2.2 mm/yr.

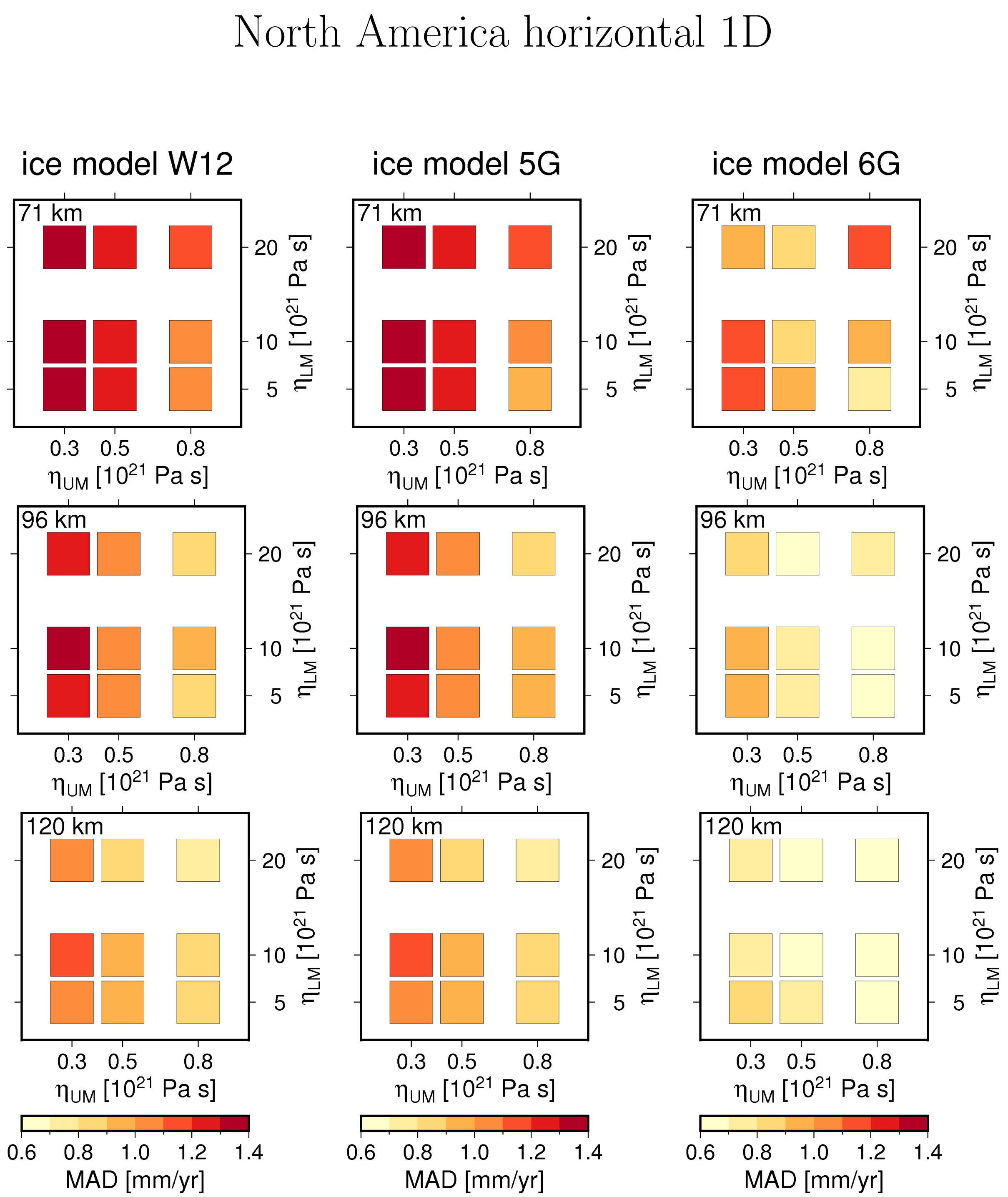

Figure D.10: MAD values in the horizontal component in North America for each 1D GIA model. Colour scale saturates at 1.4 mm/yr, maximum value is 1.7 mm/yr.

North America vertical 3D

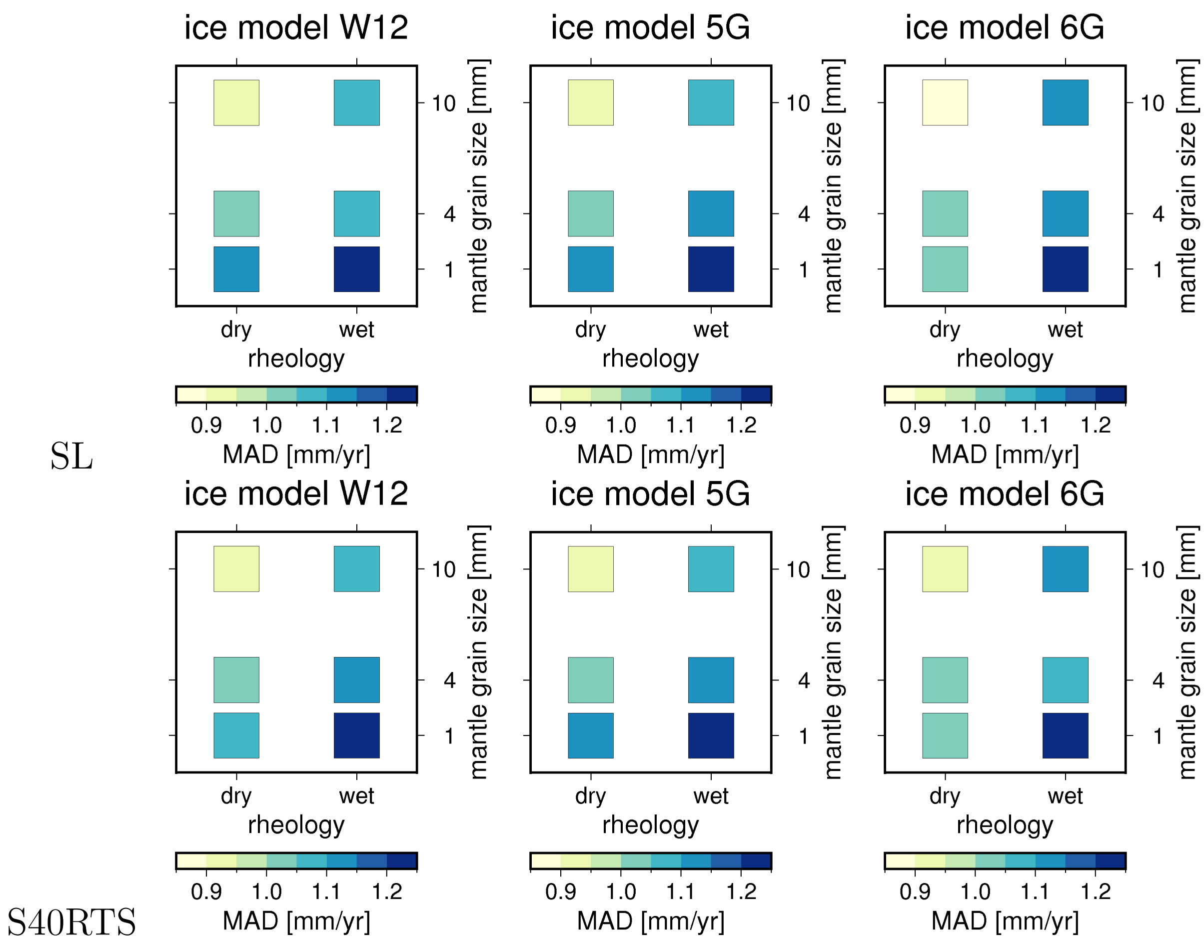

Figure D.11: MAD values in the vertical component in North America for each 3D GIA model. Top row with SL Earth model, bottom row with S40RTS Earth model

North America horizontal 3D

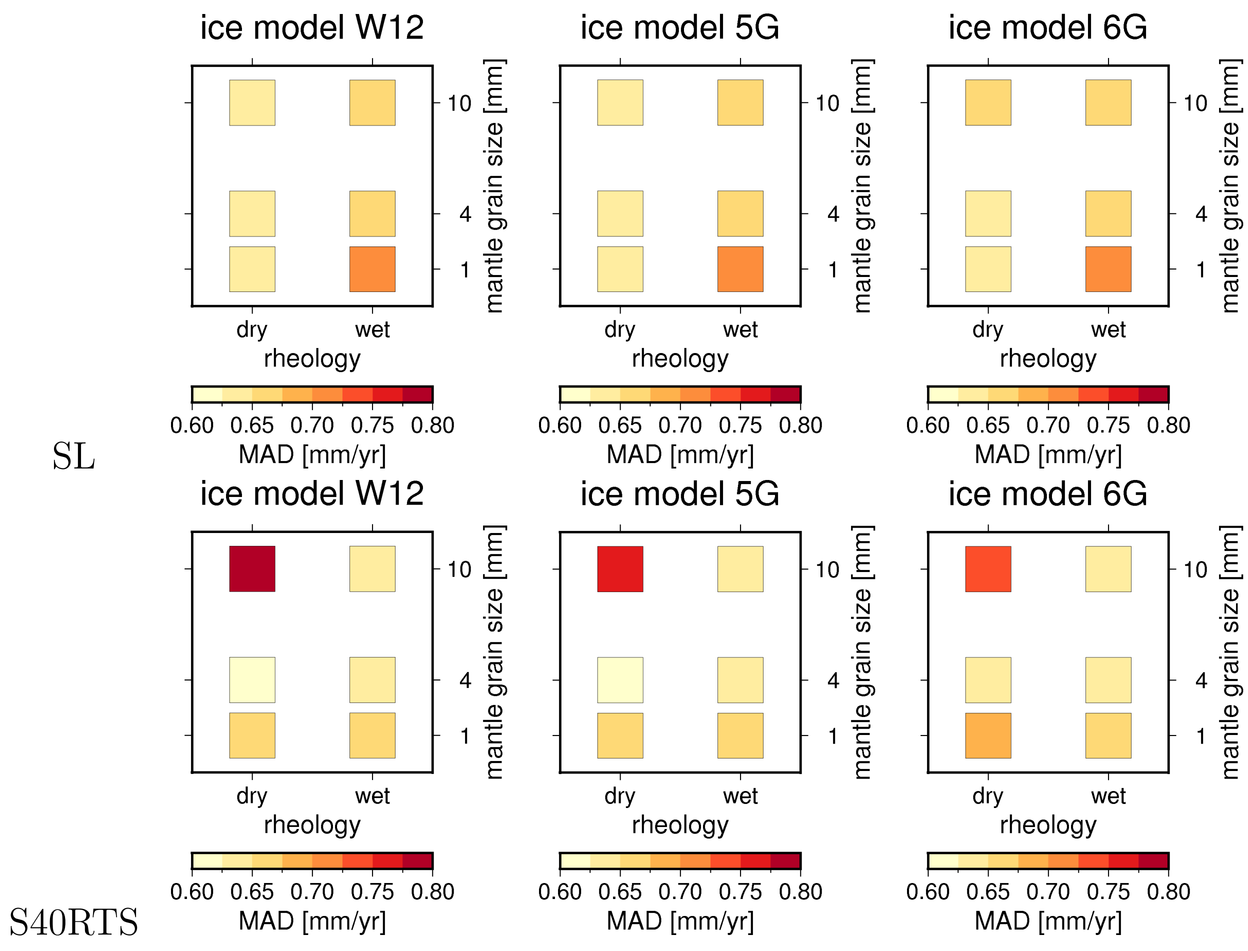

Figure D.12: MAD values in the horizontal component in North America for each 3D GIA model. Top row with SL Earth model, bottom row with S40RTS Earth model.

Antarctica vertical 1D

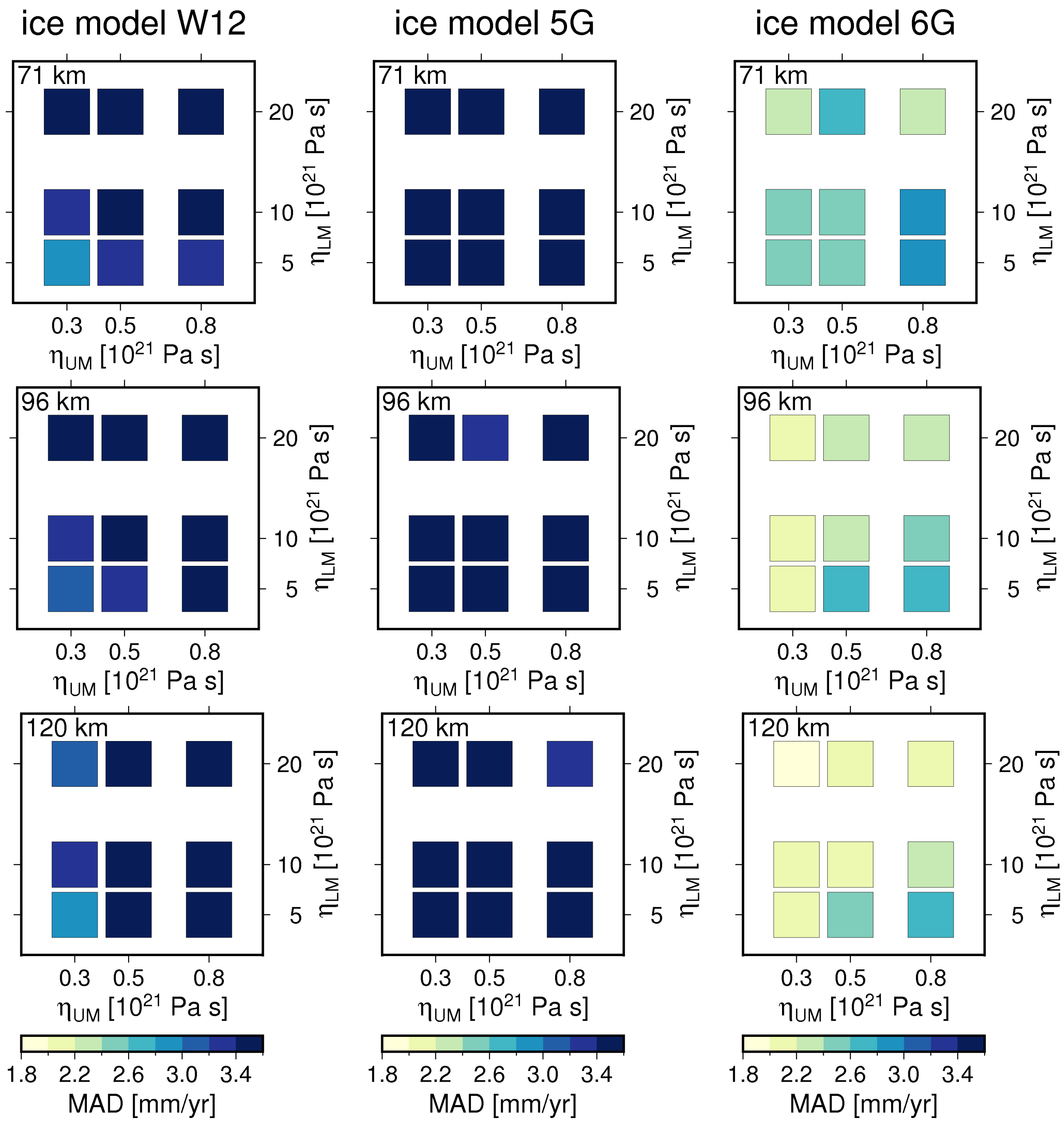

Figure D.13: MAD values in the vertical component in Antarctica for each 1D GIA model. Colour scale saturates at 4 mm/yr, maximum value is 4.3 mm/yr.

Antarctica horizontal 1D

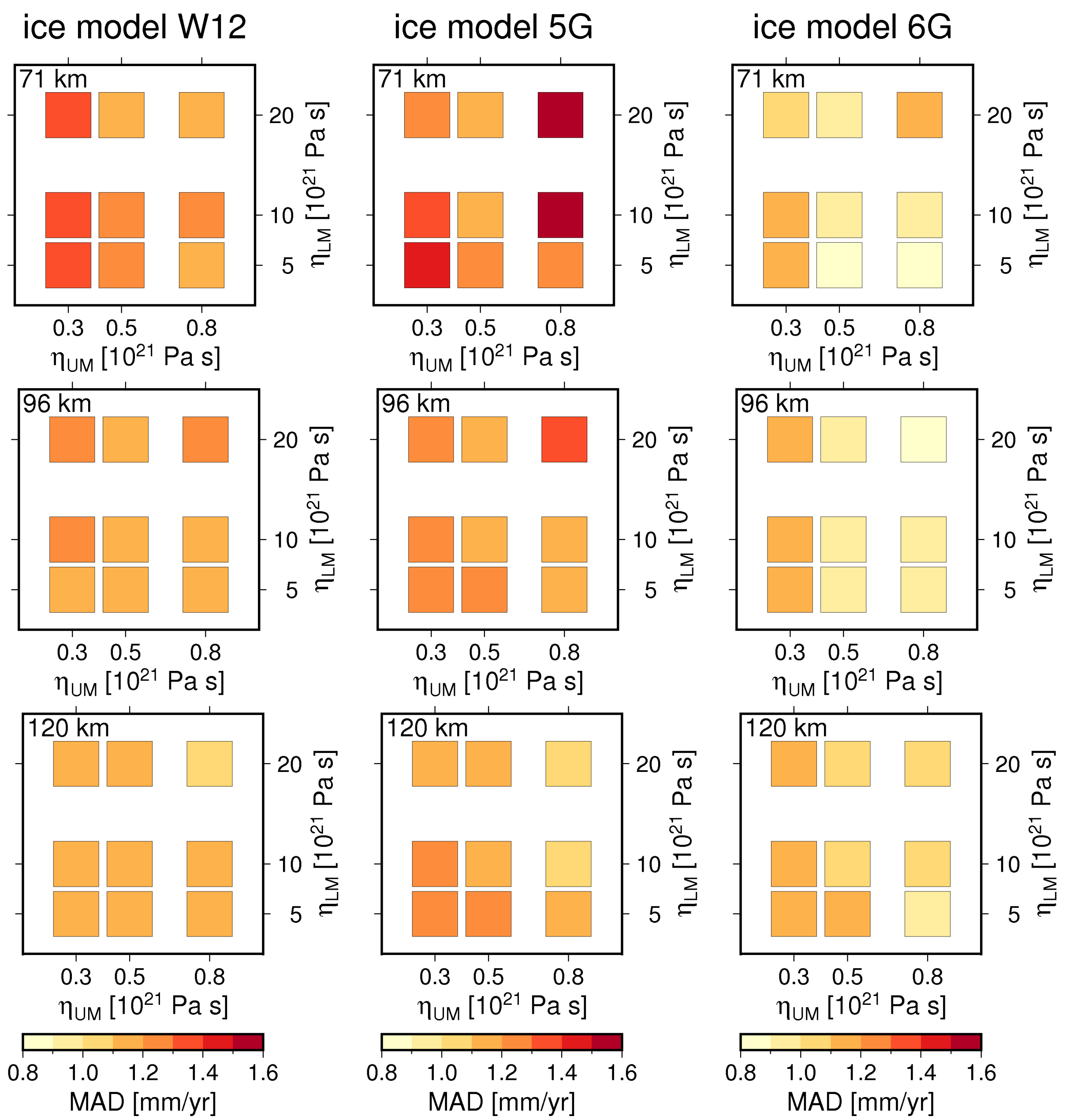

Figure D.14: MAD values in the horizontal component in Antarctica for each 1D GIA model. Colour scale saturates at 1.6 mm/yr, maximum value is 1.8 mm/yr.

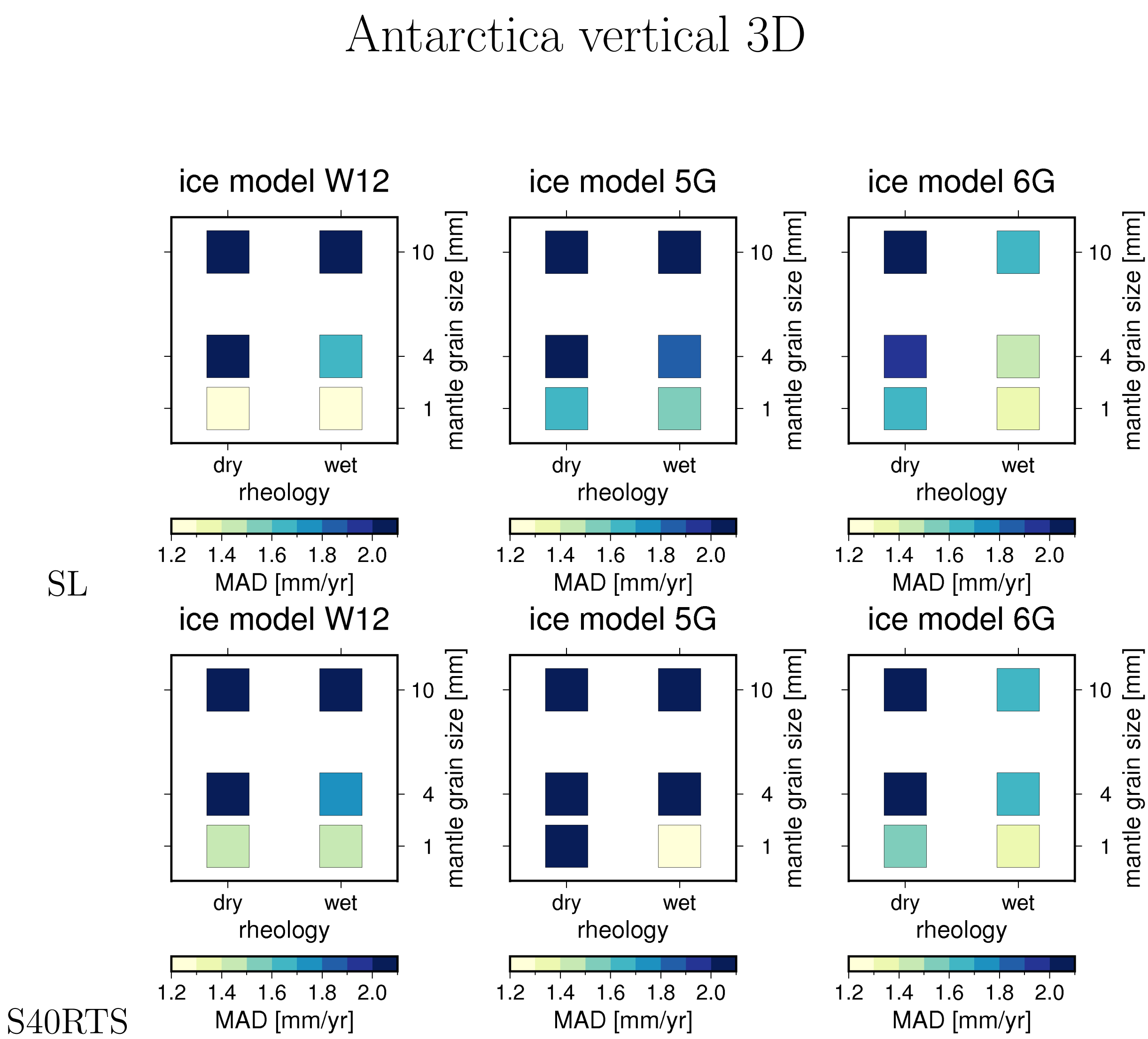

Figure D.15: MAD values in the vertical component in Antarctica for each 3D GIA model. Top row with SL Earth model, bottom row with S40RTS Earth model. Colour scale saturates at 2.3 mm/yr, maximum value is 2.7 mm/yr.

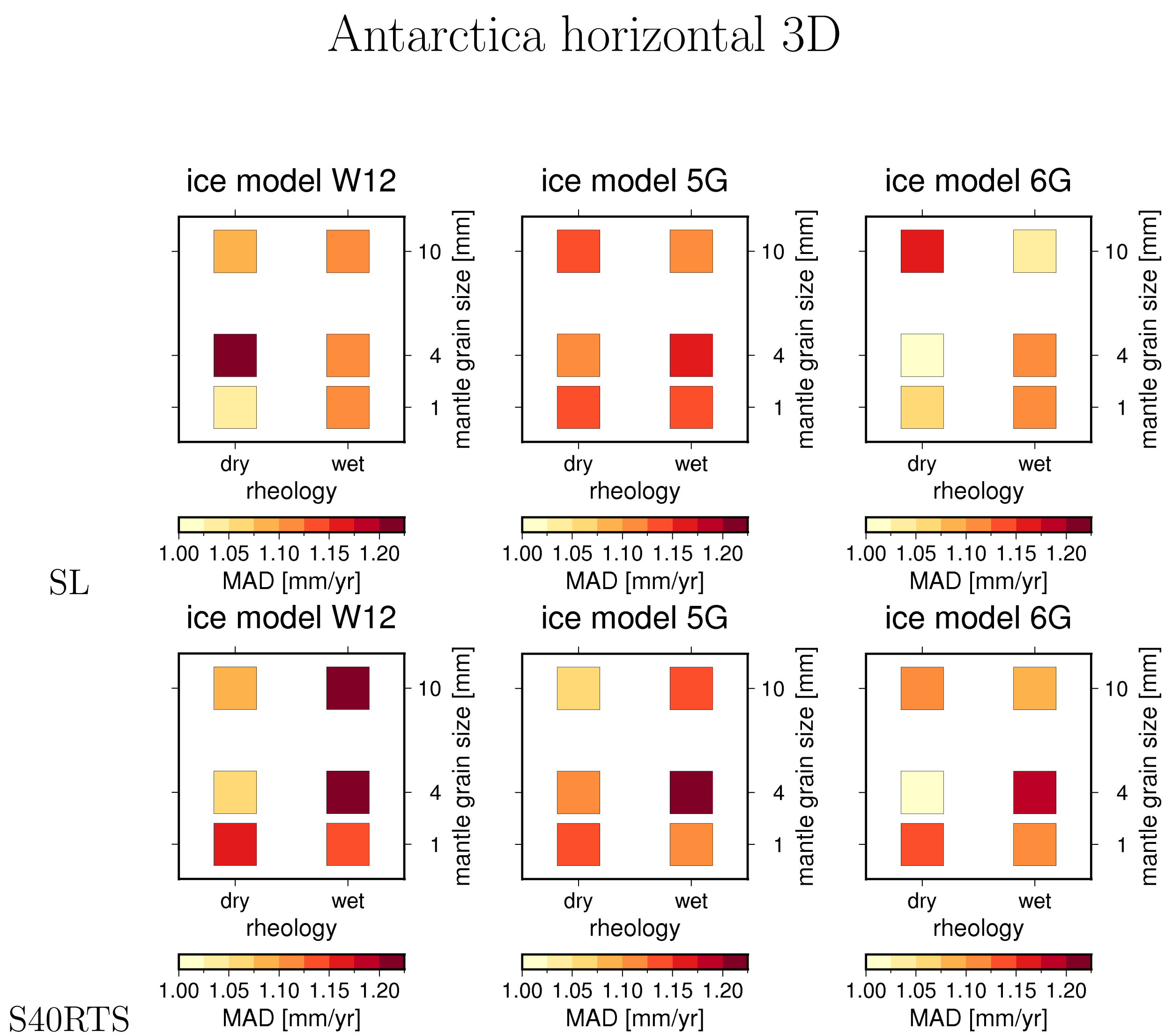

Figure D.16: MAD values in the horizontal component in Antarctica for each 3D GIA model. Top row with SL Earth model, bottom row with S40RTS Earth model.

Appendix E

Additional tables

Table E.1: The XYZ components of the estimated vector β' (in mm/yr) which represents the sum of the geocentre origin rate bias and the velocity of the reference frame in which the relevant GIA model is expressed with respect to CM, for each PMM. See section 5.1 for details.

GIA model	β_X	β_Y	β_Z
5G_SL_dry_10mm	0.061	0.345	0.849
5G_SL_dry_4mm	0.301	0.414	0.700
5G_SL_dry_1mm	0.260	0.689	0.674
5G_SL_wet_10mm	0.296	0.651	0.858
5G_SL_wet_4mm	0.235	0.763	0.687
5G_SL_wet_1mm	0.270	0.782	0.845
5G_S_dry_10mm	0.087	0.368	0.829
5G_S_dry_4mm	0.298	0.507	0.775
5G_S_dry_1mm	0.301	0.698	0.555
5G_S_wet_10mm	0.300	0.667	0.839
5G_S_wet_4mm	0.267	0.731	0.706
5G_S_wet_1mm	0.196	0.864	0.925
6G_SL_dry_10mm	0.102	0.411	0.869
6G_SL_dry_4mm	0.317	0.457	0.745
6G_SL_dry_1mm	0.243	0.729	0.706
6G_SL_wet_10mm	0.272	0.667	0.925
6G_SL_wet_4mm	0.186	0.745	0.797
6G_SL_wet_1mm	0.286	0.806	0.891
6G_S_dry_10mm	0.106	0.417	0.825
6G_S_dry_4mm	0.290	0.499	0.833
6G_S_dry_1mm	0.307	0.695	0.585
6G_S_wet_10mm	0.260	0.646	0.926
6G_S_wet_4mm	0.256	0.765	0.726
6G_S_wet_1mm	0.218	0.867	0.952
W12_SL_dry_10mm	0.080	0.345	0.862
W12_SL_dry_4mm	0.305	0.472	0.795
W12_SL_dry_1mm	0.283	0.656	0.666
W12_SL_wet_10mm	0.334	0.627	0.855
W12_SL_wet_4mm	0.256	0.739	0.691
W12_SL_wet_1mm	0.273	0.788	0.899
W12_S_dry_10mm	0.161	0.333	0.790
W12_S_dry_4mm	0.322	0.499	0.787
W12_S_dry_1mm	0.323	0.675	0.544
W12_S_wet_10mm	0.272	0.707	0.913
W12_S_wet_4mm	0.262	0.716	0.727
W12_S_wet_1mm	0.207	0.892	0.955

GIA model	β_X	β_Y	β_Z	GIA model	β_X	β_Y	β_Z
null-GIA	0.298	0.922	0.839	6G_120p310	0.101	-0.500	-0.031
5G_96p55	-0.171	0.177	0.331	6G_120p320	0.031	-0.482	-0.017
5G_96p510	-0.083	0.513	0.386	6G_120p85	-0.242	-0.468	0.204
5G_96p520	0.128	0.580	0.164	6G_120p810	-0.154	-0.075	0.065
5G_96p35	0.046	0.105	0.370	6G_120p820	-0.088	0.337	0.115
5G_96p310	-0.096	0.249	0.464	6G_71p55	-0.432	-0.197	0.243
5G_96p320	-0.130	0.397	0.527	6G_71p510	-0.451	0.094	0.239
5G_96p85	-0.062	0.392	0.108	6G_71p520	-0.167	0.541	-0.076
5G_96p810	0.224	0.638	-0.069	6G_71p35	-0.199	-0.073	0.156
5G_96p820	0.289	0.743	0.074	6G_71p310	-0.523	-0.029	0.274
5G_120p55	0.086	-0.020	0.280	6G_71p320	-0.507	0.049	0.333
5G_120p510	-0.039	0.298	0.430	6G_71p85	-0.151	0.274	-0.239
5G_120p520	0.089	0.404	0.316	6G_71p810	0.045	0.841	-0.496
5G_120p35	0.086	-0.006	0.401	6G_71p820	0.197	1.045	-0.573
5G_120p310	0.002	0.103	0.472	W12_96p55	-0.242	-0.368	0.115
5G_120p320	-0.046	0.235	0.56	W12_96p510	-0.350	-0.277	0.183
5G_120p85	-0.012	0.208	0.177	W12_96p520	-0.278	-0.081	0.227
5G_120p810	0.216	0.497	0.094	W12_96p35	0.090	-0.412	0.025
5G_120p820	0.273	0.745	0.165	W12_96p310	-0.098	-0.359	0.013
5G_71p55	-0.182	0.655	0.271	W12_96p320	-0.134	-0.318	0.063
5G_71p510	-0.019	0.973	0.186	W12_96p85	-0.266	-0.161	0.099
5G_71p520	0.186	1.030	-0.007	W12_96p810	-0.194	0.209	-0.044
5G_71p35	-0.283	0.466	0.422	W12_96p820	0.063	0.713	-0.256
5G_71p310	-0.307	0.642	0.531	W12_120p55	0.065	-0.531	-0.005
5G_71p320	-0.186	0.729	0.500	W12_120p510	-0.202	-0.461	0.115
5G_71p85	-0.095	0.641	0.005	W12_120p520	-0.174	-0.276	0.153
5G_71p810	0.288	0.720	-0.030	W12_120p35	0.137	-0.461	0.143
5G_71p820	0.296	0.854	0.167	W12_120p310	0.101	-0.500	-0.031
6G_96p55	-0.242	-0.368	0.115	W12_120p320	0.031	-0.482	-0.017
6G_96p510	-0.350	-0.277	0.183	W12_120p85	-0.242	-0.468	0.204
6G_96p520	-0.278	-0.081	0.227	W12_120p810	-0.154	-0.075	0.065
6G_96p35	0.090	-0.412	0.025	W12_120p820	-0.088	0.337	0.115
6G_96p310	-0.098	-0.359	0.013	W12_71p55	-0.432	-0.197	0.243
6G_96p320	-0.134	-0.318	0.063	W12_71p510	-0.451	0.094	0.239
6G_96p85	-0.266	-0.161	0.099	W12_71p520	-0.167	0.541	-0.076
6G_96p810	-0.194	0.209	-0.044	W12_71p35	-0.199	-0.073	0.156
6G_96p820	0.063	0.713	-0.256	W12_71p310	-0.523	-0.029	0.274
6G_120p55	0.065	-0.531	-0.005	W12_71p320	-0.507	0.049	0.333
6G_120p510	-0.202	-0.461	0.115	W12_71p85	-0.151	0.274	-0.239
6G_120p520	-0.174	-0.276	0.153	W12_71p810	0.045	0.841	-0.496
6G_120p35	0.137	-0.461	0.143	W12_71p820	0.197	1.045	-0.573

Groups of near-best models Europe			
Vertical 1D	6G_71p320	Vertical 3D	W12_SL_dry_4mm
	6G_71p310		5G_SL_dry_4mm
	6G_96p320		6G_SL_dry_4mm
	6G_96p55		5G_S_dry_4mm
	W12_71p35		W12_S_dry_4mm
	6G_120p55		6G_S_dry_10mm
	5G_71p35		5G_S_dry_10mm
	6G_96p310		6G_S_dry_4mm
	6G_96p35		W12_S_dry_10mm
	6G_96p520		W12_SL_wet_10mm
	6G_71p35		5G_SL_wet_10mm
	6G_120p520		5G_SL_dry_10mm
	6G_96p510		6G_SL_dry_10mm
	6G_120p820		W12_SL_dry_10mm
	6G_120p510		W12_S_dry_1mm
	6G_120p810		W12_SL_wet_4mm
	6G_71p55		6G_SL_dry_1mm
	5G_96p35		W12_SL_dry_1mm
	6G_120p85		
	5G_71p310		
	6G_120p320		
	W12_96p35		
	W12_71p310		
	6G_71p510		
	W12_120p35		
Horizontal 1D	6G_96p310	Horizontal 3D	6G_S_dry_4mm
	6G_96p35		5G_S_dry_4mm
	6G_120p35		W12_S_dry_4mm
	6G_120p320		6G_S_dry_1mm
	6G_120p310		6G_SL_dry_10mm
	6G_96p320		5G_S_dry_1mm
			W12_S_dry_1mm
			5G_SL_dry_10mm
			W12_SL_dry_10mm

Table E.2: Groups of near-best GIA models in Europe based on their MADs. The groups were formed by considering all models with MADs better than the null-GIA case and within 0.1/0.2 mm/yr of the best model for the horizontal and the vertical component, respectively (cf. section 6.3).

Groups of near-best models North America			
Vertical 1D	6G_120p820	Vertical 3D	6G_SL_dry_10mm
	6G_96p820		W12_S_dry_10mm
	6G_96p520		6G_S_dry_10mm
	6G_120p520		5G_S_dry_10mm
	6G_71p820		W12_SL_dry_10mm
	6G_120p810		5G_SL_dry_10mm
			W12_S_dry_4mm
			6G_S_dry_4mm
			5G_S_dry_4mm
			6G_S_dry_1mm
			6G_SL_dry_4mm
			W12_SL_dry_4mm
			6G_SL_dry_1mm
			5G_SL_dry_4mm
			6G_S_wet_4mm
			W12_S_wet_10mm
Horizontal 1D	6G_120p810	Horizontal 3D	5G_S_dry_4mm
	6G_120p520		W12_S_dry_4mm
	6G_120p85		W12_SL_dry_4mm
	6G_120p820		W12_SL_dry_10mm
	6G_120p510		5G_SL_dry_4mm
	6G_96p520		5G_SL_dry_10mm
	6G_96p85		6G_S_wet_4mm
			5G_SL_dry_1mm
			W12_SL_dry_1mm
			W12_S_wet_4mm
			5G_S_wet_10mm
			6G_S_dry_4mm
			5G_S_wet_4mm
			6G_SL_dry_4mm
			W12_S_wet_10mm
			6G_S_wet_10mm
			6G_SL_dry_1mm
			6G_SL_dry_10mm
			6G_SL_wet_10mm
			5G_SL_wet_4mm
			W12_SL_wet_4mm
			W12_S_wet_1mm
			5G_SL_wet_10mm
			6G_SL_wet_4mm
			5G_S_wet_1mm
			6G_S_wet_1mm
			5G_S_dry_1mm
			W12_SL_wet_10mm
			W12_S_dry_1mm
			6G_S_dry_1mm

Table E.3:]

Groups of near-best models in North America based on their MADs. The groups were formed as in Table E.2.

Groups of near-best models Antarctica			
Vertical 1D	∅	Vertical 3D	5G_S_wet_1mm W12_SL_dry_1mm W12_SL_wet_1mm 6G_SL_wet_1mm
Horizontal 1D	6G_71p85 6G_96p820 6G_71p55 6G_120p85 6G_96p510 6G_96p810	Horizontal 3D	6G_S_dry_4mm 6G_SL_dry_4mm 6G_SL_wet_10mm W12_SL_dry_1mm 6G_SL_dry_1mm W12_S_dry_4mm

Table E.4: Groups of near-best models in Antarctica based on their MADs. The groups were formed as in Table E.2.

Groups of near-best models globally (plate weighted)			
Vertical 1D	6G_120p820	Vertical 3D	W12_SL_dry_1mm
	6G_120p320		W12_S_dry_1mm
	6G_120p520		6G_S_dry_1mm
			6G_SL_dry_1mm
			5G_SL_dry_1mm
			W12_SL_wet_4mm
			6G_SL_wet_4mm
			6G_S_wet_4mm
			6G_SL_wet_1mm
			5G_S_dry_1mm
			W12_SL_wet_1mm
			W12_S_wet_4mm
			6G_SL_dry_4mm
			6G_SL_wet_10mm
			6G_S_wet_10mm
			5G_SL_wet_1mm
			5G_SL_wet_4mm
			W12_SL_wet_10mm
Horizontal 1D	∅	Horizontal 3D	6G_SL_wet_10mm
			W12_S_dry_4mm
			6G_S_wet_10mm
			6G_SL_dry_4mm
			5G_SL_wet_10mm
			5G_SL_dry_4mm
			5G_S_wet_10mm
			W12_SL_wet_10mm
			6G_S_dry_4mm
			6G_S_wet_1mm
			5G_S_wet_1mm
			W12_S_wet_1mm
			W12_SL_dry_1mm

Table E.5: Groups of near-best models globally based on their MADs (when weighting by plate area is applied). The groups were formed as in Table E.2.

Table E.6: Elastic deformation due to present-day ice mass changes at the Antarctic GNSS sites. Provided by Achraf Koulali (personal communication, 2020).

Site code	φ [°]	λ [°]	$\dot{N}$	$\pm\sigma_{\dot{N}}$	$\dot{E}$	$\pm\sigma_{\dot{E}}$	$\dot{U}$	$\pm\sigma_{\dot{U}}$
BACK	-74.43	-102.48	1.21	0.04	0.02	0.04	3.80	0.11
BENN	-84.79	-116.46	-0.06	0.02	-0.02	0.02	1.05	0.09
BERP	-74.55	-111.88	1.62	0.08	-0.04	0.04	4.76	0.22
BRIP	-75.80	158.47	0.01	0.00	-0.01	0.00	0.01	0.02
BUMS	-85.96	174.50	0.00	0.00	-0.01	0.00	0.31	0.02
BURI	-79.15	155.89	0.03	0.00	-0.04	0.01	0.12	0.03
CAPF	-66.01	-60.56	0.04	0.00	0.07	0.01	0.29	0.03
CAS1	-66.28	110.52	0.08	0.01	-0.12	0.01	0.28	0.03
CASM	-66.28	110.52	0.08	0.01	-0.12	0.01	0.28	0.03
CLRK	-77.34	-141.87	-0.16	0.01	-0.26	0.01	0.94	0.03
COTE	-77.81	162.00	0.02	0.01	-0.04	0.00	0.14	0.02
CRDI	-82.86	-53.20	0.02	0.01	0.10	0.01	0.52	0.03
DAVM	-68.58	77.97	-0.07	0.00	0.02	0.00	-0.18	0.01
DEVI	-81.48	161.98	0.06	0.01	-0.02	0.01	0.24	0.02
DUM1	-66.67	140.00	-0.08	0.00	-0.03	0.01	-0.15	0.03
DUPT	-64.80	-62.82	0.05	0.01	0.02	0.00	0.22	0.03
FALL	-85.31	-143.63	0.11	0.01	-0.20	0.01	0.17	0.04
FIE0	-76.14	168.42	0.02	0.00	-0.03	0.00	0.16	0.01
FLM5	-77.53	160.27	0.03	0.01	-0.04	0.00	0.13	0.03
FONP	-65.25	-61.65	0.06	0.01	0.03	0.01	0.24	0.02
FREI	-62.19	-58.98	0.03	0.00	0.01	0.00	0.16	0.01
FTP4	-78.93	162.56	0.02	0.01	-0.03	0.01	0.17	0.03
HAAG	-77.04	-78.29	-0.07	0.01	0.36	0.01	0.35	0.05
HOWE	-87.42	-149.43	-0.02	0.00	-0.07	0.00	0.24	0.01
HOWN	-77.53	-86.77	-0.33	0.02	0.65	0.02	1.25	0.09
HUGO	-64.96	-65.67	0.06	0.01	0.02	0.01	0.24	0.02
IGGY	-83.31	156.25	0.01	0.00	-0.03	0.00	0.32	0.01
INMN	-74.82	-98.88	1.55	0.08	-0.10	0.05	6.22	0.25
KHLR	-76.15	-120.73	-0.43	0.02	-0.67	0.03	3.00	0.08
LPLY	-73.11	-90.30	0.57	0.02	0.16	0.02	1.73	0.08
LWN0	-81.35	152.73	0.08	0.01	0.00	0.01	0.24	0.04
MAW1	-67.60	62.87	-0.10	0.01	-0.09	0.01	-0.27	0.05
MCAR	-76.32	-144.30	-0.02	0.01	-0.36	0.01	0.96	0.06
MCM4	-77.85	166.67	0.04	0.00	-0.02	0.00	0.15	0.02
MIN0	-78.65	167.16	0.02	0.01	-0.01	0.01	0.22	0.03

continued . . .

. . . continued

Site code	φ [°]	λ [°]	$\dot{N}$	$\pm\,\sigma_{\dot{N}}$	$\dot{E}$	$\pm\,\sigma_{\dot{E}}$	$\dot{U}$	$\pm\,\sigma_{\dot{U}}$
OHI2	-63.32	-57.90	0.04	0.01	-0.01	0.01	0.21	0.04
PATN	-78.03	-155.02	0.00	0.01	-0.17	0.01	0.55	0.03
PECE	-85.61	-68.56	-0.07	0.00	0.05	0.00	0.45	0.02
PIRT	-81.10	-85.14	-0.20	0.01	0.14	0.01	0.45	0.04
PRPT	-66.01	-65.34	0.08	0.01	0.01	0.01	0.33	0.04
RAMG	-84.34	178.05	0.03	0.02	0.02	0.01	0.22	0.07
RMBO	-83.87	-66.39	0.00	0.00	0.04	0.01	0.44	0.03
ROB4	-77.03	163.19	0.04	0.01	-0.02	0.01	0.21	0.05
ROBN	-65.25	-59.44	0.04	0.00	0.03	0.00	0.20	0.01
ROTH	-67.57	-68.13	0.05	0.01	0.04	0.01	0.33	0.03
SDLY	-77.14	-125.97	-0.40	0.01	-0.36	0.01	1.68	0.04
SPGT	-64.29	-61.05	0.04	0.00	0.02	0.00	0.19	0.01
STEW	-84.19	-86.25	-0.06	0.00	0.03	0.00	0.42	0.02
SUGG	-75.28	-72.18	-0.11	0.01	0.25	0.01	0.44	0.04
SYOG	-69.01	39.58	-0.17	0.01	0.05	0.01	-0.69	0.03
THUR	-72.53	-97.56	0.66	0.03	0.06	0.02	1.23	0.10
TOMO	-75.80	-114.66	-1.07	0.13	-1.32	0.13	9.32	0.69
UTHW	-77.58	-109.04	-1.03	0.03	-0.34	0.03	4.41	0.15
VESL	-71.67	-2.84	-0.15	0.04	0.00	0.02	-1.33	0.15
VL01	-72.45	169.73	-0.01	0.01	0.03	0.01	0.12	0.11
VL12	-72.27	163.73	-0.02	0.01	0.01	0.01	0.29	0.04
VL30	-70.60	162.53	0.07	0.04	0.12	0.11	-0.62	0.68
VNAD	-65.25	-64.25	0.07	0.01	0.02	0.01	0.26	0.04
WHN0	-79.85	154.22	0.02	0.01	-0.02	0.01	0.12	0.02
WHN5	-79.85	154.22	0.02	0.01	-0.02	0.01	0.12	0.02
WHTM	-82.68	-104.39	-0.14	0.01	-0.13	0.01	0.43	0.05
WILN	-80.04	-80.56	-0.14	0.01	0.22	0.01	0.47	0.05
WLCT	-85.37	-87.39	-0.08	0.00	0.02	0.00	0.46	0.02
WWAY	-81.58	-28.40	0.11	0.01	0.10	0.01	0.09	0.04

References

A G, Wahr J, Zhong S (2012) Computations of the viscoelastic response of a 3-D compressible Earth to surface loading: an application to Glacial Isostatic Adjustment in Antarctica and Canada. Geophysical Journal International 192(2):557–572, DOI 10.1093/gji/ggs030

Altamimi Z, Sillard P, Boucher C (2002) ITRF2000: A new release of the International Terrestrial Reference Frame for Earth science applications. Journal of Geophysical Research: Solid Earth 107(B10), DOI 10.1029/2001JB000561

Altamimi Z, Collilieux X, Legrand J, Garayt B, Boucher C (2007) ITRF2005: A new release of the International Terrestrial Reference Frame based on time series of station positions and Earth Orientation Parameters. Journal of Geophysical Research: Solid Earth 112(B9), DOI 10.1029/2007JB004949

Altamimi Z, Collilieux X, Métivier L (2011) ITRF2008: an improved solution of the international terrestrial reference frame. Journal of Geodesy 85(8):457–473, DOI 10.1007/s00190-011-0444-4

Altamimi Z, Métivier L, Collilieux X (2012) ITRF2008 plate motion model. Journal of Geophysical Research: Solid Earth 117(B7), DOI 10.1029/2011JB008930

Altamimi Z, Rebischung P, Métivier L, Collilieux X (2016) ITRF2014: A new release of the International Terrestrial Reference Frame modeling nonlinear station motions. Journal of Geophysical Research: Solid Earth 121(8):6109–6131, DOI 10.1002/2016JB013098

Altamimi Z, Métivier L, Rebischung P, Rouby H, Collilieux X (2017) ITRF2014 plate motion model. Geophysical Journal International 209(3):1906–1912, DOI 10.1093/gji/ggx136

Amiri-Simkooei A, Hosseini-Asl M, Asgari J, Zangeneh-Nejad F (2019) Offset detection in GPS position time series using multivariate analysis. GPS Solutions 23, DOI 10.1007/s10291-018-0805-z

Argus DF, Gordon RG (1991) No-net-rotation model of current plate velocities incorporating plate motion model NUVEL-1. Geophysical Research Letters 18(11):2039–2042, DOI 10.1029/91GL01532

Argus DF, Peltier WR, Watkins MM (1999) Glacial isostatic adjustment observed using very long baseline interferometry and satellite laser ranging geodesy. Journal of Geophysical Research: Solid Earth 104(B12):29077–29093, DOI 10.1029/1999JB000237

Argus DF, Gordon RG, Heflin MB, Ma C, Eanes RJ, Willis P, Peltier WR, Owen SE (2010) The angular velocities of the plates and the velocity of Earth's centre from space geodesy. Geophysical Journal International 180(3):913–960, DOI 10.1111/j.1365-246X.2009.04463.x

Argus DF, Gordon RG, DeMets C (2011) Geologically current motion of 56 plates relative to the no-net-rotation reference frame. Geochemistry, Geophysics, Geosystems 12(11), DOI 10.1029/2011GC003751

Baarda W (1968) A testing procedure for use in geodetic networks. Netherlands Geodetic Commission, Publications on Geodesy, New Series, 2(5), Delft

Barletta VR, Bevis M, Smith BE, Wilson T, Brown A, Bordoni A, Willis M, Khan SA, Rovira-Navarro M, Dalziel I, Smalley R, Kendrick E, Konfal S, Caccamise DJ, Aster RC, Nyblade A, Wiens DA (2018) Observed rapid bedrock uplift in Amundsen Sea Embayment promotes ice-sheet stability. Science 360(6395):1335–1339, DOI 10.1126/science.aao1447

Bastos L, Bos M, Fernandes RM (2010) Deformation and Tectonics: Contribution of GPS Measurements to Plate Tectonics - Overview and Recent Developments. In: Xu G (ed) Sciences of Geodesy – I, Springer, Berlin, pp 155–184, DOI 10.1007/978-3-642-11741-1_5

Baur O, Kuhn M, Featherstone W (2009) GRACE-derived ice-mass variations over Greenland by accounting for leakage effects. Journal of Geophysical Research: Solid Earth 114(6), DOI 10.1029/2008JB006239

Benoit W (2005) Mechanical properties: Anelasticity. In: Bassani F, Liedl GL, Wyder P (eds) Encyclopedia of Condensed Matter Physics, Elsevier, Oxford, pp 271 – 280, DOI 10.1016/B0-12-369401-9/00574-X

Bevis M, Brown A (2014) Trajectory models and reference frames for crustal motion geodesy. Journal of Geodesy 88:283–311, DOI 10.1007/s00190-013-0685-5

Bevis M, Kendrick E, Smalley Jr R, Dalziel I, Caccamise D, Sasgen I, Helsen M, Taylor FW, Zhou H, Brown A, Raleigh D, Willis M, Wilson T, Konfal S (2009) Geodetic measurements of vertical crustal velocity in West Antarctica and the implications for ice mass balance. Geochemistry, Geophysics, Geosystems 10(10), DOI 10.1029/2009GC002642

Bird P (2003) An updated digital model of plate boundaries. Geochemistry, Geophysics, Geosystems 4(3), DOI 10.1029/2001GC000252, 1027

Blewitt G (1998) GPS data processing methodology: from theory to applications. In: Teunissen P, Kleusberg A (eds) GPS for Geodesy, Springer, Berlin, pp 231–269, DOI 10.10071978-3-642-72011-6

Blewitt G (2003) Self-consistency in reference frames, geocenter definition, and surface loading of the solid Earth. Journal of Geophysical Research: Solid Earth 108(B2), DOI 10.1029/2002JB002082

Blewitt G, Lavallée D (2002) Effect of annual signals on geodetic velocity. Journal of Geophysical Research: Solid Earth 107(B7), DOI 10.1029/2001JB000570

Blewitt G, Bock Y, Kouba J (1994) Constructing the IGS Polyhedron by Distributed Processing. In: Zumberge J, Liu R (eds) IGS Analysis Workshop Proceedings: Densification of ITRF through Regional GPS Networks, IGS Central Bureau, Pasadena, California, USA, pp 21–37

Blewitt G, Kreemer C, Hammond WC, Gazeaux J (2016) MIDAS robust trend estimator for accurate GPS station velocities without step detection. Journal of Geophysical Research: Solid Earth 121(3):2054–2068, DOI 10.1002/2015JB012552

Bock Y, Melgar D (2016) Physical applications of GPS geodesy: a review. Reports on Progress in Physics 79(10):106801, DOI 10.1088/0034-4885/79/10/106801

Booker D, Clarke PJ, Lavallée DA (2014) Secular changes in Earth's shape and surface mass loading derived from combinations of reprocessed global GPS networks. Journal of Geodesy 88(9):839–855, DOI 10.1007/s00190-014-0725-9

Booker DPA (2012) Secular changes in Earth's shape and surface mass loading. PhD thesis, University of Newcastle upon Tyne, School of Civil Engineering and Geosciences

Bromwich D, Nicolas J (2010) Ice-sheet uncertainty. Nature Geoscience 3(9):596–597, DOI 10.1038/ngeo946

Chase CG (1978) Plate kinematics: The Americas, East Africa, and the rest of the world. Earth and Planetary Science Letters 37(3):355–368, DOI 10.1016/0012-821X(78)90051-1

Collilieux X, Altamimi Z, Coulot D, van Dam T, Ray J (2010) Impact of loading effects on determination of the International Terrestrial Reference Frame. Advances in Space Research 45(1):144–154, DOI 10.1016/j.asr.2009.08.024

Collilieux X, Métivier L, Altamimi Z, van Dam T, Ray J (2011) Quality assessment of GPS reprocessed terrestrial reference frame. GPS Solutions 15:219–231, DOI 10.1007/s10291-010-0184-6

Cross PA (1992) Advanced least squares applied to position-fixing. University of East London, Working Paper No.6, ISSN:0260-9142

Davies P, Blewitt G (2000) Methodology for global geodetic time series estimation: A new tool for geodynamics. Journal of Geophysical Research: Solid Earth 105(B5):11083–11100, DOI 10.1029/2000JB900004

Davies PBH (1997) Secular changes in Earth's shape and surface mass loading. PhD thesis, School of Civil Engineering and Geosciences, University of Newcastle upon Tyne

DeMets C, Gordon R, Argus D, Stein S (1990) Current Plate Motions. Geophysical Journal International 101:425–478, DOI 10.1111/j.1365-246X.1990.tb06579.x

DeMets C, Gordon RG, Argus DF, Stein S (1994) Effect of recent revisions to the geomagnetic reversal time scale on estimates of current plate motions. Geophysical Research Letters 21(20):2191–2194, DOI 10.1029/94GL02118

DeMets C, Gordon RG, Argus DF (2010) Geologically current plate motions. Geophysical Journal International 181(1):1–80, DOI 10.1111/j.1365-246X.2009.04491.x

Ding K, Freymueller JT, He P, Wang Q, Xu C (2019) Glacial Isostatic Adjustment, Intraplate Strain, and Relative Sea Level Changes in the Eastern United States. Journal of Geophysical Research: Solid Earth 124(6):6056–6071, DOI 10.1029/2018JB017060

Dong D, Dickey JO, Chao Y, Cheng MK (1997) Geocenter variations caused by atmosphere, ocean and surface ground water. Geophysical Research Letters 24(15):1867–1870, DOI 10.1029/97GL01849

Douglas BC (1991) Global sea level rise. Journal of Geophysical Research: Oceans 96(C4):6981–6992, DOI 10.1029/91JC00064

Dow J, Neilan R, Rizos C (2009) The International GNSS Service in a changing landscape of Global Navigation Satellite Systems. Journal of Geodesy 83:191–198, DOI 10.1007/s00190-008-0300-3

Dziewonski AM, Anderson DL (1981) Preliminary reference earth model. Physics of the Earth and Planetary Interiors 25(4):297–356, DOI 10.1016/0031-9201(81)90046-7

Ekman M, Mäkinen J (1996) Recent postglacial rebound, gravity change and mantle flow in Fennoscandia. Geophysical Journal International 126(1):229–234, DOI 10.1111/j.1365-246X.1996.tb05281.x

Farrell WE (1972) Deformation of the Earth by surface loads. Reviews of Geophysics 10(3):761–797, DOI 10.1029/RG010i003p00761

Farrell WE, Clark JA (1976) On Postglacial Sea Level. Geophysical Journal International 46(3):647–667, DOI 10.1111/j.1365-246X.1976.tb01252.x

Fowler CMR (2005) The Solid Earth: An Introduction to Global Geophysics, 2nd edn. Cambridge University Press, Cambridge, UK; New York

Gazeaux J, Williams S, King M, Bos M, Dach R, Deo M, Moore AW, Ostini L, Petrie E, Roggero M, Teferle FN, Olivares G, Webb FH (2013) Detecting offsets in GPS time series: First results from the detection of offsets in GPS experiment. Journal of Geophysical Research: Solid Earth 118(5):2397–2407, DOI 10.1002/jgrb.50152

GEBCO (2020) The GEBCO_2020 Grid — a continuous terrain model of the global oceans and land. DOI 10.5285/a29c5465-b138-234d-e053-6c86abc040b9, GEBCO Bathymetric Compilation Group

Goldberg SL, Lau HC, Mitrovica JX, Latychev K (2016) The timing of the Black Sea flood event: Insights from modeling of glacial isostatic adjustment. Earth and Planetary Science Letters 452:178 – 184, DOI 10.1016/j.epsl.2016.06.016

Gomez N, Latychev K, Pollard D (2018) A Coupled Ice SheetSea Level Model Incorporating 3D Earth Structure: Variations in Antarctica during the Last Deglacial Retreat. Journal of Climate 31(10):4041–4054, DOI 10.1175/JCLI-D-17-0352.1

Griffiths J (2019) Combined orbits and clocks from IGS second reprocessing. Journal of Geodesy 93:177–195, DOI 10.1007/s00190-018-1149-8

Gunter BC, Didova O, Riva REM, Ligtenberg SRM, Lenaerts JTM, King MA, van den Broeke MR, Urban T (2014) Empirical estimation of present-day Antarctic glacial isostatic adjustment and ice mass change. The Cryosphere 8(2):743–760, DOI 10.5194/tc-8-743-2014

Harrison CGA (2016) The present-day number of tectonic plates. Earth, Planets and Space 68(37), DOI 10.1186/s40623-016-0400-x

Hermans THJ, van der Wal W, Broerse T (2018) Reversal of the Direction of Horizontal Velocities Induced by GIA as a Function of Mantle Viscosity. Geophysical Research Letters 45(18):9597–9604, DOI 10.1029/2018GL078533

Hill EM, Davis JL, Tamisiea ME, Lidberg M (2010) Combination of geodetic observations and models for glacial isostatic adjustment fields in Fennoscandia. Journal of Geophysical Research: Solid Earth 115(B7), DOI 10.1029/2009JB006967

Hirsch RM, Slack JR, Smith RA (1982) Techniques of trend analysis for monthly water quality data. Water Resources Research 18(1):107–121, DOI 10.1029/WR018i001p00107

Hirth G, Kohlstedt D (2003) Rheology of the upper mantle and the mantle wedge: A view from the experimentalists. Washington DC American Geophysical Union Geophysical Monograph Series 138:83–105, DOI 10.1029/138GM06

Huang PP, Wu P, Steffen H (2019) In search of an ice history that is consistent with composite rheology in Glacial Isostatic Adjustment modelling. Earth and Planetary Science Letters 517:26 – 37, DOI 10.1016/j.epsl.2019.04.011

IERS (2006) IERS Message No. 103. URL www.iers.org/IERS/EN/Organization/AnalysisCoordinator/SinexFormat/sinex.html

James TS, Morgan WJ (1990) Horizontal motions due to post-glacial rebound. Geophysical Research Letters 17(7):957–960, DOI 10.1029/GL017i007p00957

Karato Si (2008) Deformation of Earth Materials: An Introduction to the Rheology of Solid Earth. Cambridge University Press, Cambridge, DOI 10.1017/CBO9780511804892

Kaufmann G, Wu P, Ivins ER (2005) Lateral viscosity variations beneath Antarctica and their implications on regional rebound motions and seismotectonics. Journal of Geodynamics 39(2):165 – 181, DOI 10.1016/j.jog.2004.08.009

Kendall RA, Mitrovica JX, Milne GA (2005) On post-glacial sea level – II. Numerical formulation and comparative results on spherically symmetric models. Geophysical Journal International 161(3):679–706, DOI 10.1111/j.1365-246X.2005.02553.x

Khan SA, Sasgen I, Bevis M, van Dam T, Bamber JL, Wahr J, Willis M, Kjær KH, Wouters B, Helm V, Csatho B, Fleming K, Bjørk AA, Aschwanden A, Knudsen P, Munneke PK (2016) Geodetic measurements reveal similarities between post–Last Glacial Maximum and present-day mass loss from the Greenland ice sheet. Science Advances 2(9), DOI 10.1126/sciadv.1600931

Kierulf HP (2017) Analysis strategies for combining continuous and episodic GNSS for studies of neo-tectonics in Northern-Norway. Journal of Geodynamics 109:32 – 40, DOI 10.1016/j.jog.2017.07.002

Kierulf HP, Plag HP, Kristiansen O, Nørbech T (2003) Towards the true rotation of a rigid Eurasia, pp 118–124

Kierulf HP, Steffen H, Simpson MJR, Lidberg M, Wu P, Wang H (2014) A GPS velocity field for Fennoscandia and a consistent comparison to glacial isostatic adjustment models. Journal of Geophysical Research: Solid Earth 119(8):6613–6629, DOI 10.1002/2013JB010889

Kierulf HP, Steffen H, Barletta VR, Lidberg M, Johansson J, Kristiansen O, Tarasov L (2021) A GNSS velocity field for geophysical applications in Fennoscandia. Manuscript submitted for publication

King MA, Altamimi Z, Boehm J, Bos M, Dach R, Elosegui P, Fund F, Hernández-Pajares M, Lavallee D, Mendes Cerveira PJ, Penna N, Riva REM, Steigenberger P, van Dam

T, Vittuari L, Williams S, Willis P (2010) Improved Constraints on Models of Glacial Isostatic Adjustment: A Review of the Contribution of Ground-Based Geodetic Observations. Surveys in Geophysics 31(5):465–507, DOI 10.1007/s10712-010-9100-4

King MA, Keshin M, Whitehouse PL, Thomas ID, Milne G, Riva REM (2012) Regional biases in absolute sea-level estimates from tide gauge data due to residual unmodeled vertical land movement. Geophysical Research Letters 39(14), DOI 10.1029/2012GL052348

King MA, Whitehouse PL, van der Wal W (2015) Incomplete separability of Antarctic plate rotation from glacial isostatic adjustment deformation within geodetic observations. Geophysical Journal International 204(1):324–330, DOI 10.1093/gji/ggv461

Klemann V, Martinec Z (2011) Contribution of glacial-isostatic adjustment to the geocenter motion. Tectonophysics 511(3):99 – 108, DOI /10.1016/j.tecto.2009.08.031, special Section on Observation and Modeling of Glacial Isostatic Adjustment

Klemann V, Martinec Z, Ivins ER (2008) Glacial isostasy and plate motion. Journal of Geodynamics 46(3):95 – 103, DOI 10.1016/j.jog.2008.04.005, glacial Isostatic Adjustment: New Developments and Applications in Global Change, Hydrology, Sea Level, Cryosphere, and Geodynamics

Koch KR (1999) Parameter Estimation and Hypothesis Testing in Linear Models. Springer-Verlag

Kolker AS, Allison MA, Hameed S (2011) An evaluation of subsidence rates and sea-level variability in the northern Gulf of Mexico. Geophysical Research Letters 38(21), DOI 10.1029/2011GL049458

Koohzare A, Vaníček P, Santos M (2008) Pattern of recent vertical crustal movements in Canada. Journal of Geodynamics 45(2):133 – 145, DOI 10.1016/j.jog.2007.08.001

Kreemer C, Blewitt G, Klein EC (2014) A geodetic plate motion and Global Strain Rate Model. Geochemistry, Geophysics, Geosystems 15(10):3849–3889, DOI 10.1002/2014GC005407

Kreemer C, Hammond WC, Blewitt G (2018) A Robust Estimation of the 3-D Intraplate Deformation of the North American Plate From GPS. Journal of Geophysical Research: Solid Earth 123(5):4388–4412, DOI 10.1029/2017JB015257

Kuchar J, Milne G, Latychev K (2019) The importance of lateral Earth structure for North American glacial isostatic adjustment. Earth and Planetary Science Letters 512:236–245, DOI 10.1016/j.epsl.2019.01.046

Lambeck K (1988) Geophysical geodesy: the slow deformations of the earth. Clarendon Press; Oxford University Press, Oxford; New York

Lambeck K, Smither C, Johnston P (1998) Sea-level change, glacial rebound and mantle viscosity for northern Europe. Geophysical Journal International 134(1):102–144, DOI 10.1046/j.1365-246x.1998.00541.x

Lambeck K, Rouby H, Purcell A, Sun Y, Sambridge M (2014) Sea level and global ice volumes from the Last Glacial Maximum to the Holocene. Proceedings of the National Academy of Sciences of the United States of America 111, DOI 10.1073/pnas.1411762111

Lambeck K, Purcell A, Zhao S (2017) The North American Late Wisconsin ice sheet and mantle viscosity from glacial rebound analyses. Quaternary Science Reviews 158:172–210, DOI 10.1016/j.quascirev.2016.11.033

Lambert A, Courtier N, James T (2006) Long-term monitoring by absolute gravimetry: Tides to postglacial rebound. Journal of Geodynamics 41(1):307 – 317, DOI 10.1016/j.jog.2005.08.032, earth Tides and Geodynamics: Probing the Earth at Sub-Seismic Frequencies

Lange H, Casassa G, Ivins E, Schröder L, Fritsche M, Richter A, Groh A, Dietrich R (2014) Observed crustal uplift near the Southern Patagonian Icefield constrains improved viscoelastic Earth models. Geophysical Research Letters 41(3):805–812, DOI 10.1002/2013GL058419

Larson KM, Freymueller JT, Philipsen S (1997) Global plate velocities from the Global Positioning System. Journal of Geophysical Research: Solid Earth 102(B5):9961–9981, DOI 10.1029/97JB00514

Lavallée DA (2000) Tectonic plate motions from global GPS measurements. PhD thesis, University of Newcastle upon Tyne, Department of Geomatics

Lavallée DA (2006) The Tanya Software, Tanyak version 1.6. Newcastle University

Li T, Wu P, Steffen H, Wang H (2018) In search of laterally heterogeneous viscosity models of glacial isostatic adjustment with the ICE-6G_C global ice history model. Geophysical Journal International 214(2):1191–1205, DOI 10.1093/gji/ggy181

Lowrie W (2007) Fundamentals of Geophysics. Cambridge University Press, Cambridge, DOI 10.1017/CBO9780511807107

Martens HR, Rivera L, Simons M (2019) Loaddef: A Python-Based Toolkit to Model Elastic Deformation Caused by Surface Mass Loading on Spherically Symmetric Bodies. Earth and Space Science 6(2):311–323, DOI 10.1029/2018EA000462

Martín-Español A, King MA, Zammit-Mangion A, Andrews SB, Moore P, Bamber JL (2016a) An assessment of forward and inverse GIA solutions for Antarctica. Journal of Geophysical Research: Solid Earth 121(9):6947–6965, DOI 10.1002/2016JB013154

Martín-Español A, Zammit-Mangion A, Clarke PJ, Flament T, Helm V, King MA, Luthcke SB, Petrie E, Rémy F, Schön N, Wouters B, Bamber JL (2016b) Spatial and temporal Antarctic Ice Sheet mass trends, glacio-isostatic adjustment, and surface processes from a joint inversion of satellite altimeter, gravity, and GPS data. Journal of Geophysical Research: Earth Surface 121(2):182–200, DOI 10.1002/2015JF003550

Melini D, Gegout P, Spada G, King MA (2014) REAR—A Regional ElAstic Rebound Calculator. URL http://hpc.rm.ingv.it/rear

Métivier L, Altamimi Z, Rouby H (2020) Past and present ITRF solutions from geophysical perspectives. Advances in Space Research 65:2711–2722, DOI 10.1016/j.asr.2020.03.031

Milne GA, Davis JL, Mitrovica JX, Scherneck HG, Johansson JM, Vermeer M, Koivula H (2001) Space-Geodetic Constraints on Glacial Isostatic Adjustment in Fennoscandia. Science 291(5512):2381–2385, DOI 10.1126/science.1057022

Minster JB, Jordan TH (1978) Present-day plate motions. Journal of Geophysical Research: Solid Earth 83(B11):5331–5354, DOI 10.1029/JB083iB11p05331

Mitrovica JX, Milne GA (2003) On post-glacial sea level – I. General theory. Geophysical Journal International 154(2):253–267, DOI 10.1046/j.1365-246X.2003.01942.x

Mitrovica JX, Milne GA, Davis JL (2001) Glacial isostatic adjustment on a rotating earth. Geophysical Journal International 147(3):562–578, DOI 10.1046/j.1365-246x.2001.01550.x

Mitrovica JX, Wahr J, Matsuyama I, Paulson A (2005) The rotational stability of an ice-age earth. Geophysical Journal International 161(2):491–506, DOI 10.1111/j.1365-246X.2005.02609.x

Montagner JP (2011) Earth's Structure, Global, Springer Netherlands, Dordrecht, pp 144–154. DOI 10.1007/978-90-481-8702-7_13

Montillet JP, Bos MS (2020) Conclusions and Future Challenges in Geodetic Time Series Analysis, Springer, Cham, pp 419–421. DOI doi.org/10.1007/978-3-030-21718-1_13

Nield GA, Barletta VR, Bordoni A, King MA, Whitehouse PL, Clarke PJ, Domack E, Scambos TA, Berthier E (2014) Rapid bedrock uplift in the Antarctic Peninsula explained by viscoelastic response to recent ice unloading. Earth and Planetary Science Letters 397:32 – 41, DOI 10.1016/j.epsl.2014.04.019

Olsson PA, Breili K, Ophaug V, Steffen H, Bilker-Koivula M, Nielsen E, Oja T, Timmen L (2019) Postglacial gravity change in Fennoscandia—three decades of repeated absolute gravity observations. Geophysical Journal International 217(2):1141–1156, DOI 10.1093/gji/ggz054

Pagiatakis SD (1990) The response of a realistic earth to ocean tide loading. Geophysical Journal International 103(2):541–560, DOI 10.1111/j.1365-246X.1990.tb01790.x

Pagiatakis SD, Salib P (2003) Historical relative gravity observations and the time rate of change of gravity due to postglacial rebound and other tectonic movements in Canada. Journal of Geophysical Research: Solid Earth 108(B9), DOI 10.1029/2001JB001676

Peltier WR (1974) The impulse response of a Maxwell Earth. Reviews of Geophysics 12(4):649–669, DOI 10.1029/RG012i004p00649

Peltier WR (2004) Global Glacial Isostasy and the Surface of the Ice-Age Earth: The ICE-5G (VM2) Model and GRACE. Annual Review of Earth and Planetary Sciences 32(1):111–149, DOI 10.1146/annurev.earth.32.082503.144359

Peltier WR, Argus DF, Drummond R (2015) Space geodesy constrains ice age terminal deglaciation: The global ICE-6G_C (VM5a) model. Journal of Geophysical Research: Solid Earth 120(1):450–487, DOI 10.1002/2014JB011176

Peltier WR, Argus DF, Drummond R (2018) Comment on An Assessment of the ICE-6G_C (VM5a) Glacial Isostatic Adjustment Model by Purcell et al. Journal of Geophysical Research: Solid Earth 123(2):2019–2028, DOI 10.1002/2016JB013844

Petit G, Luzum B (2010) IERS Conventions (2010). Tech. rep., International Earth Rotation Service (IERS), Frankfurt am Main

Plag HP, Pearlman M (2009) Global Geodetic Observing System: Meeting the Requirements of a Global Society on a Changing Planet in 2020. Springer-Verlag, DOI 10.1007/978-3-642-02687-4

Plag HP, Nørbech T, Kristiansen O (2002) Effects of intraplate deformations on fixing regional reference frames, pp 118–124

Rebischung P, Garayt B, Collilieux X, Altamimi Z (2012a) IGS Reference Frame Working Group Coordinator Report, University of Bern, Bern, pp 171–178. DOI 10.7892/boris.80303

Rebischung P, J G, Ray J, R S, X C, B G (2012b) IGS08: The IGS realization of ITRF2008. GPS Solutions 16:483–494, DOI 10.1007/s10291-011-0248-2

Rebischung P, Altamimi Z, Ray J, Garayt B (2016) The IGS contribution to ITRF2014. Journal of Geodesy 90:611630, DOI 10.1007/s00190-016-0897-6

Reuter R (1982) Über Integralformeln der Einheitssphäre und harmonische Splinefunktionen. PhD thesis, doctoral Thesis

Rietbroek R (2016) Retrieval of Sea Level and Surface Loading Variations from Geodetic Observations and Model Simulations: an Integrated Approach Determination. PhD thesis, Deutsche Geodätische Komission, Munich

Ritsema J, Deuss A, van Heijst HJ, Woodhouse JH (2011) S40RTS: a degree-40 shear-velocity model for the mantle from new Rayleigh wave dispersion, teleseismic traveltime and normal-mode splitting function measurements. Geophysical Journal International 184(3):1223–1236, DOI 10.1111/j.1365-246X.2010.04884.x

Riva RE, Gunter BC, Urban TJ, Vermeersen BL, Lindenbergh RC, Helsen MM, Bamber JL, van de Wal RS, van den Broeke MR, Schutz BE (2009) Glacial Isostatic Adjustment over Antarctica from combined ICESat and GRACE satellite data. Earth and Planetary Science Letters 288(3):516 – 523, DOI 10.1016/j.epsl.2009.10.013

Schaeffer AJ, Lebedev S (2013) Global shear speed structure of the upper mantle and transition zone. Geophysical Journal International 194(1):417–449, DOI 10.1093/gji/ggt095

Schöne T, Schön N, Thaller D (2009) IGS Tide Gauge Benchmark Monitoring Pilot Project (TIGA): scientific benefits. Journal of Geodesy 83:249–261, DOI 10.1007/s00190-008-0269-y

Schotman H, Vermeersen L (2005) Sensitivity of glacial isostatic adjustment models with shallow low-viscosity earth layers to the ice-load history in relation to the performance of GOCE and GRACE. Earth and Planetary Science Letters 236(3):828 – 844, DOI 10.1016/j.epsl.2005.04.008

Schumacher M, King MA, Rougier J, Sha Z, Khan SA, Bamber JL (2018) A new global GPS data set for testing and improving modelled GIA uplift rates. Geophysical Journal International 214(3):2164–2176, DOI 10.1093/gji/ggy235

Sella GF, Dixon TH, Mao A (2002) REVEL: A model for Recent plate velocities from space geodesy. Journal of Geophysical Research: Solid Earth 107(B4), DOI 10.1029/2000JB000033

Sella GF, Stein S, Dixon TH, Craymer M, James TS, Mazzotti S, Dokka RK (2007) Observation of glacial isostatic adjustment in “stable” North America with GPS. Geophysical Research Letters 34(2), DOI 10.1029/2006GL027081

Sen PK (1968) Estimates of the Regression Coefficient based on Kendall’s Tau. Journal of the American Statistical Association 63(324):1379–1389, DOI 10.1080/01621459.1968.10480934

Shepherd A, Ivins E, Rignot E, Van den Broeke M, Whitehouse P, Briggs K, Joughin I, Krinner G, Nowicki S, Payne A, Scambos T, Schlegel N, A G, Agosta C, Ahlstrøm

A, Babonis G, Barletta V, Blazquez A, et al (2018) Mass balance of the Antarctic Ice Sheet from 1992 to 2017. Nature 558, DOI 10.1038/s41586-018-0179-y

Shepherd A, Gilbert L, Muir AS, Konrad H, McMillan M, Slater T, Briggs KH, Sundal AV, Hogg AE, Engdahl ME (2019) Trends in Antarctic Ice Sheet Elevation and Mass. Geophysical Research Letters 46(14):8174–8183, DOI 10.1029/2019GL082182

Šidák Z (1967) Rectangular Confidence Regions for the Means of Multivariate Normal Distributions. Journal of the American Statistical Association 62(318):626–633, DOI 10.1080/01621459.1967.10482935

Simon KM, Riva REM (2020) Uncertainty Estimation in Regional Models of Long-Term GIA Uplift and Sea Level Change: An Overview. Journal of Geophysical Research: Solid Earth 125(8):e2019JB018983, DOI 10.1029/2019JB018983

Simpson M, Wake L, Milne G, Huybrechts P (2011) The influence of decadal- to millennial-scale ice mass changes on present-day vertical land motion in Greenland: Implications for the interpretation of GPS observations. Journal of Geophysical Research: Solid Earth 116(2), DOI 10.1029/2010JB007776

Simpson MJ, Milne GA, Huybrechts P, Long AJ (2009) Calibrating a glaciological model of the Greenland ice sheet from the Last Glacial Maximum to present-day using field observations of relative sea level and ice extent. Quaternary Science Reviews 28(17):1631–1657, DOI 10.1016/j.quascirev.2009.03.004, quaternary Ice Sheet-Ocean Interactions and Landscape Responses

Spada G (2016) Glacial Isostatic Adjustment and Contemporary Sea Level Rise: An Overview. Surveys in Geophysics pp 1–33, DOI 10.1007/s10712-016-9379-x

Spada G, Stocchi P (2006) The Sea Level Equation, Theory and Numerical Examples, vol 96

Spada G, Barletta VR, Klemann V, Riva REM, Martinec Z, Gasperini P, Lund B, Wolf D, Vermeersen LLA, King MA (2011) A benchmark study for glacial isostatic adjustment codes. Geophysical Journal International 185(1):106–132, DOI 10.1111/j.1365-246X.2011.04952.x

Steffen H, Wu P (2011) Glacial isostatic adjustment in Fennoscandia: A review of data and modeling. Journal of Geodynamics 52:169–204, DOI 10.1016/j.jog.2011.03.002

Steigenberger P, Rothacher M, Dietrich R, Fritsche M, Rülke A, Vey S (2006) Reprocessing of a global GPS network. Journal of Geophysical Research: Solid Earth 111(B5), DOI 10.1029/2005JB003747

Steigenberger P, Rothacher M, Fritsche M, Rülke A, Dietrich R (2009) Quality of reprocessed GPS satellite orbits. Journal of Geodesy 83:241–248, DOI 10.1007/s00190-008-0269-y

Tanaka Y, Klemann V, Martinec Z, Riva REM (2011) Spectral-finite element approach to viscoelastic relaxation in a spherical compressible Earth: application to GIA modelling. Geophysical Journal International 184(1):220–234, DOI 10.1111/j.1365-246X.2010.04854.x

Tarasov L, Dyke AS, Neal RM, Peltier W (2012) A data-calibrated distribution of deglacial chronologies for the North American ice complex from glaciological modeling. Earth and Planetary Science Letters 315-316:30 – 40, DOI 10.1016/j.epsl.2011.09.010, sea Level and Ice Sheet Evolution: A PALSEA Special Edition

Teunissen P (2017) Batch and Recursive Model Validation. In: Teunissen P, Montenbruck O (eds) Springer Handbook of Global Navigation Satellite Systems, Springer International Publishing, Cham, pp 687–720, DOI 10.1007/978-3-319-42928-1_24

Theil H (1950) A rank-invariant method of linear and polynomial regression analysis. Indagationes Mathematicae 12:85–91, DOI 10.1080/01621459.1968.10480934

Thomas ID, King MA, Bentley MJ, Whitehouse PL, Penna NT, Williams SDP, Riva REM, Lavallée DA, Clarke PJ, King EC, Hindmarsh RCA, Koivula H (2011) Widespread low rates of Antarctic glacial isostatic adjustment revealed by GPS observations. Geophysical Research Letters 38(22), DOI 10.1029/2011GL049277

Torge W, Müller J (2012) Geodesy, 4th ed. De Gruyter, Vienna, Austria

Turcotte DL, Schubert G (2002) Geodynamics, 2nd edn. Cambridge University Press, Cambridge

van Dam T, Francis O, Wahr J, Khan S, Bevis M, van den Broeke M (2017) Using GPS and absolute gravity observations to separate the effects of present-day and Pleistocene ice-mass changes in South East Greenland. Earth and Planetary Science Letters 459:127 – 135, DOI doi.org/10.1016/j.epsl.2016.11.014

van der Wal W, Barnhoorn A, Stocchi P, Gradmann S, Wu P, Drury M, Vermeersen B (2013) Glacial isostatic adjustment model with composite 3-D Earth rheology for Fennoscandia. Geophysical Journal International 194(1):61–77, DOI 10.1093/gji/ggt099

van der Wal W, Whitehouse PL, Schrama EJ (2015) Effect of GIA models with 3D composite mantle viscosity on GRACE mass balance estimates for Antarctica. Earth and Planetary Science Letters 414:134 – 143, DOI 10.1016/j.epsl.2015.01.001

Velicogna I, Wahr J (2006a) Acceleration of Greenland ice mass loss in spring 2004. Nature 443(7109):329–331, DOI 10.1038/nature05168

Velicogna I, Wahr J (2006b) Measurements of time-variable gravity show mass loss in Antarctica. Science 311(5768):1754–1756, DOI 10.1126/science.1123785

Vestøl O, Ågren J, Steffen H, Kierulf HP, Tarasov L (2019) NKG2016LU: a new land uplift model for Fennoscandia and the Baltic Region. Journal of Geodesy 93:1759–1779, DOI 10.1007/s00190-019-01280-8

Wahr J, Wingham D, Bentley C (2000) A method of combining ICESat and GRACE satellite data to constrain Antarctic mass balance. Journal of Geophysical Research: Solid Earth 105(B7):16279–16294, DOI 10.1029/2000JB900113

Wegener A (1915) Die Entstehung der Kontinente und Ozeane. Vieweg und Sohn, Braunschweig

Wessel P, Smith WHF, Scharroo R, Luis J, Wobbe F (2013) Generic Mapping Tools: Improved Version Released. Eos, Transactions American Geophysical Union 94(45):409–410, DOI 10.1002/2013EO450001

Whitehouse P, Latychev K, Milne GA, Mitrovica JX, Kendall R (2006) Impact of 3-D Earth structure on Fennoscandian glacial isostatic adjustment: Implications for space-geodetic estimates of present-day crustal deformations. Geophysical Research Letters 33(13), DOI 10.1029/2006GL026568

Whitehouse PL (2009) Glacial isostatic adjustment and sea-level change: State of the art report. Technical Report, Svensk Kärnbränslehantering, Stockholm, URL http://dro.dur.ac.uk/7480/, ISSN: 1404-0344

Whitehouse PL (2018) Glacial isostatic adjustment modelling: historical perspectives, recent advances, and future directions. Earth Surface Dynamics 6(2):401–429, DOI 10.5194/esurf-6-401-2018

Whitehouse PL, Bentley MJ, Milne GA, King MA, Thomas ID (2012) A new glacial isostatic adjustment model for Antarctica: calibrated and tested using observations of relative sea-level change and present-day uplift rates. Geophysical Journal International 190(3):1464–1482, DOI 10.1111/j.1365-246X.2012.05557.x

Wolstencroft M, Shen Z, Törnqvist TE, Milne GA, Kulp M (2014) Understanding subsidence in the Mississippi Delta region due to sediment, ice, and ocean loading: Insights from geophysical modeling. Journal of Geophysical Research: Solid Earth 119(4):3838–3856, DOI 10.1002/2013JB010928

Woodworth PL (2006) Some important issues to do with long-term sea level change. Philosophical Transactions of the Royal Society A: Mathematical, Physical and Engineering Sciences 364(1841):787–803, DOI 10.1098/rsta.2006.1737

Wu D, Yan H, S Y (2018) L1 regularization for detecting offsets and trend change points in GNSS time series. GPS Solutions 22, DOI 10.1007/s10291-018-0756-4

Wu P (2006) Sensitivity of relative sea levels and crustal velocities in Laurentide to radial and lateral viscosity variations in the mantle. Geophysical Journal International 165(2):401–413, DOI 10.1111/j.1365-246X.2006.02960.x

Yousefi M, Milne GA, Love R, Tarasov L (2018) Glacial isostatic adjustment along the Pacific coast of central North America. Quaternary Science Reviews 193:288–311, DOI 10.1016/j.quascirev.2018.06.017

Zwally HJ, Giovinetto MB, Beckley MA, Saba JL (2012) Antarctic and Greenland Drainage Systems. Internal report, URL http://icesat4.gsfc.nasa.gov/cryo_data/ant_grn_drainage_systems.php